Evolution des propriétés mécaniques des verres silicatés: impact de la composition chimique et des irradiations

Marina Barlet

École Polytechnique

Evolution of mechanical properties of silicate glasses: Impact of the chemical composition and Effects of irradiation

THÈSE

présentée et soutenue publiquement le 16 Septembre 2014

pour l'obtention du titre de

Docteur de l'École Polytechnique

(spécialité physique)

par

Marina Barlet

devant le jury composé de :

Président :	Patrick Letallec
Rapporteurs :	Russell Hand Laurence Galoisy
Examinateurs :	Véronique Doquet Tanguy Rouxel Nolwenn Chouard
Directeur de thèse :	Jean-Marc Delaye
Encadrant :	Cindy L. Rountree
Invité :	Bruno Boizot

Service de Physique de l'Etat Condensé — CEA Saclay

Mis en page avec la classe thloria.

Remerciements

Ces remerciements sont l'aboutissement de trois ans de travail durant lesquelles j'ai pu rencontrer et travailler avec beaucoup de personnes, j'espère n'oublier personne.
Avant tout, je tiens à remercier mon directeur de thèse Jean-Marc Delaye et mon encadrante Cindy Rountree pour leurs conseils, leurs disponibilités et leur confiance tout au long de ces trois ans. Je remercie tout particulièrement Cindy qui m'a suivi au quotidien et qui a su être disponible du début à la fin tout en me laissant beaucoup de libertés.
Un grand merci également á Daniel Bonamy pour sa gentillesse, sa patience, sa disponibilité.
Enfin Thierry Bernard... qu'aurions nous fait sans toi ? Tu as été d'une aide précieuse pendant ces trois années car tu étais là au quotidien pour réparer/modifier/créer des dispositifs expérimentaux. Merci à toi !
Je remercie les membres du jury d'avoir accepter d'évaluer ce travail: M. Patrick Letallec, M. Russell Hand et Mme Laurence Galoisy pour leur travail de rapporteur ainsi que Mme Véronique Doquet, M. Tanguy Rouxel et M. Nolwenn Choouard pour leur travail d'examinateur.
Ce travail expérimental résulte de nombreuses collaborations. Un grand merci à Bruno Boizot pour les mesures RPE ainsi que les discussions qui en ont découlées. Un grand merci aussi à Davy Dalmas qui m'a permis de faire des mesures de nano-indentation à SGR au laboratoire Surface du verre et Interfaces et Thibault Charpentier pour m'avoir permis de réaliser les mesures RMN.
Enfin je remercie le chef du Laboratoire de Matériaux et Procédés actifs Christophe Jégou de m'avoir accueilli quelques semaines par an pendant cette thèse. Sylvain, Olivier et Richard pour les discussions autour des spectres plus ou moins compréhensibles. Un merci particulier à Richard et Mickael pour les journées passées à indenter ou a acquérir des spectres. Je remercie également l'ensemble du LMPA.
Je finis ces remerciements par les personnes du feu SPCSI qui ont rendu les journés de thése agréables: Titi Bernard, Yannick Dappe (que pour la blague du vendredi), Bruno Dolomez, Jérémy Hieulle, Catherine Julien, Christine Prigian, Sylvain Lattil, Luc Barbier, Bruno Lectard, Claire Mathieu d'Houlgate, Jean-Baptiste Moussy, Julien Rault, Fabien Silly, Alexander Simogunov, Ludovic Tortech, Vincent Bart, Sara Gonzalez, Christophe Lubin, Romain Brisse, Maxime Rioult, Jelle Dionot, Marine Gay, Rocio De Miguel Viscasillas, Keyvan Piroid,etc. Je dois dire que Claire Mathieu d'Houlgate et Sara Gonzalez ont particulièrement contribuée à à rendre la fin de thèse agréable que ce soit au labo ou dans les bouchons ! Enfin merci à Jon Barès mon collègue de bureau pendant 2 ans pour son humour et sa bonne humeur.
Mes derniers remerciement vont à ma famille. Je tiens particuliérement à remercier mes parents qui m'ont permis de mener à bien ces longues études.
Mon dernier merci ira à toi ,Samuel pour ton soutien, tes conseils mais également pour tous ces moments partagés entre Paris et Hradec Kralové. Merci...

Contents

List of Figures

List of Tables

Introduction and motivation

Glass is one of the oldest synthetic materials used by man. The interest in glasses only grows from year to year due to their widespread applications. This results from a number of physical properties which differentiate amorphous media from their crystalline counterpart.

Oxide glasses are highly homogeneous and isotropic materials at scales larger than a few nanometers. This strong degree of homogeneity is at the origin of their most interesting properties: optical transparency, electrical and heat isolation, and large hardness to name a few. Because of this, glass finds many industrial applications including: building materials (windows glass), laboratory glassware, cookware, optical components, etc. Moreover, borosilicate glasses are integral parts of systems under external and internal irradiation (satellites, glass packages of radioactive waste...) which gradually alters the glass structure. Glass' main drawback is its brittleness.

Due to the extreme homogeneity of glasses, continuum elastic descriptions is adequate to describe stress, strain and displacement fields in the material down to very small length scales. Thus, the energy released for growing cracks is accessible numerically. At very small length scales the homogeneity of the glass ceases to exist: fluctuations in the glasses structure come about. Concentration of stresses near flaws enables low loads (applied at the continuum scale) to overcome the energy barriers (i.e. the fracture energy) needed to create new fracture surfaces or nucleate and propagate a crack. At the crack tip, dissipation processes are present within a tiny zone, so called the fracture process zone. This separation of length-scales, intrinsic to fracture mechanics, makes it impossible to replace the material by an effective homogeneous material whose toughness or life-time is given by an "average" of the various microstructure components. These mechanical properties, observed at the macroscopic scale, result from local events (damage, plastic deformation, decohesions, environment assisted chemical reactions, etc.) located around one or few dominant flaws or weak points at the scale of the material's microstructure. These things get even more complex when the material modifies internally its structural disorder because of self-irradiation, for instance.

The fundamental problem tackled in this thesis is to understand how variations in the chemical composition, the structural properties (and their eventual modification through various types of irradiations) affect the mechanical properties and more specifically the failure properties of oxide glasses. Part I of this

thesis concentrates on how the chemical composition (and thus structural properties) alters the mechanical properties of the glass, including stress corrosion cracking behavior and hardness properties. These studies concentrate on 8 SBN ($Na_2O - B_2O_3 - SiO_2$) glasses. By modulating the chemical composition, the study exposes the role of each oxide.

Part I chapter 1 reviews the current knowledge about structural and mechanical properties of glasses with a concentration on SBN glasses. Then, chapter 2 describes the glass composition studied and the experimental set-up used to investigate structural and mechanical properties. Chapter 3 addresses how the glass composition changes the physical and the structural properties of SBN glasses. Finally, chapter 4 details and links the evolution of mechanical and failure behaviors to the glass structure.

Part II of this thesis concentrates on how tweaking the structure of the glass via external irradiation alters the mechanical properties of the glass, including stress corrosion cracking behavior and hardness properties. These studies concern the storage of nuclear waste. Fission products (FP) and minor actinides (MA) from spent fuel are embedded in complex alumino boro silicate glasses (frequently R7T7 in France). Ensuring the durability of these glasses over the long-term (up to few hundreds of thousands of years) still presents a major challenge. Safety confining them dictates an understanding of their variations in micro-structural properties due to self-irradiation. Self-irradiation gives way to electronic and ballistic interactions; the latter appears to govern the evolutions of the properties. Additionally, micro-structural variations can scale up to variations in the macroscopic properties (ρ, K_C, H_V, SCC...) which also needs to be understood.

Complex borosilicate glasses contain over 60 different oxides, plus it is undergoes self-irradiation. Thus pinpointing the dominant features of the glass is cumbersome if not impossible. Moreover, the high level activity of these glasses limits experimental accessibility. Hence, scientists complement complex glasses studies with studies on model glasses. One set of model glasses used is the SBN series as the three dominant oxides in R7T7 are sodium oxide (Na_2O), boron trioxide (B_2O_3), and silica (SiO_2). Moreover, the mechanical behavior of the simplified glasses frequently mimics the mechanical behavior of R7T7. These studies concentrate on pure amorphous silica and 4 SBN ($Na_2O - B_2O_3 - SiO_2$) glasses. The SBN glasses implemented in this study are two low and two high [Na_2O] concentration glasses. Again, by controlling the mole ratios of each element, the study exposes the role of each oxide.

The aim of this part is to understand how minute variations in the structure of a glass alter the glass' mechanical properties. Electron and (light and heavy) ion irradiation tweak the structure of the glass. Subsequently, studies examine their mechanical response. Electron irradiation varies the structure of the glasses via electronic interactions. Light and heavy ions give way to both electronic and ballistic interactions. Chapter 1 provides a brief review of High Level Waste (HLW), and the type of self-irradiation damage these glasses undergo. Along with examining HLW, it also presents previous studies on simplified glasses under external or internal irradiation. Samples herein frequently reuse experimental set-ups used in Part I. However, conducting irradiation and subsequently analysis of the samples requires some new techniques. Chapter 2 describes these set-ups. Chapter 3 details structural modifications induced by electron, helium ions and gold ions irradiation on a simple glasses, pure amorphous silica. Chapter 4 presents and discusses hardness and failure properties in regard to structure modifications induced by electron on the SBN series. Chapter 5 details the same for light and heavy ions on the SBN series.

Part I

Linking mechanical properties to chemical composition

Chapter 1

Context

Contents

Glass is well known as a brittle material, i.e. it breaks abruptly without any plastic deformation. Yet, the propagation of subcritical crack growth can limit the material's life time. Despite its brittleness, glass has several advantageous properties: optical transparency, chemically resistant, easily cleaned, long life, high melting temperature, etc., which means it can be used in cook ware, laboratory beakers, windowpanes, lenses, etc. Thus, it is crucial for researchers and engineers to understand the properties of these glasses to ensure the structural integrity glass' final application. This chapter presents a review of the structure, physical, and mechanical properties of silica based glasses. The section 1.1 describes the glass structure and how the sodium content changes the glass topology according to the Yun, Dell and Bray model. Then the section 1.2 details briefly how the glass behaves under the indenter and details the fracture processes in the stress corrosion regime. Finally, the section 1.3 reviews the current knowledge of fracture mechanics.

1.1 Glass structure

Natural glass has existed since the depths of time. Early man during the stone ages used obsidian glass (formed naturally from magma that cools rather quickly preventing the formation of a crystalline material) to make arrows and other tools. The first evidence of man-made glass objects dates back to around 3500 BC in north Syria, Mesopotamia or Ancient Egypt. With the knowledge of how to make glass, glasses have undergone several major historical events including:

- 1500 BC: Egyptian craftsmen began developing a method for producing glass pots (figure 1.1).
- End of the 1^{st} century: The discovery of glass blowing techniques.
- End of the 13^{th} century: The glass industry began to flourish in Europe with the development of an industry in Venice.
- After 1890: Over the past 125 years, the development, manufacture and use of glass increased rapidly.
- Today: Glasses make up extensive components (or the principle component) of a wide variety of industrial applications: cookware, telecommunications, optics, nuclear waste protection, strained glass etc.

Despite all of these applications, how a glass structure impacts its physical and mechanical behavior remains a mystery to scientists and engineers.

Figure 1.1: Egyptian glass jar from 1500-1000 BC [4] and strained glass created in 1987-1994 by P. Soulages.

In 1982, Zarzycki [85] defined glasses as *a homogeneous non-crystalline solid which exhibits glass transformation behavior*. Non-crystalline solids concerns solids in which quenching, mechanical activation or radiation induce excess energy. Therefore they contain more energy than the crystalline phases corresponding to a metastable i.e. non-equilibrium states of matter. Glasses are usually characterized by modifications of their properties, e.g. as the temperature increases the glass approaches the glass tran-

sition (a more fluid state). As a consequence, the thermal history of glass affects significantly the glass properties.

1.1.1 Formation of glass oxides: Zachariasen's rules

In 1932, W.H. Zachariasen [84] described the ability of various oxides to form glass. This pioneering work showed that the cations and anions bound together as their crystalline counterparts but they don't have the long range order as a crystal. In the short range, the cations and anions bound together forming polyhedral units such as tetrahedral and 5 or 6-coordinated sites. Thus, glasses and crystals have the same building blocks arranged in different patterns; e.g., glasses have broader distributions of bond angles. A classic example is amorphous silica glass (figure 1.2 right) versus cristobalite (figure 1.2 left). Both have silica atoms surrounded by 4 oxygen atoms forming a tetrahedron. For the amorphous silica glass structure, the structure does not have any periodicity or symmetry at the long range (figure 1.2). Zachariasen's model titled *Random Network Theory* attempts to describe the glass network via four rules:

1. An oxygen atom links at most to two glass-forming atoms.
2. The coordination number of the glass-forming atoms is small (3-4).
3. The network former polyhedral share corners with each other, not edges of faces.
4. The polyhedral are linked in a three-dimensional networks.

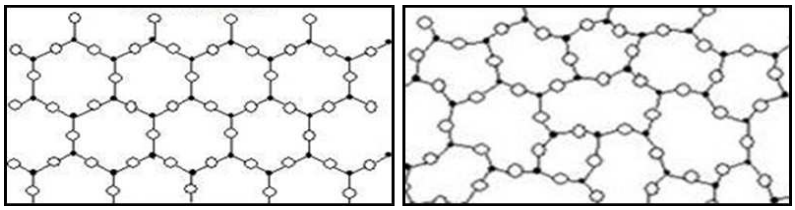

cristobalite glass

Figure 1.2: SiO_2 ring organization in cristobalite and silica glass. The solid black circles represent silica atoms. Open black circles represent oxygen atoms.

Oxides following these considerations are called *network formers*. They can form a highly cross-linked network of chemical bonds. SiO_2, B_2O_3 are the most common network formers, GeO_2 and P_2O_5 can be also cited. A few other elements, such as Al_2O_3, Fe_2O_3, TiO_2..., cannot form glassy network by themselves. Their electronegativities are less and their bonds with oxygen are more ionic. Thus they can substitute network formers. These refer to the *intermediate* elements. A third category of elements exists: *the network modifiers*. Their electronegativities are less than the oxygen ones. They cannot form a glassy network nor replace a network former as intermediates. In the glass network, they can compensate negative charge of network formers element such as boron ($^{[4]}B$) or depolymerize the glassy network by creating non-bridging oxygen atoms (NBO). They are called compensator and modifiers, respectively. Atoms included in this set incorporate alkali and alkaline earth atoms. An advantage to these elements is a decrease in the elaboration temperature. In 1985, Greaves put forth the *Modifying Random Network*

model [30]. According to this model, the modifiers form clusters of enriched areas rather than spread out randomly in the glassy network. Thus, the glass contains areas enriched in the network formers and areas enriched in modifiers figure 1.3.

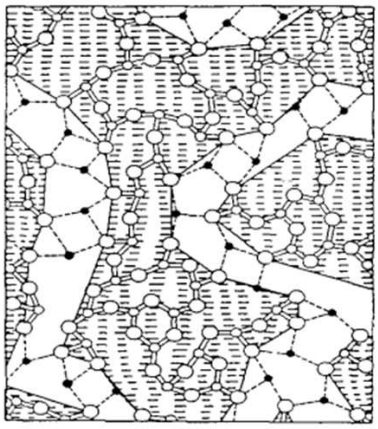

Figure 1.3: A modified random network for a 2 dimensional oxide glass. The dashed zones correspond to areas enriched in network formers. Black points represent network modifiers [30].

1.1.2 Ternary borosilicate glass make up

Borosilicate glasses are extensively used by industry. This system presents two demixion areas. For less than 20 % mol of Na_2O, phase separation occurs. Thus, one area is enriched in silica and the other one in boron and sodium. Increasing [Na_2O] ([] $\equiv$ mol %) leads to a more homogeneous glass. At [Na_2O] $\sim$ 50 %mol the glass crystallization happens. In the late 1970's and early 1980's Dell et al. published a series of papers [7, 19, 83] on how the addition of sodium to binary SiO_2-B_2O_3 glass modifies the structural units of the system[1] . Table 1.2 presents the chemical formula and the description of borate units. As presented by Feil and Feller [23], the initial addition of sodium to a binary SiO_2-B_2O_3 glass leads to the creation of $^{[4]}$B tetrahedrons and the annihilation of a planar $BO_{3/2}$ units. It is conjectured that the structure being formed during this transformation is a diborate group (2$\times$ $^{[4]}$B and 2$\times$ $^{[3]}$B with zero NBO). During this process the silica network remains undisturbed. Implying the number of NBO on silica tetrahedrons is zero. It is expected that no mixing exists between the silica and the boron networks. This process continues until R_{SBN}=$\frac{[Na_2O]}{[B_2O_3]}$=0.5. Subsequently between R_{SBN}=0.5 and R^{max}_{SBN}= 0.5 +$\frac{K_{SBN}}{16}$ (K_{SBN}=$\frac{[SiO_2]}{[B_2O_3]}$), reedmergnerite units appear to the detriment of diborate groups. Reedmergnerite units contain one four-coordinated boron bonded to 4 silica tetrahedrons (chemical composition: $\frac{1}{2}$(B_2O_3 Na_2O $8SiO_2$). The number of $^{[4]}$B still increases linearly with R_{SBN}. Otherwise the silica network remains fully coordinated with no NBO. The table 1.1 defines the f_1, f_2, f_3 and f_4 fractions. Table 1.1 defines nomenclature commonly used in literature [2, 7, 19, 23, 41, 83]. The $BO_{3/2}$ refers to planar 3 coordinated boron atoms. $f(Si_{NBO})$ defines the fraction of NBOs on each silica tetrahedra. The fractions between R_{SBN}=0 and R^{max}_{SBN} are [7, 19, 23, 41, 83]:

[1] Part of this review is contained in the Barlet et al. publication [2]

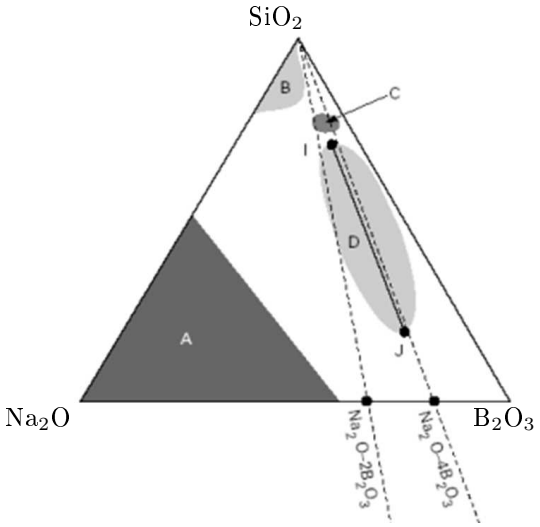

Figure 1.4: Ternary diagram of the SiO_2-B_2O_3-Na_2O system. A is the crystallization domain, B the Na_2O-SiO_2 metastable demixion domain, C composition range used for laboratory glasses and D the SiO_2-B_2O_3-Na_2O metastable demixion domain.

Fraction	Borate
f_1	$BO_{3/2}$
f_2	BO_4
f_3	$BO_{3/2}$ with 1 NBO
f_4	$BO_{3/2}$ with 2 NBO

Table 1.1: Nomenclature invoked herein, and commonly used in literature, for the fraction of the different borate structures [2, 7, 19, 23, 41, 83]. The $BO_{3/2}$ refers to planar 3 coordinated boron atoms (also called $^{[3]}$B). Another common symbology for the 4 coordinated boron atom (BO_4) is $^{[4]}$B.

$$\left.\begin{array}{rcl} f_1 & = & 1-R \\ f_2 & = & R \\ f_3 & = & 0 \\ f_4 & = & 0 \\ f(Si_{NBO}) & = & 0 \end{array}\right\} 0 < R_{SBN} < R_{SBN}^{max} = 1 + \frac{K_{SBN}}{16} \tag{1.1}$$

Beyond R_{SBN}^{max}, additional sodium causes the formation of NBO on silica units in reedmergnerite groups. This transformation is proposed to be valid until $R_{SBN}^{d1} = 0.5 + 0.25K_{SBN}$. During this process $^{[4]}$B is constant and equal to R_{SBN}^{max} [7, 19, 23, 41, 83]:

$$\left.\begin{array}{rcl} f_1 & = & 1 - R^{max}_{SBN} \\ f_2 & = & R^{max}_{SBN} \\ f_3 & = & 0 \\ f_4 & = & 0 \\ f(Si_{NBO}) & = & \dfrac{2(R - R^{max}_{SBN})}{K_{SBN}} \end{array}\right\} R^{max}_{SBN} < R_{SBN} \leq R^{d1}_{SBN} = 0.5 + 0.25 \times K_{SBN} \quad (1.2)$$

Subsequent molecules of Na_2O are shared between the diborate and reedmergnerite units and the formation of NBO on silica tetrahedrons. During this process diborate units are transformed into pyroborate units at a rate of $\dfrac{(2 - 0.25 \times K_{SBN})}{(2 + K_{SBN})}$. Reedmergnerite units are transformed into pyroborate units and silicate tetrahedrons with 2 NBOs per Si atom at a rate of $\dfrac{(K_{SBN} + 0.25 \times K_{SBN})}{(2 + K_{SBN})}$. This process continues until all 3-coordinated boron units contain at least 1 NBO or $R_{d2} = 1.5 + 0.75 \times K_{SBN}$. Thus, the fractions evolve as follow:

$$\left.\begin{array}{rcl} f_1 & = & \dfrac{(8 - K_{SBN})}{8} \times \left(0.75 - \dfrac{R_{SBN}}{2 + K_{SBN}}\right) \\ f_2 & = & \dfrac{(8 + K_{SBN})}{12} \times \left(1 - \dfrac{R_{SBN}}{2 + K_{SBN}}\right) \\ f_3 & = & \dfrac{(R - R_{1d})}{12} \times \left(\dfrac{8 - K_{SBN}}{2 + K_{SBN}}\right) \\ f_4 & = & \dfrac{(R - R_{1d})}{8} \times \left(\dfrac{8 - K_{SBN}}{2 + K_{SBN}}\right) + \dfrac{K_{SBN}}{6} \times \left(\dfrac{R_{SBN}}{2 + K_{SBN}} - 0.25\right) \\ f(Si_{NBO}) & = & \dfrac{3}{8} + \dfrac{13}{6} \times \left(\dfrac{R_{SBN} - R^{d1}_{SBN}}{2 + K_{SBN}}\right) \end{array}\right\} R^{d1}_{SBN} < R_{SBN} \leq R^{d2}_{SBN} \quad (1.3)$$

Thus, the fractions of each are estimated as follows:

$$\left.\begin{array}{rcl} f_1 & = & 0 \\ f_2 & = & \dfrac{(8 + K_{SBN})}{12} \times \left(1 - \dfrac{R_{SBN}}{2 + K_{SBN}}\right) \\ f_3 & = & \dfrac{1}{6} \times (8 - K_{SBN}) \times \left(1 - \dfrac{R_{SBN}}{2 + K_{SBN}}\right) \\ f_4 & = & \dfrac{8 - K_{SBN}}{16} + \dfrac{R_{SBN} - R^{d2}_{SBN}}{4} \times \left(\dfrac{8 - K_{SBN}}{2 + K_{SBN}}\right) + \dfrac{K_{SBN}}{6} \times \left(\dfrac{R_{SBN}}{2 + K_{SBN}} - 0.25\right) \\ f(Si_{NBO}) & = & \dfrac{3}{8} + \dfrac{13}{6} \times \left(\dfrac{R_{SBN} - R^{d1}_{SBN}}{2 + K}\right) \end{array}\right\} R^{d2}_{SBN} < R_{SBN} \leq R^{d3}_{SBN} \quad (1.4)$$

At this point, models do not predict further evolution of the silicate and borate structure. One would assume that orthoborate units are formed in this region, but not much research currently exists on this topic. Over the past 20 years, the validity of these fractions has been questioned [20,51,52]. How silicate and borate phases are mixed together is a relevant parameter. Recently, Raman investigations identify other units called *danburite* (2 B_2O_3 and 3 SiO_4) [11, 51]. This units emphasized the mixing of the

two networks below $R_{SBN} < 0.5$. As a consequence, Manara et al. [51] proposed to replace the R^{d1}_{SBN} limit by R^{d1}_{SBN}=$0.5 + K_{SBN}/(2N)$ with N being the concentration of SiO_2 in the borosilicate groups (reedmergnerite and danburite).

1.2 Contact damage in glass

Improvement of glass' strength favors the development of experimental techniques such as nano/micro indentation. Depending on the load applied to a glass surface, permanent deformation is feasible independent of a visible flaw. The cracking response results from residual stresses and processes occurring during loading and unloading. Indent pattern and crack response is linked to the glass structure and processing technique. Less brittle glass shows less contact damage and fewer cracks appear.

Glasses with the same hardness value can exhibit different indentation patterns or cracking behaviors. This is why the question of *how matter flows under indenter* is of prime interest. Under hydrostatic pressure, some glasses, such as amorphous silica ($a - SiO_2$), predominantly densify in a permanent manner [8, 21, 50]. Yet, other glasses, such as bulk metallic glasses, undergo volume conservative shear flow processes [81]. Thus, the contribution from each process highly depends on the glass's chemical composition [3, 12, 66].

Two predominant behaviors prevail when studying a glass' response to a sharp indenter: *anomalous* and *normal* behavior. *Anomalous* glasses mainly densify under high external pressure, (e.g. $a-SiO_2$). In these glasses, the atomic packing density is low; thus, under pressure the glasses favor volume shrinkage [64] via the relative movement of the Si-O-Si linkage [21, 50, 73]. On the other hand, *normal* behavior implies volume conserving shear flow. In this case, the indenter causes a pile-up on the surface of the glass by plastic flow. Under these circumstances, the density of pile-up region equates that of the bulk region [37–39, 59]. Typically, glasses with non-bridging oxygens and cations favor this phenomenon [3]. The figure 1.5 depicts these two processes.

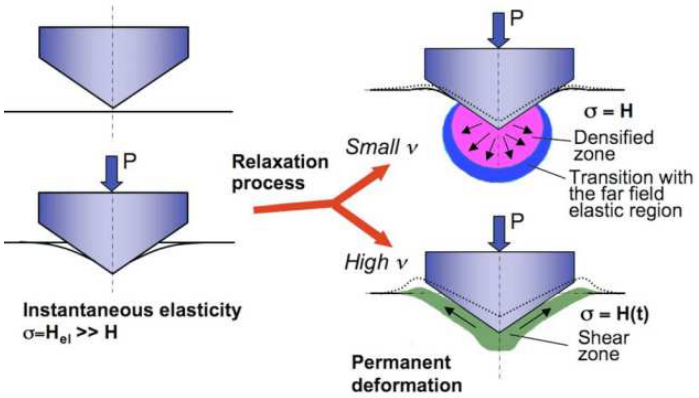

Figure 1.5: Schematic sketch of the deformation processes. Depending on the Poisson's ratio, the glass favor densification or shear flow mechanisms [65].

Borate units	Chemical composition	Description
Diborate	$Na_2O.2B_2O_3$	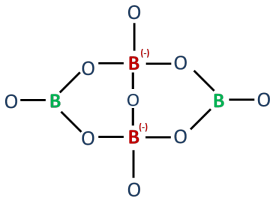
Metaborate	$1/2.Na_2O.B_2O_3$	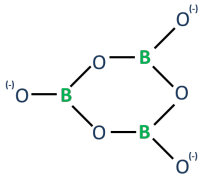
Pyroborate	$1/2.(2.Na_2O.B_2O_3)$	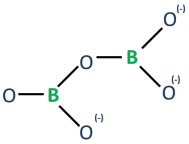
Reedmergnerite	$1/2.(Na_2O.B_2O_3.8SiO_2)$	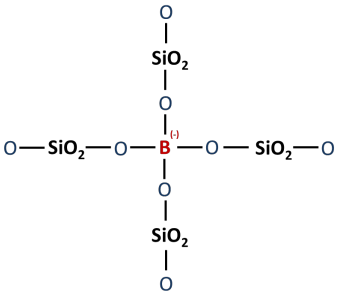
Danburite	$2.B_2O_3.3SiO_2$	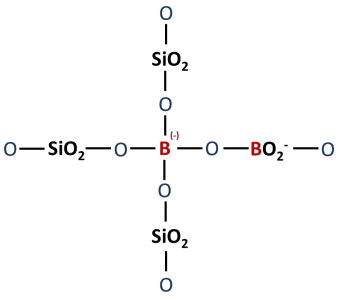

Table 1.2: Glass composition and description of borates units: diborate, metaborate, pyroborate, reedmergnerite and danburite.

In order to discriminate the contribution of each process, researchers developed a simple test to estimate the amount of permanent densification under an indenter in glasses and the amount of plastic flow [50, 68, 69, 81, 82]. Studying the volume ratio (V_R) of an indenter's imprint before and after annealing provides an easy way to estimate the amount of densified volume. Sellappan et al. [69] evidenced a sigmoid trend between the Poisson's ratio, ν, and V_R:

$$V_R = \frac{1}{\alpha_R + \beta_R exp(\chi_R \nu)} + \delta_R \tag{1.5}$$

(α_R, β_R, χ_R, δ_R) are fitting parameters. As ν increases V_R decreases, thus the contribution due to densification decreases. Figure 1.6 presents the data Sellappan et al. [69] collected along with their sigmoid fit.

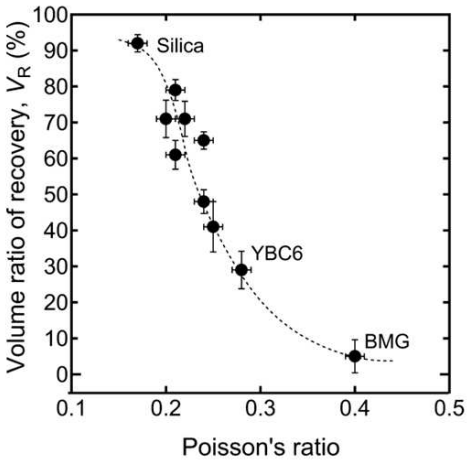

Figure 1.6: Relationship between Poisson's ratio and the volume ratio of recovery (V_R) for various glass compositions (data from [81]).

1.3 Cracking behavior

1.3.1 Fracture

Crack propagation

Linear Elastic Fracture mechanics (LEFM) effectively describes the fracture of brittle solids under tension by reducing the problem to a destabilization and growth of a dominant pre-existing crack. Irwin [42] estimated the local stress around a crack tip in mode I (opening mode; figure 1.8 left) as:

$$\sigma_{i,j} \approx \frac{K_I}{\sqrt{2\pi r}} f_{i,j}(\theta, v) \tag{1.6}$$

for an infinite plane. Figure 1.7 depicts the coordinate system ahead of the crack front: x and y (in cartesian coordinates) correspond to the direction of crack propagation and the direction of strain, respectively; and r and θ are in polar coordinates. v is the crack tip velocity, $f_{i,j}$ is a dimensionless function of the angle θ and the fracture mode. K_I is the *stress intensity factor* which is the key parameter to quantify the macroscopic forcing applying on the crack tip. K_I depends on the external load (σ) and the sample geometry. In general, cracks are not simply in mode I loading. They also undergo shearing

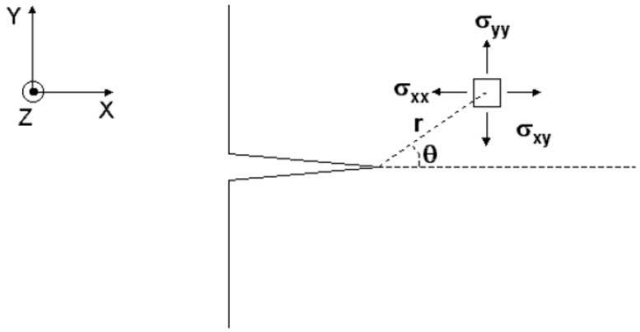

Figure 1.7: Description of the coordinate system ahead of the crack tip.

(mode II or in-plane shearing) and tearing (mode III or out-of plane shearing). Figure 1.8 depicts the three independent loading modes. Due to linear superposition, the total stress at the crack tip is the sum of the three contributions:

$$\sigma_{i,j}^{total} = \sum_{mode} \sigma_{i,j}^{mode} = \sum_{mode} \frac{K_{mode}}{\sqrt{2\pi r}} f_{i,j}^{mode}(\theta) \tag{1.7}$$

The sum is over the different modes of fracture (i.e. I, II, and III). The stress field takes a singular form similar to the equation 1.7 with K_I, K_{II} and K_{III} associated to the tensile, shearing and tearing modes, respectively. Nevertheless, the singularity at the crack tip is physically impossible. This implies that the

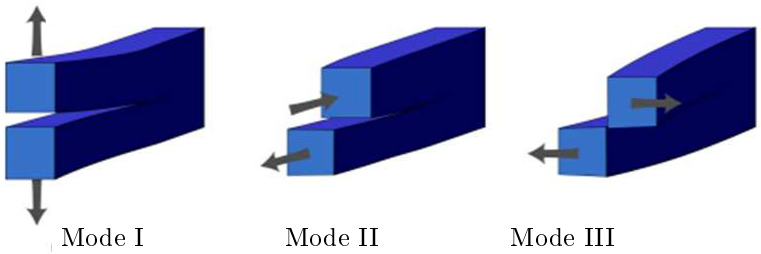

Figure 1.8: Different modes of fracture: mode I (opening), mode II (shearing) and more III (tearing) [1].

material is not linear elastic around the crack tip any more. The area where the stress field is too high to apply the LEFM is called the *Fracture Process Zone* (FPZ) and encompasses all damage and failure mechanisms.

According to Griffith's theory [31], the onset of fracture occurs when the amount of elastic energy stored in the system exceeds the energy required to create two surfaces. G corresponds to the mechanical energy released at the onset of crack propagation and is related to the stress intensity factors. In a simple case of pure tensile loading, G is related to K_I by:

$$G = \frac{K_I^2}{E} \tag{1.8}$$

where E is the Young modulus of the material. The energy dissipated to create two new surfaces of unit area is called the *fracture energy* (Γ) and is considered as a material constant. The Griffith criterion for unstable crack growth is:

$$G > \Gamma \tag{1.9}$$

The balance between the mechanical energy flowing into the FPZ and Γ governs the crack front's advance. Furthermore, a moving crack progresses along a direction so as to remain in pure tension in an homogeneous isotropic solids. The direction of propagation is chosen such as: K_{II}= K_{III}=0.

1.3.2 Stress corrosion

A glass's life-time can be reduced by the propagation of subcritical cracks (i.e. $K_I < K_C$ value). This phenomenon is called stress-corrosion cracking. Wiederhorn in the late 1960's and early 1970's extensively studied subcritical crack propagation [77–79]. Figure 1.9 presents a typical velocity (v) versus stress intensity factor (K_I) curve. Subcritical crack propagation involves three regions: (1) region I is limited

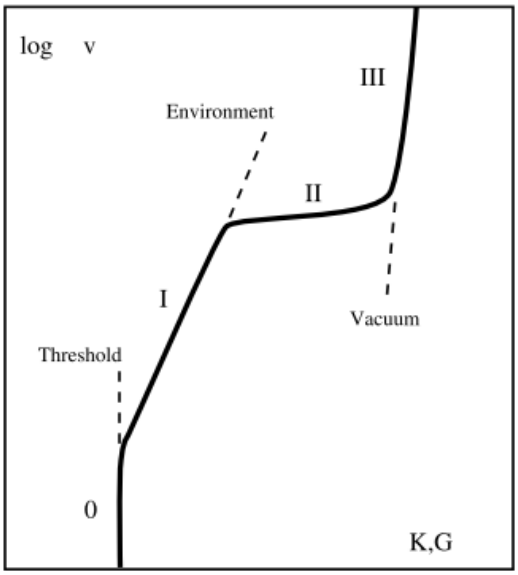

Figure 1.9: Typical v(G) or v(K) diagram for subcritical crack propagation in glass. From [17].

by time of the chemical reaction at the crack tip; (2) region II is limited by the kinetic transport of corrosive molecules to the crack tip; and (3) region III still corresponds to sub-critical crack propagation

and depends on temperature; however, it is independent on the amount of water in the environment [17]. Depending on the glass chemical composition another region (region 0 or the environmental limit, K_E) may exist. For stress intensity factors less than K_E, the crack front does not propagate.

Since the middle of last century, multiple models were proposed to describe the crack velocity dependence [16, 47, 53, 54, 56, 60, 71, 72, 74–76, 78–80] with stress and environmental parameters. The sections below detail region I and region 0 as they are the primary focus of this thesis. (Details on region II and III can be found in these references [17, 55, 78, 79]; however they will not be detailed herein.)

Region I Stress-corrosion cracking involves a complex interplay between the diffusion of reactive molecules into the crack cavity and into the glass network: the corrosion or the dissolution of the glassy network, the migration of weakly bonded alkali ions under chemical or stress gradient.... These phenomena are ideally very slow in ambient conditions for the unstressed material, but small stresses at the continuum level concentrate at the crack tip giving a high stress field at the crack tip. In region I, the crack tips velocity (v) increases as a function of stress intensity factor K_I (figure 1.9). Empirical models have been proposed to explain this trend [16, 47, 53, 60, 78] Some authors propose an exponential fit [47, 60, 78] others a power law fit [24, 35, 53]. One of the original and most commonly used models is by Wiederhorn [78–80]. His model for Region I depends on the temperature and humidity as follows [78, 80]:

$$v = v_0 \exp(\alpha K_I) = A\left(\frac{p_{H_2O}}{p_0}\right)^m \exp\left(-\frac{\Delta E_a - bK_I}{RT}\right) \tag{1.10}$$

where p_{H_2O} is the partial pressure of vapor phase in the atmosphere, p_0 is the total atmospheric pressure, R is the gas constant, and T the temperature. A, m, ΔE_a and b are four fitting parameters that depend on the glass' composition. Wierderhorn's model originates from the reaction-rate theory [80]. The reaction rate constant is:

$$K_r = \kappa\left(\frac{kT}{h}\right)\exp\left(\frac{-\Delta G_0^*}{RT}\right)\left(\frac{f_A^a f_B^b \cdots}{f^*}\right) \tag{1.11}$$

where κ is the transmission coefficient, ΔG_0^* is the Gibbs free energy of activation, and f_A^a,$f_B^b \cdots f^*$ are the activity coefficients for the reactants and for the activated state. The Gibbs free energy of activation is related to the standard chemical potentials of the reactants and the activated complex. By making the assumption that the growth rate is proportional to the rate of chemical reaction at the crack tip the velocity, v, is:

$$v = v_0 a_s \exp(\frac{\mu_{s0} + \mu_g - \mu_0^*}{RT}) \tag{1.12}$$

where a_s is the activity of the water in solutions, μ_{s0}, μ_g and μ_0^* refer to the chemical potentials of the reactants: of the water in solution, the reactive species in the glass (Si-O bonds in the case of pure silica glass) and the activated complex, respectively. Wiederhorn et. al. assumes μ_{s0} does not depend on the stress at the crack tip. On the other hand, both μ_g and μ_0^* depend on the stresses at the crack tip. It should be notice that these parameters change with the stress applied. For increasing stresses at the crack tip, the crack front propagates faster. Hence, the stress applied to the crack tip increases and μ_0^*-μ_g must decrease to expect an increase in the rate of crack growth. Finally, the slope in stress corrosion regime depends on the sensitivity of μ_0^*-μ_g to the applied stress. The greater is the sensitivity, the steeper is the slope in region I. A measurable treatment of free energy of activation ($\Delta G^* = \mu_0^*$-$\mu_{s0} - \mu_g$) stems from

two assumptions: (1) the chemical reaction occurs at the crack tip which has a radius of curvature of ρ_{ct}, and (2) Inglis relation controls the stresses on the individual bonds at the crack tip [77,80]. Wiederhorn writes ΔG_0^* as [80]:

$$\Delta G^* = -T\Delta S^* + \Delta E^* - \left[\frac{2K_I}{\sqrt{\pi\rho_{ct}}}\right]\Delta V^* - \frac{(\gamma^* V^* - \gamma V)}{\rho_{ct}} \tag{1.13}$$

where ΔS^*, ΔE^* and ΔV^* are the activation entropy, energy and volume, respectively. For a system containing a crack under loading, equation 1.13 reveals that the load will accelerate the reaction provided $\Delta V^* > 0$. If $\Delta V^* < 0$, then the reaction at the crack tip will be inhibited [77]. Substituting equation 1.13 into equation 1.12 gives:

$$v = v_0 a_s \exp\left(\frac{\rho_{ct}\left(T\Delta S^* - \Delta E^*\right) + \left(\gamma^* V^* - \gamma V\right)}{RT\rho_{ct}} + \left(\frac{2\Delta V^*}{RT\sqrt{\pi\rho_{ct}}}\right)K_I\right) \tag{1.14}$$

$(\gamma^* V^* - \gamma V)$ changes with fluctuations in the surface curvature are frequently considered negligible. In practicality, equation 1.14 simplifies by assuming constant temperature:

$$v = v_0 \exp\left(\left(-\Delta E_a + bK_I\right)/RT\right) \tag{1.15}$$

where $b = \left(\frac{2\Delta V^*}{\sqrt{\pi\rho_{ct}}}\right)$. Thus b is proportional to the activation volume for the chemical reaction. An increase in ΔV^* implies an increase in the difference between the reactants and the activation complex [77, 80]. Usually ΔV^* is determined by measuring how the reaction rate changes with stress [27]. The lack of data on the impact of tensile stress on ΔV^* makes a general prediction tricky [27]. There is no clear proof an exponential relationship links v to K_I. Literature contains other proposals [24, 53]. For example, Maugis [53] proposed a power law relation between v and K_I:

$$v = v_0\left(\frac{K_I}{K_0}\right)^n \tag{1.16}$$

where n is the slope of the curve called the fatigue parameter [35]. Generally n remains between 12 and 50 for silica based glasses [22]. This theory associates the basic mechanism of SCC with the stress-enhanced thermal activation of the dissociative hydrolysis reaction. Michalske and Freiman [56] attempt to describe the region I by a molecular mechanism by which the water can react with a strained Si-O bond. They distinguished three steps (figure 1.10a): (1) the adsorption of water molecule on strained crack tip; (2) the formation of two silanol groups by cleavage of Si-O and O-H bonds; (3) the formation of two fracture surfaces. The change in the step 1 (reactants) and 3 (products) affect the energy barrier and thus the fracture rate [56]. This model explains also how molecules such as ammonia, hydrazine, etc are able to give rise to linear stress intensity versus $\log v$ relationships: any molecule which is (1) capable to donate a proton on a side and with a lone pair of electron on the other side and (2) small enough to reach the crack tip is capable to react with strained Si-O bonds. Figure 1.11 represents the potential energy for the reaction of Si-O-Si rupture in vacuum and the reaction of Si-O-Si with a water molecule. Changes in the step 1 (reactants) and 3 (products) alter the energy barrier and subsequently the fracture rate [56]. This model also explains how other solutions (including ammonia, hydrazine, etc.)

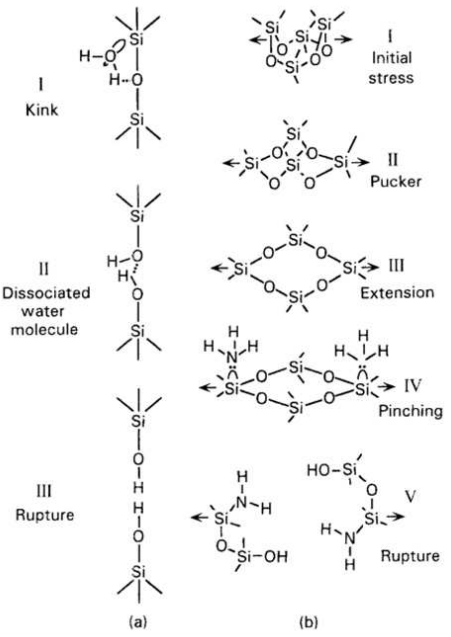

Figure 1.10: Reaction steps for water enhanced fracture of vitreous silica: a) the Michalske and Freiman model [56], and b) the Michalske and Bunker model [54].

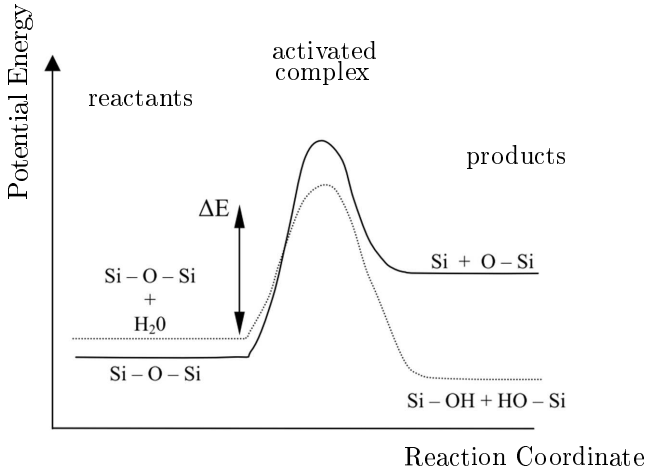

Figure 1.11: Representation of the reaction for bond rupture in silica. The solid line indicates rupture in vacuum, whereas the dashed line depicts the rupture with water from [56].

give rise to linear relationships between K_I and $\log(v)$. Any solution at the crack tip will cause SCC if it is capable of donating a proton on one a side and with a lone pair of electron on the other side. Also the solution's molecule must be small enough to reach the crack tip and react with the strained Si-O-Si bonds. However, Michalske and Freiman's model does not take into account the impact of strain on the chemical reactivity of the solid [54]. Mischalske and Bunker continued the research and developed a five steps model to incorporate strain on the Si-O-Si bonds [54]. Figure 1.10 b) depicts Michalske and Bunker's model. This model has five steps:(1) one silica ring undergoes an external stress, (2) the silica

ring adjusts to the external stress by changing its configuration, (3) the extension of Si-O-Si bond angles and variations in the O-Si-O angles, (4) adsorption of a reactive molecule, and (5) the bond rupture. West and Hench [74–76] examined the impact of the ring size with bond rupture using first principle calculations. They simulated the reaction of a water molecule with a strained 3- 4- and 5-fold silica rings. This study reveals that during SCC 5-membered rings accommodate stress better by reorganizing themselves. Smaller rings are extremely limited by the amount of reorganization possible; thus they react with water at lower energies.

Tomozawa proposed an alternative to the Wiederhorn's model to explain the interaction between the crack tip and a water molecule. For this model, the water molecule penetrates into the stressed regions. For example, Nogami and Tomozawa [58] subjected silica slides to four point bending tests under high pressures and elevated temperatures. After treatment the samples contained a hydrated layer several micrometers thick. This work was further extended by Tomozawa et al. in 1991. This test uses DCDC (Double cleavage drilled compression) samples for SCC experiments conducted in water, air, and oil. These experiments found hydrogen at depths of 10 nm [71] on post-mortem fracture surfaces. It is highly unlikely that Hydrogen penetrates to such depths in unstressed states. Recently, Lechenault et al. conducted a similar experiment as Tomozawa's et al. in 1991. These experiments were performed in heavy water atmospheres. Subsequently, the penetration depth of the heavy hydrogen was measured by neutron reflectivity [48]. Heavy water penetrated $\sim$ 6.5 to 8.5 nm perpendicular to the direction of stress corrosion crack growth in pure silica fracture surfaces. This highlights the fact high stresses near the crack front enable the water diffusion [71]. The water molecules damage the zone and aids in the further propagation.

All of these models are based on pure silica glasses. Bunker [10] attempted to enumerate the main reaction for silica and silicate glasses. Three reactions can take place: (1) hydration (penetration of water molecule into the glass network); (2) hydrolysis and condensation (break and form Si-O-Si network bonds); and (3) ion-exchange reactions (replacement of a modifier cation by a hydrogen or hydronium ion). The two last reactions are detailed below:

$$\equiv \mathrm{Si} - \mathrm{O} - \mathrm{Si} \equiv + \mathrm{H_2O} \Leftrightarrow 2[\equiv \mathrm{Si} - \mathrm{OH}]$$

$$[\equiv \mathrm{Si} - \mathrm{O} - \mathrm{Na^+}] + \mathrm{H_3O} \Leftrightarrow 2[\equiv \mathrm{Si} - \mathrm{OH}] + \mathrm{NaOH}$$

For more complex glasses, other reactions can take place and impact the stress-corrosion behavior. **Region 0** The appearance of region 0 depends on the glass composition. To date, no evidence of an environmental limit exists for pure silica [5, 57]. On the other hand, soda-lime and borosilicate glasses exhibit a steep downturn at low values of K_I suggesting a *fatigue limit or environmental limit* (K_E) below which the crack does not grow [24, 25, 29, 33, 34, 46, 79]. Two predominant theories exist to explain K_E. In 1965, Charles and Hillig modeled the delayed onset of crack propagation by crack tip blunting. This is the result of dissolution of the crack tip [29, 40]. More recently, Gehrke et al. [29] proposed a different mechanism to explain K_E. They attributed it to alkali leaching at the crack tip which provides a retarding layer. Due to the ion-exchange, the alkali ions are replaced by protons, molecular water, or hydronium

in the glass network [25, 26, 29, 33, 34]. Another idea linked to this one is the replacement of alkali ions by larger molecules within the fracture process zone. This leads to the development of a compressive stress which in turn prevents the crack from propagating [25, 26, 33, 34]. **Impact of parameters, such as glass composition, pH, temperature, humidity, etc.** Literature has multiple studies on how the chemical composition of complex glasses affects K_E and the slope in region I [18, 28, 29, 70, 78, 79]. Freiman et al. [28] compared subcritical crack growth in pure silica to that of alkali-silicate glasses. They attribute differences to the presence of modifying ions Na^+ and Ca^{2+}. The ions change the Si-O bond reactivity or change the elastic properties of the glassy networks. A priori there is no way to predict the glass behavior under stress corrosion. As for the case of chemical composition, literature has multiple studies on how temperature and pH alter K_E and region I [35, 36, 78]. The slope in region I decreases as the pH increases in pure silica glass. The position of region I shifts to the left for higher temperatures in pure silica, but the slope remains about constant [78]. Recently, it has been shown that the fictive temperature change the glasses response to fatigue [45, 49]. But the relation between T_f and the corrosion behavior is tricky [36].

Fracture in glass at nanometer scale

The fracture energy of glass is ~ 5 J/m^2 whereas surface's energy is ~ 0.3 J/m^2 [67]. Dissipative phenomena occur in a small fracture process zone around the crack tip. Direct observations of such mechanism are difficult because of the small length scales involved in the fracture of silicate glasses. Experimentally, atomic force microscopy (AFM) uncovers fracture mechanism at the nanometer scale during SCC. It should be noted that AFM imaging can acquire images only in the SCC as the crack needs to be "virtually stationary" during the time it takes to acquire one image.

Figure 1.13 presents an advancing crack front in aluminosilicate glasses captured by an AFM. Crack fracture takes place through growth and coalescence of cavities [5, 6, 13–15, 43, 61–63]. In pure amorphous silica, cavities grows to a typical size of 100 nm in length and 20 nm in width (penny shaped) then coalesces with the advancing crack front [61]. Consequently a continuous advancing crack front does not occur. Rather, it progresses by steps. Furthermore, the macroscopic velocities (captured by optical microscopes) do not capture these details but rather seize the overall picture [61]. Thus, the average (microscopic scale) crack velocity is the slow advancement of the crack front along with the instantaneous jumps of the front when it merges with damage regions. Figure 1.12 [61] is a schematic of the crack fronts movement. The origin of cavitation is found in the intrinsic toughness fluctuations induced by the amorphous structure. Glass is not homogeneous at the atomic scale (< 5 nm). Pure silica glass presents heterogeneities: silicon atoms form tetrahedral units which form rings of various sizes (predominantly 5-6 membered rings but a scatter does exist from 3 to 10). This leads to a large selection of Si-O-Si angles, yet the Si-O-Si angle centers predominantly at 146° [9, 63]. These fluctuations lead to low toughness/densities regions which concentrate stresses. They subsequently give birth to damage zones ahead of the crack tip. J.P. Guin and S. Wiederhorn attempted to evidence plastic deformations on fracture surfaces by AFM analysis [32, 34]. They concluded an almost perfect overlapping of the two specimens (~ 5 nm). One of the major difference in the two results is that one is of post-mortem surfaces and the other is in-suite measurements. Thus in-suite measurements acquire both plastic and elastic effects whereas the elastic

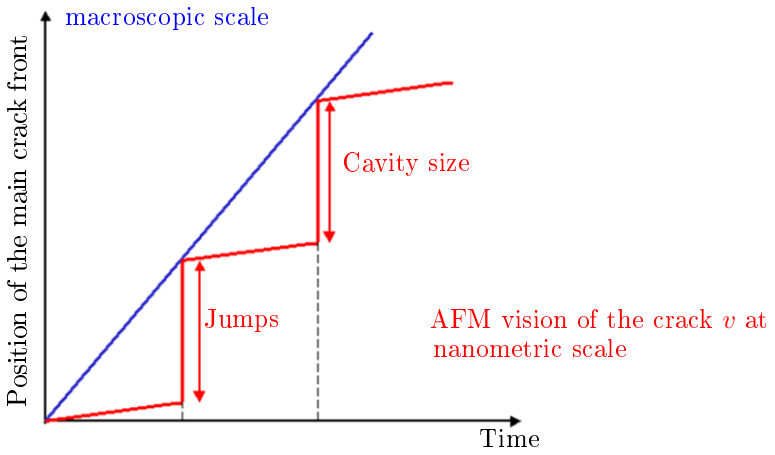

Figure 1.12: The average (microscopic scale) crack velocity (blue curve) is the slow advancement of the crack front (red curves with low slopes) along with the instantaneous jumps (discontinuous part of the red curves) of the front when it merges with damage regions [61].

effects have recover in post-mortem analysis. Crack propagation through the growth and coalescence of cavities is experimentally observed for different chemical compositions. F. Célarié found a similar mechanism for aluminosilicate glasses (Figure 1.13). Difference between pure silica and aluminosilicate glasses remain in the size and distribution of cavities. In aluminosilicate, the cavity size is around 10 nm. In complex glasses, heterogeneities enhance the cavities birth. Also, Célarié et al. found an enhanced diffusion of sodium ions in the stress-gradient field in the sub-micrometric vicinity of the crack tip (figure 1.14) [13, 15]. The elevated stresses at the crack tip enable the glass network to undergo structural modifications. This causes long-range structural changes and leads to modifications of bond angles, bond lengths, and consequently enhanced mobility of alkali. Heterogeneities in the glassy network increase

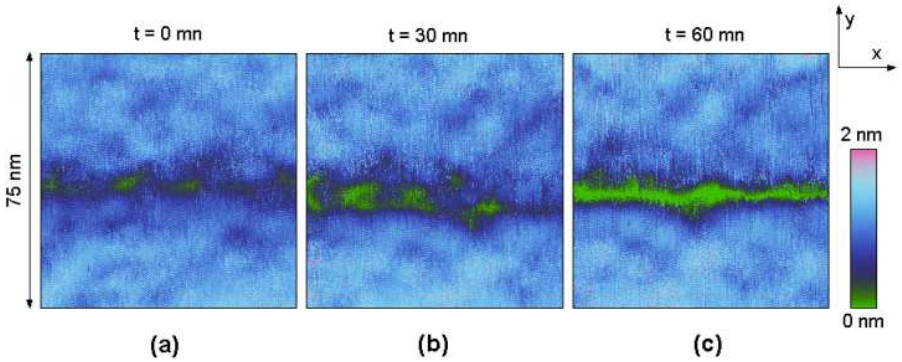

Figure 1.13: Sequence of topographical AFM images showing SCC at the surface of a glass samples. The scan size is 75 $\times$ 75 mm^2 and the height range is over 2 nm. The crack front propagates from the left to the right with an average speed of 10^{-11}m.s^{-1}. Image a) evidence the nanometric damage before the fracture advance; b) nucleation of damage and c) coalescence of damage with the advancing crack front. From [15].

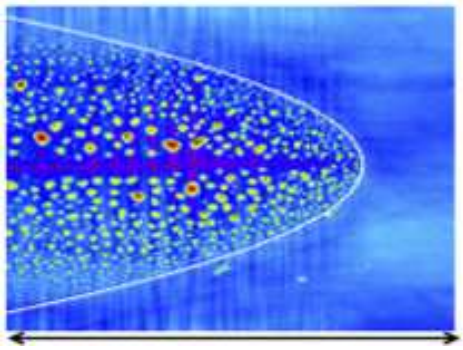

Figure 1.14: The stress gradient at the crack front enhances sodium diffusion. This figure images the sodium as it leaves the glass network to migrate to the glass surface. Dots on the image are due to sodium.

with the complexity of the glass composition. Molecular Dynamics is an excellent way to probe the fluctuations in the glass structure [9,43,44,63]. Without stress, silica glass presents ring size fluctuations. Under loading, these fluctuations concentrate stress and in turn form cavity growth. L. Van Brutzel observed cavity growth in regions containing a mixture of large and small rings rather than regions containing a mixture of 5 and 6 membered rings. Unlike silica glasses, alkali-silica glasses exhibit cavities randomly spread out [43]. Furthermore, areas enriched in sodium relax stresses [43, 44]. Molecular Dynamics results reveal similar mechanisms of damage growth and coalescence. L. Van Brutzel [9] simulated crack propagation in silica glass. During fracture, the deformation of local structure remains small: Si-O bond lengthening and Si-O-Si angles increase slightly [9]. Disorders such as fluctuation of ring densities appear sufficient to nucleate and grow damage in the fracture process zone. Rountree et al. attempted to estimate cavities size during fracture in pure silica by MD. Pores predominantly nucleate ahead of the crack front. Simulations reveal these damage regions then grow and merge with other damage regions. Subsequently they merge with the advancing crack front. Thus, the crack front is not a continuous breaking of bonds directly at the front.

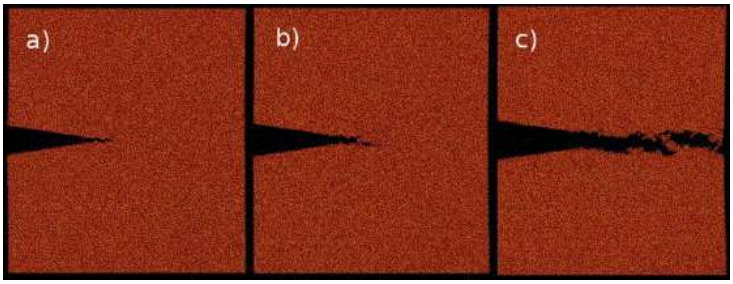

Figure 1.15: Evolution of the crack in the 15 million atoms system. From [62].

L.H.Kieu investigated the impact of chemical composition on fracture properties in ternary borosilicate glasses by MD simulations. The crack propagation occurs by the growth and coalescence of cavities. Four steps are presented: (1) elastic (nucleation of cavities), (2) plastic (cavities growth), (3) coalescence and

(4) decohesion. Existence of dissipation areas is confirmed during fracture. Crack propagation in SBN glasses depends on the oxide concentrations. More [Na_2O] decreases the number of Si-O and B-O bonds broken. Indeed as the [Na_2O] increases, less Oxide Former-O bonds break, yet there are also less of them to break because the [Na_2O] causes NBO on the oxide formers. Such result explains the variations in nucleation of cavities with sodium. For low sodium SBN glasses, the nucleation of cavities take place through an increase of ring size which breaks the OxideFormer-O bonds. A correlation between tri-coordinated boron and plasticity may exist. $^{[3]}$B-O bonds align with the stresses easier making the glasses more "plastic".

This chapter highlights the current knowledge on the structural, physical and mechanical properties of silica based glasses. The Yun, Dell and Bray model gives access to the evolution of the borate and silicate units depending on the chemical composition. As [Na_2O] changes, the coordination number of B atoms and the number of NBO evolve. Consequently, mechanical properties such as hardness and failure behavior are impacted by the glass composition. The indentation studies highlight two deformation processes: densification and shear flow. The contribution of each of them is directly linked to the glass structure. Finally, subcritical crack growth can limit the life time of a glass material. Extensive studies investigate the glass in the stress corrosion regime. Literature reported the glass breaks by nucleation and propagation of cavities ahead of the crack tip. But, how does the chemical composition affect the SCC behavior remains unclear. The first part of this thesis reveals how modulating the glass's chemical composition aids in understanding the SCC properties. The next chapter presents the glass elaboration, the techniques used to investigate the structural behavior and the mechanical properties. Chapter 3 presents results on the physical and structural test invoked on the SBN series herein. Chapter 4 details how the chemical composition (which is highly dependent on the structural properties) alters the mechanical (SCC, K_E, hardness, etc.) properties.

Bibliography

[1] J. Barès. *Failure of brittle heterogeneous materials. Intermittency, Crackeling and Seismicity.* PhD thesis, Ecole Doctorale Polytechnique, 2013.

[2] M. Barlet, A. Kerrache, J.-M. Delaye, and C.L. Rountree. Sio2-na2o-b2o3 density: A comparison of experiments, simulations, and theory. *J. Non-Cryst. Solids*, 382:32 – 44, 2013.

[3] M. Bertoldi and M. Sglavo. Soda-borosilicate glass: normal or anomalous behavior under vickers indentation. *J. Non-Cryst. Solids*, 344:51–59, 2004.

[4] J Bodswoth. Egyptian glass jar. http://commons.wikimedia.org/wiki/File

[5] D. Bonamy, S. Prades, L. Ponson, D. Dalmas, C.L. Rountree, E. Bouchaud, and C. Guillot. Experimental investigation of damage and fracture in glassy materials at the nanometre scale. *Int. J. Mater. Prod. Tec.*, 26:339–353, 2006.

[6] D. Bonamy, S. Prades, C. L. Rountree, L. Ponson, D. Dalmas, E. Bouchaud, K. Ravi-Chandar, and C. Guillot. Nanoscale damage during fracture in silica glass. *Int. J. Fracture*, 140(1-4):3–14, JUL 2006.

[7] P. J. Bray, A. E. Geissberger, F. Bucholtz, and I.A. Harris. Glass structure. *J. Non-Cryst. Solids*, 52:45–66, 1982.

[8] P. W. Bridgman and I. Simon. Effect of very high pressure on glass. *J. Appl. Phys.*, 24:405, 1953.

[9] van L. Brutzel. *Contribution à l'étude des mécanismes de rupture dans les amorphes: étude par dynamique moleculaire de la rupture de verre de silice.* PhD thesis, Université Paris VI, 1999.

[10] B.C. Bunker. Molecular mechanisms ofr corrosion of silica and silicate glasse. *J. Non-Cryst. Solids*, 179:300–308, 1994.

[11] B.C. Bunker, D.R. Tallant, R.J. Kirkpatrick, and G.L. Turner. Multinuclear nuclear-magnetic-resonance and raman investigation of sodium borosilicate glass structures. *Phys. Chem. Glasses*, 31:30–41, 1990.

[12] G. Buscarino, S. Agnello, and F. M. Gelardi. Structural modifications induced by electron irradiation in sio2 glass: Local densification measurements. *Europhys. Lett.*, 87:26007, 2009.

[13] F. Célarié. *Dynamique de fissuration à basse vitesse des matériaux vitreux.* PhD thesis, Université Montpellier II, 2004.

[14] F. Célarié, S. Pradès, D. Bonamy, A. Dickele, E. Bouchaud, C. Guillot, and C. Marliere. Surface fracture of glassy materials as detected by real-time atomic force microscopy (afm) experiments. *Appl. Surf. Sci.*, 212:92–96, 2003.

[15] F. Célarié, S. Prades, D. Bonamy, L. Ferrero, E. Bouchaud, C. Guillot, and C. Marliere. Glass breaks like metal, but at the nanometer scale. *Phys. Rev. Lett.*, 90(7):075504, FEB 21 2003.

[16] R. J. Charles. Static fatigue of glass. *J. Appl. Phys.*, 29:1549–1662, 1958.

[17] M. Ciccotti. Stress-corrosion mechanisms in silicate glasses. *J. Phys.D.*, 42(21):214006, November 2009.

[18] S.N. Crichton, M. Tomozawa, J.S. Hayden, T.I. Suratwala, and H. Campbell. Subcritical crack growth in a phosphate laser glass. *J. Am. Ceram. Soc.*, 82:3097–3104, 1999.

[19] W.J. Dell, P. J. Bray, and S. Z. Xiao. B-11 nmr-studies and structural modeling of Na_2O-B_2O_3-SiO_2 glasses of high soda content. *J. Non-Cryst. Solids*, 58(1):1–16, 1983.

[20] H. Doweidar. Considerations on the structure and physical properties of b2o3-sio2 and geo2-sio2 glasses. *J. Non-Cryst. Solids*, 357:1665–1670, 2011.

[21] F.M. Ernsberg. Role of densification in deformation of glasses under point loading. *J. Am. Ceram. Soc*, 51:545–547, 1968.

[22] A.G. Evans and S.M. Wiederhorn. Proof testing of ceramic materials-an analytical basis for failure prediction. *Int. J. Fracture*, 10:379–392, 1974.

[23] D. Feil and S. Feiller. The density of sodium borosilicate glasses related to atomic arrangements. *J. Non-Cryst. Solids*, 119:103–111, 1990.

[24] T. Fett, K. Germerdonk, A. Grossmuller, K. Keller, and D. Munz. Subcritical crack growth and threshold in borosilicate glass. *J. Matter. Sci.*, 26:253–257, 1991.

[25] T. Fett, J.P. Guin, and S.M. Wiederhorn. Interpretation of effects at the static fatigue limite of soda-lime-silicate glass. *Eng. Fract. Mech.*, 72:2774–2791, 2005.

[26] T. Fett, J.P. Guin, and S.M. Wiederhorn. Stresses in ion-exchange layers of soda-lime-silicate glass. *Fatigue Fract. Eng. Mater. Struct.*, 28:507–514, 2005.

[27] S. Freiman. The fracture of glass: Past, present and future. *Int. J. Appl. Glass Sci.*, 3:89–106, 2012.

[28] S.W. Freiman, T.L. Baker, and J.B. Wachtman Jr. A computerized fracture mechanics database for oxide glasse. *Bull. Am. Ceram.Soc.*, 64:1452–1455, 1985.

[29] E. Gehrke, Ch. Ullner, and M. Hahnert. Fatigue limit and crackarrest in alkali-containing silicate glasse. *J. Matter. Sci.*, 26:5445–5455, 1991.

[30] G.N. Greaves. Exafs and the structure of glass. *J. Non-Cryst. Solids*, 71:203–217, 1985.

[31] A. A. Griffith. The phenomena of rupture and flow in solids. *Phil. Trans. Royal Soc. London A*, 221(582-593):163–198, Jan 1 1921 1921.

[32] J. P. Guin and S. M. Wiederhorn. Surfaces formed by subcritical crack growth in silicate glasses. *Int. J. Fracture*, 140:15–26, 2006.

[33] J.P. Guin and S.M. Wiederhorn. Crack growth threshold in soda lime silicate glass: role of hold-time. *J. Non-Cryst. Solids*, 316:12–20, 2003.

[34] J.P. Guin, S.M. Wiederhorn, and T. Fett. Crack-tip structure in soda-lime-silicate glass. *J. Am. Ceram. Soc.*, 88:652–659, 2005.

[35] R. Gy. Stress corrosion of silicate glass: a review. *J. Non-Cryst. Solids*, 316:1–11, 2003.

[36] R. Gy. *Stress corrosion of glass.* Kluwer Academic Publichers, 2005.

[37] J.T. Hagan. Shear deformation under pyramidal indentations in soda-lime glass. *J. Mater. Sci.*, 15:1417–1424, 1980.

[38] J.T. Hagan and M.V. Swain. The origin of median and lateral cracks around plastic indents in brittle materials. *J. Phys.D.*, 11:2091–102, 1978.

[39] J.T. Hagan and S. Van der Zwaag. Plastic processes in a range of soda-lime-silica glasses. *J. Non-Cryst. Solids*, 64:249–268, 1984.

[40] W.B. Hillig and W.B. Charles. *High Strength Materials*, page 682. Wiley, New York, 1965.

[41] H. Inoue, A. Masuno, Y. Watanabe, K. Suzuki, and T. Iseda. Direct calculation of the physical properties of sodium borosilicate glass from its chemical composition using the concept of structural units. *J. Am. Ceram. Soc.*, 95:211–216, 2012.

[42] G.R. Irwin. Analysis of stresses and strains near the end of a crack traversing a plate. *J. Appl. Mech.*, 24:361–364, 1957.

[43] L.-H. Kieu. *Compréhension de l'origine de l'évolution sous irradiation de la ténacite des verres nucléaires.* PhD thesis, Ecole Doctorale Polytechnique, 2011.

[44] L.-H. Kieu, J. . M. Delaye, and C. Stolz. Modeling the effect of composition and thermal quenching on the fracture behavior of borosilicate glass. *J. Non-Cryst. Solids*, 358:3268–3279, 2012.

[45] A. Koike and M. Tomozawa. Fictive temperature dependance of subcritical crack growth rate of normal and anomalous glass. *J. Non-Cryst. Solids*, 352:5522–5530, 2006.

[46] K. Langford, W.A. Davis, P. Lamarche, T. Laursen, and R. Groleau. Hydration of soda-lime glass. *J. Non-Cryst. Solids*, 33:249–266, 1979.

[47] Brian Lawn. *Fracture of Brittle Solids*. Cambridge University Press, 2nd edition, 1993.

[48] F. Lechenault, C. L. Rountree, F. Cousin, J-.P. Bouchaud, L. Ponson, and E Bouchaud. Evidence of deep water penetration in silica during stress corrosion fracture. *Phys. Rev. Lett.*, 106:165504, 2011.

[49] H. Li, A. Agarwal, and M. Tomozawa. Effect of fictive temperature on dynamics fatigue behaviorof silica and soda-lime glasse. *J. Am. Ceram. Soc.*, 78:1393–1396, 1995.

[50] J.D. Mackenzie. High-pressure effects on oxide glasses. 1. densification in rigid state. *J. Am. Ceram. Soc.*, 46:461–470, 1963.

[51] D. Manara, A. Grandjean, and D.R. Neuville. Advances in understanding the structure of borosilicate glasses: A raman spectroscopy study. *Am. Mineral.*, 94:777–784, 2009.

[52] R. Martens and W. Muller-Warmuth. Structural groups and their mixing in borosilicate glasses of various compositions - an nmr study. *J. Non-Cryst. Solids*, 265:167–175, 2000.

[53] D. Maugis. Review : Subcritical crack growth, surface energy, fracture toughness, stick-slip and embrittlement. *J. Mater Sci.*, 20:3041–3073, 1985.

[54] T..A. Michalske and B.C. Bunker. Slow fracture model based on strained silicate structures. *J. Appl. Phys.*, 56:2686–2693, 1984.

[55] T..A. Michalske and B.C. Bunker. Steric effects in stress corrosion fracture of glass. *J. Am. Ceram. Soc.*, 70:780–784, 1987.

[56] T..A. Michalske and S. Freiman. A molecular mechanism for stress-corrosion in vitreous silica. *J. Am. Ceram. Soc.*, 66:284–288, 1983.

[57] M. Muraoka and H. Abé. Subcritical crack growth in silica optical fivers in wide range of crack velocities. *J. Am. Ceram. Soc.*, 79:51–57, 1996.

[58] M. Nogami and M. Tomozawa. Effect of stress on water diffusion in silica glasse. *J. Am. Ceram. Soc.*, 67:151–154, 1984.

[59] K.W. Peter. Densification and flow phenomena of glass in indentation experiments. *J. Non-Cryst. Solids*, 5:103–115, 1970.

[60] J.C. Pollet and S.J. Burns. An analysis of slow crack propagation data in pmma and brittle materials. *Int. J. Fracture*, 13:775–786, 1977.

[61] S Pradès. *Mécanismes de rupture du verre à l' é chelle nanometrique*. PhD thesis, Université Paris VI, 2004.

[62] C.L. Rountree, D. Bonamy, D. Dalmas, S. Prades, R.K. Kalia, C. Guillot, and E. Bouchaud. Fracture in glass via molecular dynamics simulations and atomic force microscopy experiments. *Phys. Chem. Glasses-B*, 51:127–132, 2010.

[63] C.L. Rountree, R. Kalia, E. Lidorikis, A. Nakano, Van Brutzel, and P. Vashishta. Atomistic aspects of crack propagation in brittle materials: Multimillion atom molecular dynamics simulations. *Annu. Rev. Mater. Res.*, 32:377–400, 2002.

[64] T Rouxel, T. Hammouda, and A. Moré ac. Poisson's ratio and the densification of glass under high pressure. *Phys. Rev. Lett.*, 100:225501, 2008.

[65] T Rouxel, H. Ji, J. P. Guin, F. Augereau, and B. Rufflé. Indentation deformation mechanism in glass: Densification versus shear flow. *J. Appl. Phys.*, 107:094903, 2010.

[66] T Rouxel, J.-C. Sangleboeuf, C Moysan, and B Truffin. Indentation topometry in glasses by atomic force microscopy. *J. Non-Cryst. Solids*, 344:26–36, 2004.

[67] H. Scholze. *Le verre*. Institut du verre, 1980.

[68] P. Sellappan. *Indentation cracking of glass: role of the composition and reinforcement by diamond particles*. PhD thesis, Université de Rennes 1, 2011.

[69] P. Sellappan, T. Rouxel, F. Celarie, E. Becker, P. Houizot, and R. Conradt. Composition dependence of indentation deformation and indentation cracking in glass. *Acta Mater.*, 61:5949–5965, 2013.

[70] C.J. Simmons and S.W. Freiman. Effect of corrosion processes on subcritical crack growth in glass. *J. Am. Ceram. Soc.*, 64:683–686, 1981.

[71] Han W.T. Tomozawa, M. and W.A. Lanford. Water entry into silica glass during slow crack-growth. *J. Am. Ceram. Soc.*, 74:2573–2576, 1991.

[72] M. Tomozawa. Fracture of glasses. *Ann. Rev. Mater. Sci.*, 26:43–74, 1996.

[73] D.R. Uhlmann. Densification of alkali silicate glasses at high pressure. *J. Non-Cryst. Solids*, 13:89–99, 1973.

[74] J.K. West and L.L. Hench. Silica fracture: Part i a ring contraction model. *J. Mater. Sci.*, 29:3601–3606, 1994.

[75] J.K. West and L.L. Hench. Silica fracture: Part ii a ring opening model via hydrolysis. *J. Mater. Sci.*, 29:5808–5816, 1994.

[76] J.K. West and L.L. Hench. The effect of environment on silica fracture: vaccum, carbon monoxide, water and nitrogen. *Philos. Mag. A*, 77:85–113, 1998.

[77] S. M. Wiederhorn, E.R. Fuller, and R. Thomson. Micromechanisms of crack growth in ceramics and glasses in corrosive environments. *Met. Sci.*, 14:450–458, 1980.

[78] S.M. Wiederhorn. Influence of water vapor on crack propagation in soda-lime glass. *Am. Ceram. Soc. Bull.*, 50:407–414, 1967.

[79] S.M. Wiederhorn and L.H. Bolz. Stress corrosion and static fatigue of glass. *J. Am. Ceram. Soc*, 53:543–548, 1970.

[80] S.M. Wiederhorn, S.W. Freiman, E.R. Fuller, and C.J. Simmons. Effects of water and other dielectrics on crack-growth. *J. Matter. Sci.*, 12:3460–3478, 1982.

[81] S. Yoshida, J.-C. Sangleboeuf, and T. Rouxel. Quantitative evaluation of indentation-induced densification in glass. *J. Mat. Res.*, 20:3404–3412, 2005.

[82] S. Yoshida, J.-C. Sangleboeuf, and T Rouxel. Indentation-induced densification of soda-lime silicate glass. *Int. J. Mater. Res.*, 98:360–364, 2007.

[83] Y.H. Yun, S.A. Feller, and P.J. Bray. Correction and addendum to nuclear magnetic-resonance studies of the glasses in the system Na_2O-B_2O_3-SiO_2. *J. Non-Cryst. Solids*, 33:273–277, 1979.

[84] W.H. Zachariasen. The atomic arrangement in glass. *J. Am. Ceram. Soc.*, 54:3841–3851, 1932.

[85] J. Zarzycky. *Les verres et l' état vitreux.* Manson, 1982.

Chapter 2

Elaboration and experimental methods

Contents

The previous chapter reviews current knowledge on the structural and the mechanical properties of silicate glasses. How the glass's structure impacts the mechanical properties remain unclear. To link variations in the glass structure to variations at the macroscopic scale, I chose to investigate ternary SiO_2-B_2O_3-Na_2O model glasses. By modulating the chemical composition, I attempt to understand the role of each oxide in the glass. This chapter presents the conditions of glass elaboration and experimental methods used to characterize their structural, physical, and mechanical properties. Section 2.1 details the fabrication techniques for the glasses with different molar concentrations in silica, boron and sodium. Understanding how the chemical composition influences the mechanical behavior requires two intermediate steps. First, sections 2.2 and 2.3 highlight spectroscopy tools (i.e. RAMAN and MAS NMR) used to study variations in the structural and the physical properties, respectively. The final section details the experimental set-ups used to study the mechanical response of the glasses (including: stress corrosion cracking tests, hardness tests...)

2.1 Fabrication and composition of glass samples

The compositions studied (Table 2.1) contain modulated amount of silica (SiO_2), diboron trioxide (B_2O_3) and sodium oxide (Na_2O). As presented in chapter 1 both silica and boron are glass formers. The addition of B_2O_3 reduces the melting point of the glass. Na_2O can have one of two roles in the glass (part 1): network modifier or charge compensator. This results in a depolymerization of the glass which leads to a further decrease of the melting point.

I prepared the glass in the SECM (Service d'Études et Comportement des Matériaux de conditionnement) at CEA Marcoule with Théodore Cozzica. Figure 2.1 sketches the thermal sequence involved in the elaboration of the SBN glasses. Glasses with molar sodium concentrations ranging between 14 and 35 % are perpetrated. Silica, orthoboric acid (H_3BO_3) and sodium carbonate (Na_2CO_3) powders were manually homogenized and put in a platinum/gold (Pt/Au) crucible for the elaboration. Pt/Au crucibles facilitate slow cooling and thermal treatments. Moreover, it enables the unsticking of the glass specimen from the crucible.

Initially, the furnace's temperature is stabilized at 200°C for 2 h. Increasing the furnace's temperature from 200°C to 800°C ensures the decarbonatation of the sodium carbonate. This step also avoids bubbles in the final glass. In a final step, glass fusion occurs at T_E (between 1100°C and 1300°C depending on the glass composition) for 3 h . Subsequently, the glass melt leaves the furnace, and it is poured into a preheated (600°C) carbon crucible. The glass melt enters a second furnace, and the cooling rate occurs at a much slower rate (10°C/h) to release the residual stresses.

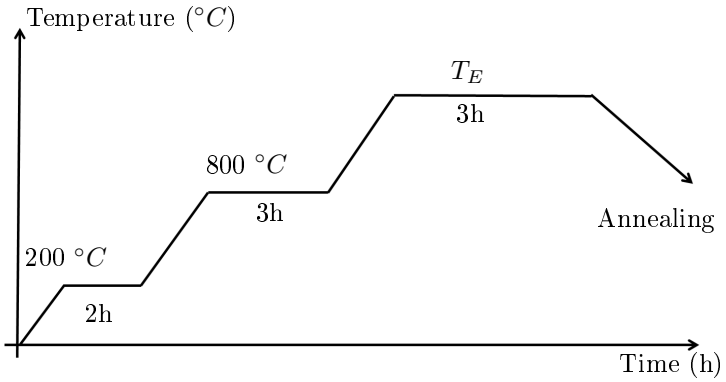

Figure 2.1: Thermal cycle of SBN glass's elaboration. T_E depends on glass composition.

To confirm the chemical composition a third party (PrimeVerre located at Montpellier) conducted chemical analyses by means of MEB-EDS (Environmental Electronic microscope coupled with an Energy Dispersive Spectrometer) and/or ICP-AES (Inductively coupled plasma atomic emission spectroscopy). MEB-EDS results revealed small amounts of impurities, less than 0.5%. The results reported in table 2.1 come from the ICP-AES measurements and have an uncertainty of 10%. The chemical compositions of the fabricated glasses are within the range of the target values. Table 2.1 also contains the ratios R_{SBN} and K_{SBN} based on the measured values.

Name	Target values			Measured via ICP-AES			R_{SBN} measured	K_{SBN} measured	Symbols
	SiO_2	B_2O_3	Na_2O	SiO_2	B_2O_3	Na_2O			
SBN 12	59.6	28.2	12.2	59.4	28.5	12.1	0.4	2.1	△
SBN 25	50.7	23.9	25.4	52.6	20.6	26.8	1.3	2.5	▷
SBN 30	47.3	22.3	30.4	51	20.1	28.6	1.4	2.5	◁
SBN 35	44	20.6	35.4	46.9	18.6	34.5	1.8	2.5	▽
SBN 14	67.8	18	14.2	70	15.8	14.2	0.9	4.4	✳
SBN 63	63.2	16.8	20	66.7	14.1	19.2	1.3	4.5	◇
SBN 59	59.2	15.8	25	61.1	13.3	25.5	1.9	4.5	○
SBN 55	55.3	14.7	30	58.0	12.9	29.1	2.3	4.5	✡

Table 2.1: Targets molar compositions and real molar compositions of elaborated glass samples measured by ICP-AES with R_{SBN} and K_{SBN} values calculated from target compositions. The last column depicts the symbols used in the rest of this document.

2.2 Structural investigation

2.2.1 Raman analysis

Raman spectroscopy techniques invoke the inelastic scattering of a monochromatic light. A laser source illuminates the specimen surface. The sample either absorbs or reflects the photons. Absorbed photons are reemitted. The relevant information stems in the frequency of the reemitted photons, which can be either equal or shifted with respect to the frequency of the laser source: Most of the incident photons undergo *elastic* Rayleigh scattering and the excited molecules return back to their fundamental state by emitting photons at the same frequency as that of the source; This component represents 99.999 % of the total signal and is useless for molecular characterization. Conversely, 0.001 % of the incident photons undergo *inelastic* scattering, yielding a shift in the frequency of the reemitted photon. This shift, so-called Raman effect, provides information on the vibrational, rotational and other transitions in the molecule involved in the process. Raman shifts toward higher and lower values are called Anti-Stokes and Stokes frequencies, respectively.

The spectra were recorded at LMPA (Laboratoire des Matériaux et Procédé actifs) in CEA Marcoule with Richard Caraballo and Mickael Gennisson. Raman spectra employ a Jobin Yvon HR800 spectrometer. The laser is a YAG laser (λ=532 nm) with an adjustable output power. Experiments are in ambient conditions. Maintaining a low laser power limits undesired heating of the samples. Resulting spectra are the average of ten measurements accumulated over ten seconds.

2.2.2 MAS NMR

The NMR techniques use the nuclear magnetic moment of an atomic nucleus to extract quantitative information on the glasses structure via an external magnetic field. Most of the nuclei in the periodic table possess a nuclear magnetic moment proportional to the nuclear spin angular momentum I:

$$\mu = \gamma I, \tag{2.1}$$

where the gyro-magnetic ratio γ is specific to each nucleus. Then, the angular momentum of a nuclear spin is a vector and can point in any direction of space. Therefore, for different nuclei with different gyromagnetic ratios, different frequencies must be applied in order to achieve resonance.

Applying a magnetic field yields a spin precession around the magnetic field axis. The associated frequency is called the Larmor frequency, ω_0. Appling an external radio-frequency pulse is added (an oscillating magnetic field of specific frequency and duration perpendicular to the magnetic field, B_0), the pulse resonates when ω_0=ω_{rf}. An oscillating magnetic field associated to the applied radio frequency pulse appears. The rf pulse flips the magnetization vector into the transverse plan, while the spins keep rotating around the magnetic field at a frequency $\omega_1 = -\gamma B_1$. After rf pulse, the spins go back to their thermal equilibrium state with a certain time called the spin-lattice relaxation. The precession of the transverse magnetization induces oscillating electric currents that can be detected and is the NMR signal. By Fourier transform, the oscillating signal can be transformed into frequency domains. The atomic nuclei are surrounded by electrons and other nuclei. The main interaction of the nucleus is the interaction with the static magnetic field. This external interaction is called the Zeeman interaction. Other interactions exist due to internal interactions: chemical shift, dipolar couplings, quadrupolar couplings...

I performed NMR measurements at LSDRM (Laboratoire de Structure et Dynamique par Résonnance Magnétique) in CEA Saclay with Thibault Charpentier and Mélanie Moskura. Tests herein invoke ten cylinder samples (0.8×2.96 mm^2) for each of the SBN composition studied in this PhD. These samples are specially designed for MAS NMR measurements. For the experiments, a boron free probe with a spinning rate of 14 kHz holds the samples. Bruker AVANCE 500 spectrometer collects the MAS NMR spectra at a frequency of 160.14 MHz and 143,03 MHz to probe boron and sodium environments, respectively.

$^{[11]}$B magic angle spinning nuclear magnetic resonance (MAS NMR) experiments provide information on the glass structure via revealing the boron environment. The spectra collections invoke a recycle delay of 2 s and a pulse length of 1 μs in order to have quantitative data. Probing the bore environment reveals the proportion of $^{[3]}$B and $^{[4]}$B. The high symmetry around $^{[4]}$B leads to a large quadrupolar coupling.

$^{[23]}$Na MAS NMR experiments provide information on the sodium atoms environment in the glass structure (compensator or modifier). The spectra collections invoke a recycle delay of 1 s and a pulse length of 1 μs in order to have quantitative data.

2.3 Physical properties

This section details the techniques used to extract the various physical properties, including ρ, E, and ν.

2.3.1 Density measurements

Archimedes' principle provides a simple method to estimate the density, ρ, of the glasses. Sample geometries were cylinders of thickness 10 mm and diameter 30 mm. Tests are conducted at 24°C using an hydrostatic balance. Initially, the glass samples are weighted in air (m_d) and water (m_w). Then, knowing the density of water (ρ_w), the density of the sample (ρ) is deduced:

$$\rho = \frac{m_d}{m_d - m_w}\rho_w \tag{2.2}$$

The density measurements were done at LDMC (Laboratoire d'Étude et de Développement de Matrices de Conditionnement) in CEA Marcoule with Bruno Penelon.

2.3.2 Elastic properties: Young modulus (E), Poisson's ratio (ν)

Ultrasonic echography techniques provide an excellent technique to determine the elastic moduli (Young modulus and Poisson ratio). These tests make use of piezoelectric acoustic transducers at 10 MHz. Tests invoke the same specimens as for the density tests (section 2.3.1). A digital micrometer measures precisely the specimen width with an accuracy of $\pm$ 1 μm. The velocities of longitudinal (V_L) and transverse (V_T) acoustic waves arise from the knowledge of this thickness and the time at which the acoustic pulses bounces at the specimen surface. Elastodynamics theory relates V_L and V_T to the Young modulus (E) and Poisson ratio (ν):

$$E = \rho * (\frac{3V_L^2 - 4V_T^2}{(V_L/V_T)^2 - 1}) \tag{2.3}$$

$$\nu = \frac{V_L^2 - 2V_T^2}{2(V_L^2 - V_T^2)} \tag{2.4}$$

2.4 Experimental methods : mechanical analysis

This section details methods used to gather velocity (v) versus stress intensity factor (K_I) curves in the stress corrosion regime. The following subsection presents how information on the advancing crack front can be obtained by analyzing the post-mortem fracture surfaces. The last section details indentation tests which not only reveal the hardness and fracture toughness but also inform on the nature of the densification and plasticity processes involved under the indenter.

2.4.1 Fracture experiments via Deben loading machine

Fracture experiments invoke several techniques to understand how stress corrosion cracking occurs in the glasses. The next subsection details the experimental setup. Subsequently, the following section explains post-imaging techniques to acquire velocity (v) versus stress intensity factor (K_I) curves.

Stress corrosion cracking (SCC) techniques

Fracture experiments invoke Double Cleavage Drilled Compression (DCDC) samples [7] which permit SCC [2, 13, 14]. The geometry of the samples within part I are cuboids of size 5×5×25 mm^3 (DCDC$_1$) with a 1 mm diameter hole drilled in the center. Figure 2.2 presents a diagram of the sample used in part I. All fracture experiments employ DCDC sample geometry.

Figure 2.3 presents the experimental fracture set-up. The specimens (schematic in figure 2.2) is placed between two jaws of the Deben machine, so that they undergo a compressive load applied perpendicularly to the two 5×5mm^2 surfaces. The jaws are brought closer at constant velocity (0.02 mm.min^{-1}).

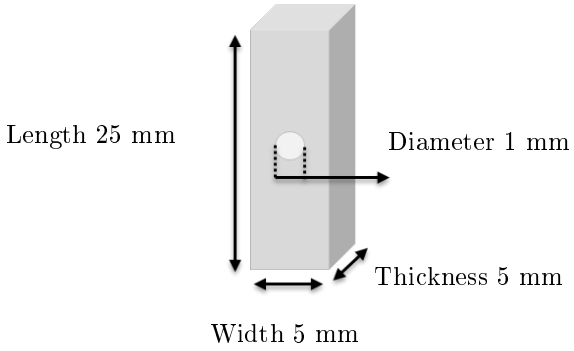

Figure 2.2: Drawing of Double Cleavage Drilled Compression samples $DCDC_1$ used to investigate failure in stress corrosion regime

I frequently monitor jaws alignment and offset were corrected by Thierry Bernard. At some time, two symmetric pre-cracks pop open off the hole along the 25 mm length of the specimen. The jaw displacement ceases. The propagation of the pre-crack slows due to the sample geometry (under constant force K_I decreases as the crack length increases). Under vacuum, the propagation would stop when the stress intensity factor K_I at the crack tip became smaller than the glass toughness K_C. However, in a corrosive environment, slow crack propagation occurs and depends on the glass's composition, K_I, and the experimental conditions (temperature and humidity). Hence, a glove box monitors the temperature and humidity of the environment during fracture experiments.

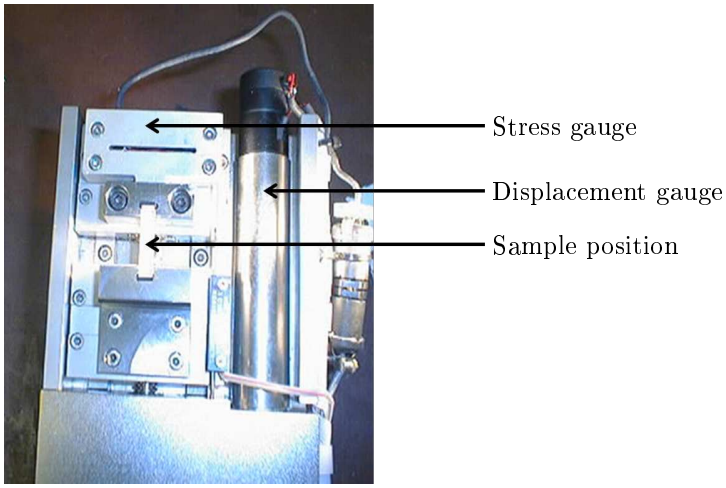

Figure 2.3: Deben machine used during experiment to propagate cracks in the SCC regime.

Due to the overall geometry of the sample (Figure 2.2) [4, 10], the crack front propagates in mode I (opening mode). The Deben loading machine monitors the time evolution of the force applied to the samples. The stress intensity factor, K_I, is calculated using references [4, 10]:

$$K_I = \frac{F}{w^2} \times \frac{\sqrt{\pi a}}{2w/a + (0.470w/a - 0.259) \times c/a}, \tag{2.5}$$

where F(units: N) is the load applying on the $5\times5\text{mm}^2$ surface, a (units: mm) is the diameter of the hole drilled in the center, w (units: mm) is the thickness of the sample and c (units: mm) is the length of the crack.

Optical system A tubular microscope coupled with an IDS uEye (1465LE-C) camera images the crack propagation at the specimen surface. The Deben machine sits on three Newport linear stage motors (LTA motor for focusing options and two CMA motors to follow the crack front). These motors permit the sample to be displaced when the crack front moves outside the tubular microscope's zone of observation. Image processing provides the time-evolution of the crack tip, and the crack velocity is subsequently inferred. The area imaged with the microscope is 2×1.5 mm^2 and the resolution is 2μm per pixel. Experiments take place for long period of time during which drifts occur. The relative position of the camera with that of the sample moves. It is important to correct these drifts on the obtained images to get the right velocity. The next section details the post-imaging processing.

Image analysis Six pictures spanning a 5 minute interval are recorded every thirty minutes and averaged. Each picture has to be checked and perhaps re-placed in case of improper lighting. Subsequently, the position of the crack tip is determined in these images and the velocity is deduced. Steps are detailed below:

- *Correction of the shift*: The first image of the series of six is considered as the reference. Due to the image size and the speed of the crack front, regions far away from the crack tip are not altered by the crack propagation. They can be used to determine the undesirable drift and to reposition the images. This is achieved by computing the 2D cross-correlation function of the images two-by-two (the image of interest and the reference image) and by determining the in-plane shift of the maximum. Shifts in x and y directions are then known and translations are applied. Figure 2.4 presents an example.

  Figure 2.4 presents the reference picture (a) and the subsequent picture (b) used in the cross-correlation. Cross-correlation techniques reveal a shift of 2 and 3 pixels in the x and y directions, respectively.

- *Determination of the crack tip's position:* For simplicity, images undergo a rotation such that the crack propagation moves from left to right. Figure 2.5 exemplifies the successive steps taken to determine the crack tip's position. Filters and smoothing techniques enhance the contrast between the crack and the background, as seen in Figure 2.5 a) and b). The path containing the crack is manually selected (Figure 2.5 c). Figure 2.5d reveals the mean pixel values along this selected path. The crack front in this setup has a high pixel value, corresponding to a whitish color in the figure. Yet, the bulk material has a low pixel number. The transition from high to low pixel values signifies the crack front position (figure 2.5e). Moreover, a Matlab program is setup for automatic detection. Figure 2.5e) displays a sample result of the automatic detection with a cross at the crack front. These images are verified one by one. The program also creates a file with the coordinates of the crack tip position as a function of time.

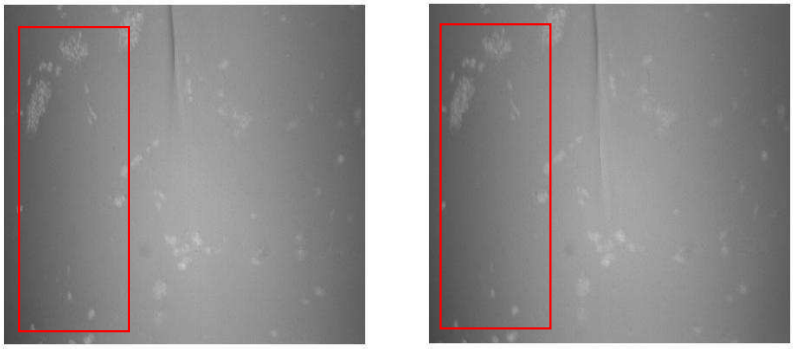

a) b)

Figure 2.4: Example of determining the shift between two images through cross-correlation function. The time between these two pictures is thirty minutes. Figure (a) is the reference and (b) is taken 30 minutes later. The red rectangle is the area selected for the cross-correlation technique.

v versus $f(K_I)$ curves: For a given load, the crack front propagates for some amount of time. Then the sample undergoes unloading which creates an arrest lines on the fracture surfaces due to backlash in the gears of the system. This is helpful to isolate the velocity regions on the post-mortem fracture surfaces. Furthermore, the position of the crack tip can be precisely determined from the post-mortem fracture surfaces. The loads applied on the $DCDC_1$ samples range from 1300 to 2300 N. From the knowledge of the crack length as a function of time and the value of the force, I can deduce the v versus K_I curves. The v vs K_I curves is impacted by the temperature and the humidity during experiments. During glass fracture, these parameters are controlled. Parameters don't vary much from one experiment to the others.

2.4.2 Post-mortem fracture surface analysis

Fracture surfaces unveil the fracture processes at the mesoscale. Post-mortem fracture surfaces result from atomic force imaging.

Atomic Force Microscope (AFM) principle

Atomic force microscopy (AFM) is a high-resolution scanning probe microscopy tool reaching fractions of a nanometer. The AFM consists of a cantilever with a sharp tip on the end. When the tip is brought in close contact with the sample surface, forces between the tip and the sample deflect the cantilever. Depending on the situation, these forces include mechanical contact forces, Van der Waals forces, capillary forces, etc. A laser spot reflects off the cantilever onto an array of photodiodes, as presented in figure 2.6. As the tip scans the surface, the photodiode details the tips movement with the surface. A feedback

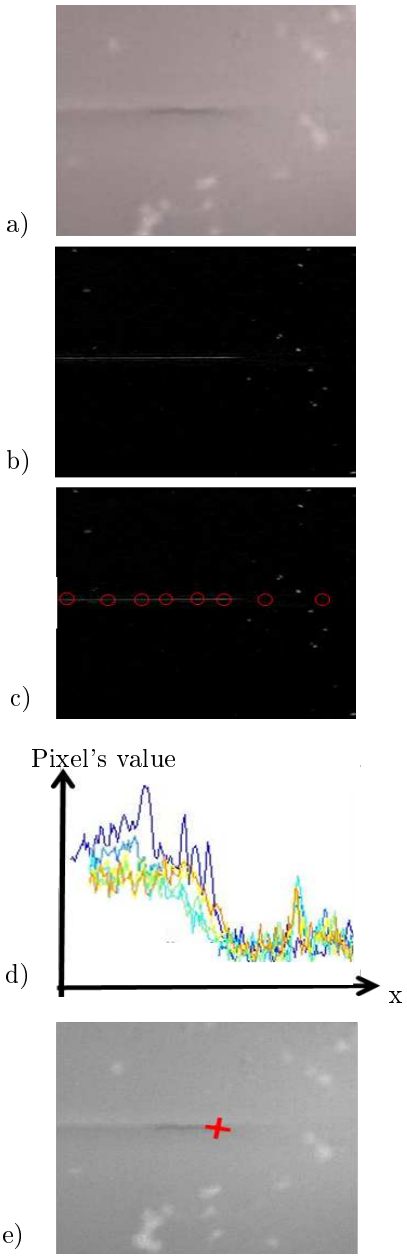

Figure 2.5: Example of images analysis step by step a) original picture rotated such that the crack front propagates from left to the right b) enhancement of the contrast between the crack and its background c) manual selection of the crack path d) determination of the cutoff e) position of the crack tip resulting from the automatic computation procedure.

mechanism enables the repositioning of the tip/cantilever to maintain constant height with the surface.

Experiments herein invoke a Dimension Icon head Nanoscope V by Bruker. An optical microscope enables the user to select the region of interest. The AFM head includes a piezoelectric tube scanner, a laser, and a quadrature optical detector to focus on the sample's analyze area. Due to the glass' high Young's modulus (70-90 GPa), tips with a high spring constant have been used. Bruker's TAP 525 and

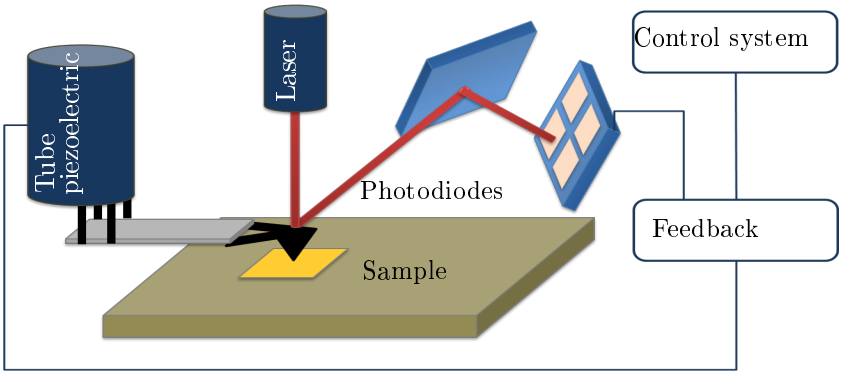

Figure 2.6: Drawing of an atomic force microscopy. A laser spot reflects off the top of the cantilever onto the array of photodiodes via a mirror.

RTESPA tips are frequently invoked. Table 2.2 presents the standard features of the tips.

Name	Tip radius (nm)	Spring constant (N/m)	Resonant frequency (kHz)
TAP525	8	200	525
RTESPA	8	40	200

Table 2.2: Nominal features of TAP 525 (or MPP-13100-10) and RTESPA (or MPP-11123610) tips : Tip radius (nm), Spring constant (N/m) and Resonant frequency (kHz).

Most of the experiments herein invoke the PeakForce Tapping mode rather than contact or tapping modes. This mode controls the force applied to the sample by the tip at every pixel. It also acquires load and unload displacement curves at every pixel. Processing the load and unload curves reveals not only the topography but nano-scale material properties such as modulus, adhesion, deformation and dissipation. All the investigations use PeakForce Tapping because this mode also minimizes damage to the probe or sample. On the other hand, the AFM tip does not penetrate significantly into the surface due to low force.

Fracture surface roughness

The RMS roughness is defined as the standard deviation of the height of the surface (h_i) from the average height of a plane (h_i^{fit}) passing through the surface:

$$RMS = \sqrt{(\frac{1}{N}) * \sum_{i=1}^{N} (h_i - h_i^{fit})^2}. \tag{2.6}$$

2.4.3 Micro-indentation test

Micro-indentation tests provide information on a material's resistance to permanent deformation induced by a harder material under stress. Directly imaging the indents gives way to calculations of the hardness, crack resistance, and fracture toughness. Annealing the indented samples provides estimates of the

fraction of densification and the fraction of isochoric shear flow. This section details the experimental procedures used to acquire these measurements.

Sample preparation

Indentation experiments require samples with two parallel surfaces. Samples herein are rectangular parallelepipeds of size 5×5×25 mm^3. Indentations take place on one of the 5×25 mm^2 faces. The surface quality affects the crack behavior of glasses; therefore diamond grinding discs are used to obtain optical polish. This work is done by Prime Verre or OPA Opticad.

Vickers Indentation

The indenter is a diamond with a square-based pyramid (i.e. standard Vickers indenter). The angle between the two opposite faces is 136° and that between two opposite edges is 148° (Figure 2.7).

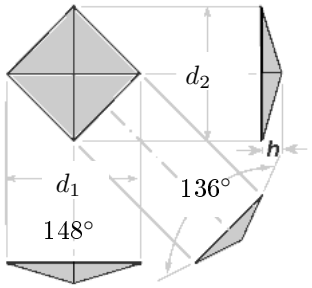

Figure 2.7: Schema of Vickers Pyramid Diamond Indenter

Once the material is indented, a camera captures the residual indent pattern. The standard residual deformation pattern is a square-based pyramid. The image reveals d, where d is the diagonal of the indentation pattern. The area of the square based pyramid is:

$$A = \frac{d^2}{2\sin 68}. \tag{2.7}$$

I performed indentation tests at LDMC ((Laboratoire d'Étude et de Développement de Matrices de Conditionnement)) in CEA Marcoule with Mickael Gennisson. The indentations are performed in a thermally regulated room, at 25 °C in air with an Anton Paar MHT-10 hardness tester. The indentation load (F), varies from 25 g to 300 g at a constant load rate. The dwelling time at maximum load is 15 sec for all tests. The tests are repeated at least 10 times.

After indentation and optical imaging, an AFM precisely characterizes various parameters. For these images, the AFM uses Bruker's RTESPA cantilever which has a silicon tip with a nominal radius of 8 nm and a nominal force constant of 40N/m (table 2.2). The scan size is sufficiently large to avoid any modifications of the indentation print during post-analysis (i.e. subtraction of one order plan fit). Typically the image sizes are greater than twice the indentation diagonal. The estimated errors for

measuring the length of indentation by AFM are less than 2% in X and Y directions and about 2% in Z direction. Post-image analysis reveals 4 parameters per indent (Figure 2.10):

1. Residual indentation depth, P_{id}
2. Indentation diagonal length, d_i
3. Indentation volume, V_i^-, volume measured below the free surface
4. Volume of pileup, V_i^+, volume measured above the free surface

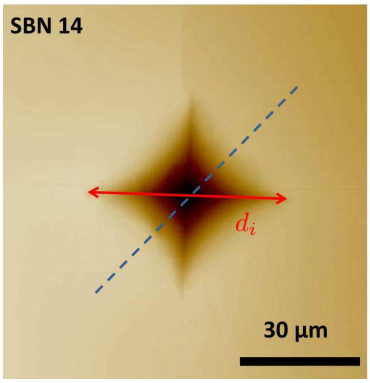

Figure 2.8: A typical indentation imprint used in determining the indentation diagonal length, (d_i and marked by a continuous line) and in evaluating the pile up profile (dotted line).

Hardness tests

Hardness tests apply a strain on the material by a sharp or a blunt indenter. The load causes the indenter to penetrate the material leading to elastic and plastic deformations. Once the indenter is unloaded, a residual deformation remains. The hardness is the ratio of the load applied (F) and the imprint surface area (A):

$$H = \frac{P}{A}. \tag{2.8}$$

Depending on the test, A is the projected area for Vickers indentations. Combining equation 2.7 and 2.4 gives:

$$H_V = \frac{1.8544F}{d^2}. \tag{2.9}$$

Due to the precision of the AFM, d in the above equation is actually the average d_i from one indent as measured from the AFM. H_V is the average of at least 10 indents.

Crack resistance, C_R

Vickers's indentation can cause cracks to pop out from the corners of the indenter. The probability of crack appearance, P_C, is the average number of radial crack per corner for a given load. This is measured at multiple loads. The load where P_C exceeds 50 % defines the crack resistance [5].

K_C measurements from indentation

Fracture toughness (K_C) characterizes the material's resistance to failure under vacuum. Herein estimates of K_C arise from the measure of the length of the cracks generated off the corners of the indenter (see figure 2.9). Various models exist in literature to estimate K_C by indentation. A common model is the Evans and Marshall's model (eq. 2.10).

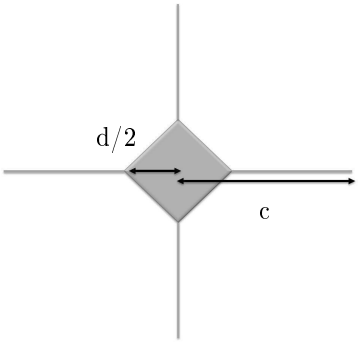

Figure 2.9: Schematic of a generic image from a Vickers indent used in determining K_C. d_i is the indentation diagonal length, and d is the average d_i for one indent. c is the crack length measured from the indentation center

Evans and Marshall's model is only valid when half-penny median-radial cracks develop [9]. These cracks emerge when the load is sufficiently high ensuring $\frac{c}{d} > 1.25$ (c being the distance from the indentation center to the crack tip and d the mean of d_i values obtained for one indent). For half-penny median-radial cracks, Evans and Marshall's model is valid and is as follow:

$$K_C = 0.057 * H_V * \sqrt{d/2} \left(\frac{E}{H_V}\right)^{2/3} * \left(\frac{c}{(d/2)}\right)^{-3/2} \tag{2.10}$$

Most of the samples herein present well-defined indentation patterns with cracks lengths fulfilling the condition $c > 1.25\ d$ at 50 g. Thus, a force of 50 g has been selected for the K_C measurements. Note that, due to stress corrosion cracking, c can vary with time after indentation [1]. To avoid substantial errors, an optical microscope images the surface crack pattern within 5 minutes after indentation.

Densification vs Shear flow

Densification and conservative shear flow are the two processes leading to permanent deformation in glasses [3, 8, 11, 12, 17]. The high pressures beneath the indenter trigger these two irreversible processes. Yoshida et al. [17] proposes a 3D technique to study indentation imprints before and after annealing to estimate the fraction of densification. Annealing the samples changes the shape of the indent pattern which is linked to the recovery of densified areas [6,8,16,17]. Thus, studying the volume ratio before and after annealing provides an easy way to estimate the amount of densification volume. Indented samples then undergo an annealing treatment at 0.9 T_g for 2 h in air. This is sufficiently long to achieve the recovery of a large proportion of the densified regions [6, 8, 16, 17]. After annealing, imprints are imaged again. Post-treatment of the images reveals d_a, l_a, P_{ad}, V_a^- and V_a^+(figure 2.10). Post-analysis of the

data unveils the following recovery volume ratio, V_R [18]:

$$V_R = \frac{(V_i^- - V_a^-) + (V_a^+ - V_i^+)}{V_i^-}. \tag{2.11}$$

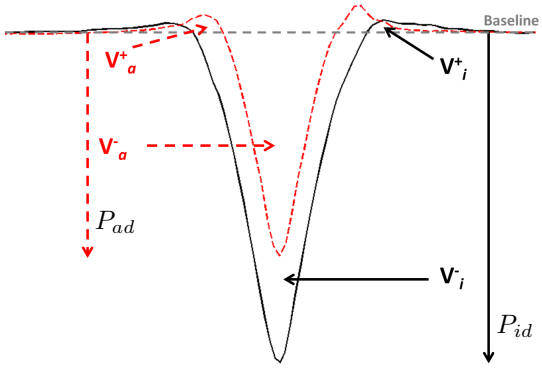

Figure 2.10: Example of the variation in the indentation prints before and after annealing

Shear flow implies plastic flow generating a displacement of matter but no volume change. The pile up around the indentation sites exposes the amount of shear flow. Profiles are extracted from figure 2.8 following the dotted blue line. Sellappan et al. [15] propose V_P to study the volume-conserving flow ratio:

$$V_P = \frac{(2V_i^+ - V_a^+)}{V_i^-} \tag{2.12}$$

(V_a^+-V_i^+) removes the densified volume contribution in the pile-up area. The denominator normalizes the shear flow.

This part presents the entire experimental set-up used to investigate the glasses structure and their mechanical properties. Density measurement, elastic moduli determination, Raman and NMR analysis give access to the physical and the structural properties of SBN glasses. The estimation of mechanical properties take place through the hardness determination, K_C, and the failure behavior. Specifically, the steps to extract the SCC curves are detailed. The two next chapters present the results on: the physical and structure properties of SBN glasses (chapter 3) and their mechanical response (chapter 4).

Bibliography

[1] G.R. Anstis, P. Chantikul, B.R. Lawn, and D.B. Marshall. A critical evaluation of indentation technique for measuring fracture toughness: I, direct crack measurement. *J. Am. Ceram. Soc.*, 64:533–538, 1981.

[2] D. Bonamy, S. Prades, C. L. Rountree, L. Ponson, D. Dalmas, E. Bouchaud, K. Ravi-Chandar, and C. Guillot. Nanoscale damage during fracture in silica glass. *Int. J. Fracture*, 140(1-4):3–14, JUL 2006.

[3] P. W. Bridgman and I. Simon. Effect of very high pressure on glass. *J. Appl. Phys.*, 24:405, 1953.

[4] M.Y. He, M.R. Turner, and Evans A. G. Analysis of the double cleavage drilled compression specimen for interface fracture energy measurements over a range of mode mixities. *Acta. Metall. Mater.*, 43:3453–3458, 1995.

[5] C. Hermansen, J. Matsuoka, S Yoshida, H. Yamazaki, Y. Kato, and Y.Z. Yue. Densification and plastic deformation under microindentation in silicate glasses and the relation to hardness and crack resistance. *J. Non-Cryst. Solids*, 364:40–43, 2013.

[6] G. Hetherington. The viscosity of vitreous silica. *Phys. Chem. Glasses*, 5:130, 1964.

[7] C. Janssen. Specimen for fracture mechanics studies on glass, ceramic society of japan. *Proc. 10th Int Cong. On glass*, pages 10.23–10.30, 1974.

[8] J.D. Mackenzie. High-pressure effects on oxide glasses. 2. subsequent heat treatment. *J. Am. Ceram. Soc.*, 46:470, 1963.

[9] D.B. Marshall and A.G. Evans. Comment on elastic-plastic indentation damage in ceramics-the median-radial crack system-reply. *J. Am. Ceram. Soc.*, 64:C181–C183, 1981.

[10] G. Pallares, L. Ponson, A. Grimaldi, M. George, G. Prevot, and M. Ciccotti. Crack opening profile in dcdc specimen. *Int. J. Fracture*, 156:11–20, 2009.

[11] A. Perriot, D Vandembroucq, E. Barthel, V. Martinez, L. Grosvalet, C. Martinet, and B. Champagnon. Raman microspectroscopic characterization of amorphous silica plastic behavior. *J. Am. Ceram. Soc*, 89:596–601, 2006.

[12] K.W. Peter. Densification and flow phenomena of glass in indentation experiments. *J. Non-Cryst. Solids*, 5:103–115, 1970.

[13] C.L. Rountree, D. Bonamy, D. Dalmas, S. Prades, R.K. Kalia, C. Guillot, and E. Bouchaud. Fracture in glass via molecular dynamics simulations and atomic force microscopy experiments. *Phys. Chem. Glasses-B*, 51:127–132, 2010.

[14] C.L. Rountree, S. Prades, D. Bonamy, E. Bouchaud, R. Kalia, and C. Guillot. A unified study of crack propagation in amorphous silica: Using experiments and simulations. *J. Allo. Compd.*, 434:60–63, 2007.

[15] P. Sellappan, T. Rouxel, F. Celarie, E. Becker, P. Houizot, and R. Conradt. Composition dependence of indentation deformation and indentation cracking in glass. *Acta Mater.*, 61:5949–5965, 2013.

[16] S Yoshida, S Isono, J. Matsuoka, and N. Soga. Shrinkage behavior of knoop indentations in silica and sodalime silica glasses. *J. Am. Ceram. Soc.*, 84:2141–2143, 2001.

[17] S. Yoshida, J.-C. Sangleboeuf, and T. Rouxel. Quantitative evaluation of indentation-induced densification in glass. *J. Mat. Res.*, 20:3404–3412, 2005.

[18] S. Yoshida, J.-C. Sangleboeuf, and T Rouxel. Indentation-induced densification of soda-lime silicate glass. *Int. J. Mater. Res.*, 98:360–364, 2007.

Chapter 3

Physical and structural investigation of SBN glasses

Contents

The previous chapter details the elaboration and experimental set-up used to investigate the structural and the mechanical properties. This chapter presents investigations on the structural properties of SBN glasses. Initially, section 3.1 describes previous models predicting how the density of the glasses evolves with elementary units. These results are part of the publication [3]. Subsequently, section 3.2 presents the evolution of Young modulus (E) and the Poisson's ratio (ν) with the glass composition. Correlations between these properties and other structure properties are examined. Sections 3.3 and 3.4 investigate the glass structure via Raman and NMR. Specifically, this section compares and contrasts ^{11}B and ^{23}Na MAS NMR spectra with the Yun, Dell and Bray model. Section 3.5 summarizes information obtained on the glass structure.

3.1 Evolution of density values with chemical composition

The density of glasses is directly linked to the variations of the underlying structural units [8,11–13,15,19]. Figure 3.1 presents the density variations as a function of $R_{SBN} = \frac{[Na_2O]}{[B_2O_3]}$ at two constant values of $K_{SBN} = \frac{[SiO_2]}{[B_2O_3]}$. The density increases as R_{SBN} increases, and reaches a plateau when R_{SBN} gets larger than ~1.5.

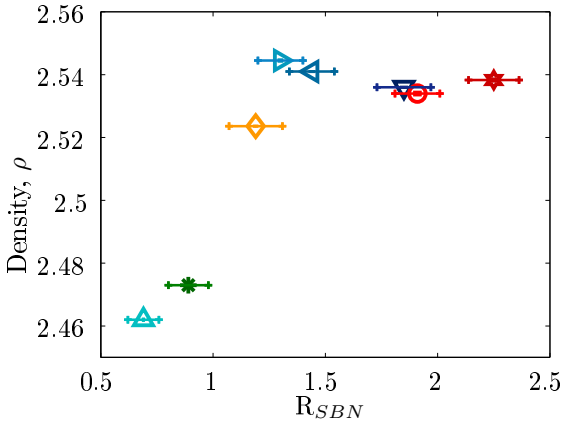

Figure 3.1: Density as a function of R_{SBN} for K_{SBN}=[SiO_2]/[B_2O_3]~2.5 (blue series) and K_{SBN} ~4.5 (red series). The density increases and, then, reaches a plateau.

Theorical models attempt to describe the evolution of the density values with the glass' chemical composition. Feil and Feller [15] proposed an equation to relate ρ to R_{SBN} and K_{SBN}:

$$\rho = \frac{\sum_{i=1}^{i=4} M_i f_i + \frac{K}{2} M'}{\sum_{i=1}^{i=4} V_i f_i + \frac{K}{2} V'} \tag{3.1}$$

M_i and V_i (where i varies from 1 to 4) correspond to the mass and volume of the borate structural units. f_i refers to the borate units define in the table 3.1. The M_i values are textbook values [33]. The V_i values come about through least square fits on the density measurements from the binary $B_2O_3 - Na_2O$ systems [15]. M' is equal to the mass of the silica network plus the mass of Na_2O attached to it. V' is the volume of the silica network with bridging and non-bridging oxygen atoms (NBOs) plus the Na^+ ions associated with the NBOs. The derivation of V' involves a least squares fit of the tertiary $SiO_2 - B_2O_3 - Na_2O$ system. The factor 1/2 comes from the fact that two B atoms exist for every Si atom. Feil and Feller's parameters in equation 3.1 underestimates ρ by $\sim$ 8 %.

Other authors modified the Feil and Feller's model [8], and recently Inoue et al. [19] proposed a new equation to estimate the density. They invoke a first-order mixture model for all the components:

$$\rho = \frac{2B_2O_3 \sum_i f_i M_i + SiO_2 \sum_i Q_i M_i'}{2B_2O_3 \sum_i f_i V_i + SiO_2 \sum_i Q_i V_i'} \tag{3.2}$$

Fraction	Borate units
f_1	$BO_{3/2}$
f_2	BO_4
f_3	$BO_{3/2}$ with 1 NBO
f_4	$BO_{3/2}$ with 2 NBO
Fraction	Silicate units
Q_0	SiO_4 tetrahedrons with 4 NBO
Q_1	SiO_4 tetrahedrons with 3 NBO
Q_2	SiO_4 tetrahedrons with 2 NBO
Q_3	SiO_4 tetrahedrons with 1 NBO
Q_4	SiO_4 tetrahedrons with 0 NBO

Table 3.1: Definition of f_1, f_2, f_3,f_4,Q_0,Q_1,Q_2,Q_3,Q_4 fractions

where f_i and Q_i are the mole fractions of the i^{th} component of the borate and silicate units. Table 3.1 recalls the f_i units and present Q_i units.
Even if Inoue's fit gives a better estimation of the density, the values measured on the SBN series are still underestimated.

Molecular dynamics (MD) simulations provide access to the basic structural building blocks of SBN glass systems. Jean-Marc Delaye performed MD simulations which give an estimation of the volumes of these elementary units by means of Voronoi tesselation. Each elementary unit's volume is defined as:

$$V_{unit} = V^V(F) + \frac{1}{2}\sum_i^{BO} V^V(BO) + \sum_j^{NBO} V^V(NBO) + N_{Na}V_{avg}(Na) \tag{3.3}$$

Here, V^V(F) is the average Voronoi volume of the network former (Si or B atom) in the group. $V^V(BO)$ and $V^V(NBO)$ are the average Voronoi volume of the bridging oxygen (BO) and non-bridging oxygen (NBO) atoms, respectively, making up the elementary unit of interest. The last term corresponds to the number of sodium ions (N_{Na}) participating to the local group multiplied by the average Voronoi volume of the Na ions which were averaged over the full box. The weighted average volume for each borate and silicate unit, V_{unit}, is estimated as follow:

$$\langle V_{unit}\rangle = 2\,[B_2O_3]\sum_i f_i V_i^{f_i unit} + [SiO_2]\sum_i Q_i V_i^{Q_i unit} \tag{3.4}$$

where the sum is taken over the different SBN compositions. f_i represents the fraction of borate elementary units and Q_i represents the fraction of silicate elementary units in each SBN glass.

A comparison between the density measured experimentally, the density predicted theoretically (from the Inoue's model) and that obtained from the MD simulations is presented in table 3.2. The MD simulations provide a good estimation (less than 0.3 % difference with the experimental values). This stems from the fact that each elementary volume unit in MD simulations is independent of the other results. The values for each units are detailed in publication [3]. Studying V_{unit} and V'_{unit} for each SBN glass reveals that they vary with [Na_2O]. Specially, V_1, V_2 and V'_4 are inversely proportional to the sodium content. Figure 3.2 highlights this trend for two volumes: V_2 and V'_3. A clear decrease in the volume of these structural units occur with [Na_2O]. A dependence with K_{SBN} is also evidenced.

Name	ρ_{exp}	ρ_{theo}	ρ_{Vor}	Symbols
SBN 12	$2.4619_{\pm 0.0003}$	2.452	2.462	△
SBN 25	$2.5446_{\pm 0.0003}$	2.527	2.550	▷
SBN 30	$2.5407_{\pm 0.0001}$	2.530	2.537	◁
SBN 35	$2.5368_{\pm 0.0001}$	2.537	2.527	▽
SBN 14	$2.4736_{\pm 0.0003}$	2.449	2.486	✳
SBN 59	$2.5344_{\pm 0.0005}$	2.535	2.539	◇
SBN 55	$2.5383_{\pm 0.0004}$	2.545	2.526	○

Table 3.2: A comparison of densities obtained from experiments, theory (Inoue's model [19] and measured ICP-AES values for the chemical composition) and Voronoi volumes V_{unit} borate units and (V'_{unit} silicate units) for each chemical composition.

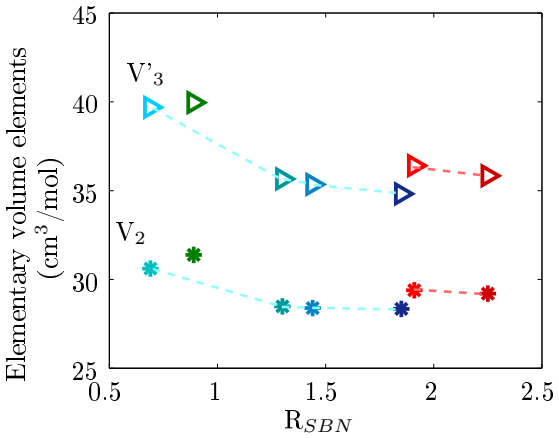

Figure 3.2: Volume of V_2 and V'_3 units as a function of R_{SBN}. The V_2 volume correspond to f_2 fraction, i.e. the BO_4 units. The V'_3 volume correspond to Q_3 fraction, i.e. SiO_4 tetrahedrons with 1 NBO units. The different colors correspond to different values of K_{SBN} : red $K_{SBN} \sim 4.5$, blue $K_{SBN} \sim 2.12$ and green $K_{SBN} \sim 4.4$.

The variation in volume of structural units with [Na_2O] is excluded from the theoretical fits. This is one reason explaining the discrepancy. This correlation is probably linked to the sodium behavior in the silicate network. The sodium ions introduced in a homogeneous silicate network occupy the interstitial free volumes, leading to a decrease of the average Voronoi volumes of the other chemical elements.

Finally, the density values first increase with R_{SBN}, with [Na_2O]. The sodium content changes the glass structure. First, the sodium content changes the coordination number of B atoms (formation of f_2 units (BO_4) at the expense of f_1 ($BO_{3/2}$)). The values of each units from the Yun, Dell and Bray model and the MD simulation are in publication [3]. Such units are denser [14] explaining the increase in ρ_{exp}. As the [Na_2O] increases again, the silica network is impacted: the Na^+ attached to the silica network decreases free volume of the glass structure because the alkali ion occupy the interstitial sites [30]. The MD simulations pointed out a decrease in the local volumes of the borate and silicate units with [Na_2O]. This can explain the plateau observed.

In the rest of this work, ρ refers to the experimental data, ρ_{exp}.

Name	V_L (m/s)	V_T (m/s)	E (GPa)	ν	Symbols
SBN 12	$3074_{\pm 17}$	$1835_{\pm 6}$	$80.1_{\pm 0.03}$	$0.208_{\pm 0.06}$	△
SBN 25	$3053_{\pm 10}$	$1789_{\pm 8}$	$80.3_{\pm 0.04}$	$0.238_{\pm 0.008}$	▷
SBN 30	$2938_{\pm 6}$	$1713_{\pm 8}$	$74.7_{\pm 0.05}$	$0.255_{\pm 0.001}$	◁
SBN 35	$3057_{\pm 15}$	$1727_{\pm 6}$	$76.7_{\pm 0.04}$	$0.264_{\pm 0.002}$	▽
SBN 14	$3049_{\pm 21}$	$1851_{\pm 32}$	$81.8_{\pm 1.02}$	$0.210_{0.015}$	✳
SBN 63	$3046_{\pm 11}$	$1809_{\pm 8}$	$81.9_{\pm 0.06}$	$0.226_{\pm 0.009}$	◇
SBN 59	$2968_{\pm 24}$	$1767_{\pm 15}$	$77.2_{\pm 0.03}$	$0.230_{\pm 0.007}$	○
SBN 55	$2931_{\pm 20}$	$1689_{\pm 4}$	$72.8_{\pm 0.06}$	$0.251_{\pm 0.005}$	✡

Table 3.3: V_L, V_T, E, and ν calculated for each SBN glass. The last column depicts the symbols used in figures.

3.2 Evolution of Young modulus, E and Poisson's ratio, ν

Macroscopic characterizations such as the elastic properties provide a glimpse of the short- and medium-range orders. Part I.2.3.2. details ultrasonic techniques used to acquire V_L and V_T. From V_L and V_T, equation 2.3 and 2.4 provides E and ν, respectively. The table 3.3 presents V_L, V_T, E, and ν calculated for each SBN sample.

Both E and ν depend on the chemical composition of the glasses. Figure 3.3 shows that E varies with [Na_2O]. Literature connects the variations in E to changes in the interatomic bonding energy, the coordination, the degree of polymerization, etc.

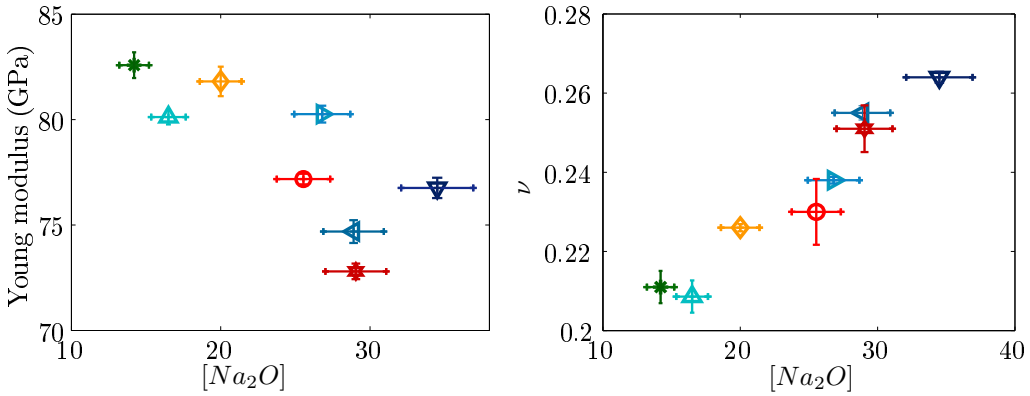

Figure 3.3: Evolution of Young modulus (E) in GPa and the Poisson's ratio (ν) with the mol % of Na_2O.

Yet, the relation between E and Na_2O is not straightforward. For the high K_{SBN} series ($K_{SBN} \sim 4.6$), a non-linear decrease of E occurs. For the low K_{SBN} series ($K_{SBN} \sim 2.5$), the behavior is more complex. This observation confirms the fact that E depends on many parameters. One of these parameters is the amount of $^{[4]}B$ in the glass. As stated previously, when [Na_2O] increases and Na^+ ions are in charge compensator role, $^{[4]}B$ elements increase at the expense of $^{[3]}B$ elements. Initially this leads to an increase in ρ which subsequently leads to an increase in E. As more sodium is added to the glass, some $^{[4]}B$ switches to $^{[3]}B$ elements, with NBO and Na^+ ions acting as network modifiers. Also, during this phase some Na^+ ions enter into the silica nework and yield the formation of NBO. Both these NBO, and the structural

transformations lead to a decrease of E due to the weaky binding BO_3 planar units [22].

There does not seems to be a one-to-one relation between E and [Na_2O]. Conversely, the Poisson ratio (ν) appears to be linearly correlated with [Na_2O] (figure 3.3). ν is an important material parameter relating a material's reaction to a uniaxial strain and its response in the other two directions. A first order approximation for a cubic isotropic system is as follows:

$$\nu = -\frac{\Delta L'}{\Delta L}. \tag{3.5}$$

ΔL is the change in length in the direction of uniaxial strain and $\Delta L'$ is the materials reaction in the other directions. Rouxel et al. link ν with the packing fraction (P_f) and the glass network's dimensionality [32]. Thus, ν provides an interesting insight into a glass's short- and medium-range order. ν depends on the dimensionality of the structural units. The packing fraction (P_f) relates the amount of volume occupied by the atoms (V_i) to the total volume of the glass:

$$Pf = \rho \times \frac{\sum f_i^{oxide} V_i^{oxide}}{\sum f_i^{oxide} M_i^{oxide}} \tag{3.6}$$

ρ corresponds to the experimental density presented in the previous section (table 3.2) . f_i^{oxide}, V_i^{oxide}, and M_i^{oxide} are the molar fraction, the molar volume, and the molar weight of the i^{th} oxide. For oxide A_xO_y, $V_i^{A_xO_y}$ is:

$$V_i^{A_xO_y} = 4/3\pi \times N \times (xr_A^3 + yr_O^3) \tag{3.7}$$

N is the Avogadro number, r_A and r_O are the radii of each element contained in the oxide. The packing fraction (P_f) cannot be accurately determined since the actual atomic radius are not known, but reference [34] gives an estimate of these values. Figure 3.4 reveals an increasing trend of ν with P_f. This trend is not limited to the SBN glasses herein; Rouxel et al. [18, 31] demonstrated this trend for a wide range of glass compositions.

Figure 3.4 left reveals that P_f increases with ν for SBN samples herein. For low [Na_2O] and ν, the glass structure has a large fraction of free volume (i.e. low glass packing density). As [Na_2O] increases, both ν and P_f increase; consequently the free volume decreases in the matrix of these glasses. Rouxel et al. [32] associated this increase with a reorganization of the glassy network. This specifically alters the connectivity of the glass network. Figure 3.4 right presents the evolution of ν with the concentration of NBO (estimated via NMR measurements see section 3.4). The higher is the polymerization degree (i.e. the less numerous are NBOs), the lower is the Poisson's ratio.

Finally, the Poisson's ratio appears to be a relevant parameter to characterize the glass's organization. Low ν value reveals a large degree of free volume and stronger bonds, whereas high ν value corresponds to less free volume and a lower degree of polymerization.

3.3 Raman spectroscopy of SBN glasses

Raman analysis characterizes the structure of borosilicate glass. Figure 3.5 presents the spectrum evolution for different SBN glasses of increasing sodium amounts. The two panels in figure 3.5 correspond to

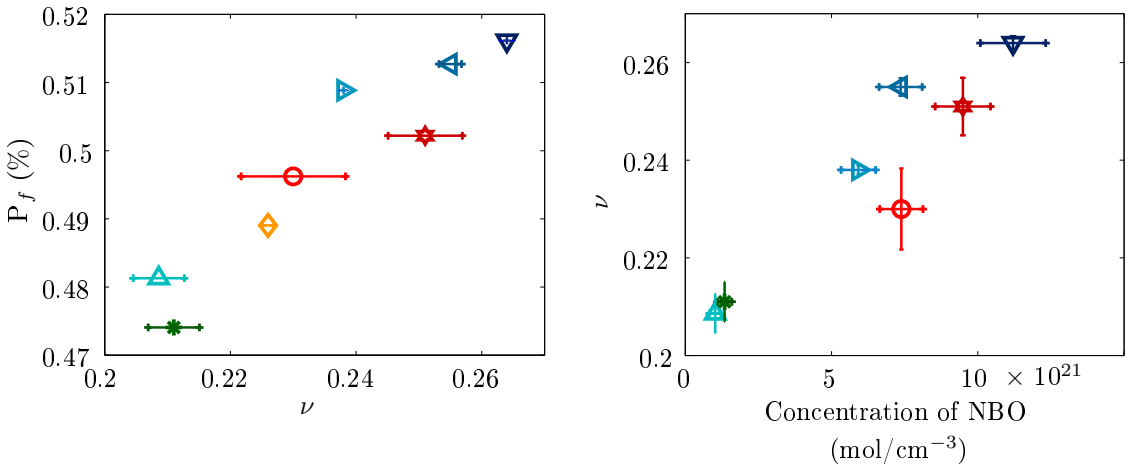

Figure 3.4: (Left) Evolution of glass packing fraction (P_f) as a function of the Poisson ratio (ν). (Right) Evolution ν as a function of the number of NBO. A good correlation is found between the Poisson' ratio and the glass organization' paramaters such as: NBO and P_f.

two different values of K_{SBN}: K_{SBN} ~2.5 (left) and K_{SBN} ~4.5 (right).

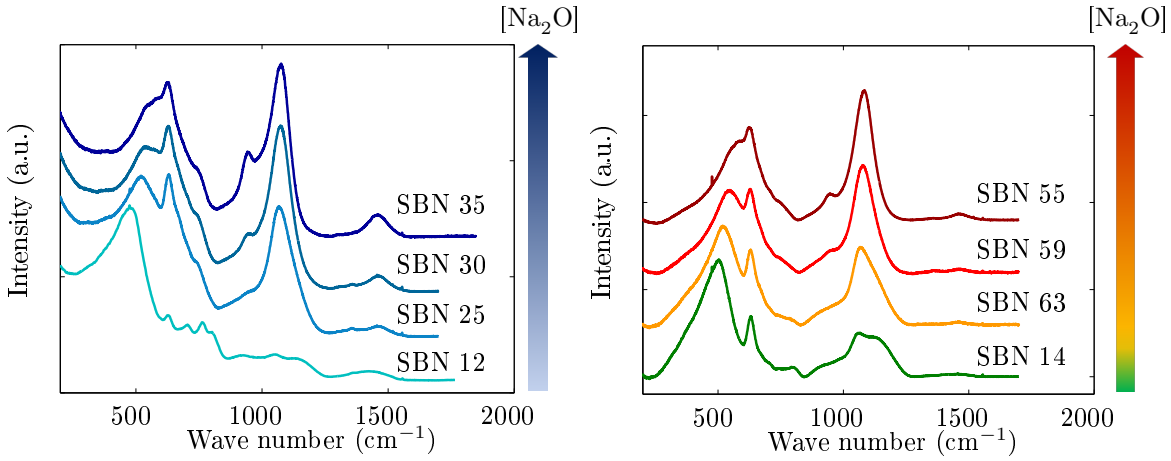

Figure 3.5: Room-temperature Raman spectra for SBN series at constant K_{SBN} (Left) $K_{SBN} \sim 2.4$; (Right) $K_{SBN} \sim 4.6$ and 3.75 (SBN 14).

Several variations occur by increasing the sodium content: (1) a shift of the main band at 430 cm^{-1} towards higher frequencies; (2) a decrease in features between 550-850 cm^{-1} , (3) a change in the contribution around 900-1200 cm^{-1}; and (4) an increase in the peak at 1450 cm^{-1}.

These Raman spectra merge several different vibrational modes. Hence, their interpretation herein emerges from the comparison and confrontation with other results of literature.

3.3.1 Low frequency Raman spectroscopy response of SBN glasses

In the low frequency region (300 to 600 cm^{-1}) several contributions appear:

The mixed stretching and bending modes of Si-O-Si units gives way to the broad band over the 300-500 cm^{-1} wave number. Pure amorphous silica has a broad band centered at 430cm^{-1}. This broad band implies multiple different Si-O-Si bond angles [27].

In densified silica, two additional peaks occur: D_1 (~495cm^{-1}) which is attributed to the vibrational modes of 4 membered rings; and D_2 (~608 cm^{-1}) which is attributed to the vibrational modes of 3 membered rings [24, 27]. The addition of [Na_2O] to pure silica (e.g. in binary $Na_2O - SiO_2$) leads to a reduction of the 435 cm^{-1} peak and the appearance of a peak at ~520 cm^{-1} [16]. Additional sodium shifts the 520 cm^{-1} peak to higher wave numbers. Some authors link this shift to a decrease in the Si-O-Si bond angle [2, 4], and to the formation of additional D_1 and D_2 [9, 23, 24]. An argument supporting this scenario is the creation of NBO on the Si atoms, which induces a reduction in the Si-O(NBO) bond length. This causes a shift to higher frequencies [24]. Matson et al. linked a peak at 500 cm^{-1} in binary $Na_2O - SiO_2$ glasses to delocalized vibrations of the silicate network with bridging and non-bridging oxygen atoms [24].

Figure 3.5 reveals a clear shift in the Si-O-Si bending vibration band to higher values with [Na_2O]. It can be due to the decrease in the average Si-O-Si bond angle or the formation of NBOs on the silica tetrahedral. Note that a decrease in polymerization degree is predicted in the Yun, Dell and Bray model [7, 10, 37].

3.3.2 Lower Mid-range frequency Raman spectroscopy response of SBN glasses

The zone around (600-850 cm^{-1}) is to be associated with the borate- and borosilicate-ring units groups.

- **633 cm^{-1}** band: This band is linked to danburite ($Si_2O_7B_2O_7$) units and/or metaborate (a planar $BO_{3/2}$ group with 1 NBO and 1 Na^+ ion nearby) groups [5]. Others attribute this peak solely to danburite units.
- **703 cm^{-1}** band: This peak is linked to the metaborate units [6, 21]
- **770 cm^{-1}** peak: This peak is linked to the vibrational mode of the borate rings with 1 or more four-coordinated boron in diborate stuctures [5, 28]
- **780 cm^{-1}** peak: This peak is linked to the vibrational mode of "caged" silica tetrahedral [6, 21, 25]
- **806 cm^{-1}** peak: The peak corresponds to the three-coordinated boron in boroxols rings [20, 28]

The contribution of borate and borosilicate ring structure change from the SBN 12 to the SBN 35, i.e. by increasing [Na_2O]. The danburite/metaborate peak (630 cm^{-1}) increases and the intensity of most of the other peaks between 700 - 808 cm^{-1} decreases with increasing concentration of sodium. A minor shoulder is observed to grow at 730 cm^{-1}. This could be due to a chain of metaborate units [21], but this peak is rather unclear. This observation is in good agreement with the well-known fact that the Na^+ ions acts as charge compensators and favor the formation of $^{[3]}B$ at the expense of $^{[4]}B$ once $R_{SBN} > 0.5 + \frac{K_{SBN}}{16}$. The increase of the danburite peak betrays an increase in the mixing of the silica and borate networks [23].

3.3.3 Upper Mid-range frequency Raman spectroscopy response of SBN glasses

The region of the spectra around 850-1250 cm^{-1} reveals the contribution of Si-O^- stretching band. Studies performed on pure silica and alkaline silicate and alumino-silicate glasses and melts permit the assignment of bands in this region [21, 26]. The bands are assigned as follow:

- **900-920 cm^{-1}** Si-O^- stretching with 3 NBO and 1 bridging oxygen (BO) (Q_1)
- **950-980 cm^{-1}** Si-O^- stretching with 2 NBO and 2 BO (Q_2)
- **1050-1100 cm^{-1}** Si-O^- stretching with 1 NBO and 3 BO (Q_3)
- **1120-1190 cm^{-1}** Si-O^- stretching with 0 NBO and 4 BO (Q_4).

From the techniques proposed by Mysen et al. [29], a deconvolution using five gaussians bands permits an estimation of each Q^n contribution. This has been applied to the investigation of the SBN glasses by G. Bureau [9] and Manara et al. [23]. They showed that the ratio Q^4/Q^3 decreases with [Na_2O]. We observe the similar behavior in the Q_n band from low to high sodium content. A depolymerization of the silicate network takes place as the sodium content increases. This result may also contribute to the shift in the Si-O-Si bending vibration band.

3.3.4 High frequency Raman spectroscopy response of SBN glasses

Finally, the high frequency (1200-1600 cm^{-1}) Raman response provides information on the $B-O^-$ bond vibrations [6, 16, 21]. This region involves numerous different types of bonds and many interpretations exist. A few of them corresponds to:

- **$\sim$1250 cm^{-1}**: B-O^- vibrations in pyroborate units [21].
- **1260 cm^{-1}**: Fraction of BO_3 units in boroxol rings [35].
- $\sim$ **1325 cm^{-1}**: *Loose* BO_3 units [35]
- $\sim$ **1380 cm^{-1}**: Metaborate units bound to $^{[4]}$B [1]
- $\sim$ **1490 cm^{-1}**: metaborate units bonded to other planar BO_3 units [1]
- $\sim$ **1530-1540 cm^{-1}**: BO_3 units in boroxols rings [35]

A significant increase of the contribution around 1480 cm^{-1} is observed in our data. Literature attribute this increase to an increase in metaborate units. This observation is correlated to the increase of the shoulder around 700 cm^{-1} (metaborate units). The addition of sodium induces a conversion of $^{[4]}$B to $^{[3]}$B, which explains the results.

[Na_2O] impact both the borate and the silicate network. The shift in the Si-O-Si bending vibration band is probably correlated to a decrease in the mean Si-O-Si angle and to an increase in NBO close to silicon atom. The Raman analyzis qualitatively describes the change in the glass structure induced by sodium content. The NMR investigation attempts to quantify variations observed.

3.4 Investigation of SBN glasses via NMR measurements

MAS NMR measurements probe the local environment of the boron and sodium atoms.

3.4.1 Investigation of the boron environment through $^{[11]}$B MAS NMR

Boron atoms have a huge impact on the structural and physical properties of glasses. This impact is conventionally referred to as *the boron anomaly* [23,36]. $^{[11]}$B NMR MAS spectra reveals the evolution of the boron environment with sodium content. Figure 3.6 presents the evolution of $^{[11]}$ B NMR MAS with the sodium content for $K_{SBN} \sim 2.5$.

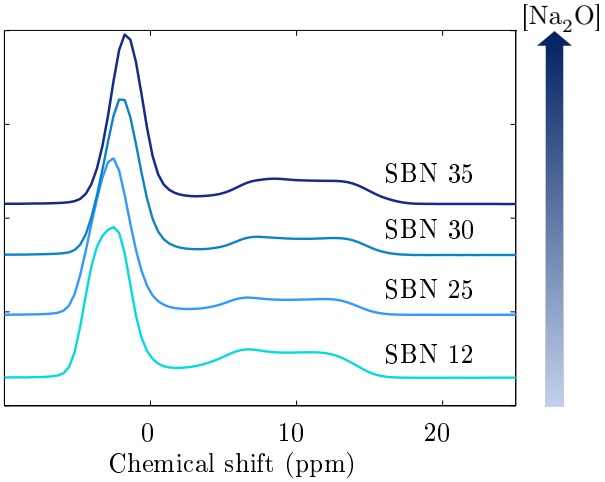

Figure 3.6: $^{[11]}$B MAS NMR spectra for the K_{SBN} ~2.5 series collected at ambient temperature. The intensity of each spectrum is normalized. From the bottom to the top, the sodium content increases.

The $^{[11]}$B MAS NMR spectra of both series consist of two broad peaks centered at 0 and 11 ppm which correspond to $^{[4]}$B and $^{[3]}$B, respectively. Integrating the area under each peak quantifies the relative proportion of $^{[4]}$B with respect to $^{[3]}$B. Thibault Charpentier proposed to deconvolute the spectra by considering four main contributions : Two for the $^{[4]}$B and two for the $^{[3]}$B.

Table 3.4 presents the results of the deconvolution. For both series, the $^{[4]}$B fraction initially increases with [NaO_2] and then decreases. The initial increase stems from the fact that sodium initially makes $^{[3]}$B switch into $^{[4]}$B and acts as a $^{[4]}$B charge compensator. But after a sufficient amount of sodium is added to the system, the trend reverses. $^{[4]}$B transfer back into $^{[3]}$B. Yet, the $^{[3]}$B have NBOs on them, and the Na^+ ion acts as a network modifier. During this second stage, the Na^+ ions also modify the silica network. In the SiO_2-B_2O_3-Na_2O system, the sodium ions, which do not contribute to the formation of $^{[4]}$B units aid in the depolymerization of the glass network by breaking Si-O-Si or Si-O-B bonds. $^{[4]}B_{YDB}$ and $^{[3]}B_{YDB}$ display the percentage of each boron according to the Yun, Dell and Bray models as explained in the previous section. These values correspond to the concentration of oxides as obtained from the ICP-AES measurements.

At $K_{SBN} \sim 2.5$, the absolute value of $^{[4]}$B increases from SBN 12 to SBN 25. Theoretically the

Name	R_{SBN}	K_{SBN}	$^{[4]}B$	$^{[3]}B$	$^{[4]}B_{YDB}$	$^{[3]}B_{YDB}$	% NBO	Symbols
SBN 12	0.4	2.5	60	40	65.6	34.4	2.1	△
SBN 25	1.30	2.5	71.5	28.5	62.2	37.8	12.5	▷
SBN 30	1.44	2.5	68.9	31.1	59.5	40.5	15.8	◁
SBN 35	1.85	2.5	62.2	37.8	51.5	48.5	25	▽
SBN 14	0.89	4.4	72	28	77.5	22.5	2.7	✳
SBN 59	1.91	4.5	79.5	20.5	73.5	26.5	15.9	○
SBN 55	2.25	4.5	76.3	23.7	68	32	20.9	✡

Table 3.4: Experimental % R_{SBN}, K_{SBN}, $^{[4]}B$ and $^{[3]}B$ determined by NMR $^{[11]}B$. Comparison with $^{[4]}B_{YDB}$ and $^{[3]}B_{YDB}$ predicted from the Yun, Dell and Bray model.

Yun, Dell and Bray model [7, 10, 37] suggests that the number of $^{[4]}B$ should display a maxima at $R^{max}_{SBN} = .5 + K_{SBN}/16 \sim 0.656$. Results herein predict the peak should occur between SBN 12 and SBN 25. After R^{max}_{SBN}, the sodium causes the formation of NBO on the silica units in the reedmergnerite groups. From SBN 25 to SBN 35, both experimental and theoretical values predict a decreasing trend in $^{[4]}B$. Similarly, a decreasing trend occurs for higher silica content, $K_{SBN} \sim 4.5$. Apart from the $^{[3]}B/^{[4]}B$ quantification, the $^{[4]}B$ units may evolve as evidenced by the shift in the $^{[4]}B$ peak towards ~ 0 ppm (figure 3.6). NMR spectra give the amount of $^{[4]}B$ in the system. Using this value and assuming that one Na^+ ion compensates one $^{[4]}B$ unit, an estimation of the fraction of sodium atoms bonded to the NBO can be done [17]:

$$N_{NBO} = N_{Na} - N_{^{[4]}B}, \tag{3.8}$$

where N_{Na}, N_{NBO}, and $N_{^{[4]}B}$ are the total number of Na^+ ions, the number of NBO, and the number of Na^+ ions acting as network compensators (equivalently the number of $^{[4]}B$) in the system, respectively. Table 3.4 details the percentage of NBO in the system. The number of NBO increases with $[Na_2O]$. This result is coherent with the analysis of the Q_n band and the $B-O^-$ band in the Raman spectra (section 3.3).

3.4.2 Investigation of sodium environment through $^{[23]}$Na NMR MAS

Figure 3.7 displays the $^{[23]}Na$ NMR MAS spectra for SBN glasses with $K_{SBN} \sim 2.5$. Each spectrum contains a single, broad asymmetrical peak which shifts to the right as the sodium content increases (from SBN 12 to SBN 35). Figures 3.8 left and right depict the correlation between the ^{23}Na chemical shift and the $[Na_2O]$ and the concentration of NBO, respectively.

The chemical shift depends on the role of the Na^+ ion in the SBN glass structure. This is coherent with literature: Na-O bonds length depends on if the oxygen atom bridges or not [2]. Na-NBO bond length is shorter than Na-BO. Varying the local environment of the sodium ions alters the chemical shift.

The NMR analyses quantitatively describe the evolution of the local environment of the B and the Na atom. The ^{11}B quantify the coordination number which increases and then decreases with $[Na_2O]$. A change in the Na^+ environment expresses a change in the role of sodium in the glassy network.

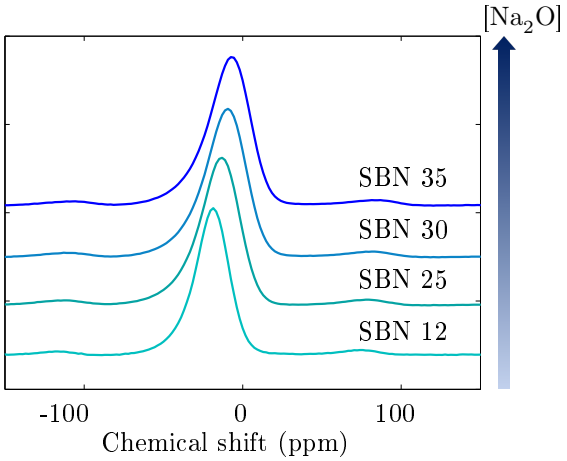

Figure 3.7: [23]Na NMR MAS spectra for the SBN series $K_{SBN} \sim 2.5$ collected at ambient temperature. The intensity of each spectrum is normalized.

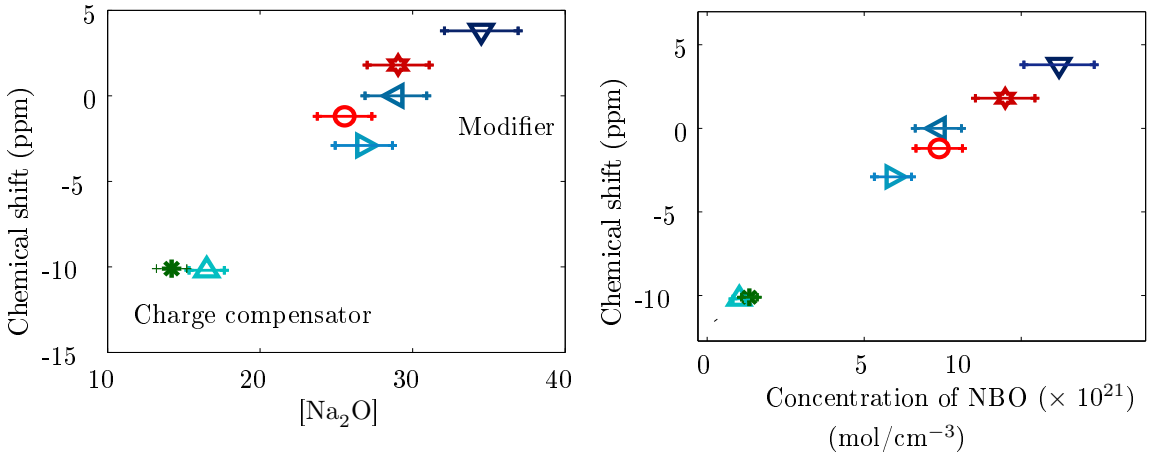

Figure 3.8: Correlation between the [23]Na chemical shift and: (left) the concentration of [Na_2O]; and (right) the concentration of NBO as deduced from the [11]B MAS NMR measurements.

3.5 Discussion on structural investigation of SBN series glasses

This part inverstigates the physical and structural properties of the SBN glasses. Density measurements provide an easy way to access to the structural units variations. Theoretical Inoue's model yields predictions of ρ in borosilicate glasses which differs from the experimentally measured by $\sim 3\%$. MD simulation permits a better estimation of the volume for each unit. [Na_2O] decreases the volume of such structural units. This effect is not taken into account in the theorical models; this is one reason explaining the discrepancies between experimental values and theorical values. The Poisson's ratio is a relevant macroscopic mechanical parameter to characterize the organization of the glassy structure. Low Poisson's ratio (and low packing fraction) display a large amount of free volume and stronger bonds (e.g. silica glass: $\nu \sim 0.17$). Whereas, high Poisson's ratio implies less free volume and weaker bounds. Specifically, a

good correlation arises between the glass connectivity and the Poisson ratio. This is confirmed by Raman analysis. Raman analysis qualitatively depicts the variations of the borosilicate structure depending on [Na_2O]. As the sodium content increases, the number of NBO increases leading to a depolymerization of the glass's network. As a consequence, the silica and borate networks evolve and NBOs emerge on both networks. The quantification of structure properties require NMR investigations. The $^{[4]}B$ concentration first increases, then decreases. Variation in the Na^+ NMR spectra reveals the two successive roles of the sodium ions in the glassy network: charge compensator (low sodium content) and modifier (high sodium content)

3.6 Conclusion

Spectroscopy techniques highlight the variations in the SBN glass structure as a function of the chemical composition. Moreover, the macroscopic properties (E, ν and ρ) depend on the basic building blocks constituting the glass network. Addition of sodium leads to major changes in the glass structural and physical properties:

1. **Theoretical roles of sodium atoms in a glassy network:**

   i) Charge Compensator: The sodium ions initially attack the borate network causing the $^{[3]}B$ units to be transformed into $^{[4]}B$ unit with a sodium nearby acting as a charge compensator.

   ii) Network Modifier: Once R_{SBN}^{max} occurs, the additional sodium ions attach to the silica network forming NBO. After $R_{d1} = .5 + 0.25 \times K_{SBN}$, theoretically Na^+ ions attacks both the silicate and borate network causing the formation NBO in both networks.

2. **Conversion of $^{[4]}B$ to $^{[3]}B$**: Raman analysis and NMR measurements evidence variations in $^{[4]}B/^{[3]}B$ with sodium content. Na^+ ions first yield a conversion of $^{[3]}B$ to $^{[4]}B$.

3. **Depolymerization of the glass network**: Q_n analysis highlights the creation of NBO associated with the silica network. Depolymerization of the glass network can explain the decrease of the Young modulus.

4. **Change in the glass organization**: ν appears to be the relevant mechanical parameter characteristics of the organization of the glassy matrix at the mesoscopic scale. Low ν corresponds to glasses with high connectivity, strong bonds, and high free volume (low density). Conversely, glasses with high ν have a high sodium content, weaker bonding, and are more dense.

This chapter provides a better understanding of structural properties of SBN glasses. This chemical composition presents two advantages: (1) simple glass composition (in short) highlights the role of each oxide. Sodium content plays a major role by modifying glass topology. The Poisson's ratio supplies access to the short-medium range order in the glass organization. The next chapter estimates the mechanical properties and links them to the glass structure.

Bibliography

[1] R. Akagi, N. Ohtori, and N. Umesaki. Raman spectra of k2o-b2o3 glasses and melts. *J. Non-Cryst. Solids*, 293-295:471 – 476, 2001.

[2] F. Angeli, O. Villain, S. Schuller, S. Ispas, and T. Charpentier. Insight into sodium silicate glass structural organization by multinuclear nmr combined with first principles calculations. *Geochim. Cosmochim. Acta*, 75:2453–2469, 2011.

[3] M. Barlet, A. Kerrache, J.-M. Delaye, and C.L. Rountree. Sio2-na2o-b2o3 density: A comparison of experiments, simulations, and theory. *J. Non-Cry. Solids*, 382:32 – 44, 2013.

[4] B. Boizot, S. Agnello, B. Reynard, R. Boscaino, and G. Petite. Raman spectroscopy study of beta-irradiated silica glass. *J. Non-Cryst. Solids*, 325:22–28, 2003.

[5] B. Boizot, G. Petite, D. Ghaleb, B. Reynard, and G. Calas. Raman study of beta-irradiated glasses. *J. Non-Cryst. Solids*, 243:268–272, 1999.

[6] J Bonfils de, S. Peuget, G. Panczer, D Ligny de, S Henry, P. Y. Noel, A. Chenet, and B. Champagnon. Effect of chemical composition on borosilicate glass behavior under irradiation. *J. Non-Cryst. Solids*, 356:388–393, 2010.

[7] P.J. Bray, S.A. Feller, G.E. Jellison, and Y.H. Yun. B-10 nmr-studies of the structure of borate glasses. *J. Non-Cryst. Solids*, 38-9:93–98, 1980.

[8] K. Budhwani and S. Feller. A density model for the lithium, sodium and potassium borosilicate glass systems. *Phys. Chem. Glasses*, 36:183–190, 1995.

[9] G. Bureau. *Comprehension structurale des effets d'auto-irradiation alpha dans les verres: couplage entre etudes spectroscopiques et modelisation atomistique.* PhD thesis, Universite Pierre et Marie Curie (Paris VI), 2008.

[10] W.J. Dell, P. J. Bray, and S. Z. Xiao. B-11 nmr-studies and structural modeling of Na_2O-B_2O_3-SiO_2 glasses of high soda content. *J. Non-Cryst. Solids*, 58(1):1–16, 1983.

[11] H. Doweidar. The density of sodium borosilicate glasses in relation to the microsctructure. *J. Phys. Chem. Solids*, 53:807–814, 1991.

[12] H. Doweidar. The density of alkali silicate glasses in relation to the microstructure. *J. Non-Cryst. Solids*, 194:155–162, 1996.

[13] H. Doweidar. Density-structure correlations in silicate glasses. *J. Non-Cryst. Solids*, 249:194–200, 1999.

[14] H. Doweidar, G.M. El-Damrawi, Y.M. Moustafa, and R.M. Ramadan. Density of mixed alkali borate glasse: a structural analysis. *Physica B*, 362:123–132, 2005.

[15] D. Feil and S. Feiller. The density of sodium borosilicate glasses related to atomic arrangements. *J. Non-Cryst. Solids*, 119:103–111, 1990.

[16] T. Furukawa, K.E. Fox, and W.B. White. Raman spectroscopic investigation of the structure of silicate galasses. iii. raman intensities and structural units in sodium silicate glasses. *J. Chem. Phys.*, 75:3226–3237, 1981.

[17] A. Grandjean, M. Malki, V. Montouillout, F. Debruycker, and D. Massiot. Electrical conductivity and $^{[11]}$b nmr studies of sodium borosilicate glasses. *J. Non-Cryst. Solids*, 354:1664–1670, 2008.

[18] G.N. Greaves, A.L. Greer, R.S. Lakes, and T Rouxel. Poisson's ratio and modern materials. *Nat. Mater.*, 10:823–837, 2011.

[19] H. Inoue, A. Masuno, Y. Watanabe, K. Suzuki, and T. Iseda. Direct calculation of the physical properties of sodium borosilicate glass from its chemical composition using the concept of structural units. *J. Am. Ceram. Soc.*, 95:211–216, 2012.

[20] W.L. Konijnendijk and J.M. Stevels. The structure of borate glasses studied by raman scattering. *J. Non-Cryst. Solids*, 18:307–331, 1975.

[21] H. Li, L.Y. Su, and D.M. Strachan. Raman spectroscopic study of gadolinium (iii) in sodium-aluminoborosilicate glasses. *J. Non-Cryst. Solids*, 292:167–176, 2001.

[22] A. Makishima and J.D. Mackenzie. Direct calculation of young's modulus of glass. *J. Non-Cryst. Solids*, 12:35–45, 1973.

[23] D. Manara, A. Grandjean, and D.R. Neuville. Advances in understanding the structure of borosilicate glasses: A raman spectroscopy study. *Am. Mineral.*, 94:777–784, 2009.

[24] D.W. Matson, S.K. Sharma, and J.A. Philpotts. The structure of high-silica alkali-silicate glasses. a raman spectroscopic investigation. *J. Non-Cryst. Solids*, 58:323–352, 1983.

[25] D.A. McKeown, F. L. Galeener, and G.E. Brown Jr. Studies of al coordination in silica-rich sodium aluminosilicate glasses and some related minerals. *J. Non-Cryst. Solids*, 68:361–378, 1984.

[26] P. McMillan. Structural studies of silicate glasses and melts-applications and limitations of raman spectroscopy. *Am. Miner.*, 69:622–644, 1984.

[27] P. McMillan, B. Piriou, and R. Couty. A raman study of pressure-densified vitreous silica. *J. Chem. Phys.*, 81:4234–4236, 1984.

[28] B.N. Meera, A.K. Sood, N. Chandrabhas, and J. Ramakrishna. Raman study of lead borate glasses. *J. Non-Cryst. Solids*, 126(3):224 – 230, 1990.

[29] B.O. Mysen, L.W. Finger, D. Virgo, and F.A. Seifert. Curve-fitting og raman-spectra of silicate-glasses. *Am. Mineral.*, 67:686–695, 1982.

[30] A. Pedone, G. Malavasi, A. N. Cormack, U. Segre, and M. C. Menziani. Insight into elastic properties of binary alkali silicate glasses; prediction and interpretation through atomistic simulation techniques. *Chem. Mater.*, 19:3144, 2007.

[31] T Rouxel, T. Hammouda, and A. Moré ac. Poisson's ratio and the densification of glass under high pressure. *Phys. Rev. Lett.*, 100:225501, 2008.

[32] T. Rouxel, H. Ji, V. Keryvin, T. Hammouda, and S. Yoshida. Poisson's ratio and the glass network topology - relevance to high pressure densification and indentation behavior. *Advanced Materials Research*, 39-40:137–146, 2008.

[33] R.C. Weast, M.J. Astle, and W.H. Beyer. *Handbook of chemistry and physics.* CRC Press, 1985-1986.

[34] E.J. Whittaker and R. Muntus. Ionic radii for use in geochemistry. *Geochim. Cosmochim. Acta*, 34:945–956, 1970.

[35] T. Yano, N. Kunimine, S. Shibata, and M. Yamane. Structural investigation of sodium borate glasses and melts by raman spectroscopy : I. quantitative evaluation of structural units. *J. Non-Cryst. Solids*, 321:137–146, 2003.

[36] Y.H. Yun and P. J. Bray. Nuclear magnetic-resonance studies of glasses in system K_2O-B_2O_3-P_2O_5. *J. Non-Cryst. Solids*, 30(1):45–60, 1978.

[37] Y.H. Yun, S.A. Feller, and P.J. Bray. Correction and addendum to nuclear magnetic-resonance studies of the glasses in the system Na_2O-B_2O_3-SiO_2. *J. Non-Cryst. Solids*, 33:273–277, 1979.

Chapter 4

Mechanical properties

Contents

Chapter 3 investigates the structural and physical properties of SBN glasses. After an initial increase in the $^{[4]}B$ count due to $[Na_2O]$, $[Na_2O]$ leads to an increase in the number of $^{[3]}B$ and NBO. A a consequence, the glassy network has a lower polymerization degree. Finally, ν (the Poisson's ratio) provides a continuum means to describe the glasses short and mid-range order: (1) low ν expresses reticulated glasses with low packing fraction, and (2) high ν corresponds to glasses with higher packing fraction and low degree of polymerization. This chapter presents the evolution of the mechanical properties in SBN glasses. Section 4.1 discusses the variation of the glass hardness with the chemical composition. Then, section 4.2 investigates the different behaviors of SBN glasses in stress corrosion. Finally, the last section summarizes and contrasts results on mechanical properties regarding the methods employed.

4.1 Evolution of the contact damages with chemical composition

After unloading the Vickers' indenter, an optical microscope visually captures the features of the indents. Figure 4.1 displays examples of indentation prints for the $K_{SBN} = \frac{[SiO_2]}{[B_2O_3]} \sim 2.5$ series (SBN 12, SBN 25, SBN 30, SBN 35). The examination of figure 4.1 reveals a clear influence of the sodium amount on the crack behavior. For low amounts of sodium (i.e. SBN 12) at 50 g, no cracks emerge, while cracks are visible at the surface in glasses with higher sodium content. In addition, the light reflection seen in SBN 35 glass can be a sign of pile-up. Figure 4.2 displays indentation prints for the $K_{SBN} \sim 2.5$ series

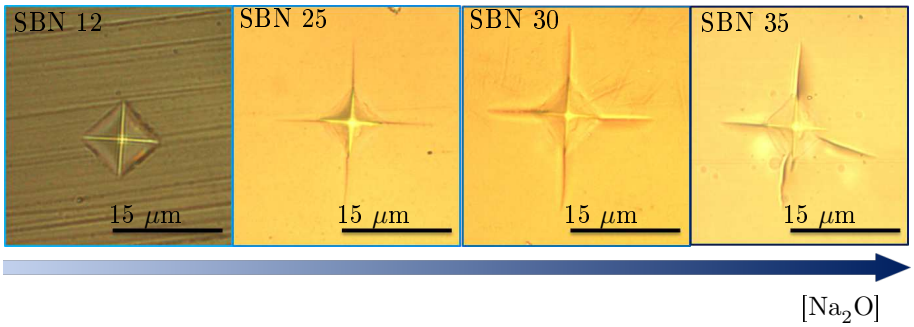

Figure 4.1: Evolution of indentation imprints for the $K_{SBN} \sim 2.5$ series (SBN 12, SBN 25, SBN 30, SBN 35) at 50 g in ambient conditions. An optical camera coupled with the Vickers's indenter captures the imprint 5 minutes after indentation. From the left to the right the sodium content increases.

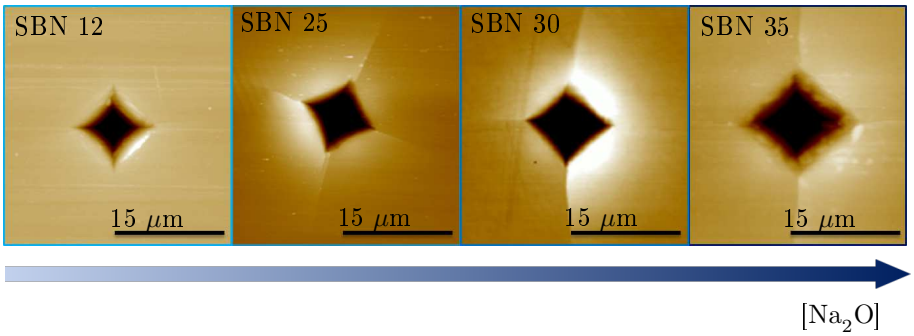

Figure 4.2: Evolution of indentation prints from the SBN 12 to the SBN 35 glasses at 50 g in ambient conditions captured via an AFM. From the left to the right the sodium content increases.

(SBN 12, SBN 25, SBN 30, SBN 35) at 50 g in ambient conditions via an AFM. Subsequently, these AFM images aid in enumerating P_{id} (the residual penetration depth), d_i (the diagonal length), V_i^- (the volume below the surface), and V_i^+ (the volume above the surface). These measurements facilitate estimates of the hardness, crack resistance, K_C, etc. Tables 4.1 and 4.2 summarize obtained values after averaging over at least 10 different indents.

4.1.1 Evolution of hardness (H_V)

Equation 2.9 provides a means to calculate H_V (Hardness via a Vickers indenter) knowing the maximum load applied during the indent ($F = 50\,g$) along with d_i of the imprints (4.1). For each sample, I performed

Name	Diagonals d_i (μ m)		H_V	C_R	K_C	Symbols
	d_1	d_2	(MPa)	(g)	(MPa.m$^{-1/2}$)	
SBN 12	10.4	10.6	$8200_{\pm 300}$	270	$0.98_{\pm 0.09}$	△
SBN 25	11.9	12.15	$6340_{\pm 100}$	26	$.69_{\pm 0.07}$	▷
SBN 30	12.7	13.3	$5400_{\pm 200}$	32	$.61_{\pm 0.06}$	◁
SBN 35	13.5	13.7	$5000_{\pm 200}$	29	$0.56_{\pm 0.06}$	▽
SBN 14	11.2	11.3	$7200_{\pm 300}$	45	$0.81_{\pm 0.08}$	✳
SBN 63	12	11.9	$6400_{\pm 200}$	38	$0.74_{\pm 0.05}$	◇
SBN 59	13.1	13.1	$5370_{\pm 90}$	37	$0.71_{\pm 0.07}$	○
SBN 55	14	13.25	$4900_{\pm 100}$	40	$0.65_{\pm 0.05}$	✡

Table 4.1: Experimental values d_i obtained from the AFM images of the indentation prints in the various SBN glasses. Estimates for H_V and K_C arises from equation 2.9 and 2.10. Section 2.4.3 describes how to estimate C_R. The last column restates the symbols used in the plots herein.

10 indentations and defined the H_V values after averaging over these 10 indents. Table 4.1 presents the obtained values. Figure 4.3 reveals the evolution of H_V (MPa) as a function of $R_{SBN} = \frac{[Na_2O]}{[B_2O_3]}$. The chemical composition of silicate glasses affects significantly the hardness values. For constant $K_{SBN} = \frac{[SiO_2]}{[B_2O_3]}$ and increasing R_{SBN} (and increasing [Na_2O]), H_V value decreases. The decrease is less pronounced for the $K_{SBN} \sim 4.5$ (i.e. samples with more SiO_2). This decrease in H_V corresponds to an increase of the residual penetration depth (P_{id}) as determined from AFM imaging (see table 4.2). As the sodium content increases, the indenter penetrates deeper into the glass.

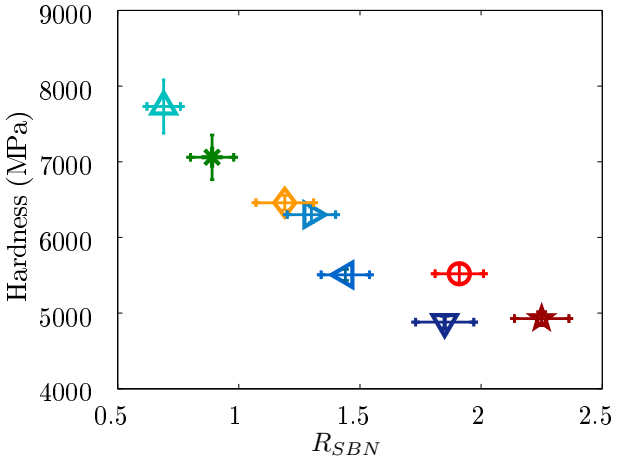

Figure 4.3: Hardness values as a function of R_{SBN} for SBN glasses (at 50 g in ambient conditions; maximum load held for 15 s).

Linking this variation to the structure is the key to understand the glass behavior. High levels of [Na_2O] reduce the SBN glasses resistance to Vickers' indentation. Above a threshold amount of sodium (i.e. $R_{SBN} > R^{max}_{SBN}$ from the Yun, Dell and Bray model) a conversion in $^{[4]}$B into $^{[3]}$B occurs and NBOs form. Figure 4.4 left and right present the evolution of hardness values for the SBN series with

the concentration of NBO and the $^{[4]}$B concentration, respectively. An inverse correlation come about with H_V and the NBO concentration. On the other hand, no distinct correlation occurs between the $^{[4]}$B concentration and H_V. NBO reduces the connectivity of the glass, which in turn alters the short

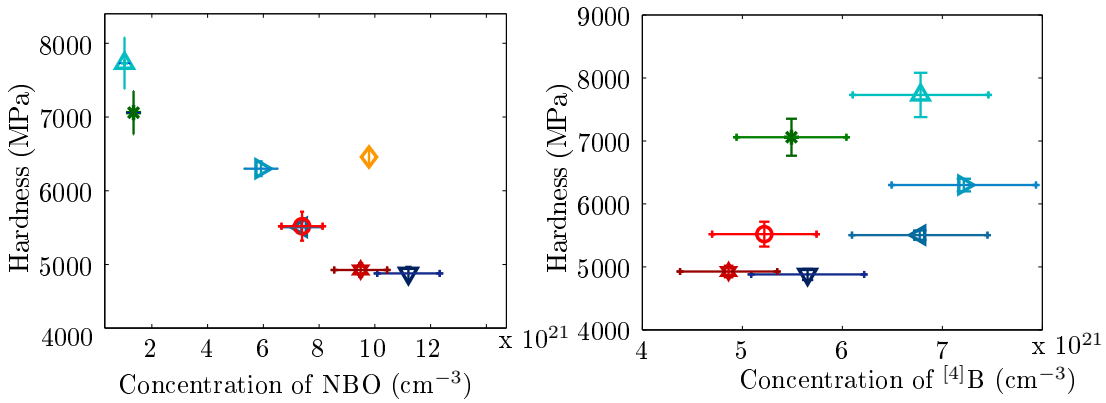

Figure 4.4: (Left) Evolution of hardness, H_V, as a function of the concentration of Non Bridging Oxygen (NBO) deduced from the NMR measurements (at 50g in ambient conditions). (Right) Evolution H_V versus $^{[4]}$B concentration deduced from the NMR measurements (at 50g in ambient conditions).

and medium-range order. Poisson's ratio (ν) provides an interesting insight into the glass's short- and medium- range order. The Poisson's ratio relates a material's reaction to a uniaxial strain and its response in the other directions. Herein, the SBN glasses exhibit a ν range of values from 0.21 to 0.27 (Table 3.3). H_V values decrease almost linearly with ν (figure 4.5). When ν is low (i.e. the glass network is reticulate), H_V is high.

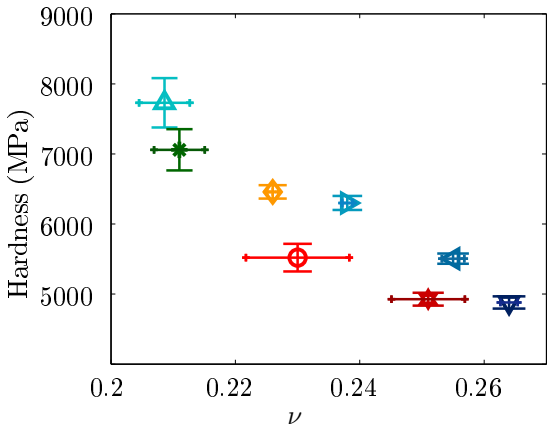

Figure 4.5: Evolution of hardness as a function of the Poisson's ratio (ν) (indentation at 50g in ambient conditions).

As stated above, additional [Na_2O] yields changes in ν. It also affects the packing fraction (P_f) which is a measure of how densely the system is packed [18]. For low values of [Na_2O] and ν, the glass structure has a large fraction of free volume (i.e. low glass packing density). Conversely, high amount

of [Na_2O] yields high ν and high P_f. This implies that free volume should decrease as [Na_2O] increases, so as the H_V value. Thus, it appears that the atomic bond strength and the reticulation of the glassy network control the behavior upon indentation. The hardness measures a materials resistance to external pressure deformation induced by a harder material. Still, two glasses with the same H_V value may exhibit significantly different overall behavior upon indentation: cracking behavior, damage, densification, plastic flow, etc. The next three subsections address these differences.

4.1.2 Crack resistance

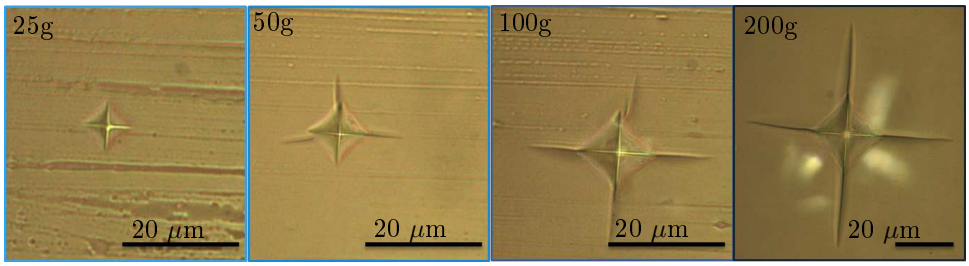

Figure 4.6: Set of optical images in SBN 14 acquired at increasing loads. As the loads increases the number of cracks initiating off the corners of the indenter increases.

The evolution of the average number of cracks per corner defined P_C, the probability of crack appearance. Figure 4.6 displays optical images for SBN 14 at different loads. At low loads ($F \leq 25$ g), no crack are observed to pop up from the corners of the Vickers's indenter. The average number of cracks initiating off the corners of the Vickers' indenter increases between 25 g and 200 g. At 200 g, all four corners have, on average, one crack. The probability of crack appearance, P_C, is the average number of cracks per corner over at least 10 indents at a given load. Figure 4.7 exemplifies the probability of crack appearance in SBN 14 (dark green stars) along with the other SBN samples. All SBN glasses, except SBN 12, rapidly increase their crack appearance probability at low loads. 100 % P_C was never reached for SBN 12 due to limitations of the experimental setup (i.e. higher loads were not feasible with the hardness tester).

As recalled in the part I chapter 2 in the section 2.4.3, the crack resistance, C_R, is defined as the load at which P_C equals 50% (estimated by looking at when the data in figure 4.7 crosses the 50% gray dotted line). Table 4.1 presents C_R for the different SBN samples. SBN 12 is significantly different than the other glasses. The crack appearance depends on the processes involved in the glass deformation. Processes occurring during indentation do not favor growth of median/radial cracks in SBN 12 as observed for other SBN glasses. Thus, complex processes such as densification and shear flow are non-negligible for C_R estimates.

4.1.3 Toughness, K_C

Part I chapter 2 in the section 2.4.3 details the requirements for estimating K_C from indentations. The formation of the median/radial cracks length permit the use of Evans and Marshall's model. Comparing K_C from one glass to another requires an equivalent maximum load. For almost all the samples, reasonable

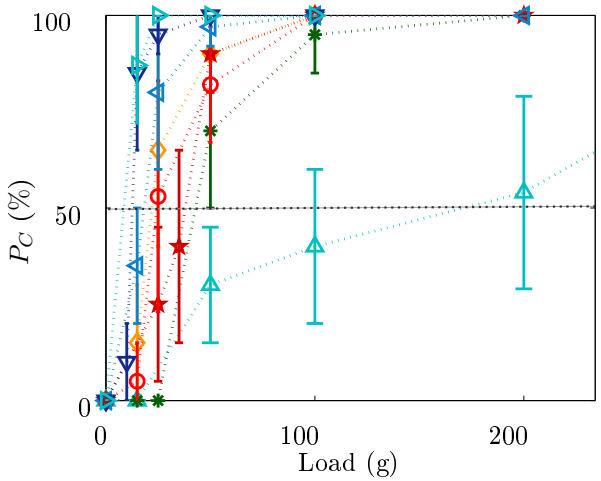

Figure 4.7: Crack appearance probability as the function of the indent load for all the SBN glasses. Blue symbols are to be associated with the K_{SBN}=2.1 series and red symbols are to be associated with the K_{SBN}=3.7 series. Note that the SBN 12 presents a singular behavior.

indentation prints plus sufficient energy to propagate cracks ($C_R > 50\%$) occurs at 50 g. The only exception here is SBN 12, which does not forms well-developed cracks and, hence, does not satisfies the criterion $c > 1.25\ d$ at 50 g. As SBN 12 is the only sample which does not exemplify median/radial cracks, the Evans and Marshall's will still be invoked for comparison purposes.

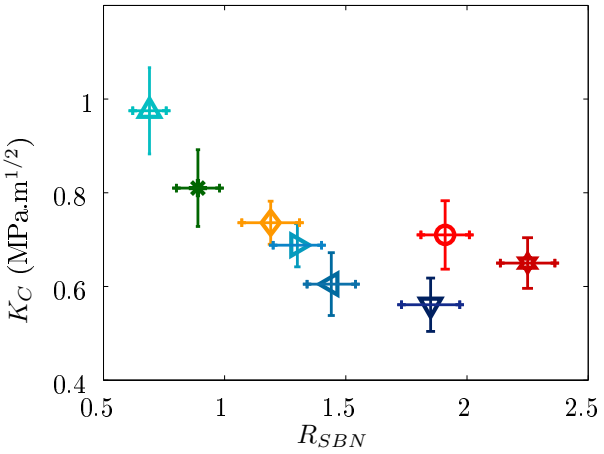

Figure 4.8: Toughness values K_C of SBN glasses as a function of R_{SBN} for $K_{SBN} \sim 2.5$ series (blue) and $K_{SBN} \sim 4.5$ series (red).

Figure 4.8 shows that K_C decreases as R_{SBN} increases for constant K_{SBN}. It should be noted that K_C for SBN 12 probably overestimates the correct value due to the lack of well-developed cracks. Conversely, the variations of K_C with ν (plotted in figure 4.9) reveals a fairly good collapse. A notable exception is the SBN 12 glass. Otherwise, figure 4.9 reveals that K_C decreases linearly with ν ($K_C = m\nu + b$ where

$m = -4.46 \pm 0.27$ and $b = 1.75 \pm 0.06$).

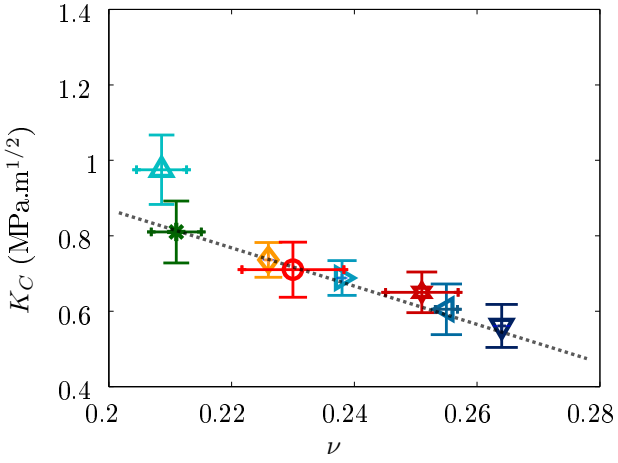

Figure 4.9: Toughness values (K_C) as a function of ν for all the SBN glasses. The line ($K_C = m\nu + b$ where $m = -4.46 \pm 0.27$ and $b = 1.75 \pm 0.06$) depicts a linear fit through all the data, excluding SBN 12.

This collapse highlights the fact that K_C is linked to the glass's short- and medium order. To investigate how ν is correlated to matter flow under the indenter, I performed complementary measurements. Measurements of K_C should be taken with care beacause is not applicable for glasses which densify under indenter (ex: pure silica).

4.1.4 Complementary measurements of Vickers indentations

AFM imaging reveals shape changes of the indentation patterns with glass chemistry (figure 4.2). Analyzing AFM images reveals changes in the volume of the pile-up V_i^+ and the volume of the indent V_i^-. Table 4.2 presents these calculations along with their ratio V_i^+/V_i^-. Variations in V_i^+/V_i^- convey the glass's tendency with [Na_2O] to pile up around the indenter under pressure [20]. Figure 4.10 left presents the normalized ratio (V_i^+/V_i^-) of the pile-up as a function of R_{SBN}. Figure 4.10 unveils two different scenarios depending on the value of K_{SBN}. For $K_{SBN} \sim 2.5$, the ratio initially increases, and subsequently stabilizes. For $K_{SBN} \sim 4.5$, the ratio first slightly decreases, an then remains stable within the error bars. Examining the two series together reveals an initial increase in the ratio V_i^+/V_i^-, and then a stabilization. In order to further confirm a general trend more SBN glasses of varying R_{SBN} and K_{SBN} values should be elaborated and tested.

A good correlation exists between V_i^+/V_i^- and ν (figure 4.10 right). This indicates that glasses with lower degrees of polymerization favor densification processes. Changing the chemical composition alters the way matter flows under the indenter. The high pressure under the indenter can cause material compaction [7,16,17,26,33]. The original structural configuration can be recovered if sufficient activation energy is supplied to the material (for instance by heating) as demonstrated by Bridgman and Simon [2] and later by Mackenzie [26]. Table 4.2 presents the parameters acquired from AFM imaging of indents before (P_{id}, V_i^- and V_i^+) and after (P_{ad}, V_a^- and V_a^+) annealing. These values are average values over at least ten indents. V_R (in part I chapter 2 in equation 2.11) provides an estimate on the amount of

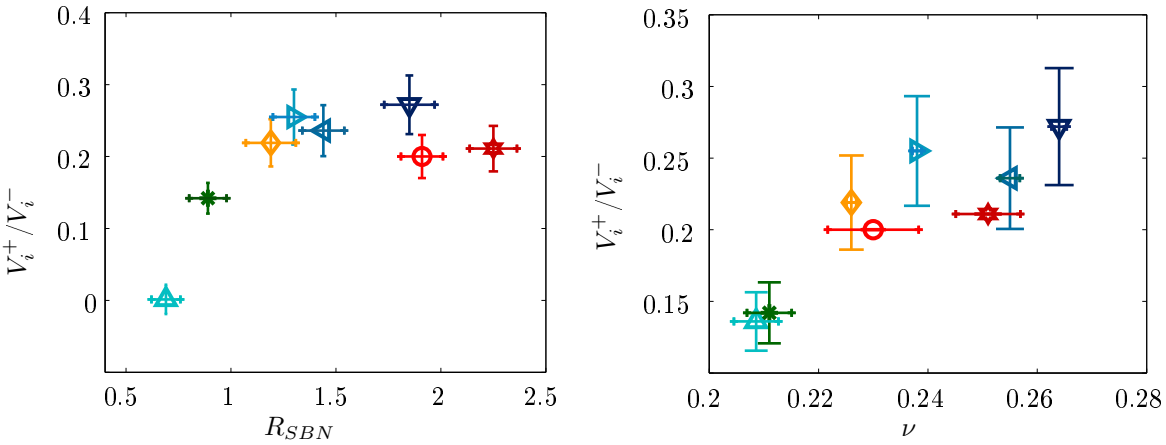

Figure 4.10: (Left) The normalized ratio (V_i^+/V_i^-) of the glasses pile-up with R_{SBN} displays two trends depending on K_{SBN}. For $K_{SBN} \sim$ 2.5, the ratio initially increases, and then stabilizes. For $K_{SBN} \sim$ 4.5, the ratio first displays a slight decrease. (Right) Evolution of V_i^+/V_i^- as a function of Poisson' ratio.

densification due to an indenter. Table 4.2 reveals the average V_R for the various SBN samples. It is well noted that annealing may not relieve all regions of densified material due to geometrical constraints.

For samples with low K_{SBN} values, the recovery volume decreases roughly linearly with R_{SBN}. ($V_R = m_{K_{SBN}\sim 2.5} R_{SBN} + b_{K_{SBN}\sim 2.5}$ where $m_{K_{SBN}\sim 2.5} = -0.409 \pm 0.005$ and $b_{K_{SBN}\sim 2.5} = 0.800 \pm 0.002$). On the other hand, the $K_{SBN} \sim 4.6$ series exhibits a significantly less pronounced decrease but approximately linear ($V_R = m_{K_{SBN}\sim 4.6} R_{SBN} + b_{K_{SBN}\sim 4.6}$ where $m_{K_{SBN}\sim 4.5} = -0.0431 \pm 0.003$ and $b_{K_{SBN}\sim 4.6} = 0.38 \pm 0.01$) (Figure 4.11).

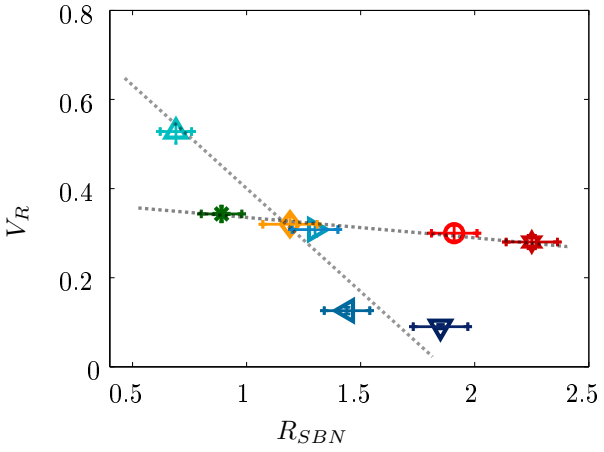

Figure 4.11: The recovery volume decreases with R_{SBN}. Yet the slopes ($m_{K_{SBN}\sim 2.5} = -0.409$ and $m_{K_{SBN}\sim 4.5} = -0.0431$) depend significantly on the K_{SBN} value.

V_P (equation 2.12 in part I chapter 2) provides an estimate of the amount of shear flow process. It permits the removal of the densified portions in the pile-up by imaging before and after annealing.

Name	P_{id} (μ m)	V_i^+ (μ m^3)	V_i^- (μ m^3)	V_i^+/V_i^- (%)	V_a^+ (μ m^3)	V_a^- (μ m^3)	P_{ad} (μ m)	V_R	V_P	Symbols
SBN 12	1.012	5	36.7	13.6	4	14.4	0.665	52.8	16.3	△
SBN 25	1.037	13	54.8	23.7	12	31.1	0.805	30.8	25.6	▷
SBN 30	1.19	17	62	27.4	16.3	47.2	0.912	12.6	28.6	◁
SBN 35	1.2	19.1	70.1	27.3	15.5	60.2	1.08	9	32.4	▽
SBN 14	0.88	7	35.2	19.8	10	26.1	0.822	34.3.0	11.3	✳
SBN 63	0.99	10.8	49.3	21.9	9	31.7	0.844	32	25.6	◇
SBN 59	1.03	12	55.3	21.7	15	41.7	0.846	30	16.3	○
SBN 55	1.1	12	56.8	21.1	15	43.9	0.857	28	15.8	✡
Errorbar	± 5 %	± 5 %	± 10 %	± 5 %	± 5 %	± 5 %	± 10 %	± 10 %	± 10 %	

Table 4.2: Experimental values P_{id}, V_i^+ (μ m^3), V_i^- (μm^3), V_i^+/V_i^- (%), V_a^-, V_a^+ and P_{ad} obtained from the AFM images of the indentation prints, V_R and V_P obtained from annealing investigations in the various SBN glasses. The symbols used for each glass composition are recalled.

Annealing relieves densified areas; this highlighting variations in isochoric shear flow. Figure 4.12 depicts how V_P varies with R_{SBN} for the different series of glasses. For $K_{SBN} \sim 2.5$, the ratio increases roughly linearly. Yet, for $K_{SBN} \sim 4.6$, the ratio decreases, but it appears not to be linear. Literature suggests

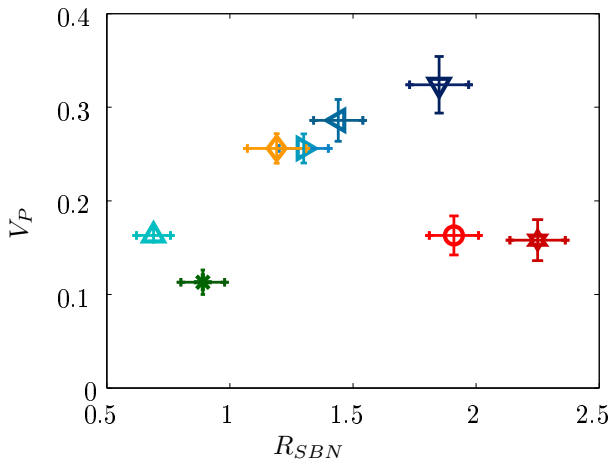

Figure 4.12: Pile up ratio (V_P) which characterizes the volume-conserving shear flow versus R_{SBN}. The tendencies are drastically different for approximately constant K_{SBN}.)

that the chemical compositions have more impact on V_R than on H_V [28, 29, 41, 42]. Figure 4.13 unveils two different scenarios when looking at approximately constant K_{SBN}. For samples with $K_{SBN} \sim 2.5$, the recovery volume decreases with ν ($V_R = m_{K_{SBN}\sim 2.5}\nu + b_{K_{SBN}\sim 2.5}$ where $m_{K_{SBN}\sim 2.5} = -8.40 \pm 0.60$ and $b_{K_{SBN}\sim 2.5} = 2.34 \pm 0.13$). As the sodium content increases for low $K_{SBN} \sim 2.5$, V_R decreases quickly. On the other hand, the $K_{SBN} \sim 4.6$ series exhibits a significantly less pronounced decrease ($V_R = m_{K_{SBN}\sim 4.5}\nu + b_{K_{SBN}\sim 4.5}$ where $m_{K_{SBN}\sim 4.5} = -1.02 \pm 0.30$ and $b_{K_{SBN}\sim 4.6} = 0.68 \pm 0.07$).

Nevertheless, Sellappan et al. attempted to develop an universal behavior for V_R with ν [30](equation 4.1). As ν increases V_R decreases, thus the contribution of densification occurring in the system decreases.

Figure 4.13 presents the data collected herein, their data, and the sigmoid fit they proposed (dash black line):

$$V_R = \frac{1}{\alpha_R + \beta_R exp(\chi_R \nu)} + \delta_R \tag{4.1}$$

(α_R, β_R, χ_R, δ_R) are fitting parameters. The data for the SBN glasses does fit the spread of data presented in Sellappan et al. [30]. Yet, we can observed left shift (toward smaller values of ν) as compared to the glasses of Sellappan et al. A better fit (solid brown line in the figure 4.13 for the SBN glasses would occur with (α_R, β_R, χ_R, δ_R) = (.99, .003, 29, -.007).

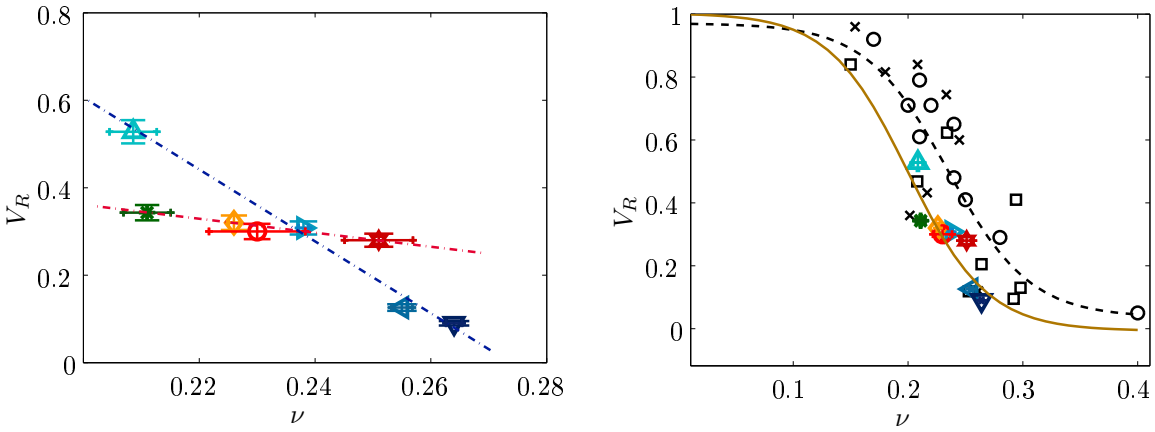

Figure 4.13: (Left) The figure depicts the evolution of the volume recovery ratio (V_R) as a function of the Poisson's ratio (ν) for the SBN data. The blue color line depicts a linear fit to the data for $K_{SBN} \sim 2.5$ ($V_R = m_{K_{SBN}\sim 2.5}\nu + b_{K_{SBN}\sim 2.5}$ where $m_{K_{SBN}\sim 2.5} = -8.40 \pm 0.60$ and $b_{K_{SBN}\sim 2.5} = 2.34 \pm 0.13$). The red color line depicts a linear fit to the data for $K_{SBN} \sim 4.5$ ($V_R = m_{K_{SBN}\sim 4.5}\nu + b_{K_{SBN}\sim 4.5}$ where $m_{K_{SBN}\sim 4.5} = -1.02 \pm 0.30$ and $b_{K_{SBN}\sim 4.6} = 0.68 \pm 0.07$). (Right) The figure depicts a comparison of V_R versus ν relationships found herein along with published data, black data points [21, 30, 41]. The black dashed line depicts the sigmoid fit proposed by Sellappan et al. The brown solid fit depicts the best sigmoid fit, (α_R, β_R,χ_R, δ_R) = (.99, .003, 29, -.007), for the SBN data assuming 2 sudo points: (0,1) and (.5, 0).

.

Understanding shear flow requires V_P. Figure 4.14 (left) unveils two different scenarios when looking at approximately constant K_{SBN}. For samples with $K_{SBN} \sim 2.5$, V_P increases with ν ($V_P = m_{K_{SBN}\sim 2.5}\nu +$ $b_{K_{SBN}\sim 2.5}$ where $m_{K_{SBN}\sim 2.5} = 0.30 \pm 0.022$ and $b_{K_{SBN}\sim 2.5} = -0.42 \pm 0.05$). On the other hand, the $K_{SBN} \sim 4.5$ series exhibits a drastic decrease in V_P with ν. Sellappan et al. [30] evidenced a sigmoid increasing trend between ν and V_P (equation 4.2). Thus, the amount of volume-conserving shear flow increases with ν. Figure 4.14 right presents the data collected herein, their data (black point), and their sigmoid fit (dash black line):

$$V_P = \frac{1}{\alpha_P + \beta_P \exp(\chi_P \nu)} \tag{4.2}$$

(α_P, β_P, χ_P) are fitting parameters. Our data for the SBN glasses does fit the spread of data presented in Sellappan et al. [30]. A better fit for the SBN glasses would occur with (α_P, β_P, χ_P) = (.94, 152, -16). SBN glasses do fit the general spread of data when considering previously published V_P verse ν data.

Conversely, the sigmoid fits miss the subtleties of the SBN glasses for constant K_{SBN}. Moreover, the V_P curve is drastically different for the two K_{SBN} series herein. $K_{SBN} \sim 2.5$ has a tendency to increase; and $K_{SBN} \sim 4.5$ has a tendency to decrease. A possible explanation as to why SBN 55 and SBN 59 decrease is annealing may not only relieve densified regions, but it may of also induced some plastic flow. To understand this more research is required.

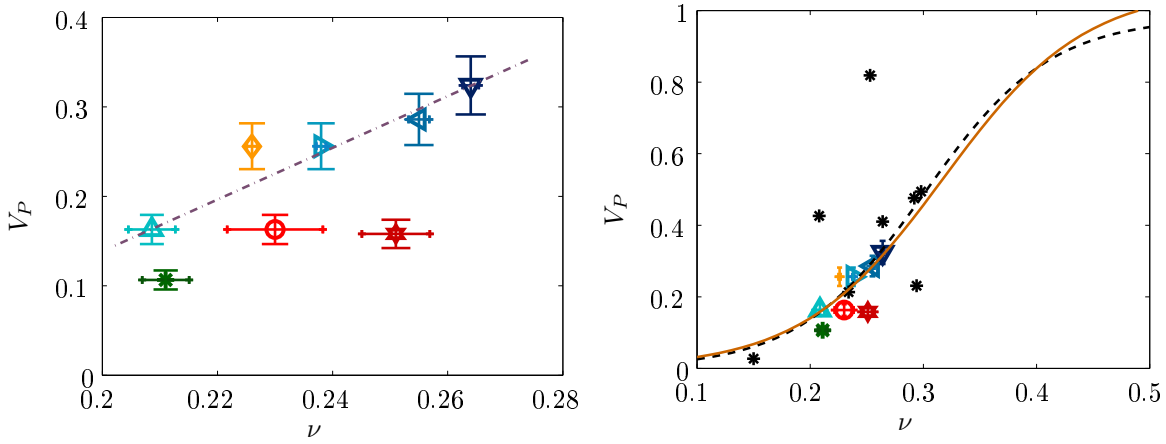

Figure 4.14: (Left) The figure depicts the evolution V_P versus ν for SBN data. The purple color line depicts a linear fit to the data for $K_{SBN} \sim 2.5$ ($V_P = m_{K_{SBN}\sim 2.5}\nu + b_{K_{SBN}\sim 2.5}$ where $m_{K_{SBN}\sim 2.5} = 0.30 \pm 0.022$ and $b_{K_{SBN}\sim 2.5} = -0.42 \pm 0.05$). For $K_{SBN} \sim 4.5$, the data does not fit a linear extrapolation. (Right) The figure compares the curve V_P vs ν resulting from our work with other published data [21, 30, 41]. The black dashed line depicts the sigmoid fit proposed by Sellappan et. al. The beige color fit depicts the best sigmoid fit, (α_R, β_R, χ_R) = (.94, 152, -16), for the SBN data herein assuming 2 sudo points: (0,0) and (.5, 1).

The V_R and V_P trends are coherent with results in literature [30]. The SBN 12 presents a singular behavior regarding the SBN series. No cracks are visible after Vickers' indentation at 50 g. Furthermore, increasing the load (200 g) did not facilitate the development of cracks popping up from the indentation corners (figure 4.7). Complementary investigation highlights the huge contribution of the densification process during the indentation (50 %). This changes the mechanism yielding crack formation: (1) change in the residual stresses resulting from these processes [1], (2) appearance other type of cracks under indentation which would limit the propagation of visible cracks. This section highlights the significant impact of the glass composition on the hardness and deformation mechanisms. The next section investigates the failure behavior of SBN glasses in stress corrosion regime.

4.2 Evolution of SCC curves with chemical composition

In vacuum, the stress intensity factor must exceed the fracture toughness value, K_C, to make the propagate. However, stress corrosion cracking ($K_I < K_C$; i.e. chemically assisted cracking) can lead to premature failure of a material. This is because water opens strained bonds at the crack front. This section investigates the impact of the chemical composition on stress corrosion cracking. This test re-

quires DCDC samples. Under compression, two cracks emerge and the displacement of the crack front is recorded. From the external stress applied to the samples, I am in a position to determine K_I via equation 2.5. Chapter 1 reviews two different models to fit the SCC curves: Wiederhorn proposed an exponential relationship (equation 1.15) whereas other authors suggested a power law (equation 1.16). The results herein take the both models into account. The b value refers to the slope of the curve $\log(v)$ vs K_I whereas n refers to the exponent provided a power law relationship $v \propto K^n$.

4.2.1 SBN curves

Figure 4.15 displays the crack front velocity (v) versus the stress intensity factor (K_I) for all the SBN glasses. As expected from literature [25, 38, 39] two distinct regions appear:

- Region 0: environmental limit (K_E) below which the crack front will not propagate.
- Region I: the *stress corrosion* zone where the chemical reactions at the crack tip control the propagation of the crack front.

Variations are observed as the glass's chemical composition changes. Two major modifications take place as the sodium content increases: (1) the SCC curves shift toward higher K_E values; and (2) the slope in region I increases. Table 4.3 presents b (from [36, 38, 40]); n (from [27]) and K_E for the SBN glasses. The vertical line of K_E for SBN 59 and SBN 63 was not acquired herein.

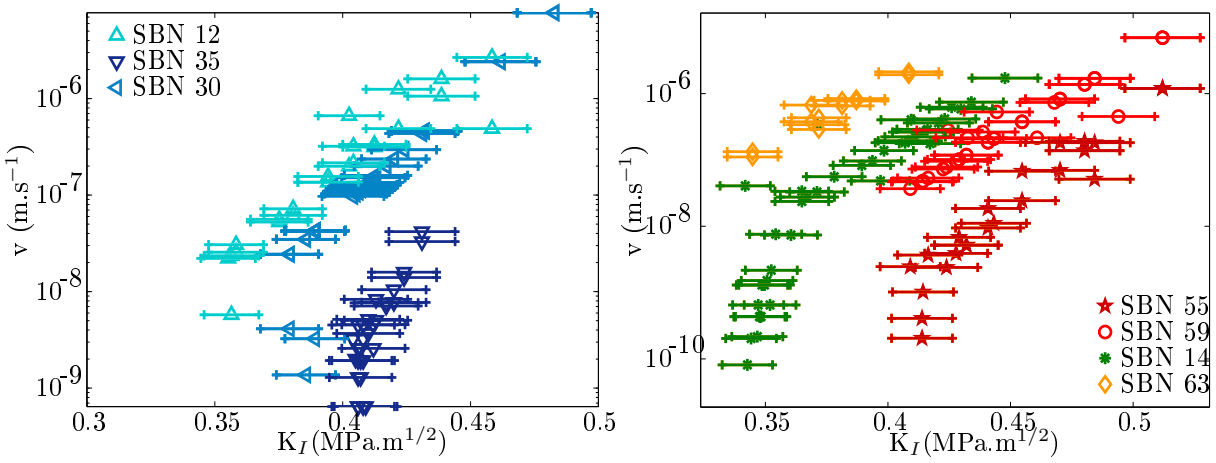

Figure 4.15: Evolution of stress-corrosion curves for SBN glasses. (Left) The SCC curves for SBN 12, SBN 30 and SBN 35, i.e. [Na_2O] increases for K_{SBN} (~ 2.5) remains constant. (Right) The SCC curves for SBN 14, SBN 63, SBN 59 and SBN 55, i.e. [Na_2O] increases yet K_{SBN} (~ 4.5) remains constant.

4.2.2 Shift in K_E

Figure 4.16 presents the evolution of K_E with [Na_2O]. Clearly the K_E values increase with [Na_2O]. This result means that the crack propagation commences at higher loads as [Na_2O] increases. Literature highlights the important role of the alkali content on K_E [8, 9, 12, 13, 38, 39]. An important phenomenon

Glass name	b	n	K_E	Symbols
SBN 12	$46_{\pm 3}$	$19_{\pm 1.3}$	$0.356_{\pm 0.017}$	△
SBN 30	$59_{\pm 3}$	$23.3_{\pm 0.4}$	$0.380_{\pm 0.019}$	◁
SBN 35	$113_{\pm 5}$	$33_{\pm 2}$	$0.407_{\pm 0.012}$	▽
SBN 14	$50_{\pm 3}$	$19.9_{\pm 0.7}$	$0.352_{\pm 0.015}$	✳
SBN 63	$52_{\pm 3}$	$20_{\pm 1.6}$	//	◇
SBN 59	$53_{\pm 2}$	$23.5_{\pm 1.2}$	//	○
SBN 55	$68_{\pm 3}$	$29.4_{\pm 1.2}$	$0.413_{\pm 0.012}$	✡

Table 4.3: Estimated values for b (from [36, 40], i.e. exponential), n (from [27], i.e. power law) and K_E for the SCC in figure 4.15 for SBN glasses. The vertical line of K_E for SBN 59 and SBN 63 was not acquired herein. The last column recalls the symbols used in the plots.

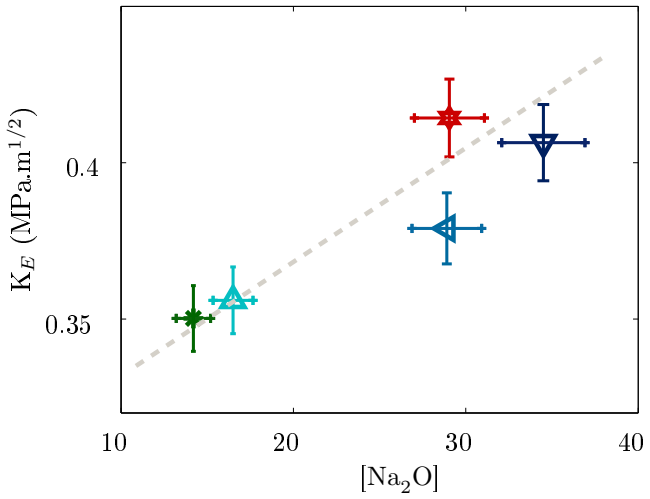

Figure 4.16: Correlation between K_E and the sodium content $[Na_2O]$.

occurring is ion exchange [3, 5]. During SCC experiments, the stress applied to the crack front enhances the mobility of Na^+ permitting an easy exchange between the glass and the environment (See part I chapter 1 in section 1.3.2). To date it is inconclusive as to whether H^+, H_2O, or H_3O^+, enters the glass network. Yet, Fett [8, 9] and Guin [12, 13] suggest that hydronium H_3O^+ enters the glass network. In this case, the fracture process zone develops a compressive stress leading to a shielding effect. Impact of this shielding effect on the crack tip causes a decrease in the applied stress at the crack tip. Figure 4.17 presents a schematic representation of this mechanism [25]. The light gray block represents the material which obeys linear elasticity. The dark gray zone deviates from this and dissipative phenomena occur. The stress felt at the crack tip K_f is [25]:

$$K_f = K_{appl} + K_* \tag{4.3}$$

where K_{appl} is the external stress applied and K_* denotes the shielding contribution to the material toughness. A shielding contribution requires $K_* < 0$. In this case, as the shielding zone develops due to

the globally applied stresses, the stresses at the crack tip decreases. Other phenomena are feasible. For example, the width of the hydrated layer varies from low to high sodium glasses. Indeed, the hydrated layer thickness can increase with the sodium content as observed in pure corrosion experiments. In this case, the thickness changes the shielding contribution which decreases K_f. Finally, the sodium content may impact an indirect effect of global stresses in glass structure.

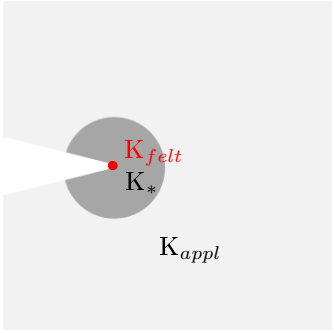

Figure 4.17: Schematic representation of shielding effect and its impact on the K$_f$, stress felt at the crack tip. K$_{appl}$ is the external stress applied and K$_*$ is the contribution of the dissipative zone.

The chapter 3 of this thesis highlights the role of sodium content on the ternary glass structure. For the two series herein, the number of NBO increases and the coordination number of boron decreases from 4 to 3. These changes alter the way the glass can accommodates the stress. Kieu et al. [23] studied the impact of the structure on the failure properties of SBN glasses by means of Molecular Dynamics simulations. He drew attention to the fact that $^{[3]}$B induces more plasticity than $^{[4]}$B. This is because the $^{[3]}$B structures have more degrees of freedom. It is also likely, but to date unstudied, that NBO atoms yield additional degrees of freedom to the glass network in SBN glasses. He also observed an increase of glass plasticity due to Na-NBO and $^{[3]}$B bonds because they deform plastically [22]. These changes in the glass topology induced by sodium content probably increase the dissipative phenomena in the FPZ.

4.2.3 Changes in slopes in stress corrosion regime

From low sodium glasses (SBN 12 and SBN 14) to high sodium glasses (SBN 35 and SBN 55), the slope changes significantly. The slope in region I equates $\frac{d\log v}{dK}$. Thus, an increasing slope implies a significant increase of the velocity: a step of 0.02 MPa.m$^{1/2}$ in K_I, increase the velocity by 150 % for the SBN 12 and 240 % for the SBN 35. There is no common understanding on mechanisms occurring at the crack tip.

- **The Wiederhorn's model** From the reaction rate theory, Wiederhorn links the slope in region I to an activation volume ΔV^* [40]. Other authors [10] suggest that change in elastic properties of the network bond also influence the slope in SCC zone. Yet, all models limit their interpretation of b (or n) to the reaction of water with $\equiv \mathrm{Si-O-Si} \equiv$. In the case of SBN glasses, the interaction of Si-O-Si with water is probably not the predominant reaction. MD simulation performed by J-.M. Delaye on SBN glasses (with chemical compositions similar to the ones used herein) evidence possible paths along which the crack front can propagate so that it never breaks a $\equiv \mathrm{Si-O-Si} \equiv$ bond. Due to the slowly evolving dynamics

of the SCC regime, the crack growth is slow enough to pass through the weakest points. From [36, 40], b is proportional to the activation volume, ΔV^* and inversely proportional to $\sqrt{\rho_{ct}}$ (ρ_{ct} is the crack tips curvature radius).

Inverse proportionality of $\sqrt{\rho_{ct}}$ with b implies that as the slope increases the crack tip's radius should get smaller. Yet, as the sodium content increases the crack tip is expected to blunt more [12] or show no variation [15]. Thus, these two ideas are incompatible at the light of our data.

Turning to ΔV^*, ΔV^* represents a variation in volume between the activated complex (with water molecule) and the unreacted state. Table 3.3 depicts the elastic properties for the SBN glasses herein. In general, the Young modulus varies from 72 to 82 GPa and the Poisson's ratio from 0.21 to 0.26. The change is to slight to expect such a huge increase in b and n. From MD simulation, it is possible to extract the bonds inside the different SBN compositions: Si-O-Si, Si-O-B, B-O-B bonds and OSi_3, OSi_2B, OSi_1B_2, and OB_3 units. Figure 4.18 presents the relation between these terms and b and n. These plots reveal no clear relationship. The slope in stress corrosion is not governed by one bond in the glassy network. This correlation exemplifies the fact that considering the Si-O-Si bonds only cannot

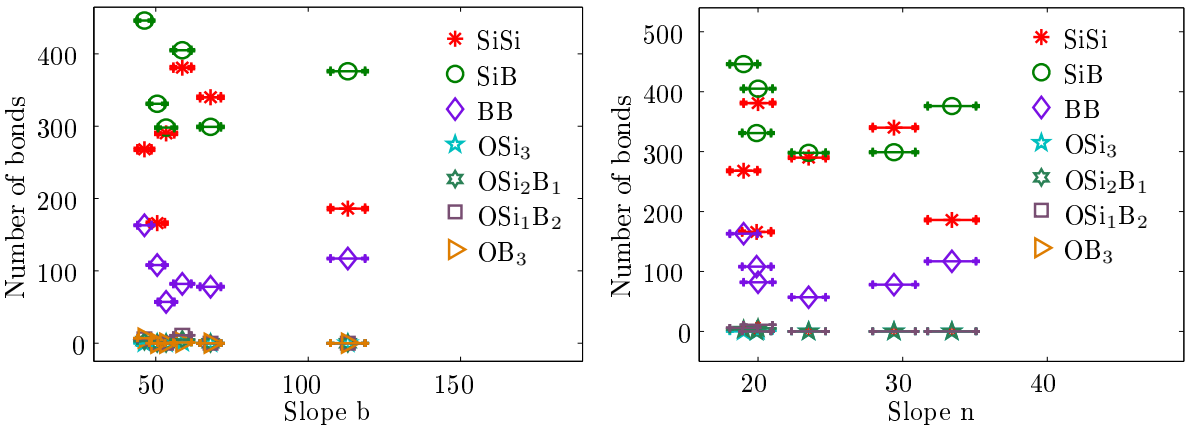

Figure 4.18: Correlation between Si-O-Si, Si-O-B, B-O-B with two coordinated O and OSi_3, OSi_2B, OSi_1B_2, and OB_3 units with three coordinated O calculated by MD simulations and (left) the slope b from the Wiederhorn's model and (right) the slope n from Maugis equation.

prodive a full picture of the fracture behavior. The chemical reaction may change drastically from one glass to another. The experimental set-up does not give us access to these mechanisms at the crack tip. West and Hench pointed out the role of the ring sizes in pure silica glasses on the SCC properties [34,35]. Due to changes in ring structure and changes in polymerization degree with sodium content, the reaction rate changes with stresses. Today, ReaxFF could provide the keys to understanding the chemical reactions at the crack tip. They are big enough to take into consideration the glass structure, but also can simulate chemical reactions at and near the crack tip.

The slope variation has been discussed with respect to the Wiederhorn's model and the reaction rate theory. Tomozawa proposed another explanation for the subcritical crack growth.

- **The Tomozawa's model** Tomozawa concluded that diffusion of water into the crack tip aids subcritical crack propagation. Moreover this decreases the toughness and permits crack propagation [31,32]. Figure 4.19 depicts b (from [36,40]) and n (from [27]) with [Na_2O] content. From one composition to the other,

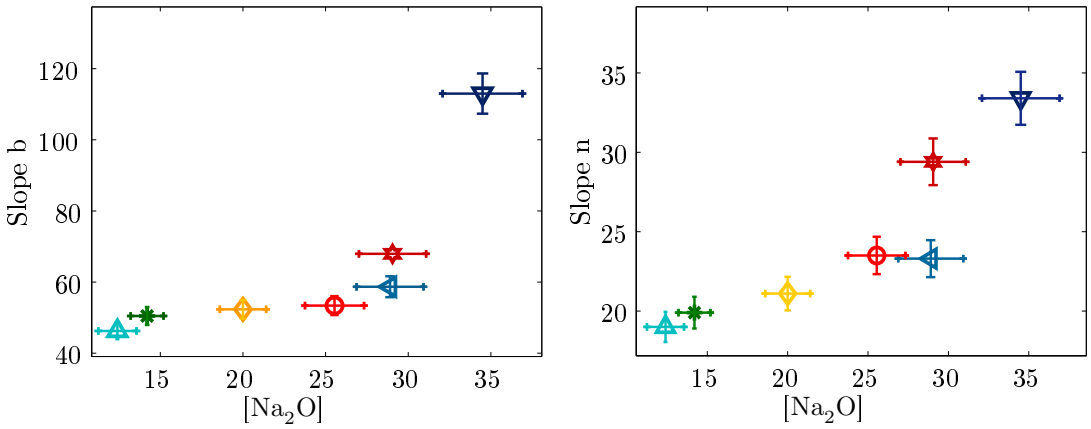

Figure 4.19: Correlation between the slope: (left) b from the Wiederhorn model [40] where b is linked to ΔV^*; and (right) n is the slope from the power law relationship [27] and the sodium content.

the water penetration may favor non-bridging oxygen atoms. Hence, changing the chemical composition favors water penetration and hence increases the slope. Célarié [4,6] specifically observed the migration of sodium ions towards the free surface. If this mechanism occurs, preferential paths may be created for the penetration of water from Tomozawa's theory. Finally, Tomozawa found a better resistance of glass which he attributes to an enhanced plastic flow at the crack tip [19,24]. It is true that plastic flow at the crack tip will shift K_E to higher K_I values, but if it was to aid in deterring the velocity of the crack front the slope should be lower. This is not compatible with our data, since the glasses with the higher slopes are found to be the ones with the higher plastic flow as determined by indentation studies.

The interpretation of the slope in the region I cannot be captured by the Wiederhorn's model. Tomozawa's theory may explain the huge variation in slope due to the sodium content. On the other hand, if the slope was impacted by plastic flow processes, the slope should decrease rather it increases. The penetration of water molecules sets up a preferential path along sodium rich regions (and their corresponding NBO). Moreover, the increase in [Na_2O] increases the glasses reactivity with water. This in turn forms a weaker glass and due to the depolymerization of the glass the slope increases (Figure 4.20).

4.3 Evolution of fracture surfaces with chemical composition

Post-mortem fracture surfaces reveal how a crack front propagates through the bulk of the glasses. Thus, they unveil the fracture processes at the microscale and mesoscale. Once the crack propagates throughout the sample, two stress-corrosion fracture surfaces exist. Figures 4.21 top ($K_{SBN} \sim 2.5$) and bottom (left $K_{SBN} \sim 4.5$; others $K_{SBN} \sim 4.5$) depict AFM images of these fracture surfaces when the velocity of the crack front was approximately 10^{-7}-10^{-8} m.s^{-1}.

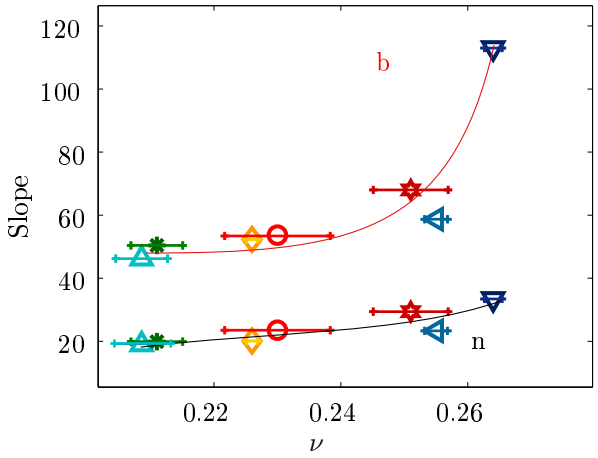

Figure 4.20: Correlation between the slope: (left) b from the Wiederhorn model [40] where b is linked to ΔV^*; and (right) n is the slope from the power law relationship [27] with the Poisson's ratio.

In general, the roughness and other features of a fracture surface depend on the velocity of the crack front. Slower velocities give rougher surfaces [37]. Hence, all the measurements presented in figure 4.21 are done in the same velocity range. Figure 4.22 presents the evolution of the RMS values for SBN glasses. RMS variations depend significantly on the K_{SBN} series. For $K_{SBN} \sim 2.5$, a noteworthy decrease in the roughness occurs between SBN 12 and SBN 25. In the same series ($K_{SBN} \sim 2.5$), a significant increase of the RMS values occur between SBN 25 and SBN 35. On the other hand, the $K_{SBN} \sim 4.6$ series present a linear increase in the RMS value with a lower amplitude. The principle of local symmetry governs the growth direction [11]. This leads to a local value of K_{II}=0 (stress intensity factor in mode II). This means than an initially homogeneous material loaded in mode I would grow along a straight plane. But inhomogeneities yield distortions in the crack front. Thus, the roughness and its variations can be attributed to microscopic stresses associated with structural variations within the glass's microstructure.

The Yun, Dell and Bray model assumes that SBN 12 glass consists of two networks with areas enriched in silica and in boron. This leads to heterogeneities which explain the high RMS value of SBN 12. As the sodium content increases, the two networks mix together, leading to a more homogeneous glass. A further increase of [Na_2O] leads to a depolymerization favoring inhomogeneities. This explains the variations observed in the red series too (i.e. the small increase in the RMS from SBN 14 to SBN 55). The discrepancy between the blue and the red series highlights the degree of homogeneities.

4.4 Discussion on the mechanical properties of SBN series

The mechanical properties strongly depend on the glass structure. The hardness values appear to be linked to the reticulation of the glassy network: lower network reticulation (i.e. higher is the NBO) decreases the hardness. But glasses with similar H_V values present different behaviors regarding the cracks appearance, the fracture toughness K_C, etc. Poisson's ratio (ν) appears to be the key parameter in understanding how the matter flows under an indenter. Densification and shear flow contributions

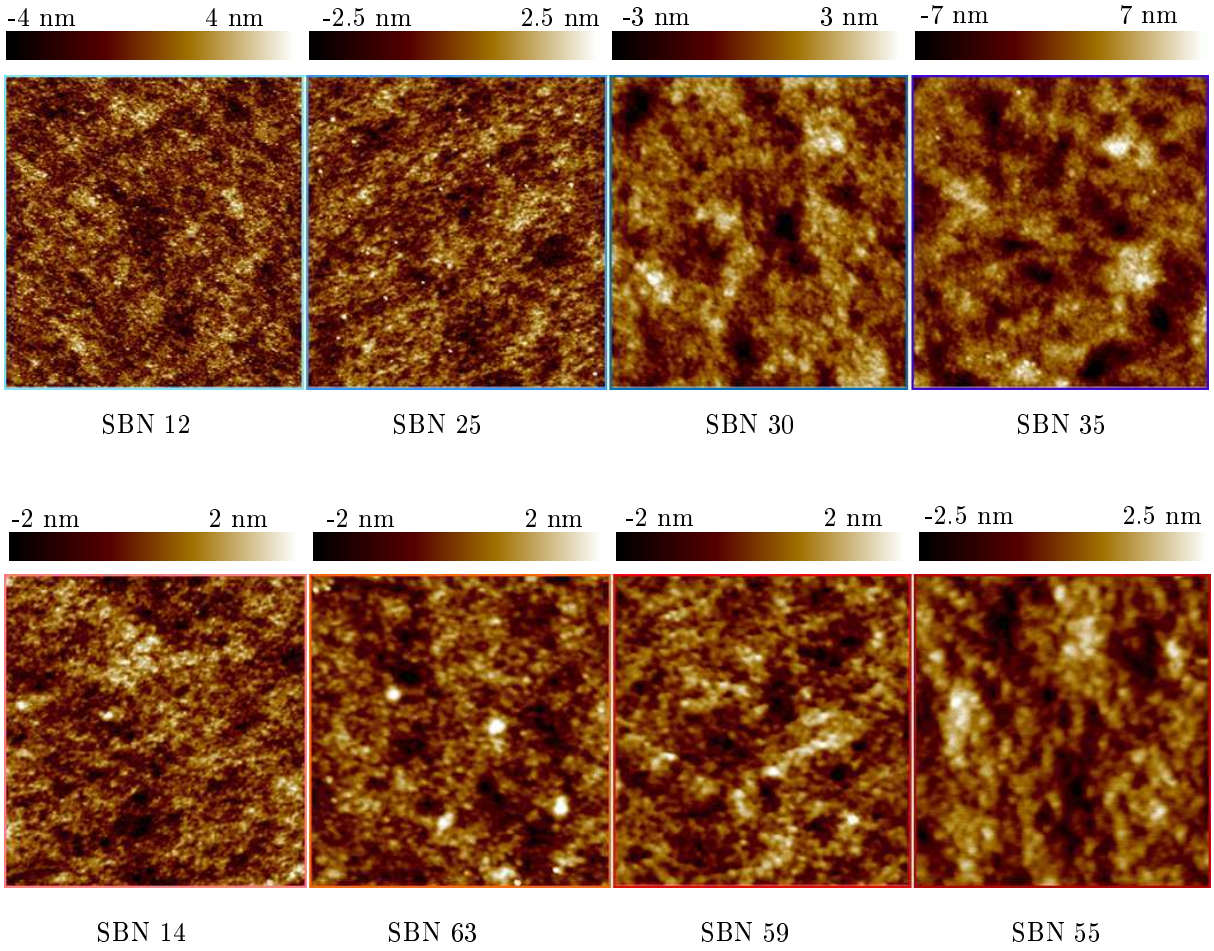

Figure 4.21: AFM images of fracture surface of SBN glasses (top) (K_{SBN} ~2.5) SBN 12 (light blue) to SBN 35 (dark blue) 5 μm × 5 μm in Tappingmode in 10^{-7}-10^{-8} m.s^{-1} regime; (bottom) K_{SBN} ~3.7 SBN 14 (light red; left) and K_{SBN} ~ 4.5 SBN 63 to SBN 55 (dark red) 5 μm × 5 μm in Tappingmode in 10^{-7}-10^{-8} m.s^{-1} regime.

depend on ν. Decreasing ν favors densification process, whereas as increasing ν favors shear flow processes. Consequences of these two processes are not equivalent regarding the cracking behavior. High ν favor the propagation of well-developed median/radial cracks. The residual stress field contribution change depending on ν: the stress field enhances the propagation of median-radial cracks at high ν. As a consequence, K_C does not truly express a toughness but rather how the glass flows under indenters. This leads to a good correlation between the K_C and ν and the lack of well-developed crack for low ν glasses. The stress corrosion investigation highlights two major changes: a shift in K_E towards higher K_I and an increase of the slope in region I as the sodium content increases. The shift in K_E signifies an increased plasticity (irreversible phenomena) of SBN glasses which occurs during the load. As the sodium content increases the glass accommodates higher external stresses. This plasticity can be explained by the structural variations (creation of NBO, sodium pockets, conversion of $^{[3]}$B at the expense of $^{[4]}$B, etc.) and/or the diffusion of sodium. Interpreting variations in the slope is tricky due to a lack of a general understanding on the mechanisms at the crack tip. Increasing the amount of [Na_2O] impacts the SCC

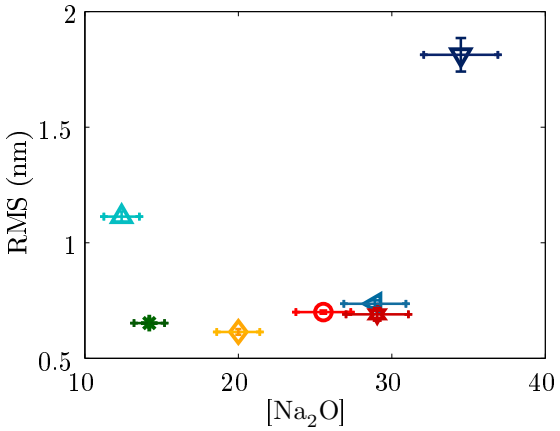

Figure 4.22: RMS values extracted from the fracture surfaces of the SBN series.

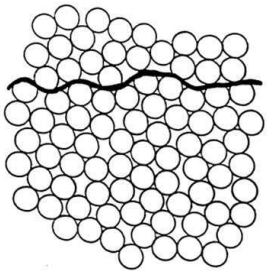

Figure 4.23: Schematic of a crack (and its subsequent surface) passing through weak regions in an inhomogeneous glass structure. The fracture surface is indicated by the black solid curve [14].

response of the glass. [Na_2O] increases the glasses reactivity with water creating a weaker glass and due to the depolymerization of the glass the slope increases. Topographical changes in the fracture surfaces underline significant change in the crack path. The RMS is correlated to the amount of disorder along with the number of weakest points.

Chapter 2 highlights the change in the glass topology with [Na_2O]. After an initial increase in the $^{[4]}$B count due to [Na_2O], [Na_2O] leads to an increase in the number of $^{[3]}$B and NBO at the expense of the $^{[4]}$B count. This decreases the degree of polymerization of the glassy network. This change increases the glass's plasticity. This impacts both the behavior during indentation and the failure mechanisms. Under the indenter NBO favor plastic flow processes. This leads to a decrease in the K_C values determined from indentation. Plastic flow processes also favor shifts in K_E to higher values due to a shielding effect. Yet, the decrease in the degree of polymerization and the increase in [Na_2O] forms a weaker and more reactive glass with water.

4.5 Conclusion

This chapter clearly displays a dependence of the mechanical properties on the chemical composition.

- **The Poisson' ratio (ν) is a key parameter in understanding the mechanical response of the glass.** It gives information on mechanisms occurring during indentation and is highly correlated to K_C. Thus, the toughness determined by indentation is not a true estimate of the glass's resistance to fracture. Rather, it reflects how matter flows under the Vickers' indenter giving way to crack propagation.
- **Both indentation and SCC tests evidence a clear increase in the glass's plasticity with sodium content.** Hardness investigations point out an increase of pile-up process with [Na_2O]. The SCC studies feature a shift in K_E with the sodium content. Thus the glass is better able to adjust under external stresses. The plasticity decreases K_C as determined by Vickers indentation whereas it increases the load at which the cracks propagates in stress corrosion regime.

This chapter presents the evolution of the mechanical properties of SBN glasses. This study highlights the important role of the Poisson's ratio in the mechanisms of deformation under pressure. Glasses with high sodium content present a lower hardness and a low K_C from indentation measurements. The stress corrosion behaviors depend on the chemical composition. Clearly plasticity increases the K_E values. Current models in literature cannot simply explain the increase in slope with [Na_2O]. *Rather, ν (which gives a measure of the degree of depolymerization due to Na^+ ions and the strength of the glass network) is correlated with the slope. Thus, [Na_2O] weakens the glass and makes it more reactive with water.*

Bibliography

[1] A. Arora, D.B. Marshall, and B.R. Lawn. Indentation deformation/fracture of normal and anomalous glasses. *J. Non-Cryst. Solids*, 31:415–428, 1979.

[2] P. W. Bridgman and I. Simon. Effect of very high pressure on glass. *J. Appl. Phys.*, 24:405, 1953.

[3] B.C. Bunker. Molecular mechanisms ofr corrosion of silica and silicate glasse. *J. Non-Cryst. Solids*, 179:300–308, 1994.

[4] F. Célarié. *Dynamique de fissuration à basse vitesse des matériaux vitreux.* PhD thesis, Université Montpellier II, 2004.

[5] F. Célarié, S. Pradès, D. Bonamy, A. Dickele, E. Bouchaud, C. Guillot, and C. Marliere. Surface fracture of glassy materials as detected by real-time atomic force microscopy (afm) experiments. *Appl. Surf. Sci.*, 212:92–96, 2003.

[6] F. Célarié, S. Prades, D. Bonamy, L. Ferrero, E. Bouchaud, C. Guillot, and C. Marliere. Glass breaks like metal, but at the nanometer scale. *Phys. Rev. Lett.*, 90(7):075504, FEB 21 2003.

[7] F.M. Ernsberg. Role of densification in deformation of glasses under point loading. *J. Am. Ceram. Soc*, 51:545–547, 1968.

[8] T. Fett, J.P. Guin, and S.M. Wiederhorn. Interpretation of effects at the static fatigue limite of soda-lime-silicate glass. *Eng. Fract. Mech.*, 72:2774–2791, 2005.

[9] T. Fett, J.P. Guin, and S.M. Wiederhorn. Stresses in ion-exchange layers of soda-lime-silicate glass. *Fatigue Fract. Eng. Mater. Struct.*, 28:507–514, 2005.

[10] S.W. Freiman, T.L. Baker, and J.B. Wachtman Jr. A computerized fracture mechanics database for oxide glasse. *Bull. Am. Ceram.Soc.*, 64:1452–1455, 1985.

[11] R.V. Goldstein and R.L. Salganik. Brittle fracture of solids with arbritary cracks. *Int. J. Fracture*, 10:507–523, 1974.

[12] J.P. Guin and S.M. Wiederhorn. Crack growth threshold in soda lime silicate glass: role of hold-time. *J. Non-Cryst. Solids*, 316:12–20, 2003.

[13] J.P. Guin, S.M. Wiederhorn, and T. Fett. Crack-tip structure in soda-lime-silicate glass. *J. Am. Ceram. Soc.*, 88:652–659, 2005.

[14] P.K. Gupta, D. Inniss, C.R. Kurkjian, and Q. Zhong. Nanoscale roughness of oxide glass surfaces. *J. Non-Cryst. Solids*, 262:200–206, 2000.

[15] R. Gy. *Stress corrosion of glass.* Kluwer Academic Publichers, 2005.

[16] J.T. Hagan. Micromechanisc of crack nucleation during indentations. *J. Mater Sci.*, 14:2975–2980, 1979.

[17] J.T. Hagan. Shear deformation under pyramidal indentations in soda-lime glass. *J. Mater. Sci.*, 15:1417–1424, 1980.

[18] R. L. Henderson and N. W. Ashcroft. Perturbation theory of structure in mixtures near phase separation. *Phys. Rev. A*, 13:859–871, 1976.

[19] S. Ito and M. Tomozawa. Stress corrosion of silica glass. *J. Am. Ceram. Soc.*, 64:160, 1981.

[20] H. Ji, E. Robin, and T. Rouxel. Compressive creep and indentation behavior of plasticine between 103 and 353 k. *Mech. Mater.*, 41:199–209, 2009.

[21] Y. Kato, H. Yamazaki, Y. Kubo, S Yoshida, and d Akagi R. Matsuoka, J. a. Effect of B_2O_3 content on crack initiation under vickers indentation tests. *J. Ceram. Soc. Jpn.*, 9:792–798, 2010.

[22] L.-H. Kieu. *Compréhension de l'origine de l'évolution sous irradiation de la ténacite des verres nucléaires.* PhD thesis, Ecole Doctorale Polytechnique, 2011.

[23] L.-H. Kieu, J. . M. Delaye, and C. Stolz. Modeling the effect of composition and thermal quenching on the fracture behavior of borosilicate glass. *J. Non-Cryst. Solids*, 358:3268–3279, 2012.

[24] A. Koike and M. Tomozawa. Fictive temperature dependance of subcritical crack growth rate of normal and anomalous glass. *J. Non-Cryst. Solids*, 352:5522–5530, 2006.

[25] Brian Lawn. *Fracture of Brittle Solids.* Cambridge University Press, 2nd edition, 1993.

[26] J.D. Mackenzie. High-pressure effects on oxide glasses. 1. densification in rigid state. *J. Am. Ceram. Soc.*, 46:461–470, 1963.

[27] D. Maugis. Review : Subcritical crack growth, surface energy, fracture toughness, stick-slip and embrittlement. *J. Mater Sci.*, 20:3041–3073, 1985.

[28] T. Rouxel, H. Ji, V. Keryvin, T. Hammouda, and S. Yoshida. Poisson's ratio and the glass network topology - relevance to high pressure densification and indentation behavior. *Advanced Materials Research*, 39-40:137–146, 2008.

[29] P. Sellappan. *Indentation cracking of glass: role of the composition and reinforcement by diamond particles.* PhD thesis, Université de Rennes 1, 2011.

[30] P. Sellappan, T. Rouxel, F. Celarie, E. Becker, P. Houizot, and R. Conradt. Composition dependence of indentation deformation and indentation cracking in glass. *Acta Mater.*, 61:5949–5965, 2013.

[31] Han W.T. Tomozawa, M. and W.A. Lanford. Water entry into silica glass during slow crack-growth. *J. Am. Ceram. Soc.*, 74:2573–2576, 1991.

[32] M. Tomozawa. Fracture of glasses. *Ann. Rev. Mater. Sci.*, 26:43–74, 1996.

[33] D.R. Uhlmann. Densification of alkali silicate glasses at high pressure. *J. Non-Cryst. Solids*, 13:89–99, 1973.

[34] J.K. West and L.L. Hench. Silica fracture: Part ii a ring opening model via hydrolysis. *J. Mater. Sci.*, 29:5808–5816, 1994.

[35] J.K. West and L.L. Hench. The effect of environment on silica fracture: vaccum, carbon monoxide, water and nitrogen. *Philos. Mag. A*, 77:85–113, 1998.

[36] S. M. Wiederhorn, E.R. Fuller, and R. Thomson. Micromechanisms of crack growth in ceramics and glasses in corrosive environments. *Met. Sci.*, 14:450–458, 1980.

[37] S. M. Wiederhorn, J.M. Lopez-Cepero, J. Wallace, J. P. Guin, and T. Fett. Roughness of glass surfaces formed by sub-critical crack growth. *J. Non-Cryst. Solids*, 71:1582–1591, 2007.

[38] S.M. Wiederhorn. Influence of water vapor on crack propagation in soda-lime glass. *Am. Ceram. Soc. Bull.*, 50:407–414, 1967.

[39] S.M. Wiederhorn and L.H. Bolz. Stress corrosion and static fatigue of glass. *J. Am. Ceram. Soc*, 53:543–548, 1970.

[40] S.M. Wiederhorn, S.W. Freiman, E.R. Fuller, and C.J. Simmons. Effects of water and other dielectrics on crack-growth. *J. Matter. Sci.*, 12:3460–3478, 1982.

[41] S. Yoshida, J.-C. Sangleboeuf, and T. Rouxel. Quantitative evaluation of indentation-induced densification in glass. *J. Mat. Res.*, 20:3404–3412, 2005.

[42] S. Yoshida, J.-C. Sangleboeuf, and T Rouxel. Indentation-induced densification of soda-lime silicate glass. *Int. J. Mater. Res.*, 98:360–364, 2007.

Conclusion Part I

Part I investigates the evolution of the physical, structural and mechanical properties of SiO_2-B_2O_3-Na_2O (SBN) glass system. I chose to investigate model glasses by modulating the chemical composition to highlight the role of each oxide on their properties.

Glass sample elaboration occurred at CEA Marcoule. The concentration of [SiO_2], [B_2O_3] and [Na_2O] varied from one set of glasses to another. Many researchers group SBN samples based on their $R_{SBN} = \frac{[Na_2O]}{[B_2O_3]}$ and $K_{SBN} = \frac{[SiO_2]}{[B_2O_3]}$ ratios. Hence, two K_{SBN} series (i.e. K_{SBN} held constant) were chosen herein. After elaboration, studies analyzed the physical and structural properties of the glasses. Tables 3.2 and 3.3 revealed density and the elastic moduli of the samples. Raman analysis and NMR measurements describe and quantify the structural variations, respectively. Then, mechanical property tests employ hardness tests and fracture experiments on the SBN glasses. Indentation tests estimate H_V, K_C plus matter flow via sample annealing. Stress corrosion experiments make use of DCDC samples under compressive loads. Crack propagation occurs for subcritical stresses, $K_I < K_C$.

By maintaining $K_{SBN} \sim$ constant, an inceasing [Na_2O] changes the topological network of the glasses. For $R_{SBN} < 0.5$, sodium attacks the borate network causing the conversion of $^{[3]}$B into $^{[4]}$B . The sodium acts as a charge compensator. Furthermore, during this phase, many authors report a demixing of the silicate and borate network. Subsequently, between $0.5 < R_{SBN} < R_{SBN}^{max}$, sodium continues to attach to the borate network; however Reedmergnerite groups form assisting the connectivity of the two networks. Raman spectra of SBN 12 revealed signs of phase separation; this glass boarders these two zones. Increasing R_{SBN} (i.e.$R_{SBN}^{max} < R_{SBN} < R_{d1}$), the sodium begins to attach to the silica network forming NBO on the silicate network. For $R_{d1} < R_{SBN} < R_{d3}$, Na_2O modifies both the silicate and the borate network by adding NBO to the network. During this phase, $^{[3]}$B form at the expense of $^{[4]}$B . As a consequence, glass's degree of polymerization decreases. A quantity easily assessable and related to the degree of polymerization is the Poisson's ratio, ν. Generally literature attributes an increasing degree of polymerization with a decrease in ν, results herein corroborate this result.

Understanding how the chemical composition impacts the glass' toughness aids in insuring structural integrity of glasses. Hardness tests provide an estimation of H_V, K_C plus the proportion of densifica-

tion/shear flow after indentation. H_V values depend on the glass network reticulation: increasing the NBO concentration decreases H_V. The SBN glasses also exhibit different behavior regarding to their indentation patterns and their cracking behaviors. ν appears to be the key parameter in understanding how matter flows under an indenter. Glasses with low values of ν favor densification. Increasing ν decreases the densification processes and increases shear flow processes. Variations in both processes alter cracking behavior. Higher ν values favors the propagation of the lateral-radial crack. Thus, a good correlation exists between the K_C determined by indentation and ν. Rather than a real glass toughness, K_C values for the SBN glasses studied herein express how matter flows under Vickers' indenter.

Understanding how the chemical composition impacts the glass' SCC behavior will aid in preventing premature failure of systems. For $K_{SBN} \sim$ constant, increasing [Na_2O] shifts K_E towards higher K_I values. This shift corresponds to an increase in the glass' plasticity. Topological changes (increase in $^{[3]}B$, sodium pockets, etc) in the glass' structure enable it to accommodate higher stress loads. These changes in effect allow for a greater shielding of the crack tip from externally applied stresses. Finally, the slope drastically increases with [Na_2O]. Results herein discount mechanisms currently proposed in literature. Herein, three parameters display trends with the slope (n or b): ν; the number of NBO; and [Na_2O]. Yet, these parameters are intrinsically linked. The mechanisms at the crack tip lead to variations in the crack path as displayed by the variations in the RMS.

Future works concerns the understanding on the mechanisms occurring at the crack tip. Due to the complexity of the systems, how the chemical composition impacts the slope in region I remains unclear. Simulations using ReaxFF could help in a better understanding of these processes.

Part II

Impact of irradiation on structural and mechanical properties of pure silica and simplified borosilicate glasses

Chapter 1

Introduction: A review of structural and mechanical properties due to irradiation in nuclear glasses

Contents

This part concerns the storage of nuclear waste. Frequently, complex alumino boro silicate glasses (frequently R7T7 in France) embed fission product (FP) and minor actinides (MA) from spent fuel. Ensuring the durability of these glasses over the long-term (up to a few hundreds of thousands of years) still presents a major challenge. Moreover future high level wastes (HLW) will contain more fission product (FP) and minor actinides (MA). As a consequence, radioactivity and time of storage will increase. To safety confine them, it's crucial to know how irradiation impacts the structural and the mechanical properties of glasses.
This chapter presents the motivation behind studying the impact of irradiation on the mechanical properties of borosilicate glasses. In order to understand the issues, the first section briefly details the origin of HLW and its management. Section 1.1 details the origin and types of self-irradiations the HLW glasses undergo. These self-irradiations (along with external irradiation) lead to structural modifications. Section 1.4 presents these modifications in pure silica, sodium borosilicate glasses and complex borosilicate glasses. These structural modifications subsequently invoke modifications in the physical and mechanical properties of the glasses (detailed in section 1.5).

1.1 Nuclear waste management

1.1.1 Origin of nuclear waste and classification

Radioactive waste comes from various sources. As a consequence, scientists deal with radioactive materials of different concentrations and different physical and chemical forms. The predominant source of radioactive wastes comes from the nuclear industry: operation or decommissioning of nuclear installations, research reactors, spent fuel, etc. The first step in the nuclear fuel cycle is the production of the nuclear fuel. The uranium or thorium ores are mined. Tailings resulting from the mining of uranium ores generally contain elevated levels of radionuclides (such as radon) and required to be managed as radioactive waste for safety reasons. Mills process richer ores containing uranium to extract uranium from other elements. This involves crushing and chemical processing. At each step managing byproducts which contain decay products is essential. Moreover, tailings from processing contain significant amounts of heavy metals which also need to be safety confined. Once the nuclear fuel pellets are formed they enter into a nuclear reactor. After usage in the reactor core, the fuel is considered as *spent fuel*. They contain fissile material (^{235}U), fertile material (^{238}U) and other radioactive elements such as fission product (FP) and minor actinides (MA). France chose to chemically reprocess uranium and plutonium from spent fuel. The PUREX (Plutonium and Uranium Recovery by EXtraction) process is a liquid-liquid extraction method used to extract uranium and plutonium from the fission product. Reprocessed plutonium and uranium reenter the fuel cycle as MOX (Mixed OXide) fuel. Organic solvents require treatment and safety management. The life cycle of nuclear fuel produces varying forms of nuclear wastes. These wastes are chemically and physically different and have varying levels of activity. To facilitate the confinement and subsequent disposal, nuclear wastes are classified. The classification parameters include the levels of activity and the half-lives of the radionuclides contained in the waste. Figure 1.1 presents a conceptual illustration of the waste classification. The vertical axis presents the waste's activity content and the horizontal axis the half-lives of the radionuclides contained in the waste.

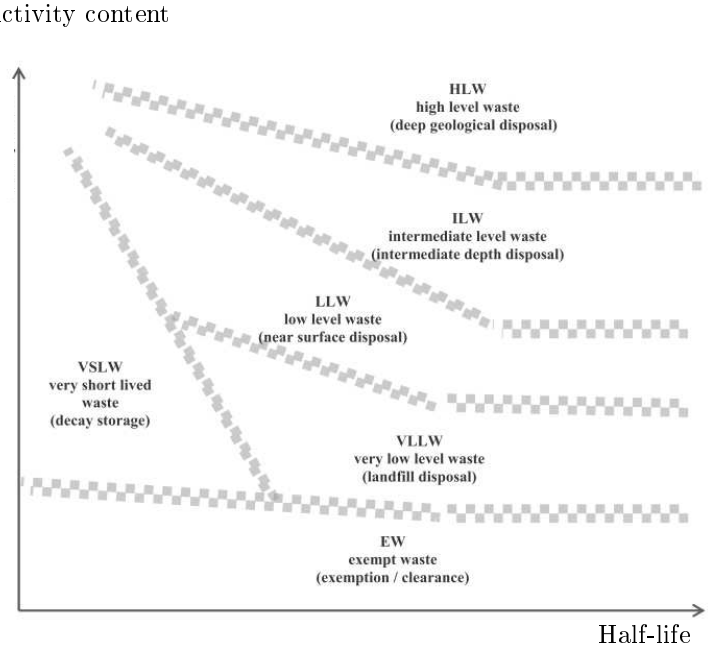

Figure 1.1: Scheme of the waste classification from [36].

Exempt waste (EW) does not require regulatory control for radiation protection. Then very short lived wastes (VSLW) and very low level wastes (VLLW) are under regulatory control, but they do not require high level of confinement. Low level wastes (LLW) can include short lived radionuclides at higher levels of activity concentration. LLWs also include long lived radionuclides with relatively low levels of activity concentration. This class concerns steel and concrete during the decommissioning process of nuclear power plants. Such wastes are stored near surface facilities for a period of up to a few hundred years. The intermediate level wastes (ILW) contain long lived radionuclides and require a greater degree of isolation than LLW. Wastes with highest levels of activity (HLW) frequently arise from spent fuel or reprocessing solutions containing FP and MA. HLW emit α particles and produce a significant amount of heat due to the radioactive decay process. They also contain a large amount of long lived radionuclides. One solution for long-term storage of these wastes is deep geological disposal (tens to a few hundred of meters) in stable geological formations. France vitrifies HLW frequently in La Hague (AREVA).

1.1.2 HLW confinement

High level wastes account for over 95 % of the total radioactivity produced in the nuclear power process but less than 3 % of the total volume (with LLW ∼90% and ILW ∼7%). After reprocessing, high level wastes are in liquid state. To avoid any leakage, waste storage requires a stable and compact solid. The release of radionuclides should be insignificant, i.e. the matrix should have a good chemical durability. Packaging fission product requires a structure able to accommodate the multiple elements and to be chemically resistant to water and self-irradiations, etc. Vitrification appears to be the most favorable from an industrial point of view [7]. Moreover, glasses partake in numerous advantages. The glassy network can incorporate both FP and MA. Also, it presents a good chemical durability, low porosity and

permits the confinement in low volume for transportation.

Elaboration of French R7T7 glass at La Hague involves two steps (figure 1.2):

- Evaporation of water and calcination step: converts most of the elements present into oxides. This step takes place at elevated temperatures (100°C to 400°C).
- Vitrification step: the output of the calcination step is mixed with glass frit via rotating tube and vitrified forming the glass melt. The frit is incorporated into the network of oxides produced in the calcination step and forms the glass package which embeds the fission products into its glassy network.

The steps are carried out in a continuous manner, on two distinct pieces of equipment.

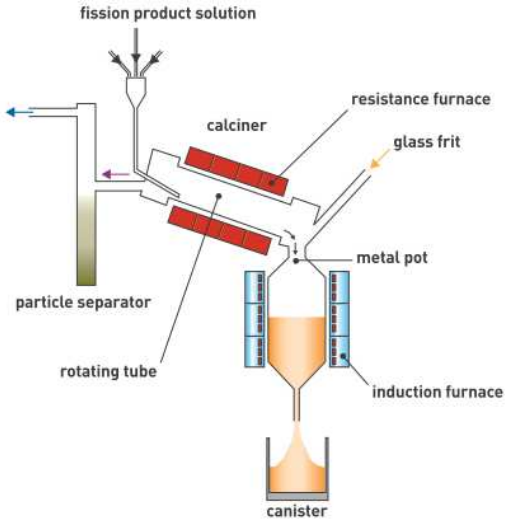

Figure 1.2: Hot crucible process of R7T7 glass elaboration from [1].

The formulation of nuclear glasses permit:

- High solubility of elements contained in the nuclear wastes.
- Temperature of elaboration below 1150°C for industrial process.
- Chemical durability to leaching, self-irradiation and demixing.

1.1.3 French nuclear waste glass: R7T7

France chose to develop the R7T7 glass, which contains $\sim$ 30 oxides. Table 1.1 details the composition of R7T7. Network formers, which aid in the polymerization of the glass network, typically found in R7T7 include silicon, boron, and aluminum. They induce strong bonds whereas network modifiers such as sodium break these bonds, decreasing the polymerization degree. Network modifiers also decrease the melting point and have a favorable effect on the viscosity and reactivity of the molten glass. Hence, they facilitate the elaboration processes. CaO increases the chemical durability. Other elements facilitate the

processes from industrial point of view: e.g. nickel oxide permits a control of the thermal conductivity. The incorporation of fission products is restricted to 18.5 %. At the end of the fabrication the R7T7 glass is homogeneous at the macroscopic scale. The non-active equivalent to R7T7 is SON68 glass.

Oxydes	%mass
SiO_2	45.1
B_2O_3	13.9
Na_2O	10.0
CaO	4.0
Al_2O_3	4.9
Fe_2O_3	3.0
ZnO	2.5
P_2O_5	0.3
NiO	0.4
Cr_2O_3	0.5
Li_2O	2.0
ZrO_2	1.0
Platinoids	1.6
PF	10.4
MA	0.4

Table 1.1: Chemical composition range for the R7T7 glasses [1].

The advantage to glass networks is the composition flexiblility. Thus it can be modified to incorporate more FP. Current research and technology permits the incorporation of 22.5 % mass of FP into the glass network in laboratory. Finally, other matrixes confine specific elements such as iodine, cesium, etc.

Ceramic matrixes present also advantages for the immobilization of high level waste: (1) good chemical durability, (2) ability to confine radioactive elements, (3) good behavior under self-irradiation. However, their elaboration processes are difficult to manage (ex: high pressure). The confinement of the iodine requires low temperature process such as Spark Plasma Sintering (SPS) and can be confinement in apatite ceramics. A good candidate to confine radionuclide elements is glassy-ceramics which are polycrystalline materials produced through controlled crystallization growth in glasses. They can increase the ability of glasses to incorporate certain elements with low solubility in glass, good thermal stability and mechanical properties and easier to elabore than ceramics.

1.2 Interaction of particles within the long term storage confinement

1.2.1 Origin of the irradiation

Irradiation during the long term storage mainly arises from fission products (e.g. ^{137}Cs) and the minor actinides (e.g. ^{241}Am) through β- and α-decay, respectively. FP contained in HLW (^{137}Cs, ^{90}Sr) induce β-decay, whereas minor actinides contained in HLW generate α-decay characterized by the emission of

helium nuclei (α particles) and a recoil nucleus:

$$^{244}_{96}Cm \Rightarrow ^{240}_{94}Pu + ^{4}_{2}He. \tag{1.1}$$

(α,n) reactions (ex:^{10}B(n,α)^{7}Li) also induce irradiation but at lower magnitude. Interactions of β- and α-decays with matter depend on whether the energy is dissipated in elastic or inelastic manner. The energy of a particle can be lost in two independent manners:

$$\left(\frac{dE}{dx}\right)_{total} = \left(\frac{dE}{dx}\right)_{inelastic} + \left(\frac{dE}{dx}\right)_{elastic} \tag{1.2}$$

β-decay is the main source of irradiation for the first 300 years of storage. Then, α-decays dominate during the remainder of the glasses' life-time. It's crucial to understand how these two components impact the long term behavior of the glass matrix.

1.2.2 Interaction between β decay and matter

During β-irradiation, energy dissipation mainly takes place through electronic excitation or ionization. Point defects and ionic/covalent bonds rupture can also occur. The energy of electrons is from 0.1 to 1.18 MeV. β decay also produces recoil nucleus of low energy ($\sim$ eV) and photons γ.

1.2.3 Interaction between α decay and matter

α-decay occurs when an atom spontaneously decays emitting 2 protons and 2 neutrons (i.e. an $^{4}_{2}$He also called an α-particle). The atom ($^{A}_{Z}$X) which releases the α-particle decays undergoes the following transformation

$$^{A}_{Z}X \Rightarrow ^{A-4}_{Z-2}Y + ^{4}_{2}He \tag{1.3}$$

$^{A-4}_{Z-2}Y$ is the recoil nucleus with high mass. It invokes ballistic damage with rather low energy, approximately 0.1 MeV, through collision cascades. The collision cascade involves secondary projectiles which also interact with the glassy network. The α-particle in equation 1.3 has a high energy and a small atomic mass. Interactions involving α-particles predominantly undergo inelastic interactions. As its kinetic energy decreases (i.e. the path in the matter increases), probability of nuclear interaction increases leading also to atom displacements. In this case, dissipation of the initial energy takes place through electronic ($\sim$ 99 %) interactions then ballistic (less than 1%) interactions. Table 1.2 summarizes the different contributions due to α-decay.

Particule	Energy (MeV)	Path length	Dissipation of initial energy through	
			Electronic interaction	Nuclear interaction
α-particule	$\sim$ 5	$\sim$ 20 μm	$\sim$ 99.7 %	$\sim$ 0.3 %
Recoil nucleus	$\sim$ 0.1	$\sim$ 40 nm	$\sim$ 37 %	$\sim$ 63 %

Table 1.2: α particle and recoil nucleus features from an α-decay.

1.3 Laboratory testing methods employed

It is mandatory to accelerate the time scale to simulate possible consequence of self-irradiation on the glass structure and mechanical properties. Several laboratory aging methods exists:

- Actinide doped glasses Actinide doped glasses are frequently used to understand how α-decay invokes modifications in the glassy structure. Model α-decay experiments incorporate short-lived elements in the glass matrix. This method is close to the phenomena occurring during final storage because: (1) it takes into account the impact of particles and helium accumulation; and (2) the actinides are homogeneously distributed in the glass. The main drawback is the activation of samples which leads to regulatory conditions to confine the samples and limit techniques used to characterize the glass evolution.

- External irradiation Frequently, light and heavy ions, electrons, or γ-ray bombardment of samples simulate the nuclear and elastic interaction issued from the β- and α-decays, and recoil nucleus. By varying the projectile (mass, charge and energy), one can shifts the expected damage from predominantly electronic to ballistic damage. Thus, scientists can isolate how the electronic damage differs from the ballistic damage. Helium, krypton and gold ions can be implemented. Samples remain non-active and a complete set of characterizations can be employed (Raman, NMR, WAXS, XANES, etc.). However, external irradiation does not homogenously irradiate the samples as in the case of doped R7T7 samples: in particular, heavy ions bombardment only deposits energy with in a thin layer close to the surface.

- Atomistic simulation Molecular dynamics (MD) simulation gives access to displacement cascades due to recoil nucleus in simplified borosilicate glasses. This method follows a display cascade in a glass under irradiation, i.e. simulation of recoil nucleus' path and all dynamic phenomena resulting from its passage is feasible.

The study herein employs external irradiation by electron, light (He^{2+}) ion and heavy (Au^{+}) ions irradiation. The next section summarizes previous results on irradiated simplified and complex glasses.

1.4 Structural modifications

1.4.1 Pure silica glasses

β and light ion and heavy ion irradiation change the structure of the silica glasses, specifically its density [26, 43, 65]. Electron irradiation (β_{e-}) commonly creates paramagnetic defects, which can be probed via EPR (Electron Paramagnetic Resonance) measurements. Griscom et al. [30–32] extensively characterized these point defects in pure silica glasses:

1. E' centers: E' centers are electrons trapped at an oxygen vacancy ($\equiv Si^{\bullet}$). Oxygen vacancies form either by elastic collisions with energetic particles or radiologically by decaying of self-trapped excitons (bound electron-hole pairs created by ionizing radiation). The displaced oxygen atoms move to an interstitial positions where they readily dimerise to form molecular oxygen [65].

2. NBOHC centers: Non-bridging-oxygen centers (≡Si-O$^\bullet$) results from radiolysis of the OH group: ≡Si-OH → ≡Si-O$^\bullet$ +H$^\bullet$

3. POR centers: Peroxy radical centers represented as ≡Si-O-O$^\bullet$. EPR signal is very similar to the NBOHC centers.

4. STHs: Self-trapped holes on the Si atom (≡Si$^\circ$)

The dose kinetics of defect creation processes arises by considering intrinsic (breaking of Si-O bond) and extrinsic (due to impurities) defects creation processes and a possible recombination of defects under irradiation [37, 64].

Boizot et al. [8] studied pure amorphous silica glass structure a $-$ SiO_2 before and after electron irradiation by Raman analysis. Significant modifications were evidenced: (1) a shift in the band around 450 cm^{-1} which is correlated to a decrease of the mean Si-O-Si angle together with a decrease in the dispersion around this mean value; (2) an increase of the band localized at 602 cm^{-1} (D_2) assigned to 3-membered silica rings; and (3) an appearance of O_2 explained by the following reaction: $2\ Si-O^- \rightarrow Si-O-Si + 1/2\ O_2$. These variations are consistent but weaker than those observed by neutron [26,57] and α-irradiation [44]. Buscarino et al. [17] examined the role of impurities such as Cl and OH on the

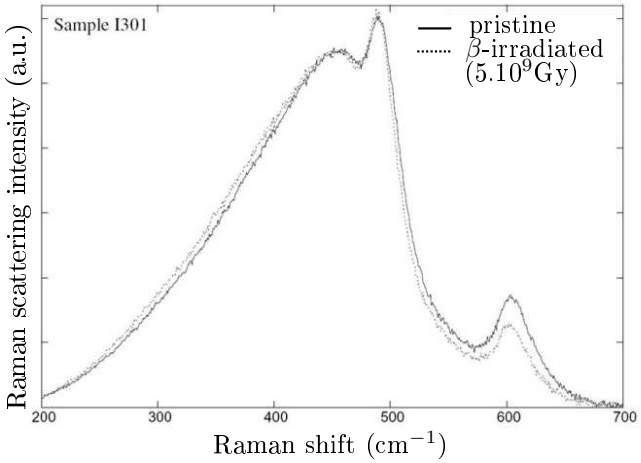

Figure 1.3: Raman spectra of pristine and β-irradiated (5×10^9 GGy) silica glass samples after subtraction of linear baseline (From [8])

glass structure. Cl is not a relevant element under electron irradiation; yet, as the OH content increases the local degree of densification decreases [17].

The similar compaction and increases in the refractive index of silica glass occur for electron and ion irradiations [3, 27, 56]. Recently Mendoza et al. [44] observed a densification of 3.3 % for silica submitted to 74 MeV Kr ions. a $-$ SiO_2 undergoes several structural variations due to neutron/ion irradiations: (1) densification; (2) increase in the D2 peak (3-membered rings); (3) significantly larger decrease in the average bond angle as compared to samples which undergo hydrostatic pressure at room temperature [25];

and (4) increased etching rate [26]. Devine hypothesized that neutron irradiation induces inhomogeneity in a $-SiO_2$: an increase in D2 (3-membered rings) count via Raman spectra; and a creation of voids which lead to an increase in the acid etching rate [26]. These variations in irradiated a $-SiO_2$ cannot be attributed solely to the concentration of irradiation-induced E' centers because they saturate before significant densification occurs.

MD simulations of 0.6 keV heavy atom cascade displacements in a $-SiO_2$ uncovered an increase in the number of three-membered silica rings [21]. Structural and density changes in SiO_2 during ion and β irradiation could be explained by the fact that point defects act as precursors for structural evolution under irradiation. **Both processes (electronic and ballistic interactions) densify the silica glasses. However nuclear interactions appear to be more effective [3, 27, 56].**

1.4.2 Simplified borosilicate glasses: 6 or less oxides

The understanding of the structural evolution of nuclear glasses is crucial to ensure the long term disposal. However, the structural behavior of complex glasses remains unclear. Simplified borosilicate glasses with 3, 4, 5 or 6 oxides (the principal oxides in R7T7 glass) are usually employed to investigate the structural modification induced by irradiation. β and light and heavy ions irradiations change the structure of the simplified borosilicate glasses. Yet, the scaling up of these microscopic variations to macroscopic variations depends on the glass's chemistry [13,16]. The next section details the microscopic variations due to β_{e-}-irradiation. The subsequent section presents the variations in simplified borosilicate glasses due to ion irradiation.

Electronic excitation,β_{e-}-irradiation

The silicate network in SBN glasses can undergo the same type of electronic excitations as presented in section 1.4.1. Nonetheless, the boron, sodium and aluminum atoms also introduce a further source of point defects. Defects associated in addition of the defects detailed in section 1.4.1 are:

1. BOHC: Boron oxygen hole center concerns a non-bridging oxygen atom bonded to a B atom (≡B-$O^\bullet$) [35].
2. HC_1 and HC_2: HC are hole centers trapped on oxygen atoms near alkali ion (≡Si-$O^\bullet Na^+$) [34]
3. ALOHC: Al Oxygen Hole Center, (≡Al-$O^\bullet$) may also appear [11]

Paramagnetic centers resulting from electron trapping processes on Fe^{3+} and Zr^{4+} also exist. Two different BOHC signals in the form of a quartet and a quintet (figure 1.4) are known for low and high alkali content [6].

Boizot et al. [9, 10] studied the impact of impurities on the defect creation in simplified borosilicate glasses. A few percent of iron limits the defect creation in the structural changes [18, 33, 46, 62]. The reduction processes of Fe^{3+} under irradiation may explain this result. Debnath [18] proposed a possible hopping process consuming the excitons produced during the electron irradiation which cannot be used for the production of defects. This charge trapping processes on cations under irradiation induced by electronic excitations are common in glasses containing, e.g. Fe^{3+}, Zr^{4+}, and U^{4+}. These processes could

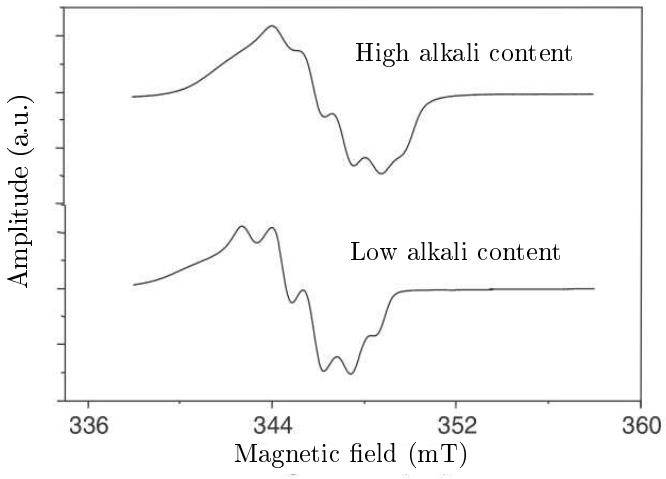

Figure 1.4: Comparison of EPR spectra for low and high amount of total alkali ions from [6].

therefore limit structural changes under irradiation if a correlation between some precursor defects and migration of alkaline ions exists. No dose rate dependence exists in a range between 2×10^3 and 2×10^4 Gy.s^{-1} [11]. Boizot et al. [12] performed Raman analysis on 4-, 5- and 6-oxide glasses irradiated by electron. Spectra presented below are similar to those obtained previously. Several changes occur: (1)

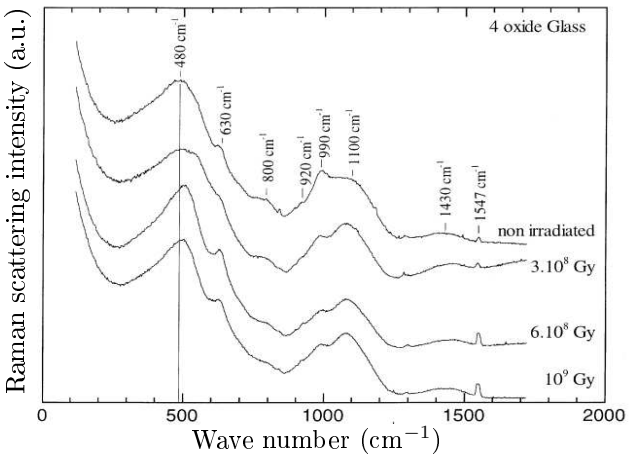

Figure 1.5: Evolution of the Raman spectrum of the 4-oxide glass as a function of the β-radiation dose from [12].

shift of the Si-O-Si band interpreted as a decrease of the mean Si-O-Si angle and a decrease in the mean size of the silica ring, (2) variation in the Q_n band and an increase of the Q^3/Q^2 ratio, i.e. an increase of the polymerization degree of the silica network due to alkali migration, then (3) appearance of molecular oxygen. During irradiation, a large number of Si-O$^-$ bonds are produced by the migration of alkali ions in glasses. The recombination of Si-O$^-$ lead to the formation of Si-O-Si, which increase the polymerization

of the silica network. Such changes in the chemical composition are also accompanied with changes of glass structure and the formation of ≡Si-O-O-Si≡ bonds implying the formation of new big rings [66].

Finally, phase separation or oxygen bubbles can take place [63]. At 10^{12} GGy, borosilicate glass presents phase separation with areas enriched in silica and other areas in boron. Number, size and bubble distribution depend on the temperature, fluence and type of irradiation [47]. For electron irradiation, bubble can appear between 10^{10} and 10^{13} GGy; they are not randomly spread out in the glass structure and depend on the ability of alkali to diffuse. Among these alkali, sodium is the most susceptible alkali to migrate due to variation of the local electric field by charged particles. Moreover, sodium can move towards the free surface of the glassy network depending on the charge of the ion irradiating. [45].

Heavy ions irradiation in simplified borosilicate glasses

To improve the understanding of structural modifications induced by irradiation, J. de Bonfils [13] studied simplified nuclear glasses irradiated by heavy ions. Figure 1.6 presents evolution of density in simplified borosilicate CJ1 and CJ7 glasses irradiated by Au^+ ions. The swelling appears to increase with

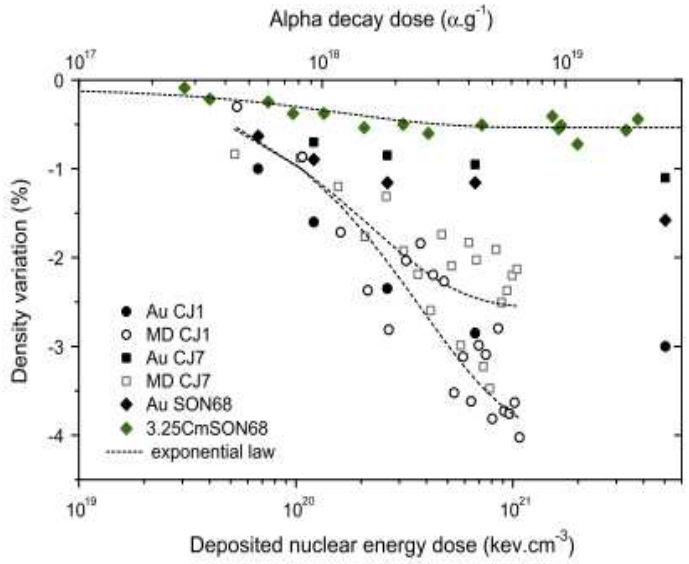

Figure 1.6: Density evolution for simplified borosilicate glasses (3-7oxides) submitted to gold irradiation.

the irradiation fluence and depends on the chemical composition, especially the alkali content. Na^+ ions in a modifying role increases the swelling. The swelling can originate from the structural modifications. Raman analysis permits to investigate structural variation induced by Au^+ irradiation [13,15].

Figure 1.7 presents the evolution of Si-O-Si band shift with deposited nuclear energy dose. The peak of the band shifts by about 10 cm^{-1} (from $\sim$ 496 to 506 cm^{-1}). This change is associated to a decrease of the mean angle between the silicon tetrahedra. Morever, this band shift stabilizes for a deposited nuclear energy dose equivalent to an energy deposited of 5×10^{18} $\alpha.g^{-1}$. These experiments revealed also changes in the silica environment (change in Q_n bands), especially Q^3 species increases which reveals the

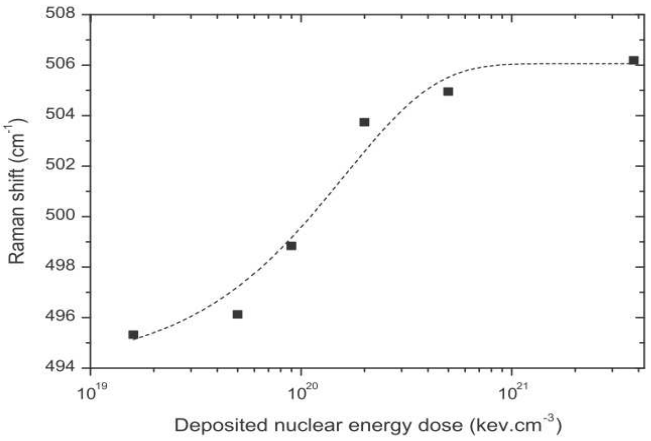

Figure 1.7: Si-O-Si bending band peak versus deposited nuclear energy dose for SBN 14 irradiated by gold ions. The dash curve was obtained by fitting the experimental data with an exponential law (from [52]).

creation of NBO on the silica network. MD simulations also confirm this trend. Other authors suggest a depolymerization induced by the conversion of $^{[4]}$B to $^{[3]}$B [16].

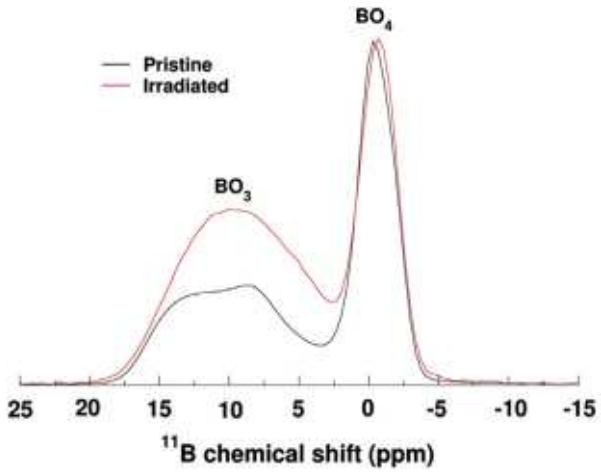

Figure 1.8: ^{11}B spectra for simplified glasses (CJ1) before (black line) and after (red line) irradiation by gold ions.

Figure 1.8 shows the ^{11}B spectra before and after gold irradiation. ^{11}B MAS NMR measurements reveal a conversion of $^{[4]}$B to $^{[3]}$B (17 %) and a decrease in the Na-O distance. Again, the variation's amplitude depends on the initial coordination state of boron atoms. Sodium ions are then free to move and to become modifiers in the glassy network. Moreover, G. Bureau [16] emphasized the importance of the initial polymerization degree to irradiation impact.

Structural variations are assessed by MD simulation during ballistic irradiation [22–24]. The glass possesses a good capacity to reorganize after irradiation by recoil nuclei. Nevertheless, a depolymerization of the glass network is still observed: it goes along with an increase of $^{[3]}$B and NBOs.

Finally, the analysis of ion irradiation uncovers the dominating influence of nuclear interaction on the structural modifications. Yet, some authors [4, 5] link density changes to ionization processes through investigations of irradiation by ions at lower energies.

1.4.3 Heavy ion irradiation on R7T7 and complex borosilicate glasses

R7T7 glasses irradiated by electrons do not exhibit density variation [29]. R7T7 is a very complex chemical composition; thus, glass is probably less sensitive to electronic interactions than simplified glass. For example, additions of transition elements or lanthanides reduce or vanish the structure modification induced by electron irradiation. Peuget et al. investigate the impact of α-decay on the density of SON68 glasses [52]. Figure 1.6 displays the density variation for SON68 glass after irradiation. A swelling is observed followed by stabilization in the density variation. At low doses, the density rapidly decreases of about (0.5/0.6 %). Some authors [41] suggest a possible role of the dose rate on the amplitude of the density variation, but Peuget et al. did not confirm this effect [49, 52, 54]. The radioactivity of doped glasses limits structural characterizations.

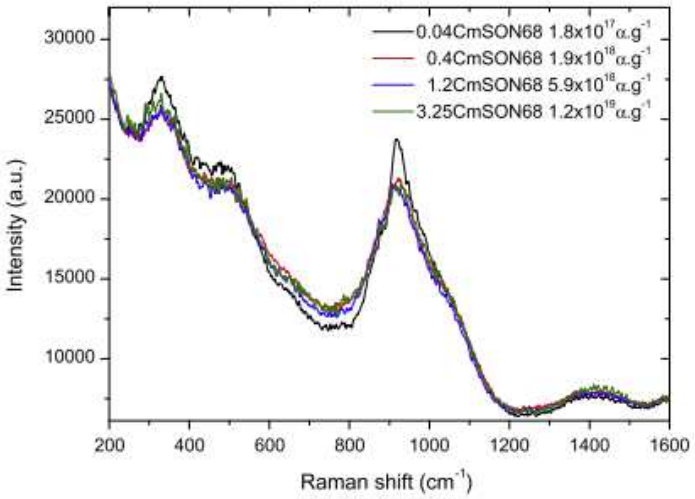

Figure 1.9: Raman spectra of the SON 68 glasses doped with curium from [52].

Raman analysis exposes the structural evolution of SON 68 glass doped with curium [49, 51],(figure 1.9). Modification of the glass structure occurs between 2.10^{17} α/g and 2.10^{18} α/g. First, examining the signatures of the silicate network (band peaked around 490 cm^{-1}) reveals variations in the Si-O-Si angle (shift in the Si-O-Si band to higher wavenumbers). Then, the Q_n band changes between 2.10^{17} α/g and 2.10^{18} α/g. After 10^{19} α/g, no modifications occur. Structure changes coincide with results obtained by J. de Bonfils on external irradiated simplified glass samples [13, 14]. Xanes measurements show a decrease of the boron coordination number in SON 68 doped glass. Furthermore, no phase separation or crystallization take place in the dose range presented. Interpretation of such variations is tricky because R7T7 contains a significant number of oxides. Some authors suggest [4, 5] that ionization or presence of bubbles induce glass swelling. However, T. Fares showed no correlation between glass swelling and

helium content after irradiation in reactor on SON 68 glass in which reactions $^{10}B(n,\alpha)^{7}Li$ generate high concentration of helium. Moreover, density variation in doped glasses, externally irradiated glasses, and MD simulations tend to highlight the role of ballistic effects with structural variations to explain density changes [15,21,54].

1.4.4 Correlation density-structure variations

The volume variation observed in glass irradiated samples by neutron, heavy ions and actinides-doped glass are coherent [2,13,16,52,54]. However a slight discrepancy in the amplitude is found: irradiations by heavy ions (Au^{+}) lead to a swelling of 1% whereas a swelling of 0.5% occurs in doped complex glasses. Molecular dynamics simulations highlight the reorganization in the glassy network after the displacements cascades due to a primary knock on atom (i.e. a simulated recoil nucleus) [22–24].

MD simulations observe a density variation as their experimental counterparts: the glass swells followed by a stabilization phase [16]. Swelling in SBN glasses appears to originate from a decrease in the local coordination number of B, Na and O atoms. The number of NBOs increases, and boron undergoes a conversion from $^{[4]}B$ to $^{[3]}B$ changing the sodium role (from charge compensator to network modifier). Other structural modifications occur but are not linked to density variations [21]: (1) a decrease of the mean Si-O-Si angles (figure 1.10); (2) a decrease of the mean ring size; and (3) a widening of the structural distributions (angle, distance, etc.) [21]. Simulations reveal more disordered in the glass structure due to irradiation. Finally, MD simulations showed that the cores of displacement cascades have a lower density: the PKA atom knock other atoms outside of the track of the projectile leading to a density fluctuation. The global similarities between simulations and experiments (external and internal irradiation) suggest the origin of modification arise from the same mechanism.

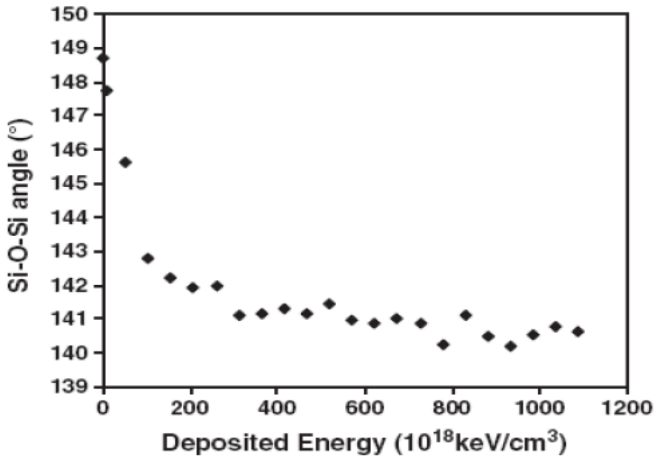

Figure 1.10: Decrease of Si-O-Si angles depending on the deposited energy for SBN 14 glass from MD simulations. Displacement cascade commenced by a 0.600 keV heavy ions [21].

1.4.5 Ballistic disordering and fast quenching

Analogy between the structural state created by ballistic interaction and thermal quenching is usually invoked to explain the structural variation [16, 26, 28, 53, 60]. Cascades of displacements in the glass network disorganize the structure: the local disorganization of the glass due to a displacement cascade is equivalent to a significant temperature rise. The glass structure resembles a structure frozen from a high temperature state because it cannot relax [26]. In a nuclear glass, the variations of the structural properties can then be considered in terms of fictive temperature caused by irradiation. This hypothesis has been postulated to account for the evolution of amorphous silica under irradiation by several authors [26, 28, 60]. Based on this hypothesis, the accumulation of events throughout the glass volume results in a totally damaged material. A new glass structure is then formed at the end the accumulation leading to a *quenched* glass, i.e. glasses with higher fictive temperature. Authors [42] propose to describe structural changes in the glass under ballistic irradiation via the ballistic disordering fast quenching accumulation model. Destabilization of $^{[4]}$B units due to the cascades of displacements and formation of $^{[3]}$B units coincides with variations in the $^{[4]}$B/$^{[3]}$B fraction observed for high temperature [61]. This is also coherent with the depolymerization of the silicate network. MD simulations also reveal this phenomenon [22]: the quenching rate after cascade displacements is higher than the quenching rate used for elaboration. Moreover similarities between both mechanisms come into sight. The increase of quenching rate leads to a decrease of the polymerization degree (decrease of mean Si-O-Si angle), increase of NBOs, and an increase of $^{[3]}$B. This description of the quenched glasses follows the Marples' model which explains the saturation observed once the entire glass is damaged. New perturbations in this volume do not give further structural variation because the new glass structure reaches an equilibrium state with irradiation. Recently, differences in variations induced by ion irradiations and fast quenching were highlighted [44] and this comparion has to be taken with care.

In summary, simple and complex borosilicate glasses swells after irradiation, either due to doping or to external irradiation. The density of SON 68 glasses doped with curium decreases by about 0.6 %. The glass remains homogeneous and no bubbles formation takes place in the α-decay doses investigated. Experimental results plus MD simulations point out that the ballistic effects have the potential to significantly alter the structure. After cascade of displacements, the structure evolves toward a more disordered structure. Moreover, the accumulation of displacement cascades lead to a *quenched* glass, i.e. glasses with higher fictive temperature. Recently, research highlights the differences induced by these two processes.

1.5 Mechanical properties

As stated in the introduction, irradiation can lead to variations in the physical and mechanical properties of glasses. This section reviews the current knowledge of the evolution of the physical and mechanical properties under irradiation.

1.5.1 Young modulus evolution

Complex glasses irradiated by helium ions at 1.7 MeV present a decrease of 0.6 % in the acoustic velocity; whereas the same glasses irradiated by heavy ions display a decrease of 8.7 % [20,49,52]. Peuget et al. [49] studied the evolution of the reduced modulus, E_R in complex glasses (SON 68) doped with actinides (^{144} Cm). E_R is approximately 15 % less than its pristine counterpart. This result is confirmed by MD simulations. The acoustic velocity has been measured throughout the accumulation of displacement cascades [19, 20]. The relative variations for the longitudinal and transverse velocity decrease with the number of accumulated cascades, as presented in figure 1.11

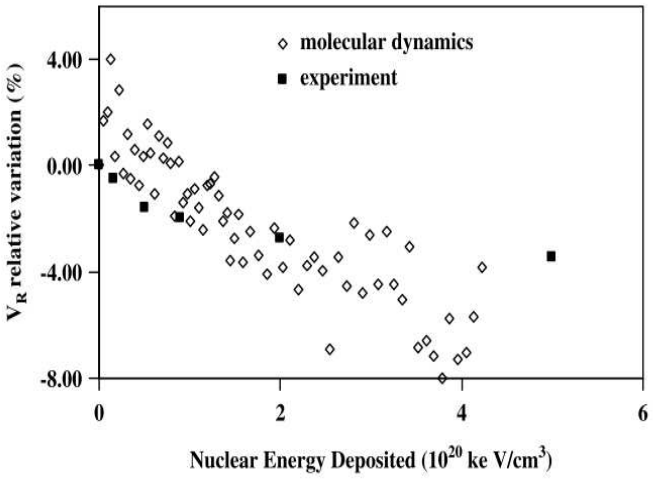

Figure 1.11: Experimental and simulated relative variation of Rayleigh velocity in CJ1 (3 oxides) irradiatied simplified glasses.

After electron irradiation until E_{elec} equivalent to 2.3 10^{18} α/g no variation is observed. This suggests that nuclear interaction is the predominant process responsible for changes in the value of Young modulus.

1.5.2 Hardness evolution

External β_{e-} irradiation

Yang et al. studied the impact of electron (1.2 MeV) on the hardness properties (H) in borosilicate glasses [66]. Figure 1.12 depicts the evolution of H with energy deposited by external irradiation. For the electron irradiated glasses, H value decreases slightly. Yang et al. [66] attributed this decrease with an increase of the polymerization in the silica network and formation of new ring in the electron-irradiated glass.

External irradiation by light and heavy ions

Along with β_{e-} irradiation, Yang et al. [66] also examined the effect of irradiation with light ions (α, 0.5 MeV). Figure 1.12 depicts the evolution of H with energy deposited by external irradiation. H decreases

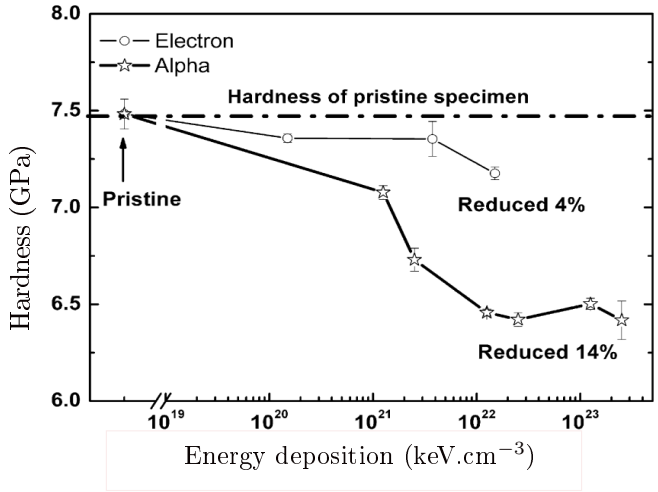

Figure 1.12: Evolution of the mean hardness of glasses irradiated with electron (circles) and He ions (stars) irradiation versus energy deposition [66].

steadily from 0 to 10^{22} keV/cm^{-3}. The total reduction in hardness is $\sim 14\%$. Subsequently, H stabilizes at $\sim 14\%$ reduction. Yang et al. concluded that the nuclear energy deposition governs the reduction in H. J. de Bonfils studied the evolution of H in simplified borosilicate glasses irradiated by gold ions [13,14]. H values decrease by about $\sim 35\%$ at 10^{18} α/g. After which, H stabilizes. Authors linked the hardness decrease to depolymerization of the glass network by irradiation [14]. Over the past decade, Peuget et al.

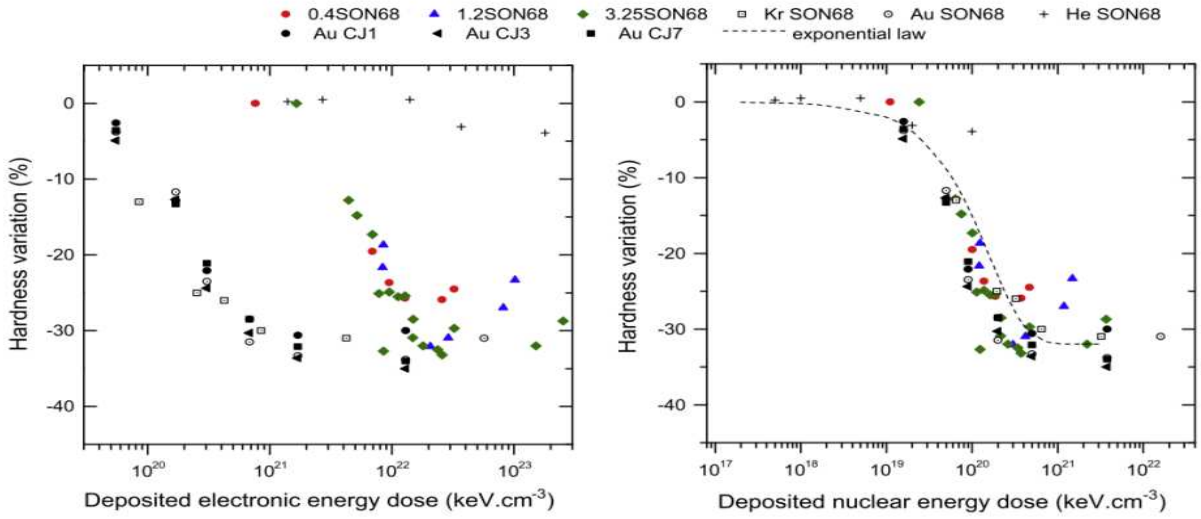

Figure 1.13: Hardness variation in SON68 and simplified glass irradiated under various condition with energy dose deposited by electronic interaction (left) and nuclear interaction (right)

conducted multiple experiments on how H varies in complex glasses (SON 68) with varying external doses and irradiation type (i.e. light and heavy ions) [48,49,52,54]. Figure 1.13 displays the hardness evolution in SON 68 and simplified glass irradiated under several conditions with energy deposited. Concerning

He^{2+} irradiation, the hardness is not impacted until E_{elec} exceeds $3\times\ 10^{18}$ α/g. On the other hand, H decreases when E_{nucl} exceeds $1.5\times\ 10^{18}$ α/g for Au- and Kr-ions irradiation. SON68 actinide-doped glasses also present a decrease in hardness of $\sim$ 30 %. Figure 1.13 compares the hardness evolution with the energy deposited by electronic and nuclear interaction. Examining variations of H due to electronic and nuclear deposited energy, Figure 1.12 evidences a collapse of the data with deposited nuclear energy. This suggests that ballistic effects are responsible for hardness variations [49]. Recently, Kilymis et al. suggested that the change in the glass topology (e.g. increase in the number of NBOs and $^{[3]}$B) increases the glass plasticity giving way to decrease in H [40].

1.5.3 Evolution of fracture toughness (K_C)

K_C variation by indentation measurement

Indenting the glass samples can cause crack to propagate off the indenter. Examining their length and the quantity of cracks, as revealed in part I chapter 2, gives K_C (fracture toughness) and P_C (crack appearance probability).

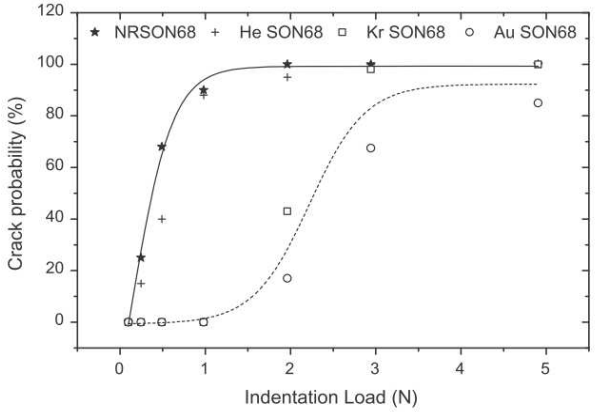

Figure 1.14: Evolution of crack appearance probability versus load for Vickers microindentation of the non-radioactive glass (SON68), and the glass irradiated by He, Kr and Au ions from [52].

Figure 1.14 reveals the crack appearance probability, P_C for a Vickers indenter in SON68 glass irradiated by different ions: He, Kr, and Au. Helium irradiation gives similar results as pristine SON68 samples; thus Helium irradiation does not change significantly P_C 1.14) [50, 52]. On the contrary, Kr and Au irradiation influence P_C. The irradiated glasses appear to be more *plastic*, and their crack resistance increases. P_C decreases when the dose increases in doped curium SON68 glasses [49]. Again nuclear interactions appear to govern the evolution of P_C.

The toughness value (K_C) increases by about 25 % after gold irradiation [50]. Similarly, Matzke studied the evolution of K_C in R7T7 like glasses, MCC 76-88 (American glass), and GP 98/12 (German glass). These glasses were doped with curium and stored for 10 years. During this period, K_C increases by 100 %.

K_C variation by fracture test through MD simulations

Molecular dynamics simulations investigated fracture properties in simplified glasses (3-oxides glasses) [38, 39]. L.-H. Kieu evidenced crack propagation in SBN systems via the nucleation, growth and coalescence of nanocavities (figure 1.15) [38,39]. Literature also evidences a similar scenario in pure amorphous silica [55, 58, 59].

SBN fracture simulations reveal two competing effects: (1) the swelling as presented in section 1.4.2, and (2) the increase of $^{[3]}$B at the expense of $^{[4]}$B. As the free volume increases, nanocavitation occurs and the resistance to crack propagation decreases. On the other hand, $^{[3]}$B are more able to accommodate stress [38, 39] and this process increases the resistance to fracture propagation. Kieu et al. also investigate the Si-O, B-O and Na-O radial distribution functions at different times during fracture experiment. They highlight elongation of the Si-O and B-O bond in $^{[4]}$B units. On the other hand, B-O bond in $^{[3]}$B units and Na-O bonds do not elongate rather they adapt to local stresses. As a consequence,

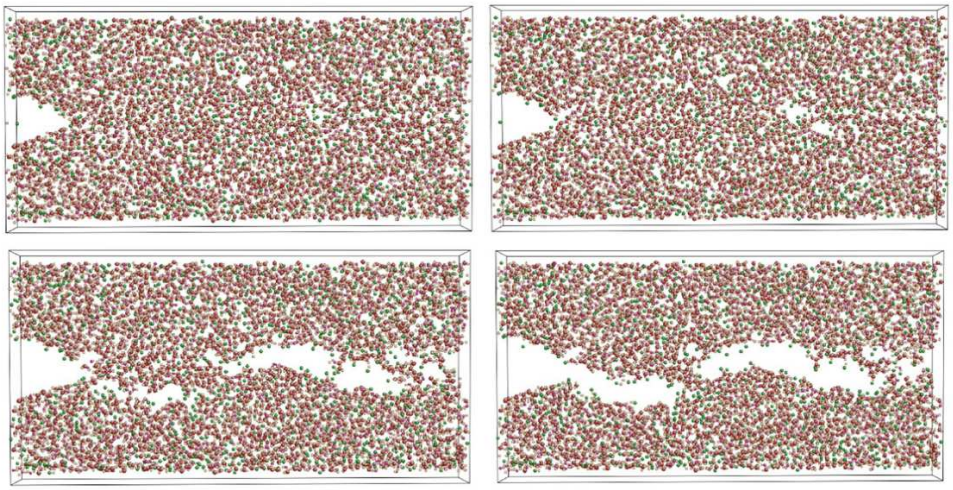

Figure 1.15: Four images of the SBN 14 glass fracturing. (Top left) 26ps; (Top right) after 32ps; (Bottom left): after 40ps; (Bottom right) after 44ps from [39].

L.-H. Kieu found an increase, decrease and stabilization of the K_C in the disordered structure regarding to their counterparts because the impact of both effects depends on the initial glass composition. **Mechanical properties evolve after irradiation. Accumulation of α-decay in actinide-doped SON68 glasses diminishes their hardness (∼30 %), their Young modulus and increases their fracture toughness determined by indentation. The behavior during fracture experiments is complex due to different competing effects. Overall, the ballistic effects appear to be predominant in these mechanical changes.**

1.6 Summary

Variation in the structural properties of the glass due to irradiation can lead to the swelling or densification of the glass packages [2, 13, 16, 49, 54]. Due to the confinement of the glass package within the canister this will lead to variations in the stresses. α decay causes curium doped SON68 to swell by ~ 0.6 % [52, 54].

At 2×10^{18} α/g the glass package reaches a stabilization point. From 2×10^{18} α/g to 10^{19} α/g, the density does not evolve. Raman, NMR and XANES studies plus MD simulations pointed out changes in the glassy network for simple and complex glasses [13, 14, 16, 22–24, 50–52]. Changes in the boron coordination number and increase of NBO take place. Beside, modification in the medium-range order also occur: bond angles between network formers, broadening of the ring size distribution. Glass structure appears to be more disordered after irradiation. As a consequence, mechanical properties vary. Young modulus decreases after α-decay [20, 52, 54]. This appears to be well correlated to the decrease of the polymerization degree in the glassy network. After irradiation, the glassy network appears less rigid due to (1) increase of NBOs in the silica network and (2) conversion of $^{[4]}$B to $^{[3]}$B, increasing freedom around boron atoms. Ballistic interactions induce significant variations in the mechanical properties: (1) decrease of H (30 %) and (2) increase of K_C. As previously noticed, a stabilization appears between 2×10^{18} α/g to 10^{19} α/g [52]. Several explanations have been proposed to elucidate the hardness and fracture toughness variations. Several authors concluded the glass depolymerization aids in their variations [40,44]. Moreover, the increase of $^{[3]}$B favors viscous flow at the crack tip [38, 39].

This chapter presents the current knowledge on how the structural, physical and mechanical properties of silica based glasses are impacted by irradiation. Literature reports irradiation increases in the glass disorder and plasticity. As a consequence, the hardness decreases and the toughness increases. Comparison between electronic and ballistic interactions pointed out the dominant role of the latter one. I investigate the impact of external irradiation on the simplified borosilicate samples. As presented, the interactions are localized in a thin layer of the glass samples. Specific experimental set-up is required to estimate the impact on mechanical properties. The next chapter presents the chosen chemical compositions for the studied glasses, the techniques used to investigate the structural behavior and the mechanical properties after irradiation.

Bibliography

[1] Cold-crucible fabrication of nuclear glasses. *CLEFS CEA*, 59:17–23, Summer 2010.

[2] A. Abbas. *Contribution de l'etude de l'effets de l'irradiation alpha sur les verres nucleaires.* PhD thesis, Universite Paris VI, 2001.

[3] G. W. Arnold. Ion-implantation effects in glasses. *Radiat. Eff. Defects Solids*, 65:17–30, 1982.

[4] G. W. Arnold. Ion-implantation effects in alkali-borosilicate glasses. *Radiat. Eff. Defects Solids*, 98:55–61, 1986.

[5] G. W. Arnold. Ion-implantation-induced stress in glasses - variation of damage mode efficiency with changes in glass structure. *Nucl. Instrum. Methods Phys. Res. B, Beam Interact. Mater.*, 32:504–507, 1988.

[6] S. Baccaro, N. Catallo, A. Cemmi, and G. Sharma. Radiation damage of alkali borate glasses for application in safe nuclear waste disposal. *Nucl. Instrum. Methods Phys. Res. B, Beam Interact. Mater.*, 269:167–173, 2011.

[7] R. Boen. *Le colis de verre et les procedes d' élaboration.* Monographie de l'énergie nucl éaire, 2009.

[8] B. Boizot, S. Agnello, B. Reynard, R. Boscaino, and G. Petite. Raman spectroscopy study of beta-irradiated silica glass. *J. Non-Cryst. Solids*, 325:22–28, 2003.

[9] B. Boizot, N. Ollier, F. Olivier, G. Petite, D. Ghaleb, and E. Malchukova. Irradiation effects in simplified nuclear waste glasses. *Nuclear Instruments & Methods In Physics Research Section B-beam Interactions With Materials and Atoms*, 240:146–151, 2005.

[10] B. Boizot, G. Petite, D. Ghaleb, and G. Calas. Radiation induced paramagnetic centers in nuclear glasses: an epr spectroscopy study. *Vide Science, Technique et Applications*, 1998.

[11] B. Boizot, G. Petite, D. Ghaleb, and G. Calas. Dose, dose rate and irradiation temperature effects in beta-irradiated simplified nuclear waste glasses by epr spectroscopy. *J. Non-Cryst. Solids*, 283:179–185, 2001.

[12] B. Boizot, G. Petite, D. Ghaleb, B. Reynard, and G. Calas. Raman study of beta-irradiated glasses. *J. Non-Cryst. Solids*, 243:268–272, 1999.

[13] J Bonfils de. *Effets d'irradiations sur la structure de verres borosilicates-Comportement a long terme des matrices vitreuses de stockage des dechets nucleaires.* PhD thesis, Université Claude Bernard - Lyon I, 2007.

[14] J Bonfils de, S. Peuget, G. Panczer, D Ligny de, S Henry, P. Y. Noel, A. Chenet, and B. Champagnon. Effect of chemical composition on borosilicate glass behavior under irradiation. *J. Non-Cryst. Solids*, 356:388–393, 2010.

[15] J Bonfils de, Peuget S., G. Panczer, D Ligny de, S Henry, P.Y. Noel, A. Chenet, and B. Champagnon. Effect of chemical composition on borosilicate glass behavior under irradiation. *J. Non-Cryst. Solids*, 356:388–393, 2010.

[16] G. Bureau. *Comprehension structurale des effets d'auto-irradiation alpha dans les verres: couplage entre etudes spectroscopiques et modelisation atomistique.* PhD thesis, Universite Pierre et Marie Curie (Paris VI), 2008.

[17] G. Buscarino, S. Agnello, F. M. Gelardi, and R. Boscaino. The trole of impurities in the irradiation unduced densification of amorphous sio2. *Journal of physics condensed matter*, 22:255403, 2010.

[18] R. Debnath. Thermally-reversible gamma-ray-induced redox reaction between substitutional iron and aluminium impurity centers in a silica glass. *J. Mat. Res.*, 16:127–131, 2001.

[19] N. Deladerriere, J. M. Delaye, S. Peuget, and G. Bureau. Effect of elastic collisions on acoustic wave propagation in simplified nuclear glass: Molecular dynamics simulation. *Nucl. Instr. Meth. Phys. Res. B*, 266:2687–2690, 2008.

[20] N. Deladerriere, J.M. Delaye, F. Augereau, G. Despaux, and S. Peuget. Molecular dynamics study of acoustic velocity in silicate glass under irradiation. *J. Nucl. Mater.*, 375:120–134, 2008.

[21] J M. Delaye, S. Peuget, G. Bureau, and G. Calas. Molecular dynamics simulation of radiation damage in glasses. *J. Non-Cryst. Solids*, 357:2763–2768, 2011.

[22] J.M. Delaye and D. Ghaleb. Dynamic processes during displacement cascades in oxide glasses: A molecular-dynamics study. *Phys. Rev. B*, 61:14481–14494, 2000.

[23] J.M. Delaye and D. Ghaleb. Combining two types of molecular dynamics for rapid computation of high-energy displacement cascades. i. description of the method. 71:224203, 2005.

[24] J.M. Delaye and D. Ghaleb. Combining two types of molecular dynamics for rapid computation of high-energy displacement cascades. ii. application of the method to a 70-kev cascade in a simplified nuclear glass. *Phys. Rev. B*, 71:224204, 2005.

[25] R. A. B. Devine, R. Dupree, I. Farnan, and J. J. Capponi. Pressure-induced bond-angle variation in amorphous sio2. *Phys. Rev. B*, 35:2560–2562, 1987.

[26] R.A.B. Devine. Macroscopic and microscopic effects of radiation in amorphous sio2. *Nucl. Instr. Meth. Phys. Res. B*, 91:378–390, 1994.

[27] E.P. EerNisse. Compaction of ion-implanted fused silica. *Journal of Applied Physics*, 45:167, 1974.

[28] Galeener F.L. Geissberger, A.E. Raman studies of vitreous sio2 versus fictive temperature. *Phys. Rev. B*, 27:3266–3271, 1983.

[29] N. Godon. Rt/dtcd/2004/06. Technical report, 2004.

[30] D. Griscom. E' center in glassy sio2 : microwave saturation properties and confirmation of the primary 29si hyperfine structure. *Phys. Rev. B*, 20:1823–1834, 1979.

[31] D. Griscom. Self-trapped holes in amorphous silicon dioxide. *Phys. Rev. B*, 40:4224–4227, 1989.

[32] D. Griscom. Electron-spin-resonance characterization of self-trapped holes in amorphous-silicon dioxide. *J. Non-Cryst. Solids*, 149:137–160, 1992.

[33] D. Griscom, C. Merzbacher, R.A. Weeks, and R.A. Zuhr. Electron spin resonance studies of defect centers induced in a high-level nuclear waste glass simulant by gamma-irradiation and ion- implantation. *J. Non-Cryst. Solids*, 258:34–47, 1999.

[34] D.L. Griscom. Electron-spin-resonance studies of trapped hole-centers in irradiated alkali silicate-glasses - a critical comment on current model for hc1 and hc2. *J. Non-Cryst. Solids*, 64:229–247, 1984.

[35] D.L. Griscom. Trapped-electron centers in pure and doped glassy silica : A review and synthesis. *J. Non-Cryst. Solids*, 357:1945–1962, 2011.

[36] IAEA. Classification of radioactive waste. Technical report, Safety standards series No.GSG-1, 2009.

[37] H. Imai and H. Hirashima. Intrinsic- and extrinsic-defect formation in silica glasses by radiation. *J. Non-Cryst. Solids*, 179:202–213, 1994.

[38] L.-H. Kieu. *Compréhension de l'origine de l'évolution sous irradiation de la ténacite des verres nucléaires.* PhD thesis, Ecole Doctorale Polytechnique, 2011.

[39] L.-H. Kieu, J. . M. Delaye, and C. Stolz. Modeling the effect of composition and thermal quenching on the fracture behavior of borosilicate glass. *J. Non-Cryst. Solids*, 358:3268–3279, 2012.

[40] D. A. Kilymis and J-.M. Delaye. Nanoindentation studies of simplified nuclear glasse using molecular dynamics. *J. Non-Cryst. Solids In press*, 2014.

[41] J.A.C. Marples. Dose-rate effects in radiation-damage to vitrified radioactive-waste. *Nucl. Instrum. Methods Phys. Res. B, Beam Interact. Mater.*, 32:480–486, 1988.

[42] E.A. Maugeri, S. Peuget, and D. Staicu. Calorimetric study of glass structure modification induced by α-decay. *J. Am. Ceram. Soc.*, 95:2869–2875, 2012.

[43] C. Mendoza. *Caracterisation et comportement sous irradiation de phases powellites dopées terres rates - Application au comportement à long terme des matrices de confinement des dechets nucleaires.* PhD thesis, Universite Claude Bernard-Lyon 1, 2010.

[44] C. Mendoza, S. Peuget, T. Charpentier, M. Moskura, R. Caraballo, O. Bouty, A.H. Mir, I. Monnet, C. Grygiel, and C. Jegou. Oxide glass structure evolution under shift heavy ion irradiation. *Nucl. Instr. Meth. Phys. Res. B*, 325:54–65, 2014.

[45] A. Miotello, G. Cinque, P. Mazzoldi, and C.G. Pantano. Alkali-metal segregation at glass surfaces during electron-irradiation. *Phys. Rev. B*, 43:3831–3836, 1991.

[46] N. Ollier, B. Boizot, B. Reynard, D. Ghaleb, and G. Petite. Analysis of molecular oxygen formation in irradiated gkasses: a raman depth profile strudy. *J. Nucl. Mater.*, 340:209–213, 2005.

[47] N. Ollier, G. Rizza, B. Boizot, and G. Petite. Effects of temperature and flux on oxygen bubble formation in li borosilicate glass under electron beam irradiation. *J. Appl. Phys.*, 99(7):073511, April 2006.

[48] S. Peuget, V. Broudic, C. Jegou, P. Frugier, D. Roudil, X. Deschanels, H. Rabiller, and P. Y. Noel. Effect of alpha radiation on the leaching behaviour of nuclear glass. *J. Nucl. Mater.*, 362:474–479, 2007.

[49] S. Peuget, J. N. Cachia, C. Jegou, X. Deschanels, D. Roudil, V. Broudic, J. M. Delaye, and J. M. Bart. Irradiation stability of r7t7-type borosilicate glass. *J. Nucl. Mater.*, 354:1–13, 2006.

[50] S. Peuget, J. . M. Delaye, D. Ghaleb, and X. Deschanels. Technical note. Technical report, DTCD/SECM/2005/15, 2005.

[51] S. Peuget, J. M. Delaye, G. Bureau, R. Do Quang, Betremieux, C. Jegou, F. Chamssedine, T. Sauvage, T. Fares, G. Calas, G. Henderson, and X. Deschanels. Irradiation stability of r7t7-type borosilicate glass. In *Global 2009, Paris*, 2009.

[52] S. Peuget, J. M. Delaye, and C. Jegou. Specific outcomes of the research on the radiation stability of the french nuclear glass towards alpha decay accumulation. *J. Nucl. Mater.*, 444:76–91, 2014.

[53] S. Peuget, E.A. Maugeri, T. Charpentier, C. Mendoza, M. Moskura, T. Fares, O. Bouty, and C. Jegou. Comparison of radiation and quenching rate effects on the structure of a sodium borosilicate glass. *J. Non-Cryst. Solids*, 378:201–212, 2013.

[54] S. Peuget, P.Y. Noel, J.L. Loubet, S. Pavan, P. Nivet, and A. Chenet. Effects of deposited nuclear and electronic energy on the hardness of r7t7-type containment glass. *Nucl. Instrum. Methods Phys. Res. B, Beam Interact. Mater.*, 246:379–386, 2006.

[55] S. Prades, D. Bonamy, D. Dalmas, E. Bouchaud, and C. Guillot. Nano-ductile crack propagation in glasses under stress corrosion: spatiotemporal evolution of damage in the vicinity of the crack tip. *Int. J. Solids Struct.*, 42:637–645, 2005.

[56] H.M. Presby. Variation of refractive-index with wavelength in fused silica optical fibers and preforms. *Appl. Phy. Lett*, 24:422–424, 1974.

[57] W. Primak and R. Kampwirth. The radiation compaction of vitreous silica. *J. Appl. Phys.*, 39:5651, 1968.

[58] C.L. Rountree, D. Bonamy, D. Dalmas, S. Prades, R.K. Kalia, C. Guillot, and E. Bouchaud. Fracture in glass via molecular dynamics simulations and atomic force microscopy experiments. *Phys. Chem. Glasses-B*, 51:127–132, 2010.

[59] C.L. Rountree, S. Prades, D. Bonamy, E. Bouchaud, R. Kalia, and C. Guillot. A unified study of crack propagation in amorphous silica: Using experiments and simulations. *J. Allo. Compd.*, 434:60–63, 2007.

[60] I. Simon. Structure of neutron-irradiated quartz and vitreous silica. *J. Am. Ceram. Soc.*, 40:150–153, 1957.

[61] J. F. Stebbins and S. E. Ellsworth. Temperature effects on structure and dynamics in borate and borosilicate liquids: High-resolution and high-temperature nmr results. *J. Am. Ceram. Soc.*, 79:2247–2256, 1996.

[62] R. Stosser, G. Scholz, M. Nofz, T. Grande, and S. Assland. On the nature and role of fe^{3+} ions in oxide and fluoride glasses. *Ber. Bunsen-Ges. Phys. Chem.*, 100:1588–1592, 1996.

[63] K. Sun, L.M. Wang, R. C. Ewing, and W.J. Weber. Electron irradiation induced phase separation in a sodium borosilicate glass. *Nucl. Instr. Meth. Phys. Res. B*, 218:368–374, 2004.

[64] L. Vaccaro, M. Cannas, B. Boizot, and A. Parlato. Radiation induced generation of non-bridging oxygen hole center in silica: Intrinsic and extrinsic processes. *J. Non-Cryst. Solids*, 353:586–589, 2007.

[65] W. J. Weber, R. C. Ewing, C. A. Angell, G. W. Arnold, A. N. Cormack, J. M. Delaye, D. L. Griscom, L. W. Hobbs, A. Navrotsky, D. L. Price, A. M. Stoneham, and W. C. Weinberg. Radiation effects in glasses used for immobilization of high-level waste and plutonium disposition. *J. Mat. Res.*, 12:1946–1978, 1997.

[66] K.J. Yang, T.S. Wang, G.F. Zhang, H.B. Peng, L. Chen, L.M. Zhang, C.X. Li, F. Tian, and W. Yuan. Study of irradiation damage in borosilicate glass induced by he ions and electrons. *Nuclear Instruments and Methods in Physics Research B*, 307:541–544, 2013.

Chapter 2

Experimental methods dedicated to the irradiated samples

Contents

Chapter 1 presents the current knowledge of impact of irradiation on the structural and mechanical properties. Due to the glass complexity, I chose to study SBN series because they contain the three dominant oxides in R7T7 (the real glass used in France to store nuclear byproducts). This chapter details the experimental set up used to investigate irradiated glass samples. Structural, physical, and mechanical analysis techniques implement many of the same techniques presented in Part I Chapter 2. The descriptions herein concern modifications to these techniques. From the eight glasses studied in the part I, four glass compositions plus pure silica are selected and presented in section 2.1. Samples undergo one of three types of external irradiation: electron, helium or gold ions. Section 2.2 details conditions chosen for each irradiation. Structural and physical analysis techniques implement many of the same techniques presented in chapter 2 of the first part. Section 2.3 presents the other techniques that were used during my phD work to analyze the density and electronic paramagnetic response of irradiated samples and briefly reviews the Raman spectra protocols. Section 2.4 presents the mechanical response tests implement herein including SCC tests and micro-indentation tests. However, the thin layer of damage due to He^{2+} and Au^{+} irradiation requires new techniques to study this region. This chapter also addresses these techniques. A prototype is underway to overcome the limitations of SCC and is presented in this section.

2.1 Glass composition investigated

Four SBN glass samples from part I plus pure silica underwent irradiation for the tests herein. Studies herein employ glasses with low/high sodium content to highlight the role of glass composition on its response to irradiation. Table 2.1 summarizes the chemical compositions of the samples. It should be noted that SBN 14 contains (in proportion) the same amount of silicon, boron and sodium as R7T7.

Name	Target values			Measured via ICP-AES			R_{SBN}	K_{SBN}	Symbols
	SiO_2	B_2O_3	Na_2O	SiO_2	B_2O_3	Na_2O			
Silica	100	//	//	100	//	//	//	//	//
SBN 12	59.6	28.2	12.2	59.6	23.9	16.5	0.4	2.5	△
SBN 35	44	20.6	35.4	46.9	18.6	34.5	1.7	2.5	▽
SBN 14	67.8	18	14.2	70	15.8	14.2	0.7	4.4	✳
SBN 55	55.3	14.7	30	58.0	12.9	29.1	2	4.5	✡

Table 2.1: Target molar compositions and measured ICP-AES values. R_{SBN} and K_{SBN} correspond to the measured ICP-AES values. The last column remains for SBN glasses the symbols used in figures.

2.2 Conditions of irradiation

Radioactive decay and transmutation processes can lead to high energy particles being ejected from an atom along with a recoiling nucleus. When possible, conditions of irradiation are chosen to be close to reality.

2.2.1 β_{e^-}-irradiation

The β_{e^-}-irradiation employs a Van de Graaff accelerator (SIRIUS). I performed experiments with Bruno Boizot at LSI (Ecole Polytechnique, Palaiseau,France). SIRIUS bombards samples with 2.5 MeV electrons with an average current of 13 μA to prevent significant heating of the sample. Moreover, the sample temperature remains below 40°C to avoid recombination of defects. The integral doses for samples range from 0.05 to 2 GGy depending on the chemical composition.

2.2.2 He^{2+}-irradiation

He^{2+}-irradiations were done at JANNuS Saclay at CEA-Saclay, France. The energy of the He^{2+} ions is 6 MeV. This energy was selected since in the problem of nuclear storage, radioactive decay and transmutation processes yield the emission of high energy alpha particles at 5 MeV (see chapter 1). The dose is 3.8×10^{15} ions/cm^2. Again, the temperature remains below 40°C to avoid any impact of the temperature.

2.2.3 Au^{+}-irradiation

The Au^{+}-irradiation was done at JANNuS-Orsay, France with Cyril Bachelet. This irradiation employs multi-energy doses to maintain an almost constant elastic deposition on the first 3 μm from the free surface. Table 2.2 presents the energy and fluence during the Au^{+}-irradiation.

Ions	Energy (MeV)	Fluence (ions/cm^2)
Au^{+}	1	4.6×10^{13}
Au^{+}	3.5	1.4×10^{14}
Au^{+}	7	3.2×10^{14}

Table 2.2: Energy and fluences used to damage the glasses by gold irradiation.

2.3 Physical and structural investigation

2.3.1 Density measurements

The Archimedes' principle presented in previous part I, requires large samples, yet β_e^--irradiation employs small samples. Thus, the density measurements require a helium pycnometer. Moreover, density measurements only involve β_{e^-}-irradiation as the other samples are not uniformly irradiated. The density is simply the ratio of the mass of the sample (m_d) divided by the volume of the sample (V_d). The glass samples are weighted in air (m_d) at 24°C using an hydrostatic balance. Then, the pycnometer operates by Archimedes principle of gas displacement to determine the volume. In other words, the sample displaces an amount of fluid equal to its volume. A gas pycnometer measures the pressure difference between an empty sample cell and the cell including sample. The increase in pressure corresponds to the volume of gas displaced.

2.3.2 Electronic paramagnetic resonance, EPR

The EPR techniques probe and quantify paramagnetic elements. Paramagnetic effects correspond to unpaired electron. EPR measurements reveal impurities such as Fe^{3+}, Mo^{+} or Zr (even at very low concentrations, a few ppm) and defects induced by irradiation. The simplest example of EPR techniques corresponds to the case of one single unpaired electron. Applying a magnetic field to an unpaired electron with spin $s = +1/2$ invokes a splitting between the two Zeeman levels ($2s + 1 = 2$), i.e. the Zeeman Effect. The level energies are

$$E = m_s \times g \times \mu_B \times H \tag{2.1}$$

where $m_s = \pm 1/2$ is the spin quantum number, H is the magnetic field intensity, μ_B Bohr magneton and g is the Lande factor of the considered element. The energy between the two states is

$$\Delta E = g \times \mu_B \times H. \tag{2.2}$$

The existence of two Zeeman levels, and the possibility to invoke transitions from the lower energy level to the higher energy level is the essence of EPR spectroscopy. Applying an electromagnetic wave with frequency ν causes the electron in the lower state to absorbs the wave's energy ($h\nu$, where h is the Planck constant) when $\Delta E = h\nu$. This equation is the resonance condition in EPR.

Experimentally, other phenomena change the number, the shape and the intensity of the EPR transitions. It is possible to do a complete quantic description of the paramagnetic resonance:

$$\hat{H} = \mu_B \times \mathbf{g} \times \mathbf{H} \times \mathbf{S}. \tag{2.3}$$

g and **H** are tensors and **S** the spin matrix of the considered species. In the specific case of glasses, i.e. amorphous materials, the magnetic moments are randomly oriented. Thus, the EPR spectra are the sum of the transitions in all directions. In reality as compared to the simple 1 electron case, more interactions have to be taken in consideration. In EPR measurements, three types of interactions can occur:

- Hyperfine interaction: This corresponds to the interaction of the magnetic nucleus moment with the magnetic moment of its own unpaired electrons.

- Super hyperfine interaction: This corresponds to the interaction of the magnetic nucleus moment with the magnetic moment of unpaired electrons in another atom.

- Spin-spin interaction: This corresponds to the interaction between two unpaired electrons on different atoms normally within a molecule.

I have done experiments at LSI with Bruno Boizot using a MX Bruker EPR spectrometer. This equipment has a 100 kHz field modulation. Experiments utilize microwave powers of 10μ W, 1mW and 10W. The measurements take place in ambient conditions and use a fixed frequency (X band ν=9.82 GHz).

2.3.3 Raman analysis

The chapter 2 of the first part details the Raman protocols; herein is a basic review. The same experimental set-up were used for irradiated samples as pristine. Raman spectra employ a Jobin Yvon HR800 spectrometer. The laser is a YAG laser (λ=532 nm) with an adjustable output power. Experiments are in ambient conditions. Maintaining a low laser power prevents significant heating of the samples. Resulting spectra are the average of ten measurements accumulated over ten seconds.

2.4 Mechanical investigation

β_e–-irradiated samples require a slight modification for homogeneous irradiation. On the other hand, light and heavy ion irradiations do not permit uniform irradiation. Direct SCC results are not available for these samples. Hence, samples are broken in two via the regular DCDC samples presented in part I chapter 2. A new experimental protocol overcomes the limitations of the DCDC samples and propagates cracks only in the damaged region. Section 2.4.2 presents the experimental protocol. However it is still in the testing phase, so SCC results are not available for light and heavy ion irradiations.

2.4.1 β_e–-irradiation

Fracture experiments invoke DCDC samples for SCC tests of β_e–-irradiation. The conditions of β_e–-irradiation permit homogeneous irradiation though 0.8 mm of glass. Thus, DCDC sample thickness was reduced along with the other parameters. To avoid confusion the name for the β_e–-irradiated sample will be referred to as $DCDC_2$. $DCDC_2$ samples are cuboids of $2\times0.8\times25$ mm^3 with a 0.4 mm diameter hole drilled in the center as presented in figure 2.1. The samples undergo a compressive load applied normal

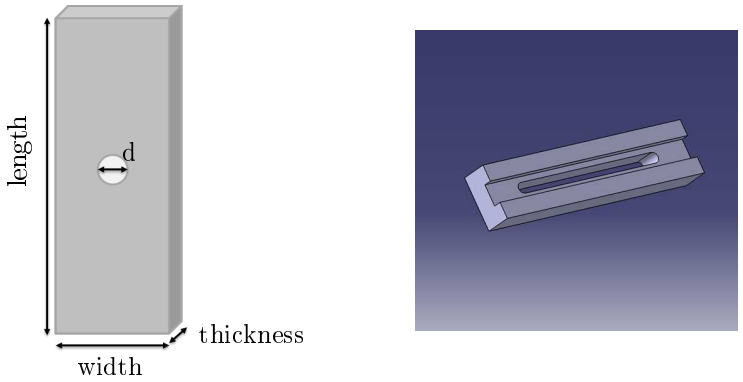

Figure 2.1: (Left) Sketch of Double Cleavage Drilled Compression samples, $DCDC_2$, used to investigate failure in stress corrosion regime in β_e–-irradiated samples. The diameter is 0.4 mm, the thickness 0.8 mm, the width 2 mm and the length 25 mm.; (Right) Drawing of the guide used to perform SCC experiments.

to the 2×0.8mm^2 surface via the Deben machine. Due to the thin thickness and to avoid buckling, a guide keeps the sample in plane. To verify that the sample geometry and the guide did not influence the SCC behavior, at least two samples of $DCDC_2$ (i.e. samples for β_e–-irradiation) and at least 3 samples of the regular $DCDC_1$ samples (i.e. samples from part I) were broken for each of the composition presented in table 2.1. Neither sample geometry nor the guide greatly influenced SCC properties. Variations result

from the uncertainties in the positioning on the sample, the location of the hole, the size of the hole, etc. Finally, the sample thickness hinders the observation of the crack path and the automatic determination of the crack tip position during propagation. This leads to an increase in the error bar. The path containing the crack is manually selected and the position of the crack front manually determined.

2.4.2 Ion irradiation

Both He^{2+}- Au^{+}-irradiation fracture tests invoke $DCDC_1$ samples as presented in part I. A drawback of this format is the bulk of the samples dominate the SCC properties. Thus, little information on SCC properties can be gained in suit.

To overcome this short coming, we developed a new experimental device with Thierry Bernard. Coupled with the AFM for imaging, the crack is initiated by Vickers indentation and then propagates in SCC in the irradiated zone [2, 3]. Figure 2.2 depicts the experimental setup. Samples are specially designed for this

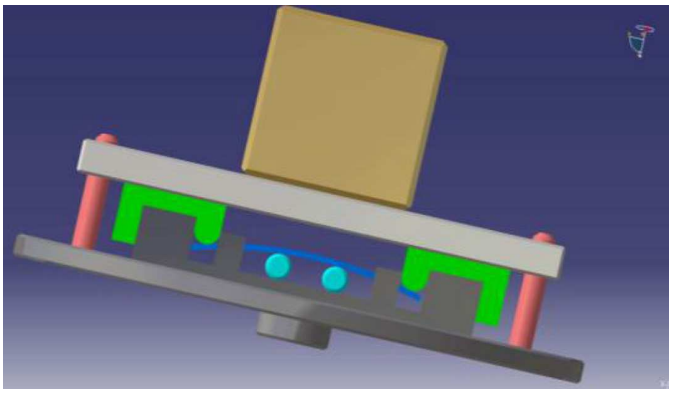

Figure 2.2: Drawing of 4-point bending experimental set-up.

apparatus. They are thin plates of size $1\times\ 2\ \times\ 40\ mm^3$. A Vickers indenter produces four perpendicular crack in the center of the $2\times40\ mm^2$ rectangular face. The sample is then loaded into a 4-point bending experimental set-up (figure 2.2). The samples positioning is such that the indentation mark is between the two cylinders (light blue) which rotate. The other two points of contact are two semi-circles shown in green. The load (brownish cube) comes from a mass uniformly distributed on the green semi-circles. The gray block and the red pillars (guides) help in equally disturbing the load. Controlling the load ensures slow crack propagation. Once upon stress, the setup becomes AFM compatible by removing the mass, the gray block, and the red pillars. Moreover, the crack front propagates in mode 1, opening mode. The AFM then images the propagation of the crack front at the nano-scale. Currently, techniques are beginning developed to extract the nanoscale stress intensity factors from AFM images ([1]).

2.4.3 Micro and nano-indentation tests

Indentation tests provide information on the material's resistance to permanent deformation induced by a harder material under stress. Part 1 chapter 2 details the micro-indentation tests which will be used for β_e−-irradiated samples herein. Recalling, subsequent AFM imaging of the indents gives way

to hardness measurements. Herein, the experiments repeat the procedures in chapter 2; however, they occur on the smaller samples ($2\times25mm^2$ faces). Surface polishing and quality are the same as in the previous part. Only β_{e^-}-irradiated samples (due to homogeneous irradiation) can take advantage micro-indentation tests. Inhomogeneous irradiated samples require nano-indentations which can probe the thin irradiated zone. Nano-indentation tests use a nanoindenter XP (MTS Nano Instruments) with a Berkovich tip. These experiments were done at Saint-Gobain Recherche with Davy Dalmas. Figure 2.3 presents a drawing of a Berkovich indenter. The control parameter is the depth of penetration rather

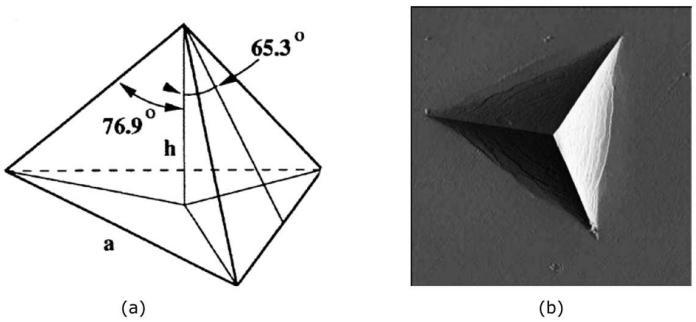

Figure 2.3: Sketch of a Berkovich indenter. Hardness values will be referenced as H_B

than the load, and the load (F) is an output of the test. The hardness, is the ratio of the load applied (F) and the imprint surface (A) in equation 2.4 :

$$H = \frac{P}{A}. \tag{2.4}$$

However, the area of the imprint changes due to a variation in the shape of the indenter. The theoretical area of the triangular based pyramid is: :

$$A = 26.43 \times h^2. \tag{2.5}$$

After indentation, AFM imaging characterizes h and the area of the indent at the surface. To distinguish measurements performed by Vickers and Berkovich indenter, we note H_V the hardness determined by Vickers indentation (only used for β_{e^-}-irradiations) and H_B the hardness from Berkovich indentation. Figure 2.4 left depicts the indentation position depending on the type of irradiation. The black crosses present the nano-indentation position. For helium irradiation, the zone impacted by irradiation is about 30 μm. Nano-indentations were done on fracture surfaces from the free surface towards the bulk with constant depth of penetration. Figure 2.4 depicts a series of these tests. Unfortunately, the layer for Au^+-irradiation was too thin (3 μm) for experiments on the fracture surface. The indentations were done on the irradiated surface.

This part presents the experimental set-up used to investigate the glasses structure and their mechanical properties after irradiation. The glass composition selected from the part I is recalled. Then condition of β_{e^-}-, He^{2+}- and Au^+-irradiations are presented. Density measurement, Raman and EPR analysis give access to the physical and the structural properties of SBN glasses after irradiation. The estimation of

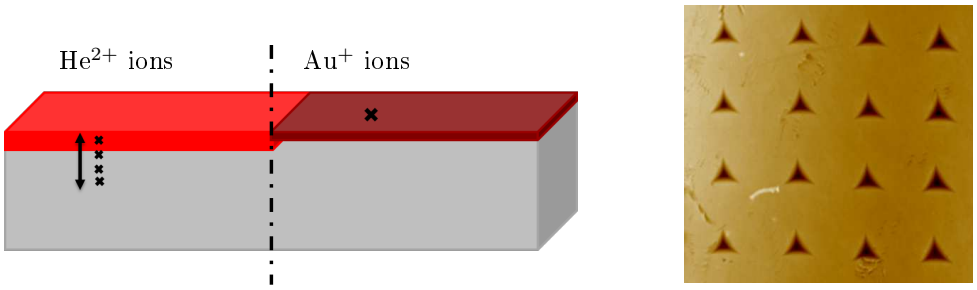

Figure 2.4: (Left) Position of nano-indentation depending on the type of irradiation; (Right) AFM images of indentation for the SBN 12 irradiated He^{2+}.

mechanical properties take place through the hardness determination, that of K_C, and the failure behavior. The three next chapters present the results on: Impact of irradiation on pure silica glasses (chapter 3) and impact of electron irradiation and ions irradiation on SBN glass composition (chapters 4 and 5, respectively).

Bibliography

[1] K. Han, M. Ciccotti, and S. Roux. Measuring nanoscale stress intensity factors with an atomic force microscope. *Europhys. Lett.*, 89:66003, 2010.

[2] S. Henaux and F. Creuzet. Crack tip morphology of slowly growing cracks in glass. *J. Am. Ceram. Soc.*, 83:415–417, 2000.

[3] J.C. Newman and I.S. Raju. Crack fronts and damage in glass at the nanometre scale. *J. Phys-Condens. Matt.*, 15:185–192, 1981.

Chapter 3

Pure silica glass: Impact of electron, light and heavy ions irradiation

Contents

The previous chapter details the experimental set-up employed to investigate the impact of irradiations on glasses. The EPR and Raman analysis give access to the structural modifications, whereas the indentation tests and failure analysis probe the mechanical properties. This chapter presents the evolution of the mechanical properties of pure amorphous silica $a-SiO_2$ *irradiated by electron* (β_{e^-})*, light ions* (He^{2+}) *and heavy ions* (Au^{+})*. Barlet et al. [4] contains the results on the structure, hardness, stress corrosion properties of pristine and* β_{e^-}*-irradiated pure amorphous silica (Corning* 7980®*) presented herein. Section 3.1 details the predictions in terms of energy deposition via electronic and nuclear interactions. Section 3.2 presents the structural variations induced by the different types of irradiations. Raman and Electronic Paramagnetic Resonance (EPR) spectra were used to record these structural variations. The last section details the variations of mechanical properties, including the hardness evolution and the stress corrosion experiments.*

3.1 Damages induced by irradiation

Irradiation can induce electronic and/or nuclear interactions depending on the conditions of irradiations (energy, fluence, ions, etc.). In order to isolate the effects of electronic and nuclear damage, we selected different particles (electron and light ions and heavy ions) to irradiate the samples. However, we chose to never use a combination of particles onto the same sample. The structural, physical, and mechanical properties are demonstrated to depend on the nature of the irradiating particles, their incident energy and the flux. This section uses programs such as ESTAR and SRIM/TRIM to estimate the stopping power of the incident particles on the glass.

3.1.1 β_{e^-} irradiation

EStar is a NIST (National Institute of Standards and Technology) program used to calculate electron stopping power and range of electrons [1]. It uses as input the type of material (chemical formula and density) and the energy of the bombarding particles (2.5 MeV). From this data, it provides: 1) the collision stopping power (average energy lost per unit length due to Coulomb collisions); 2) the radiative stopping power (average energy lost due to collisions with atoms and their electrons per unit length); and 3) the total stopping power (sum of collision and radiative stopping power).

For pure silica (EStar input: SiO_2 and 2.22 g/cm^3), figure 3.1 (EStar's output) provides an estimation of the stopping power during irradiation. For the current experiment with 2.5 MeV incidented electrons, the stopping power is about $\sim 3.55\times10^{-4}$ keV/nm. In the case of 0.8 mm thick samples, the energy is homogenously deposited throughout the whole sample.

3.1.2 Light and heavy ions: SRIM calculations

SRIM calculations [51] estimate the stopping power and range of ions [2]. It uses as input the type of target material (chemical formula and density) and the bombarding ion's mass, energy, and incident angle.

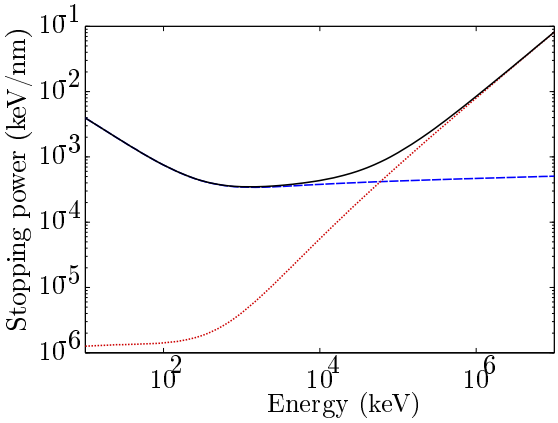

Figure 3.1: Stopping power of the electrons in pure silica (EStar input: SiO_2 and ρ=2.2g/cm^3) from ESTAR program. The lines refer to collision stopping power (dotted purple), radiative stopping power (hashed blue) and total stopping power (black line).

Helium irradiation (He^{2+})

Part II chapter 2 presents the irradiation facility and conditions for He^{2+}-irradiation. For pure silica irradiated with 6 MeV He^{2+} ions, SRIM calculations provides an estimation of the nuclear and electronic stopping power during the irradiation with the penetration of helium ions in pure silica glass (figure 3.2 left). The energy deposited mainly takes place through electronic interactions ($\sim$ 99%), which increases

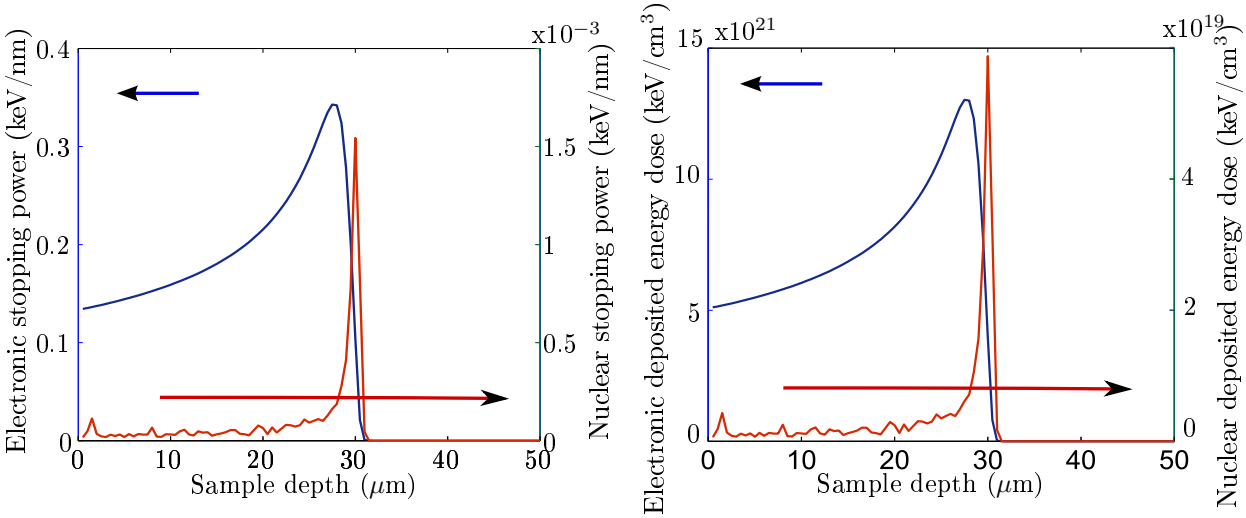

Figure 3.2: SRIM simulation for pure silica irradiated by 6 MeV helium ions at a dose of 3.8×10^{15} ions/cm^2 with the penetration depth: (Left) Electronic (blue line) and nuclear (red line) stopping power; (Right) Electronic (blue line) and nuclear (red line) deposited energy dose. The arrow towards the left and the arrow towards the right axes refer to the electronic and ballistic interactions, respectively. Electronic interactions dominate over the 30 μm into the glass sample. The nuclear interactions are maximum around 30 μm.

from the free surface (0 μm) to (30 μm). The electronic deposited energy dose is maximum ~30 μm . From the SRIM estimation, only the first 30 μm of the glass thickness will be damaged by the 6 MeV He^{2+} ions. To observe the ion track formation, (dE/dx) should be on the order of 2 to 4 keV/nm [3, 26, 27]. In these conditions, the maximum value of (dE/dx) is $\sim$ 0.34 keV/nm, which is far below the threshold value for ion track formation in pure silica. Thus, the amount of ion track formation is expected to be negligible. The right figure 3.2 presents the electronic and nuclear deposited energy doses with the irradiated depth in silica. For significant damage in silica, the nuclear energy dose should exceed 10^{20} keV/cm^3 [39]. Herein, nuclear interactions ($\sim 10^{18}$ keV/cm^3) are below the dose required. Consequently, irradiation's condition should not lead to ion tracks formation.

Gold irradiation (Au^+)

Ions	Energy (MeV)	Fluence (ions/cm^2)
Au^+	1	4.6×10^{13}
Au^+	3.5	1.4×10^{14}
Au^+	7	3.2×10^{14}

Table 3.1: Energy and fluences used to damage the glasses by gold irradiation.

Part II chapter 2 presents the irradiation facility. Au^+-irradiation uses three different energies in order to have a significant ballistic region near the surface. Table 3.1 presents the Au^+-irradiation conditions. Figure 3.3 provides the electronic and nuclear energy loss (dE/dx) with the penetration depth of Au^+ ions estimated by SRIM computations.

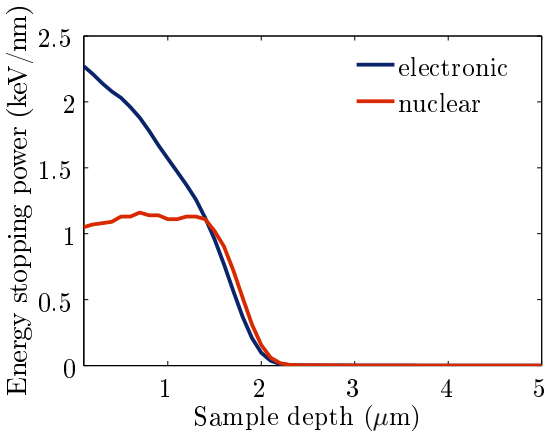

Figure 3.3: Electronic (blue line) and nuclear (red line) stopping power versus the irradiated depth for the SiO_2 glass irradiated by gold ions (Au^+) at different energy: 1, 3.5 and 7 MeV

Nearly, a homogenous nuclear energy stopping power occurs over the first layer 2 μm in the glass sample (figure 3.3). 75 % of the energy loss is due to electronic interactions [10, 11]. Energy deposited through nuclear excitation is 5×10^{20} keV/cm^3, i.e. above the dose required to damage the silica glass sample [39]. These conditions should create ions tracks formations and damage the silica glass.

Type of irradiation	E (MeV)	E_{elec} (keV/cm^3)	E_{nucl} (keV/cm^3)
He^{2+}	6	1.3×10^{22}	5.8×10^{19}
Au^{+}	1/3.5/7	5.0×10^{20}	1.7×10^{21}

Table 3.2: Irradiation conditions used: energy of incident particle (E) and deposited electronic (E_{elec}) and nuclear energies(E_{nucl}).

3.1.3 Conclusion

Table 3.2 summarizes the experimental conditions for the irradiations, and the simulation results for the stopping power. β_{e^-} and He^{2+} irradiation should not lead to significant structural changes in silica. Gold irradiation should create ion track formation and associated structural changes. β_{e^-} irradiation induces homogeneous irradiation through the glass sample. Both He^{2+} and Au^{+} irradiations remain localized within the first 30 μm and 2 μm from the specimen surface, respectively.

3.2 Structural analysis

3.2.1 β_{e^-} irradiation

EPR measurements

EPR spectra reveal the creation of paramagnetic defects in a-SiO_2 due to β_{e^-}-irradiation (figure 3.4). A null EPR signal occurs for non-irradiated silica glass (black line), and a non-zero signal for irradiated samples. Literature [20, 43] permits the interpretation of the signals. The weak signal around $g \sim 2.002$ is well known as the E' center and evidences an electron trapped at an oxygen vacancy ($\equiv Si^-$) [43]. The broad signal exists around $g \sim 2.004$-2.008 is attributed to the Non-Bridging Oxygen Hole Centers (NBOHC, $\equiv Si - O^{\cdot}$) or Peroxy Radical defects ($\equiv Si - O - O^{\cdot}$). Figure 3.4 depicts the EPR spectra of β_{e^-}-irradiated samples at microwave powers of 1 mW (left) and 1 μW (right). Modulating the microwave power highlights certain defects: the NBOHC/POR centers are better imaged at 1 mW and the E' centers are acquired at 1 μW. E' center EPR line saturates for microwave power higher than 10 μW. We can therefore conclude from the figure 3.4 that the defects produced in silica glass are mainly hole centers. The inset of figure 3.4 left zooms in on NBOHC and POR g_z components. From figures 3.4, the damage as measured from EPR spectra depend on the integrated dose.

Quantification of the defect requires a double integration of the EPR spectra after normalization. Figure 3.5 depicts the total amount of defects as a function of the dose. For the doses herein, the total amount of defects increases with the irradiation dose and does not reach a saturation point. The defects concentration does not increase linearly with integrated doses. Vaccaro et al. [42] also highlight this trend. Authors reported two growths: (1) a growth with a saturating tendency and (2) a sublinear growth. During irradiation two processes take place: *extrinsic process* linked to the rupture of OH linkage and *intrinsec process* associated to the rupture of Si-O bonds [21, 42].

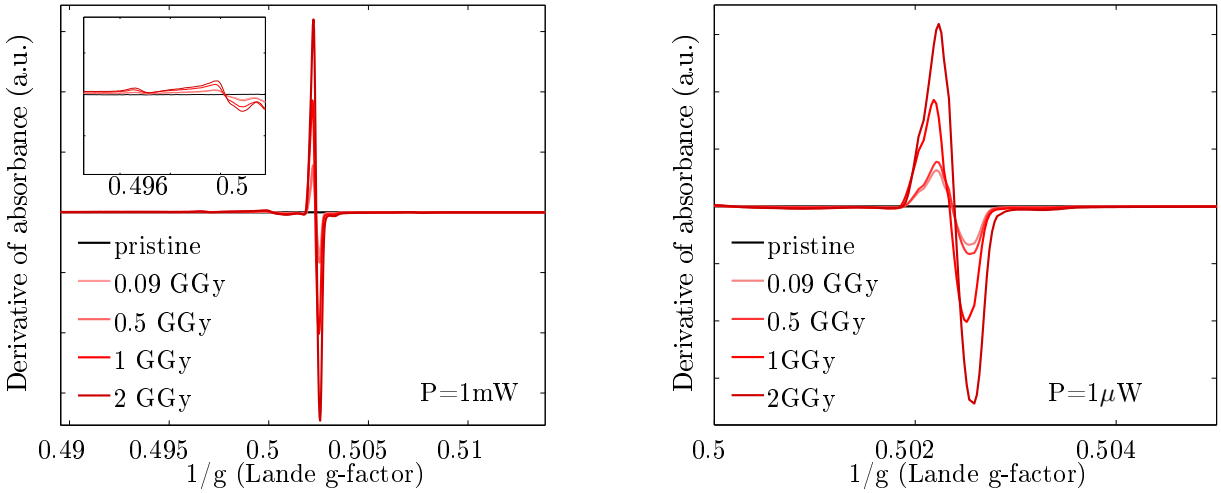

Figure 3.4: EPR spectra on Corning 7980® pristine (black line) and electron irradiated (0.09 to 2 GGy): (Left) P=1 mW, f=9.82 GHz and (Right) P=1 μW, f=9.82 GHz.

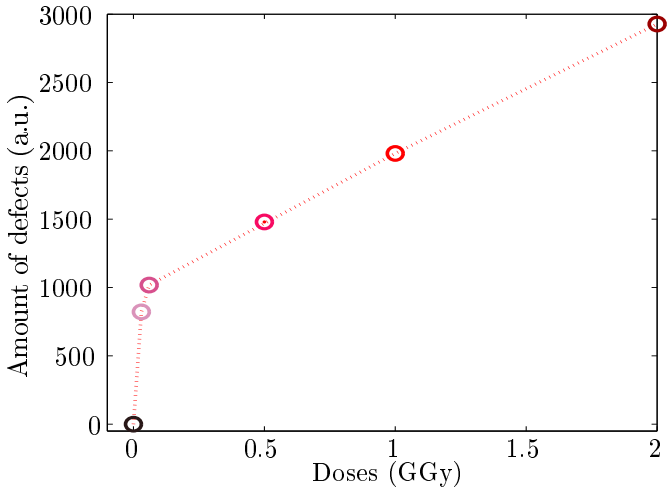

Figure 3.5: Evolution of the total defects with integrated doses (P=1 μW, f=9.82 GHz).

Raman

Figure 3.6 presents the Raman spectra for pristine and β_{e^-} irradiated samples (1 and 2 GGy) between 150 and 1650 cm^{-1}. The black line represents the Raman spectra of pristine sample. The intense broad band around 450 cm^{-1} dominates the Raman spectrum. This broad peak is associated with the bond bending vibrations of $Si-O-Si$ angle which corresponds to the five- and six- membered ring structures [18, 34]. There is generally an inverse correlation between the frequency of this band and the Si-O-Si angle in silicate glasses [30]; the width may be linked to angle distributions. The sharp bands at 490 cm^{-1} (D1) and 602 cm^{-1} (D2) correspond to the symmetric oxygen breathing vibration of the four and three membered (respectively) siloxane rings of SiO_4 tetrahedra [35]. The band at 810 cm^{-1} reflects the $Si-O$

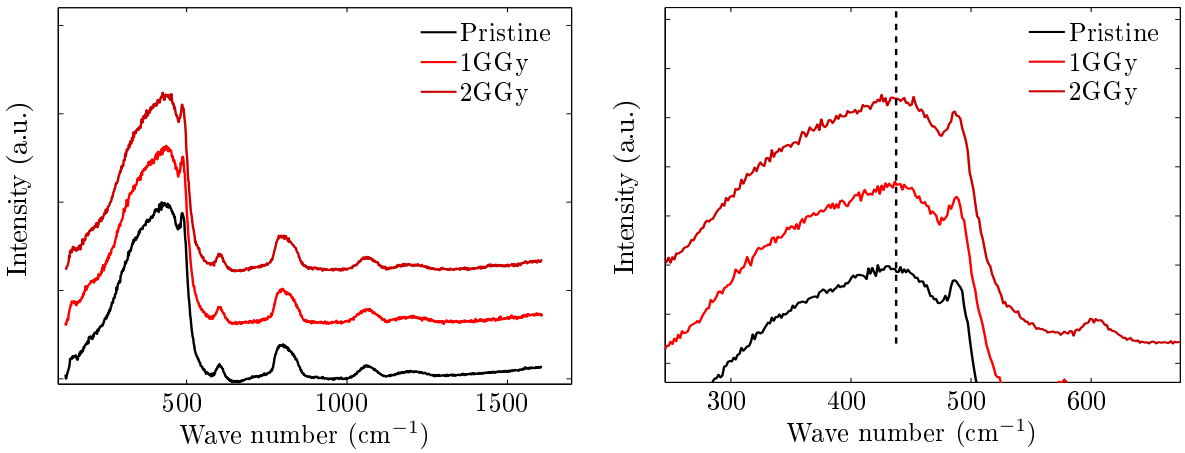

Figure 3.6: (Left) Raman spectra normalized at the highest peak of pristine and electron irradiated samples at 1 and 2 GGy. (Right) A zoom (250-700 cm^{-1}) of the Raman spectra around the highest peak in pristine and 1 and 2 GGy electron irradiated samples; (λ=532 nm).

symmetric bond stretching [32]. Weak Raman bands at 1060 cm^{-1} and 1200 cm^{-1} are attributed to asymmetric $Si-O$ stretching vibration. The region around 850-1250 cm^{-1} reveals the contribution of Si-O^{-} stretching band. This band is the Q_n band where Q_n corresponds to Si-O^{-} stretching with n bridging oxygen atoms. The position of each Q_n band is detailed in the part I in chapter 3. Finally two contributions may appear at the high wave number: (1) O_2 dissolved into the glass structure and (2)vO_2 of air [8]. No significant differences are observed in the Raman spectra between pristine and irradiated samples. Especially, no contribution of O_2 molecular is observed.

3.2.2 Light and heavy ions irradiation

Both light and heavy ions irradiations impact a thin layer near the surface of bombardment. EPR spectra cannot access this information. The Raman analysis can probe the structural evolution with the depth of penetration. Thus, this section contains information on how the structure of the glasses evolves with the ion type and the depth of penetration.

Helium irradiation

Raman analysis investigates the structure evolution with the depth of penetration. Figure 3.7 depicts Raman evolution from the free surface (0 μm) to the bulk for a He^{2+}-irradiated sample. Unlike electron irradiation, Raman spectra of helium irradiated silica evidence huge structural variations. These variations include: (1) a shift of the Si-O-Si bending vibration band to higher frequencies and a slight decrease in the FWHM (full-width half max); (2) a shift and broadening of D_1 band at 495 cm^{-1}; (3) an increase of D_2 peak at 603 cm^{-1}; and (4) an appearance of luminescence contribution. These variations concentrate between 15-35 μm.

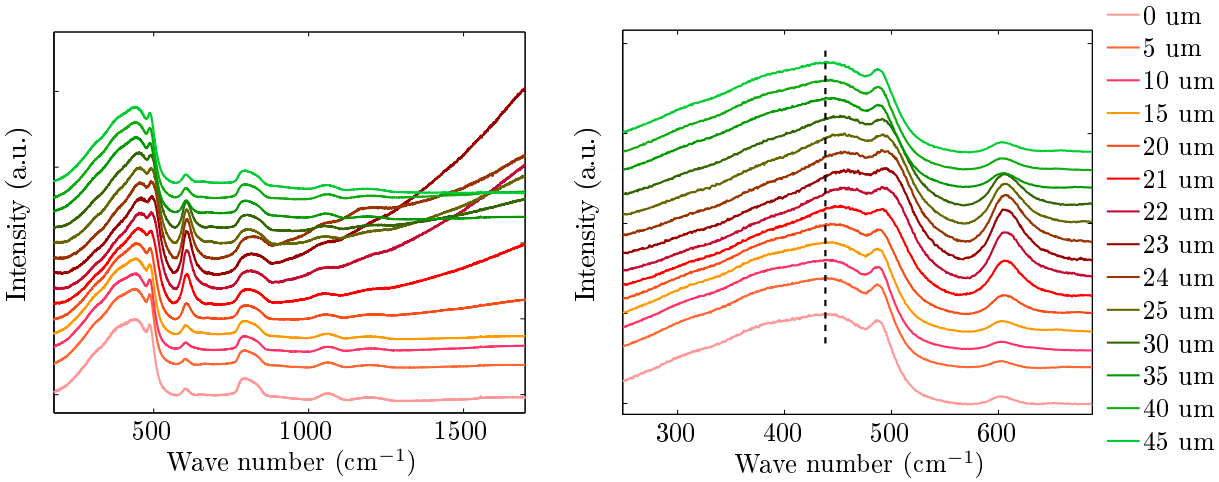

Figure 3.7: (Left) Raman spectra (normalized at the highest peak) from the glass' free surface (0 μm; bottom spectra) to the bulk (45 μm; top spectra); (Right) Zoom of the zone around 300-700 cm^{-1}. The dotted black line features the Si-O-Si position band from spectra at 45 μm(λ=532 nm).

The broad band around 450 cm^{-1} is associated with the vibrational modes of the Si-O-Si bond. The position and width of Si-O-Si band is correlated to the mean Si-O-Si angle and the angular distribution, respectively. A typical Raman response in pristine glasses corresponds to vibrational modes of five- and six- membered ring structures. Close to the free surface (0 μm) and deeper into the glass (35-40 μm) the Raman spectra resemble that of pristine silica. On the other hand, the signal shifts towards higher wave numbers between 15 and 35 μm implying smaller Si-O-Si bond angles. A decrease of the band width also occurs. This implies that (1) the mean value of the Si-O-Si bond angle get smaller and (2) the standard deviation of this angle is also reduced. In addition, the D_2 peak increases between 15 and 35 μm implying a larger number of 3-membered rings. This response is similar to what is seen in densified silica [7, 18]. The interpretation of spectra after 1000 cm^{-1} is tricky due to the luminescence contribution. The major modifications take place at the Bragg's peak (figure 3.2), i.e. where the nuclear interactions reach a maximum.

Gold irradiation

Figure 3.8 left depicts the Raman spectra from the free surface (0 μm; bottom) to the bulk for a Au^+-irradiated sample. Raman spectra of the Au^+ irradiated silica samples exhibit huge structural variations. These variations include: (1) a shift of the Si-O-Si bending vibration mode band to higher frequencies and a decrease in the FWHM; (2) a shift and broadening of the D_1 band at 495 cm^{-1}; (3) an increase of the D_2 peak at 603 cm^{-1}; and (4) a variation in the Q_n band. An increase of the O_2 molecular peak. These variations take place between 8 μm and 5 μm in depth. The Si-O-Si bending vibration mode band shifts towards higher wave numbers for depths smaller than 5 μm, which implies smaller Si-O-Si bond angles. The width of this band is also observed to decrease. This implies that both the average Si-O-Si bond angle and its standard deviation decreases. The glass densifies under gold irradiation.

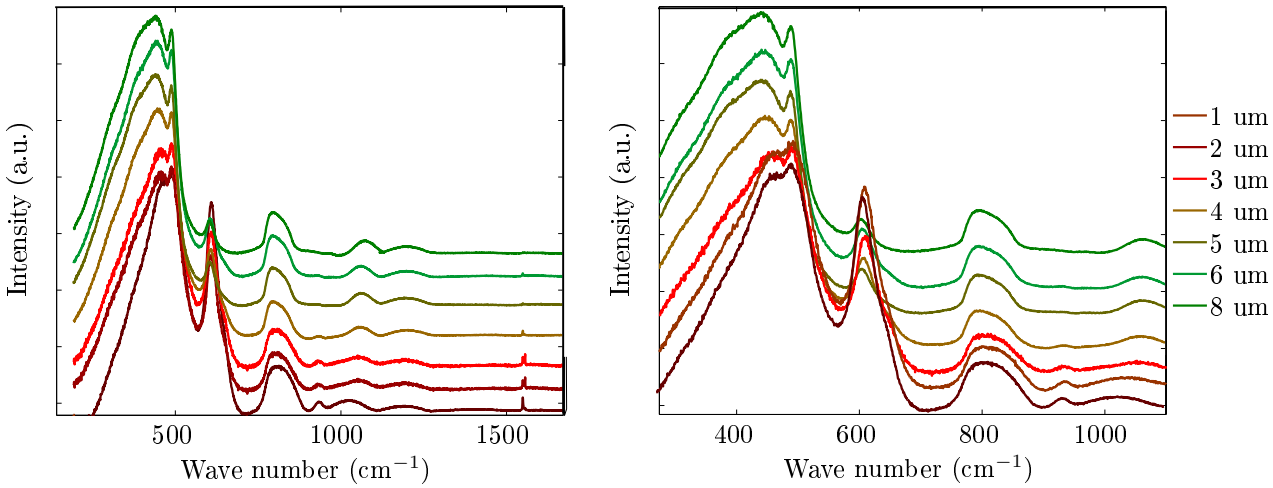

Figure 3.8: (Left) Raman spectra normalized at the highest peak from the Au^+ irradiated glass free surface (0 μm; bottom spectra) to the bulk (8 μm; top spectra); (Right) Left figure zoom of the zone around 300-1100 cm^{-1}. (λ=532 nm).

3.2.3 Conclusion

Contrary to what was observed for electronic irradiation, irradiation upon He^{2+} and Au^+ change the glass structure. Figure 3.9 depicts the evolution of Raman spectra for the pristine, electron and ions irradiated glasses. No significant variation take place for β_{e^-}-irradiation. Both He^{2+} and Au^+ ions irradiations change the glass structure and lead to a denser glass structure. Furthermore, ballistic interactions due to He^{2+} and Au^+ ion irradiation reveals similar types of structural variations.

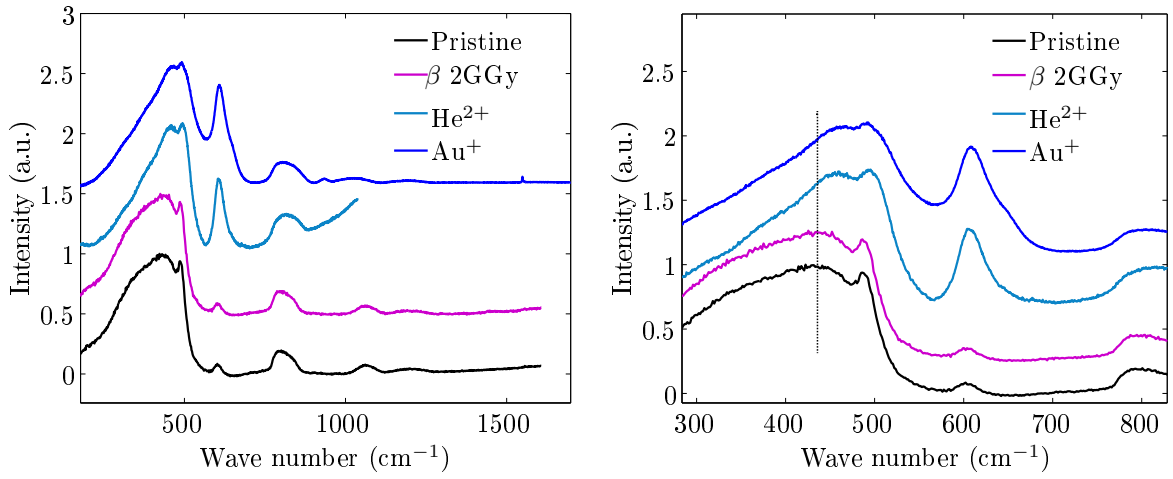

Figure 3.9: (Left) Raman spectra normalized using the highest peak for pristine (black line), electron irradiated (purple line), helium irradiation (light blue line; depth 24 μm) and gold irradiated (dark blue line; depth 2 μm); (Right) Zoom on the zone ranging from 300 to 700 cm^{-1}. For helium and gold irradiation, major modifications are observed (see text for interpretation). (λ=532 nm).

β_{e^-} irradiation

Microscale paramagnetic point defects, revealed by the EPR measurements (figure 3.4), do not scale up with the significant variations observed in the RAMAN spectra (figure 3.6). This is coherent with the literature since variations in the $Si-O-Si$ angle and ring size were only observed in samples subjected to electronic irradiations above 5 GGy [7]. Indeed, defect accumulation in pure silica during the irradiations leads to slight structural variations at a critical point. Buscarino et al. reported local densification in pure amorphous silica (a-SiO_2) depending on the electron irradiation doses [12]. The discrepancy between previous works and the work herein may be due to impurities which can moderate the effect of the electron irradiation [13]. Finally, two types of structural damage occur in silica glass: intrinsic/extrinsic processes.

Ions irradiation

Various researchers investigated the effects of ion tracks in amorphous silica [5, 22, 23, 25, 49]. Depending on the experiments [3, 26, 27], the threshold values of ions track formation range from 2 to 4 keV/nm. Considering the values of energy loss (electronic and nuclear) computed herein (see section 3.1), I do not expect ion tracks formation for the helium irradiation. Au^+ irradiation should induce ion tracks formations. After ions irradiation, major modifications take place: (1) shift of the Si-O-Si bending vibration band attributed to a decrease in the mean Si-O-Si angle [33, 38]; and (2) increase of the D_2 peak assigned to the formation of additional small rings [35]. For the two types of irradiation, the silica densifies. We can also notice the similar effects induced by the He^{2+} in the ballistic part and the Au^+-irradiation.

3.3 Mechanical analysis

3.3.1 Hardness

The part II chapter 2 presents micro- and nano-indentation techniques. Herein these techniques probe the material's resistance to external forces. For β_{e^-}-irradiation, I used micro-indentation tests to determine the hardness since the irradiation damage are uniformly distributed throughout the $a-SiO_2$ samples. For ion irradiated samples hardness tests invoked nano-indentation techniques since the irradiation damage are localized in a thin layer at the specimen surface. In this case, the hardness tests make the use of a Berkovich tip (H_B). For helium irradiated samples, the layer impacted is of ~ 30 μm. Investigation of hardness can be performed on the fracture surfaces. After gold irradiations, the layer impacted is over ~ 3 μm, thus, the indentation tests were done on the irradiated surface.

Electron

Figure 3.10 left presents the variations of hardness (H_V) as a function of the irradiation dose. There is a slight tendency for the hardness to decrease at 1.5 GGy. However, due to the large error bars and the limited number of irradiation doses, we cannot therefore make any real conclusion.

Figure 3.10 right depicts the indentation profiles in pristine and β_{e^-}-irradiated samples under high pressures. At indentation load of 50 g, the Vickers' indenter penetrates deeper in the pristine sample

than at the 1 GGy and 2 GGy-irradiated samples. Corning 7980® samples do not evidence pile-up, i.e. no volume of matter exist above the surface of the indentation (V_i^+, i.e. matter above the baseline).

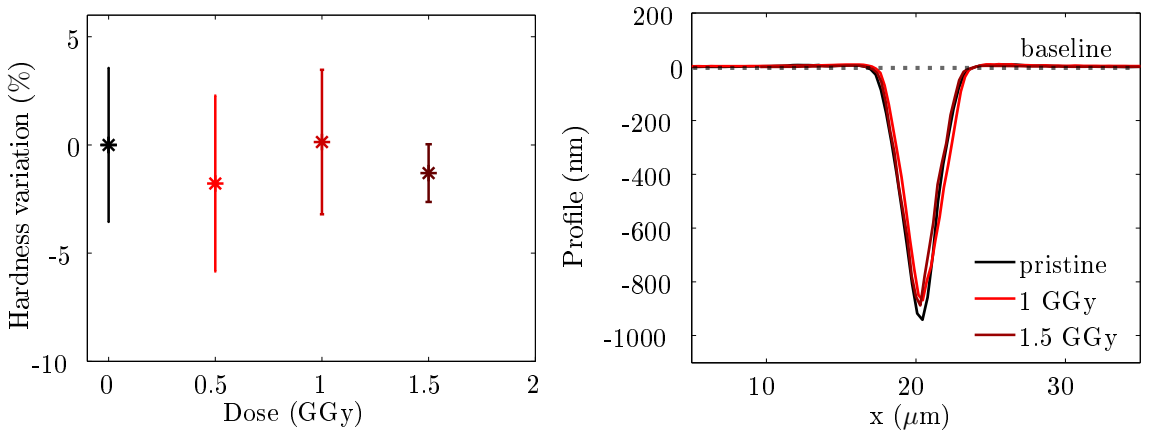

Figure 3.10: (Left) Hardness variation with the integrated doses of irradiation, (Right) AFM profiles of the indentation imprint in pristine (black line) and irradiated samples at 1 GGy (red line) 1.5 GGy (doted red line). The maximum indentation load is 50 g. The profiles are parallel to the edges of the indentation. The shown profiles result from the averaging over 5 profiles extracted from 5 different indentations. The baseline refers to the surface's level.

Ions irradiation

Nano-indentation experiments permit an evaluation of the hardness in the thin layer. Here, the indentation estimation occurs via a Berkovich indenter. H_B denotes the hardness of the Berkovich indenter. Thus this technique is excellent for ion-irradiated samples where damage concentrates near the surface. **Helium irradiation** He^{2+}-irradiated samples contain a large zone of damage (up to $\sim$ 35 μm). I performed nano-indentation measurement on the post-mortem fracture surfaces (see figure 3.11 left). This provides H_B as a function of the ion penetration depth (distance from the bombarded surface). Figure 3.11 (right) presents the depth profiles for H_B. Over the first 5-15 μm H_B value is approximately constant (within the errorbars). Then, H_B decreases with a minima occurring around $\sim$ 25 μm. Finally, above $\sim$25 μm, H_B increases again and saturates. This saturation value 9.2 GPa corresponds to the value deeper into the system , at $\sim$50 μm. This also corresponds to H_B measured in pristine silica via nano-indentation. It should be noted that the hardness over the first 5-15 μm is slightly lower than H_B determined in the bulk. **Gold irradiation** As presented in section 3.1.2, the impact of irradiation appears over the first $\sim$ 3μm of the glass sample. In this case, indentation experiments come about on the surface of ion bombardment. Figure 3.12 presents the load-displacement curves in pristine and Au^+-irradiated glasses. Table 3.3 presents H_B in pristine and Au^+-irradiated samples using the same experimental set-up. Au^+-irradiation induces a decrease H_B by $\sim$ 10%.

Discussion

Table 3.3 presents H for the different irradiations. β_{e^-}-irradiation induces minor changes in H_V. On the other hand, He^{2+} and Au^+-irradiation provoke significant changes. In the case of He^{2+}-irradiation, the

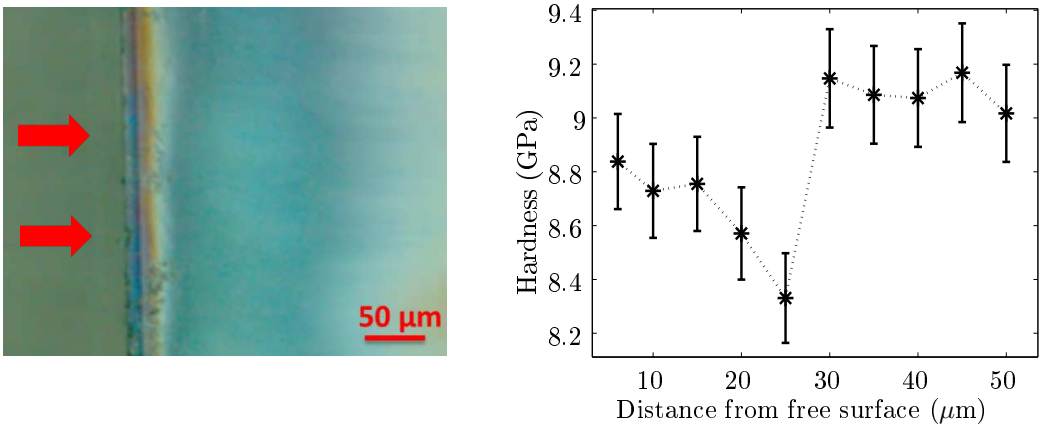

Figure 3.11: (Left) A photo of the fracture surface containing the zone irradiated by He^{2+}, the arrows show the direction of irradiation. (Right) Hardness value (in GPa) as a function of the distance from the free surface. Each point results from the averaging over 5 indents.

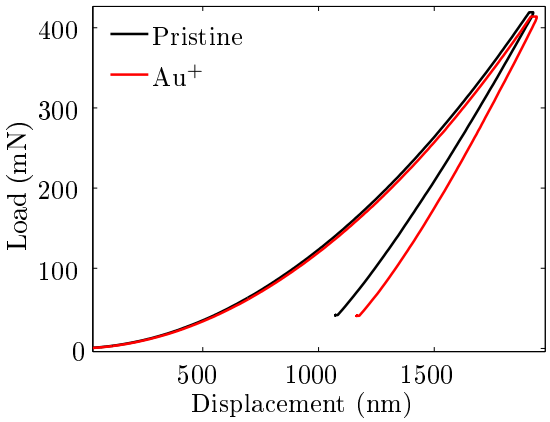

Figure 3.12: Load-displacement curves for nano-indentation performed in pristine and irradiated a$-SiO_2$.

most significant variation in H_B occurs at depths between 15 and 30 μm from the free surface. Raman analysis demonstrates densification of the silica network in this region after irradiation. The decrease in this region may be related to an increase of the weak points [6] and an increase of glass plasticity. Moreover, Devine suggested the formation of voids after irradiations; this should also lead to a decrease in hardness values. Again, the ballistic part of He^{2+} ion irradiation induces similar variation of H_B as found in Au^+ ion irradiation.

3.3.2 Fracture experiments

Mechanisms localized at the crack tip govern the stress corrosion cracking (SCC) behavior. Thus due to the high stresses at the crack tip, minute defects can play a major role in SCC. Samples and techniques used to extract SCC curves are presented in chapter 2 of the parts I and II. SCC experiments reveal v versus K_I curves for pristine and β_e--irradiated samples. v refers to the velocity of the crack front, and

Type of irradiation	$H_{pristine}$	$H_{irradiated}$	Δ (%)
Silica β_{e^-}	7.82± 0.15	7.58± 0.1	↘ 3
Silica He^{2+}	$9.14_{\pm\ 0.18}$	$8.31_{\pm\ 0.15}$	↘ 9
Silica Au^{+}	$8.55_{\pm\ 0.08}$	$7.68_{\pm\ 0.22}$	↘ 10

Table 3.3: Summary of the H values recorded in pristine and irradiated samples. Different experimental set-ups were used for each sample due to technical difficulties. Indentation on β_{e^-}-irradiation refers to Vickers indenter and includes a minor change. The hardness determined by Berkovich indenter on He^{2+}-Au^{+}-irradiated sample include more important changes in the hardness. ↘ means a decrease.

K_I refers to the external stress applied on the system. The SCC fracture surfaces reveal variations in the crack path due to irradiation. This is assembled in for all types of irradiations investigated. The RMS of the surfaces is also presented herein.

Electron

SCC curves

Figure 3.13 presents variations of the SCC curves (i.e. v vs. K_I) for pristine and β_{e^-}-irradiated (1 GGy and 2 GGy) samples. As presented in the part I.1.3.2, v in region I increases with the stress intensity factor (K_I) [19,29,46,47]. Crack propagation in pure silica occurs by the hydration (penetration of a water molecule into the glass network) and hydrolysis (breaking of the $Si-O-Si$ network bonds) [14, 40, 48]. Results in literature [37, 46, 47] do not evidence a static fatigue limit for pure silica. Moreover, pure silica experiments were done in our laboratory by S. Pradès, and also evidence a crack propagation until $v \sim\ 10^{-11}$m.s^{-1}. Data are available in [9]. Within the error bars, results herein do not evidence a static fatigue limit neither for pristine and irradiated samples.

A small shift in the position, i.e. v vs K_I, of the curve occurs. Conversely, no significant variation of the slope is observed between pristine and samples at 1 GGy and 2 GGy. Hence, due to experimental uncertainties the hypothesis that the curves are the same cannot be eliminated.

Fracture surface analysis Post-mortem fracture surfaces are the signature of the crack path during the fracture experiment. Figure 3.14 presents image of the fracture surfaces in pristine and β_{e^-}-irradiated (2 GGy) samples. The surface morphology before and after irradiation look the same, the RMS presents the roughness of these surfaces. The $\text{RMS}_{pristine}$ and $\text{RMS}_{irradiated\ 2\ GGy}$ are also similar. It appears that β_{e^-}-irradiation does not significantly impact the crack path. The glass disorder is not changed significantly after β_{e^-}-irradiation.

Irradiation by ions

The bulk region dominates SCC properties in ion irradiated samples. Thus, no information can be directly extracted on the SCC properties in the ion-irradiated zone. Statistical analysis of fracture surface can provide clues on whether or not the crack path varies (in comparison to the bulk zone) in the irradiated zone. **Fracture surface analyses,** He^{2+} A nano-mechanical atomic force microscope captures the variations in the surface topography, adhesion, and reduced modulus from the free surface (i.e. surface of bombardment) towards the bulk. Figure 3.15 presents the adhesion of the AFM tip with the fracture

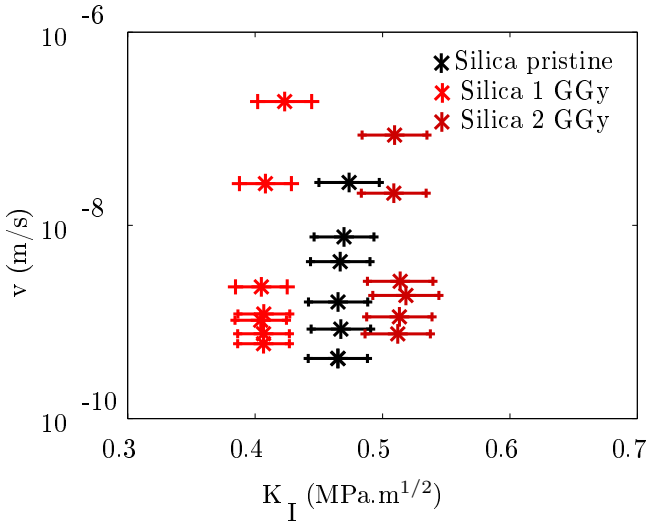

Figure 3.13: Velocity of the crack front versus the stress intensity factor (K_I) in pristine and electron irradiated Corning 7980 samples at 1 and 2 GGy. Fracture experiments are conducted at T=27^oC and H=40%.

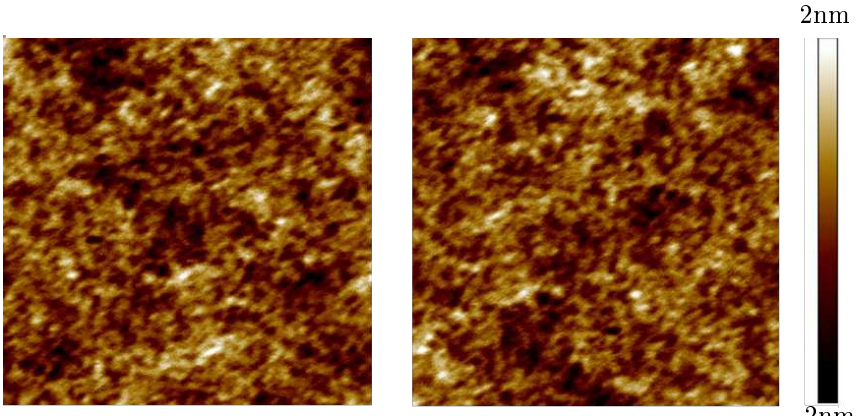

Figure 3.14: AFM images 2×2 μm of pristine (left) and 2GGy irradiated (right) silica glasses by β_{e-} fracture surfaces. Figures use the same colorbar. The RMS calculated for each image is: $0.523_{\pm 0.02}$ and $0.542_{\pm 0.01}$ for the pristine and irradiated glass, respectively

surface in the irradiated zone. The free surface of the sample is on the right, and this area corresponds to 0 μm. Between 0-15 μm from the free surface, the surface is featureless. From 15-30 μm, features as spots appear perpendicularly from the He^{2+} beamline. The size and the number of spots increase and reach a maximum at 30 μm. After this point, the features disappear. Similar patterns appear in the topographical images. Figures 3.16 left and right display height images centered at 25 μm and 5μm, respectively. Analyzing topographical images, the area close to the free surface (i.e. RMS) compares favorably with results acquired in the bulk area. Yet, morphological variations are observed between

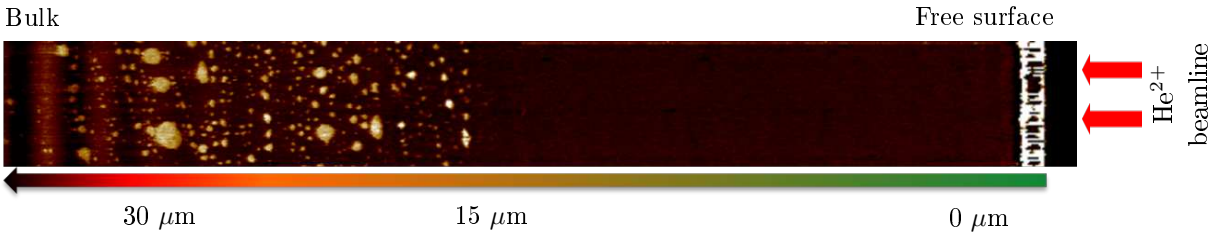

Figure 3.15: AFM image of fracture surface of silica irradiated by helium ions. The color represents variations in adhesion on the fracture surface. The mode acquisition is the PeakForce Tapping. The figure is the result of 4 images (20×20 μm^2) taken at 10, 20, 30 and 40 μm.

these two regions.

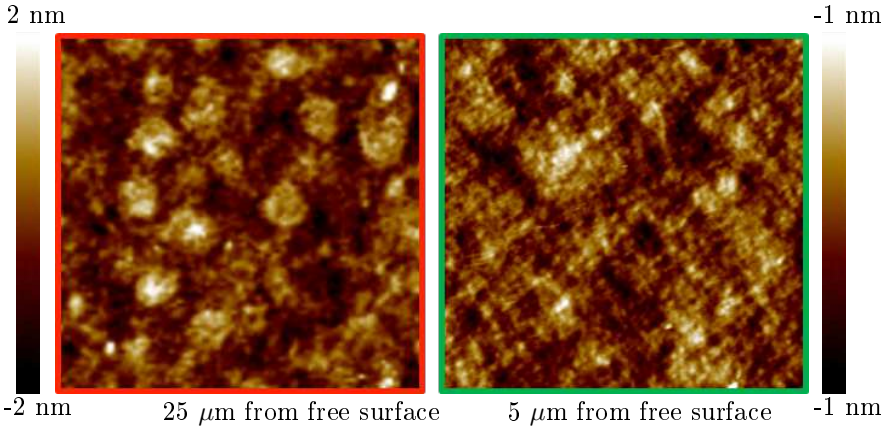

Figure 3.16: Height AFM images (5×5 μm^2) of silica surfaces. (Left) Center of the image is $\sim 25\mu$m from the free surface. Spots are present and there typical size is $\sim$ 4 nm; (Right) Center of the image $\sim 5\mu$m from the free surface.

Figure 3.17 presents the evolution of number and area of spots with the distance from the free surface. The methods I used to extract this information is provided in appendix A. From 0 to 10 μm, no significant amount of spots exist. From 10 μm to 25 μm the number and the size of spots increase up to a maximum around 25 μm. After this maximum, the number and the size of the spots decrease. The appearance of spot corresponds to the increasing nuclear interaction contributions. Furthermore they maximizes (at $\sim$ 25 μm) and fall off together.

He^{2+} ions induce a network compaction which is confined in a small zone of 20-30 μm. Several factors may be behind the formation of these spots. In particular, the densification process upon irradiation likely induces stresses due to the constraining bulk material. Thus, irradiation may also create microvoids perpendicular to the irradiation beam. The growth and coalescence of microvoids can lead to the formation of microcracks. The microcrack can join as the main crack front advance. This phenomenon may be similar to mechanisms occurring during crack front advance [17]. **Fracture surface analysis in Au^+ irradiated samples** Au^+-irradiation takes place at higher energy. Ion tracks formations are predicted to appear. Moreover, the glass structure accommodates the displacement cascades. The new structure

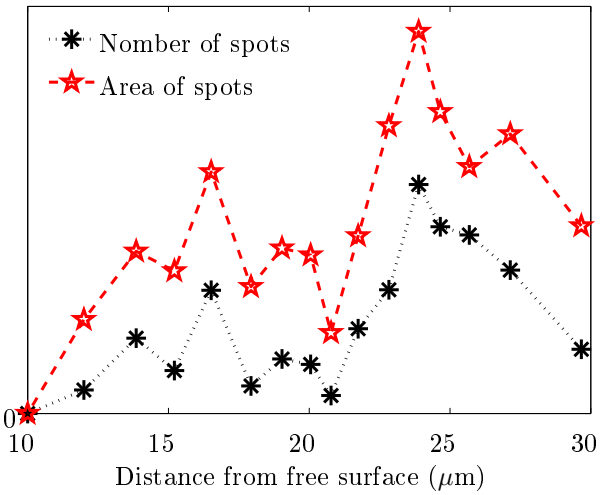

Figure 3.17: Evolution of number and area of spots with the distance to the free surface. The method employed to extract these information is detailed in appendix A.

is more disordered which explains the observed increase in the RMS (Figure 3.18).The fracture surface of pristine glass (black frame) has a RMS$\sim$ 0.5 nm, the irradiated RMS$\sim$ 1.5 nm.

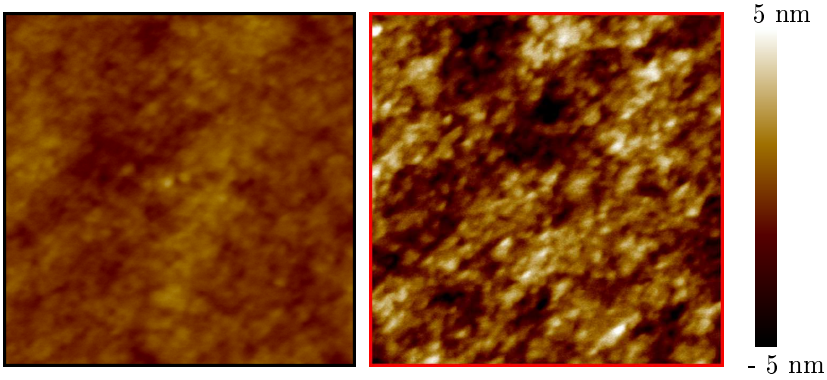

Figure 3.18: Evolution of fracture surfaces for the silica glass: (left) in the bulk (black frame) and (right) at 3 μ from the free surface (red frame). The investigation is performed on the same area by varying the distance from the free surface; thus the velocity is supposed to be equivalent. The colorbar is kept constant for the two images. A clear increase is observed.

3.3.3 Discussion

β_e^--irradiations do not induce changes in the SCC behavior neither on fracture surface. The crack path appears unaffected by electron irradiation for the doses studied herein. He^{2+}-irradiation lead to the formation of spots on the fracture surfaces after SCC experiments. This is probably linked to the creation of microvoids which join with the main crack front during experiment. The number and the size of spots increase with the nuclear energy deposited. The fracture surfaces after Au^+-irradiation do not reveal such pattern (figure 3.15 and 3.16). An explanation could be the localization of the ballistic interactions.

Au^+ irradiation changes the first few μm of the glass samples: a thin layer from the free surface towards the bulk is impacted. On the contrary, ballistic interactions concentrate around 25-30μm during helium irradiation, i.e. the impacted layer is confined by the first 20 μm from the free surface (slight damages) and the bulk. Thus the thin layer of ballistic interactions cannot relax.

3.4 Linking mechanical properties to structure variations

3.4.1 Hardness

Amorphous silica is a well-known *anomalous* glass: under stress the glass deforms mainly by densification [50]. Due to the low atomic packing density, the volume shrinkage occurs via the relative movements of the Si-O-Si linkage [16, 28, 41]. The densified area has smaller rings which form at the expense of the larger ones. This phenomenon results in shrinkage of the Si-O-Si angle distribution. Raman reveals and qualifies the densification process [36]. Recently, Kilymis et al. [24] highlight a secondary mechanism, tetrahedral rotation, which works alongside the densification by compaction.

Raman spectra of silica glasses do not change after β_e^--irradiation. Hardness investigation shows only 3% decrease (included in the errorbar).

Ions irradiation causes a $-SiO_2$ structural variations to occur in the ballistic regions. These structural variations resemble pristine silica under compression [15]. An increase of the D_2 peak (small rings) and a decrease of Si-O-Si angle occur after ion irradiation. Thus, it is assumed that irradiation induces a densified region where ballistic interactions occur. Moreover, these variations are interpreted as an increase of the glass disorder [31].

H_B decreases by 10% after light/heavy ions irradiation in the ballistic region for He^{2+}-irradiation and Au^+-irradiation. This result is coherent with Mendoza et al. [31] investigation. They found a 18% decrease in H for 74 MeV Kr ions irradiated samples. An increase of the glass plasticity (increase of NBO) should explained the hardness decrease [31].

Finally, electronic deposition by He^{2+} and β_e^--irradiation differ for the same dose (1 GGy). The former induces deposition over a few μm, whereas the latter penetrates the sample (0.8 mm). This is a possible reason for such discrepancy.

3.4.2 SCC

Despite the creation of defects, the SCC curves are only slightly altered by β_{e-}-irradiation, and a null response cannot be eliminated. More samples at the same and intermediate doses are needed to reduce the experimental uncertainties. Higher doses, near 5 GGy, are an especially interesting continuation of this work. This would aid in seeing if the SCC wobble persists or if a clear shift occurs. . Raman analyses for ion-irradiated samples do reveal variations in the Si-O-Si bond angles. But due to the thin layer impacted, no information on SCC can be extracted. Turning to simulations, West and Hench studied [44, 45], via AF1 (semiempirical quantum-mechanical-based Austin method) MO (molecular orbital) method, the impact of silica ring size on hydrolysis rate. They studied the energy barrier to hydrolysis in strained 3-fold, 4-fold; 5-fold rings. Smaller rings under strain hydrolyze at lower energies. According to West

and Hench, SCC is not governed by the hydrolysis of the bond immediately at the crack front; but rather by the arrangement of the rings in the immediate vicinity of the crack tip. As the ring rearrangement are facilitated by the open space of larger ring sizes, the energy to hydrolyze the Si-O-Si bond increases. Densification increases the amount of small rings which are easiest to hydrolyze. From West and Hench, the SCC curve's slope could increase.

3.5 Conclusion

For the doses studied herein, the structural and mechanical properties of pure silica glasses remain unchanged after β_{e^-}-irradiation. Ion-irradiation induces compaction of silica ring structure. Furthermore, variations appear to be governed by nuclear interaction.

1. **He^{2+} ions** induce major changes in the thin layer localized around 20-30 μm from the free surface. The structure and the mechanical properties change significantly (densification, decrease of H_B). The creation of microcracks which join the main crack front during experiment can explain the fracture surface pattern observed.

2. **Au^{+} ions** impact the first 3 μm of the glass sample. The damaged zone is denser and presents a lower hardness value.

Finally, impact ballistic interaction generated by He^{2+} and Au^{+} ions induce similar changes in the structural and mechanical properties of pure silica glasses.

This chapter results on the evolution of the mechanical properties of pure amorphous silica irradiation by electron, light ions (He^{2+}) and heavy ions (Au^{+}). No significant variation is visible after electron irradiation. Ions irradiation induces mainly densification of the silica network and decrease of hardness. Nuclear interactions appear to be the predominant process. The rest of the part II details impact of such irradiation on SBN glasses. The chapter 4 details the impact of β_e^--irradiation and the chapter 5 the impact of ions-irradiation.

Bibliography

[1] http://physics.nist.gov/physrefdata/star/text/estar.html.

[2] http://www.srim.org/.

[3] W.M. Arnoldbik, N. Tomozeiu, and F.H.P.M. Habraken. Electronic sputtering of thin SiO_2 films by mev heavy ions. *Nucl. Instr. Meth. Phys. Res. B*, 203:151–157, 2003.

[4] M. Barlet, J-.M Delaye, M. Gennisson, R. Caraballo, B. Boizot, D Bonamy, and C. L. Rountree. Influence of electronic irradiation on failure and hardness properties of pure silica glasses. *Proc. Mat. Sci.*, submitted, 2014.

[5] A. Benyagoub, S. Loffler, M. Rammensce, and G. Klaumunzer, S. Saecmann-Ischenko. Plastic deformation in SiO_2 induced by heavy-ion irradiation. *Nucl. Instr. Meth. Phys. Res. B*, 65:228–231, 1992.

[6] N. Bibent, A. Faivre, G. Ferru, J.L. Bantignies, and S. Peuget. Silica structural changes induced by thermal treatment or ionic implantation as probed by ir reflectance spectroscopy. *J. Appl. Phys.*, 106:063512, 2009.

[7] B. Boizot, S. Agnello, B. Reynard, R. Boscaino, and G. Petite. Raman spectroscopy study of beta-irradiated silica glass. *J. Non-Cryst. Solids*, 325:22–28, 2003.

[8] B. Boizot, G. Petite, D. Ghaleb, B. Reynard, and G. Calas. Raman study of beta-irradiated glasses. *J. Non-Cryst. Solids*, 243:268–272, 1999.

[9] D. Bonamy, S. Prades, C. L. Rountree, L. Ponson, D. Dalmas, E. Bouchaud, K. Ravi-Chandar, and C. Guillot. Nanoscale damage during fracture in silica glass. *Int. J. Fracture*, 140(1-4):3–14, JUL 2006.

[10] J Bonfils de. *Effets d'irradiations sur la structure de verres borosilicates-Comportement a long terme des matrices vitreuses de stockage des dechets nucleaires.* PhD thesis, Université Claude Bernard - Lyon I, 2007.

[11] J Bonfils de, S. Peuget, G. Panczer, D Ligny de, S Henry, P. Y. Noel, A. Chenet, and B. Champagnon. Effect of chemical composition on borosilicate glass behavior under irradiation. *J. Non-Cryst. Solids*, 356:388–393, 2010.

[12] G. Buscarino, S. Agnello, and F. M. Gelardi. Structural modifications induced by electron irradiation in sio2 glass: Local densification measurements. *Europhys. Lett.*, 87:26007, 2009.

[13] G. Buscarino, S. Agnello, F. M. Gelardi, and R. Boscaino. The trole of impurities in the irradiation unduced densification of amorphous sio2. *Journal of physics condensed matter*, 22:255403, 2010.

[14] M. Ciccotti. Stress-corrosion mechanisms in silicate glasses. *J. Phys.D.*, 42(21):214006, November 2009.

[15] R.A.B. Devine. Macroscopic and microscopic effects of radiation in amorphous sio2. *Nucl. Instr. Meth. Phys. Res. B*, 91:378–390, 1994.

[16] F.M. Ernsberg. Role of densification in deformation of glasses under point loading. *J. Am. Ceram. Soc*, 51:545–547, 1968.

[17] X.-Q. Feng and Y. Huang. Mechanics of smart-cut® technology. *Int. J. Solids Struct.*, 41:4299–4320, 2004.

[18] F. L. Galeener and A. E. Geissberger. Vibrational dynamics in si30-substituted vitreous SiO_2. *Phys. Rev. B*, 27:6199–6204, 1983.

[19] E. Gehrke, Ch. Ullner, and M. Hahnert. Fatigue limit and crackarrest in alkali-containing silicate glasse. *J. Matter. Sci.*, 26:5445–5455, 1991.

[20] D.L. Griscom. Trapped-electron centers in pure and doped glassy silica : A review and synthesis. *J. Non-Cryst. Solids*, 357:1945–1962, 2011.

[21] H. Imai and H. Hirashima. Intrinsic- and extrinsic-defect formation in silica glasses by radiation. *J. Non-Cryst. Solids*, 179:202–213, 1994.

[22] J. Jensen, A. Razpet, and G. Skupinski, M.and Possnert. track formation below 1 mev/u in thin films of amorphous SiO_2. *Nucl. Instr. Meth. Phys. Res. B*, 243:119–126, 2006.

[23] J. Jensen, A. Razpet, M. Skupinski, and G. Possnert. Ion tracks in amorphous SiO_2 irradiated with low and high energy heavy ions. *Nucl. Instr. Meth. Phys. Res. B*, 245:269–273, 2006.

[24] D. A. Kilymis and J. . M. Delaye. Nanoindentation of pristine and disordered silica: Molecular dynamics simulations. *J. Non-Cryst. Solids*, 382:87–94, 2013.

[25] S. Klaumunzer. Ion tracks in quartz and vitreous silica. *Nucl. Instr. Meth. Phys. Res. B*, 225:136–153, 2004.

[26] S. Klaumunzer, C. Li, S. Loffler, M. Rammensee, and G. Schumacher. Plastic flow of vitreous silica and pyrex during bombardment with fast heavy ions. *Nucl. Instr. Meth. Phys. Res. B*, 39:665–669, 1989.

[27] P. Kluth, C.S. Schnohr, O.H. Pakarinen, F. Djurabekova, D.J. Sprouster, R. Giulian, M.C. Ridgway, A.P. Byrne, C. Trautmann, D.J. Cookson, K. Nordlund, and M. Toulemonde. Fine structure in swift heavy ion tracks in amorphous SiO_2. *Phys. Rev. Lett.*, 101:175503, 2008.

[28] J.D. Mackenzie. High-pressure effects on oxide glasses. 1. densification in rigid state. *J. Am. Ceram. Soc.*, 46:461–470, 1963.

[29] D. Maugis. Review : Subcritical crack growth, surface energy, fracture toughness, stick-slip and embrittlement. *J. Mater Sci.*, 20:3041–3073, 1985.

[30] P. McMillan. Structural studies of silicate glasses and melts-applications and limitations of raman spectroscopy. *Am. Miner.*, 69:622–644, 1984.

[31] C. Mendoza, S. Peuget, T. Charpentier, M. Moskura, R. Caraballo, O. Bouty, A.H. Mir, I. Monnet, C. Grygiel, and C. Jegou. Oxide glass structure evolution under shift heavy ion irradiation. *Nucl. Instr. Meth. Phys. Res. B*, 325:54–65, 2014.

[32] B.O. Mysen. *Structure, properties of silicate melts.* Elsevier, 1988.

[33] B.O. Mysen and J.D. Frantz. Silicate melts at magmatic temperatures- in-situ structure determination to 1651-degrees-c and effect of temperature and bulk composition on the mixing behavior of structural units. *Contrib. Mineral. Petrol.*, 117:1–14, 1994.

[34] M. Okuno, B. Reynard, Y. Syono, and C. Willaime. A raman spectroscopic study of shock-wave densification of vitreous silica. *Phys. Chem. Miner.*, 26:304–311, 1999.

[35] AL Pasquarello and R. Car. Identification of raman defect lines as signature of ting structure in vitreous silica. *Appl. Phy. Lett*, 80:5145, 1998.

[36] A. Perriot, D Vandembroucq, E. Barthel, V. Martinez, L. Grosvalet, C. Martinet, and B. Champagnon. Raman microspectroscopic characterization of amorphous silica plastic behavior. *J. Am. Ceram. Soc*, 89:596–601, 2006.

[37] S. Prades, D. Bonamy, D. Dalmas, E. Bouchaud, and C. Guillot. Nano-ductile crack propagation in glasses under stress corrosion: spatiotemporal evolution of damage in the vicinity of the crack tip. *Int. J. Solids Struct.*, 42:637–645, 2005.

[38] S.K. Sharma, J.F. Mammone, and M.F. Nicol. Raman investifation of ring configuration in vitreous silica. *Nature*, 292:140–141, 1981.

[39] E. Snoeks, T. Weber, A. Cacciato, and A. Polman. Mev ion irradiation induced creation and relaxation of mechanical stress in silica. *J. Appl. Phys.*, 78:4723–4732, 1995.

[40] M. Tomozawa. Fracture of glasses. *Ann. Rev. Mater. Sci.*, 26:43–74, 1996.

[41] D.R. Uhlmann. Densification of alkali silicate glasses at high pressure. *J. Non-Cryst. Solids*, 13:89–99, 1973.

[42] L. Vaccaro, M. Cannas, B. Boizot, and A. Parlato. Radiation induced generation of non-bridging oxygen hole center in silica: Intrinsic and extrinsic processes. *J. Non-Cryst. Solids*, 353:586–589, 2007.

[43] R.A. Weeks. Paramagnetic resonance of lattice defects in irradiated quartz. *J. Appl. Phys.*, 27:1376–1381, 1956.

[44] J.K. West and L.L. Hench. Silica fracture: Part ii a ring opening model via hydrolysis. *J. Mater. Sci.*, 29:5808–5816, 1994.

[45] J.K. West and L.L. Hench. The effect of environment on silica fracture: vaccum, carbon monoxide, water and nitrogen. *Philos. Mag. A*, 77:85–113, 1998.

[46] S.M. Wiederhorn. Influence of water vapor on crack propagation in soda-lime glass. *Am. Ceram. Soc. Bull.*, 50:407–414, 1967.

[47] S.M. Wiederhorn and L.H. Bolz. Stress corrosion and static fatigue of glass. *J. Am. Ceram. Soc*, 53:543–548, 1970.

[48] S.M. Wiederhorn, S.W. Freiman, E.R. Fuller, and C.J. Simmons. Effects of water and other dielectrics on crack-growth. *J. Matter. Sci.*, 12:3460–3478, 1982.

[49] T. Yang, Y Gao, X. Huang, Y. Zhang, M. Toulemonde, J. Xue, S. Yan, and Y. Wang. The transformation balance between two types of structural defects in silica glass in ion-irradiation processes. *J. Non-Cryst. Solids*, 357:3245–3250, 2011.

[50] S. Yoshida, J.-C. Sangleboeuf, and T. Rouxel. Quantitative evaluation of indentation-induced densification in glass. *J. Mat. Res.*, 20:3404–3412, 2005.

[51] F. Ziegler, J.P. Biersack, and U. Littmark. *The stopping and range of ions in matter*. Pergamin Press, 1985.

Chapter 4

SBN glass: Impact of electron irradiation on glass structure and mechanical properties

Contents

This chapter presents the evolution of the SBN glass structure after electron (β_{e^-}) irradiation. Studies herein use four of the eight glasses from part I: SBN 12, SBN 14, SBN 35 and SBN 55. Section 4.1 details the irradiation conditions and estimates the energy loss through electronic processes for each glass composition. Section 4.2 presents the structural variation induced by β_{e^-}-irradiation as observed through EPR and Raman measurements. Then, section 4.3 details the consequences of irradiation on the mechanical properties trhough hardness and stress corrosion experiments.

4.1 Damages induced by β_{e^-} irradiation

ESTar program [1] investigates damage induced by β_{e^-}-irradiation. It is feasible to estimate the electron stopping power knowing the type of material (chemical formula and density; table 4.1) and the electron's energy [1]. For an energy of 2.5 MeV, Figure 4.1 presents the collision stopping power, the radiative stopping power, and the total stopping power for SBN 14.Table 4.1 summarizes the stopping powers for SBN 12, SBN 14, SBN 35 and SBN 55. For all the samples, we expect an homogeneous deposition of the energy, approximately the same in all the samples irrespectively of the composition.

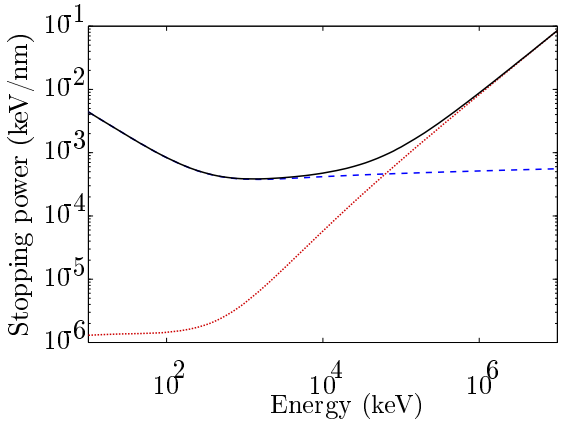

Figure 4.1: Electron stopping power for SBN 14 glasses calculated from the ESTar program [1]. The dotted lines refer to collision stopping power (purple), the hashed line to the radiative stopping power (blue) and the black line to the total stopping power. The total stopping powers are given in table 4.1.

Name	Real chemical composition			R_{SBN}	K_{SBN}	ρ_{exp} (keV/cm)	Stopping power $\times 10^{-4}$	Symbols
	SiO_2	B_2O_3	Na_2O					
SBN 12	59.6	28.3	12.2	0.45	2.5	$2.4619_{\pm 0.0003}$	3.93	△
SBN 14	70.0	15.8	14.2	0.89	4.4	$2.4736_{\pm 0.0003}$	3.95	✳
SBN 35	46.9	18.6	34.5	1.85	2.5	$2.5368_{\pm 0.0001}$	4	▽
SBN 55	58.0	14.7	30	1.91	4.5	$2.5383_{\pm 0.0004}$	4.04	✡

Table 4.1: Various glass parameters presented in chapter 2 summarized here along with the total stopping power of each glass calculated from the ESTAR program. The last column recalls the symbols used in plots.

4.2 Evolution of physical and structural properties of SBN glasses

4.2.1 Density variations induced by β_{e^-}

The helium pycnometer techniques (presented in chapter II.2) provide an estimate of the SBN 12 and SBN 14 density prior to and after irradiation[2]. Table 4.2 presents the variation between ρ (pristine sample's density) and ρ_{e^-} (β_{e^-}-irradiated sample density). The SBN 14 sample swells after irradiation by ~ 1.6 %. A slight amount of swelling appears for the SBN 12 sample, but it is within the error bar. Thus, a null response cannot be eliminated for the SBN 12 sample.

Name	Density variation (%)
SBN 12	$\searrow 0.05_{\pm 0.06}$
SBN 14	$\searrow 1.6_{\pm 0.08}$

Table 4.2: Density variation measured via helium pycnometer techniques for SBN 12 and SBN 14 glasses. $\searrow$ implies a decrease in ρ or equivalently a swelling in the glass.

4.2.2 Structural variations induced by β_{e^-}-irradiation

This section investigates the consequences of the β_{e^-}-irradiation on the glass structure. First, Electron Paramagnetic Response (EPR) measurements qualify and quantify the paramagnetic defects induced. Then, Raman analysis aids in the understanding how the small scale paramagnetic defects scale up to larger scale variations in the glass structure.

EPR investigation

EPR spectra reveal and quantify the creation of paramagnetic defects. Before irradiation, pristine SBN glasses reveal a non-zero EPR response. EPR measurements highlight small impurities in the glasses such as Fe^{3+} and/or Zr^{4+} (figure 4.2). For example, a signal outside of the noise exists at g ~ 4.3. This corresponds to Fe^{3+} ion [33]. MEB-EDS results reveal low quantities (a few ppm) of these impurities. The source for such impurities likely arises from the contamination during elaboration (for example, crucibles are reused from previous melts). Literature details the impact of such elements in the defect creation process literature [11,17,28]. Hopping process can take place depending on the concentration of impurities: blockage of defects creation occurs under β_{e^-}-irradiation when glasses have more than 1 wt% of Fe_2O_3 [28]. Impact creation defects should not be affected herein as the concentration of impurities is low. Figures 4.3 and 4.4 elucidate β_{e^-}-irradiation induced paramagnetic defects. Literature postulates various types of paramagnetic defects relevant herein: (1) BOHC (Boron oxygen hole centers) defects - unpaired electrons on oxygen atoms with a boron atom in the vicinity [14, 21, 22, 34], (2) HC_1 and HC_2 defects, hole centers near alkaline ions [5, 6, 18, 23], (3) Oxy, oxygen hole center, (4) SHC_1 and SHC_2, silicon hole centers and (5) E' centers. Table 4.3 details the theoretical g-values. EPR spectra of the SBN glasses exhibit two shapes: (1) the *five-plus-shoulder* for SBN 12 and SBN 14 glasses; and (2) the *four-plus-shoulder* observed for SBN 35 and SBN 55 glasses (Figure 4.5). Literature already mentions these two shapes for low and high alkali content [3]. Baccaro et al. suggest that, the change in boron

[2]Due to limited access to the Helium pycnometer the densities of SBN 55 and SBN 35 were not measured.

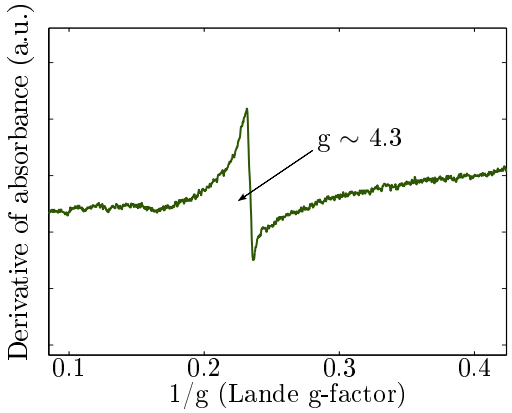

Figure 4.2: EPR spectra of SBN 14 before irradiation P=10 mW, f=9.82 GHz. The resonance of Fe^{3+} appear at g $\sim$ 4.3.

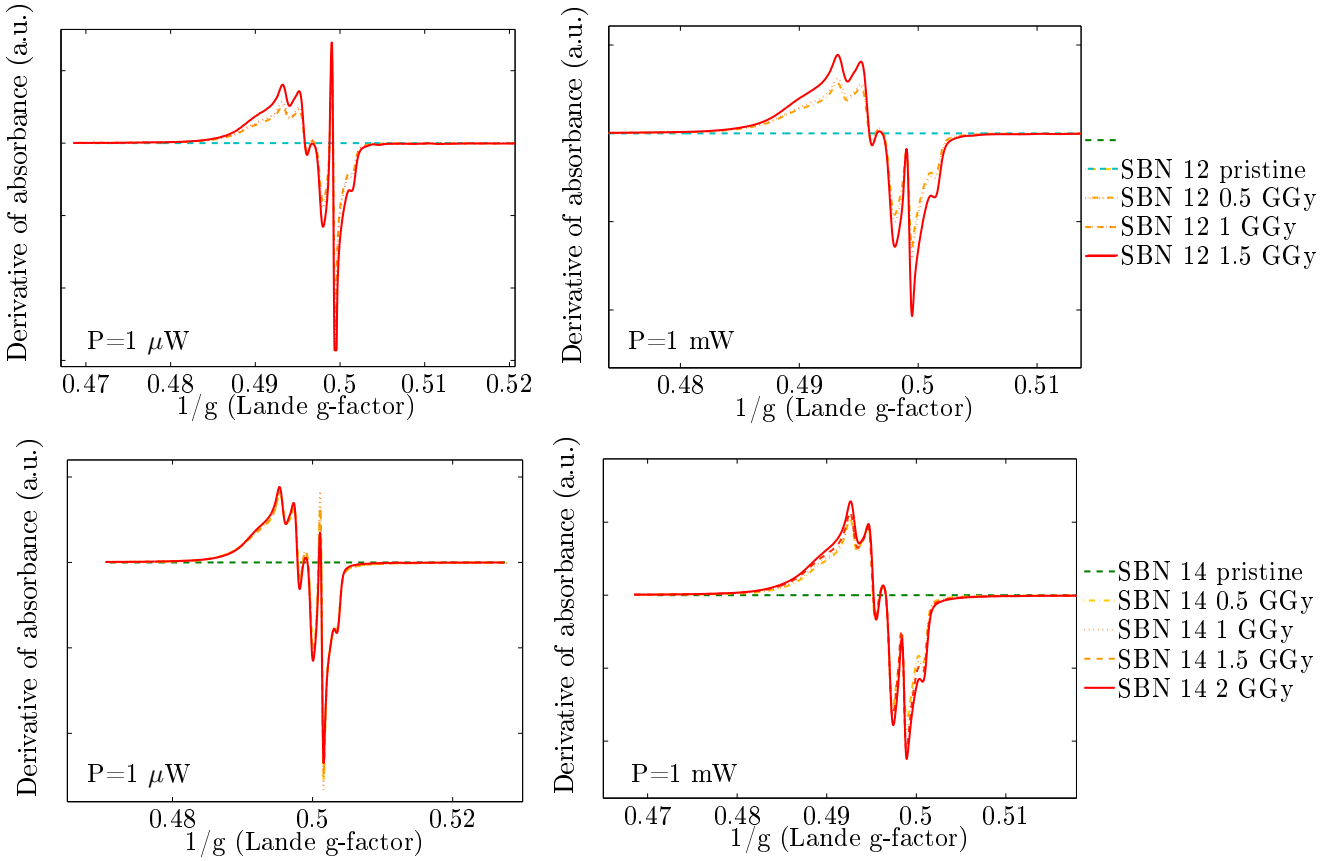

Figure 4.3: EPR spectra of SBN glasses: SBN 12, SBN 14. Two different powers were used to characterize the hole and electron trapped: (Left) P=10 μW, f=9.82 GHz and (Right) P=1 mW, f=9.82 GHz.

environment due to alkali content transforms the five-peak into a four-peak signal [3]. Figure 4.5 presents comparisons between SBN glasses with low and high alkali content for K $\sim$ constant.

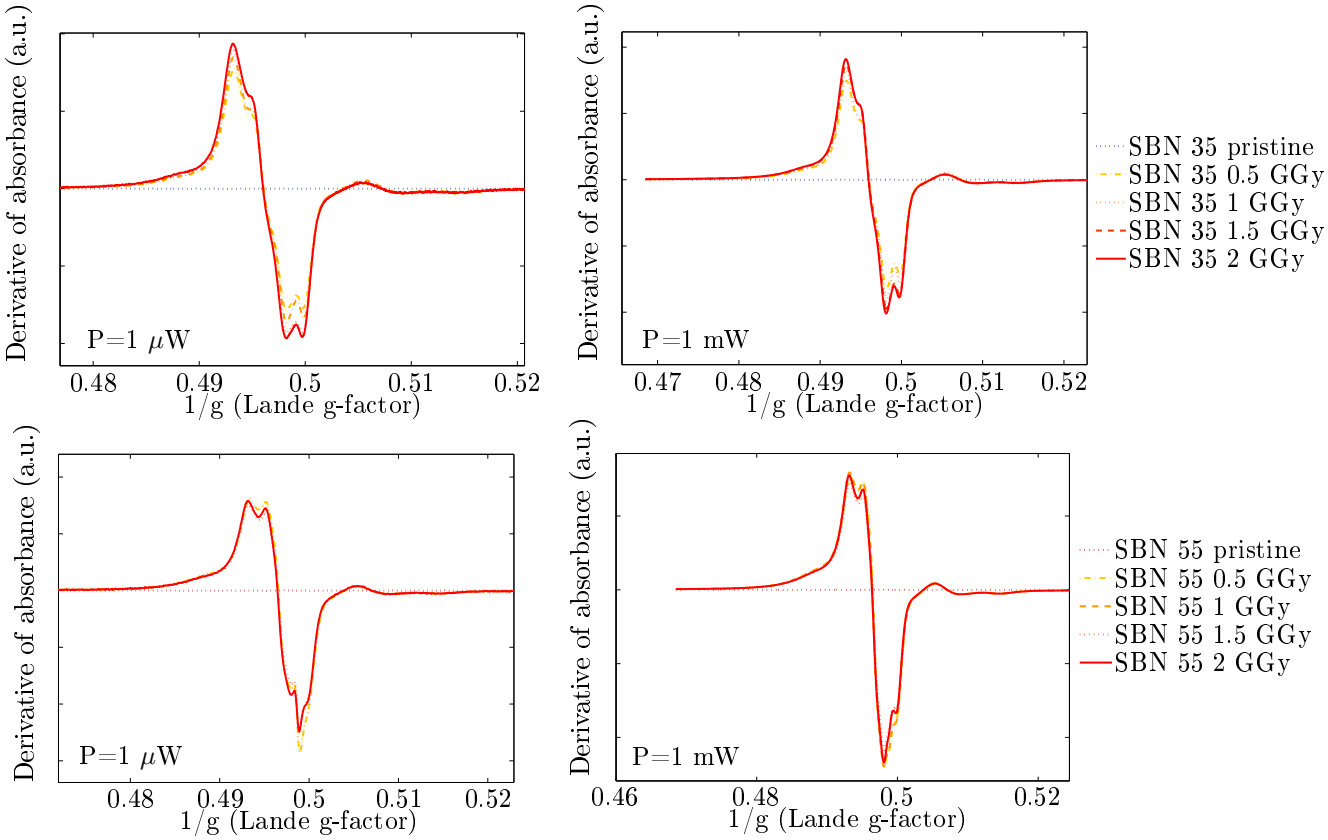

Figure 4.4: EPR spectra of SBN glasses: SBN 35 and SBN 55. Different powers were used to investigate electron holes and electron trapping: (Left) P=10 μW, f=9.82 GHz and (Right) P=1 mW, f=9.82 GHz.

Defects	g_x	g_y	g_z	Ref
BOHC	2.0029	2.0115	2.05	[6, 14, 21, 22]
Oxy	2.0024	2.0110	2.0439	[6]
SHC_1	2.0026	2.0093	2.049	[15, 16]
SHC_2	2.0054	2.0073	2.012	[15, 16]
HC_1	2.0026	2.0088	2.0213	[18]
HC_2	2.0118	2.0127	2.0183	[18]
E'	2.0011	2.0011	2.0011	[18]

Table 4.3: Theoretical g-values of paramagnetic defects expected from literature in SBN glasses after β_e–-irradiation.

Literature extensively details the structure of BOHC defects [20–22,29,32]. Kordas [20–22] postulate the existence of several BOHC centers which different g-values. For low sodium content (SBN 12 and SBN 14), the $BOHC_1$ signal (non-bridging oxygen attached to 3-coordinated boron [22]) dominates the spectra. Increasing the amount of sodium (e.g. SBN 35 and SBN 55) probably employs other BOHC defects. Moreover, increasing the $[Na_2O]$ concentration inhibits the formation of the E' centers ($\equiv Si^{-}$; [7]).

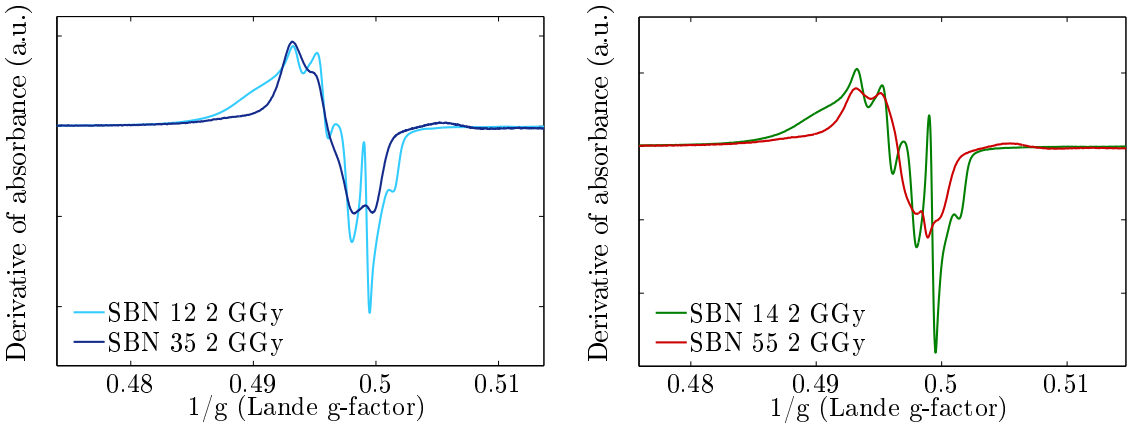

Figure 4.5: This figure compares the EPR spectra of SBN glasses: (Left) SBN 12 (light blue; low sodium content) and SBN 35 (dark blue; high sodium content); K $\sim$ 2.5; and (Right) SBN 14 (green; low sodium content) and SBN 55 (dark red; high sodium content); K $\sim$ 4.5. All spectra are recorded at P=10 μW, f=9.82 GHz. The intensity of spectra does not correspond to the real intensity.

Defects	g_x	g_y	g_z
$BOHC_1$	2.0020	2.0103	2.035
$BOHC_2$	2.0049	2.0092	2.0250
$BOHC_{1c}$	2.0000	2.0107	2.0415
$BOHC_{1a}$	2.0025	2.0118	2.037

Table 4.4: g theorical values of BOHC paramagnetic defects from [21]

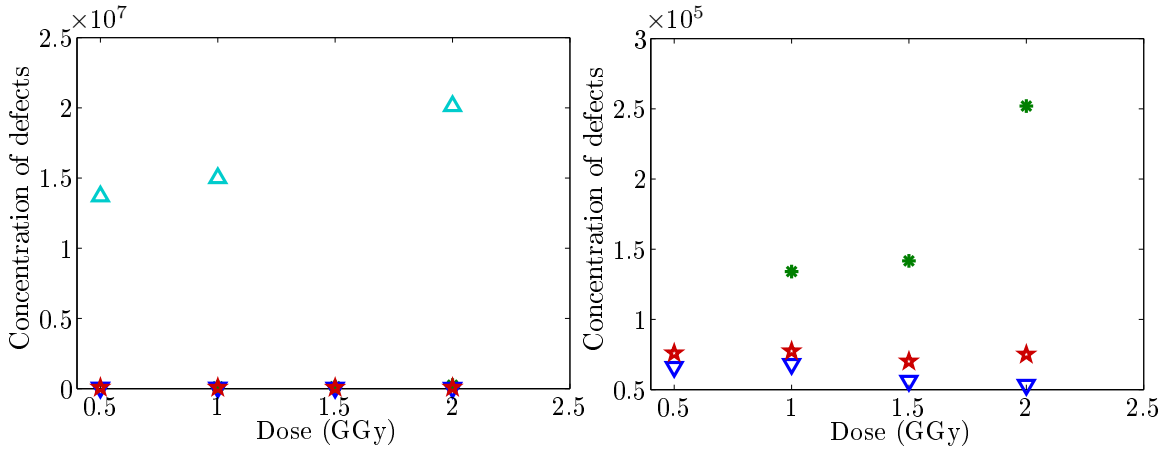

Figure 4.6: Total amount of defects calculated by double integration over EPR spectra at P=1 mW, f=9.82 GHz: (left) SBN 12, SBN 14, SBN 35 and SBN 55 and (right) SBN 14, SBN 35 and SBN 55.

A double integration of the spectra in Figures 4.3 and 4.4 gives the total amount of defects (see figure 4.6). Two behaviors prevail: (1) low sodium content (SBN 12 and SBN 14); and (2) high sodium content (SBN 35 and SBN 55). For low sodium glasses, the amount of created defects is higher and increases at 2 GGy. More irradiation would reveal if the 2 GGy samples have reached the saturation of defects.

High alkali content glasses reach a saturation because no significant variations takes place from 0.5 GGy to 2 GGy. Furthermore, the amount of defects is significantly lower for high [Na_2O] glasses than for low [Na_2O] ones (figure 4.6).

Raman investigation

Raman analysis investigates the evolution of borosilicate glasses' structure after irradiation. Figure 4.7 presents the evolution of SBN glasses after the electron irradiation. **SBN 12** Figure 4.7 top left reveals

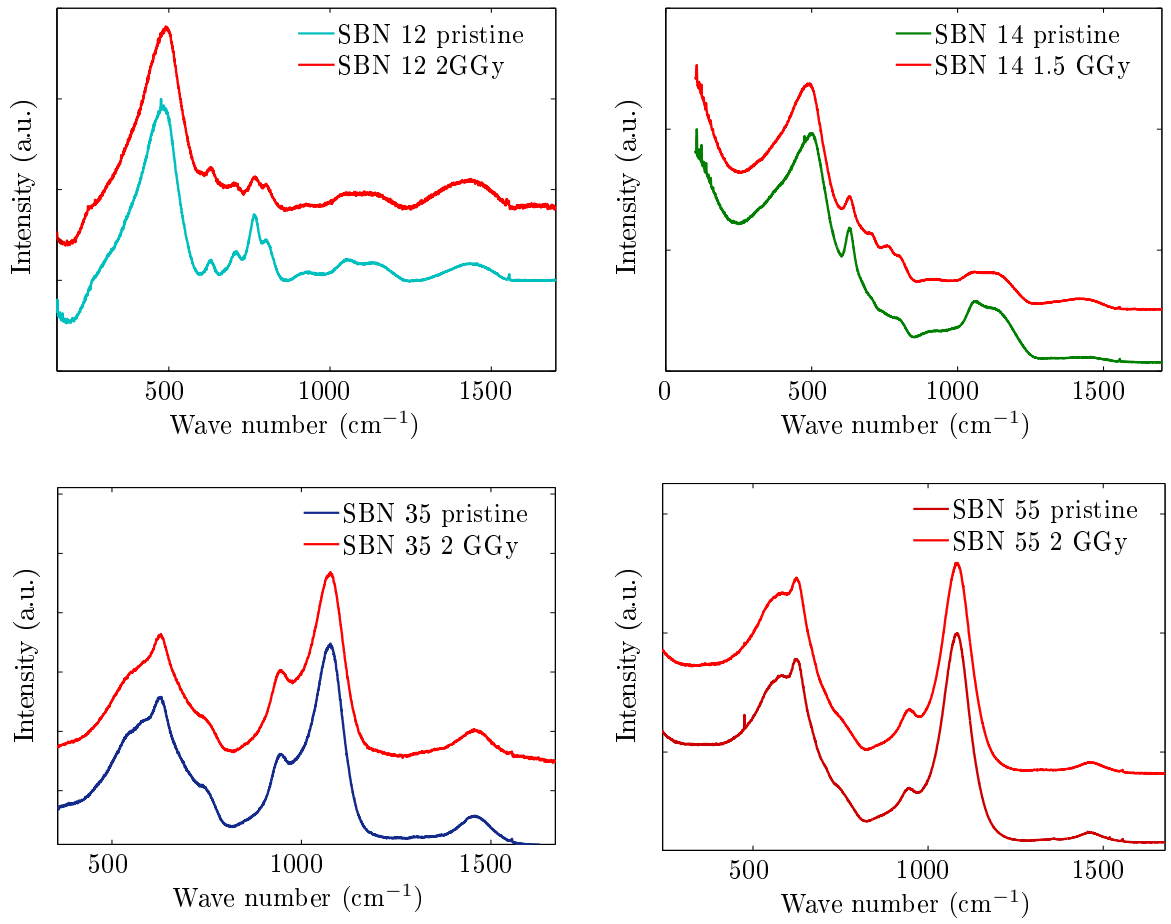

Figure 4.7: Raman spectra of SBN glasses prior and after irradiation: (Top left) SBN 12 pristine (light blue) and irradiated (red) at 2 GGy; (Top right) SBN 14 pristine (green) and irradiated (red) at 1.5 GGy; (Bottom left) SBN 35 pristine (dark blue) and irradiated (red) at 2 GGy; and (Bottom right) SBN 55 pristine (dark red) and irradiated (red) at 2 GGy. Spectra of β_{e^-}-irradiated (red curves) appear above the pristine samples.

the Raman spectra of pristine (light blue curve) and β_{e^-}-irradiated (red curve) SBN 12 samples . The pristine spectrum was previously presented in part I.3.3. of this thesis. Several variations occur before and after irradiation: (1) shift of the Si-O-Si band to smaller wave numbers; (2) decrease of the signal in the range 600-850 cm^{-1}; and (3) variation in the Q^n band. The Si-O-Si bending vibration band shift to

higher wave numbers can be interpreted as a decrease in the Si-O-Si angles [25,26] as the sodium content should not significantly change.

SBN 14 Figure 4.7 top right reveals the Raman spectra of pristine (green curve) and β_{e^-}-irradiated (red curve) SBN 14 glass. The pristine spectra was previously presented in section Part I chapter 3 of this thesis. Electron irradiation significantly modifies SBN 14 glass: (1) a shift in the Si-O-Si vibration band to lower wavenumbers; (2) a decrease in the danburite peak's intensity after irradiation (633 cm^{-1}); (3) the appearance of new signals between 700 and 810 cm^{-1}; and (4) an increase in the B-O^- signal.
SBN 35 and SBN 55 Figures 4.7 bottom left and right reveal the Raman spectra of pristine SBN 35 and SBN 55 glass, respectively. The red curve in each figure depicts its corresponding β_{e^-}-irradiated Raman spectra. Electron irradiation does not modify SBN 35 nor SBN 55 significantly.

4.2.3 Discussion

EPR measurements permit to estimate the nature and the quantities of paramagnetic defects created after β_{e^-}-irradiation. Raman spectra reveal qualitative changes in the glass structure after irradiation. All the experiments highlight two behaviors depending on the sodium content. Thus, the discussion below will be divided into low and high sodium content.

Low sodium content: SBN 12 and SBN 14 glasses

EPR spectra unveil a huge amount of defects created: $BOHC_1$, E' centers, HC_1 and HC_2, etc. Raman analyzes show a significant variation after irradiation for the two glasses. Yun, Dell and Bray model [10, 12, 37] glasses such as SBN 12 glass as glasses containing two separate networks: one enriched with borate atoms and one enriched with silicate atoms. Features of the pristine SBN 12 sample do allude to some demixing of the silica and borate networks (see section part I chapter 3). Features in the 600-850 cm^{-1} decrease slightly after irradiation. Contributions at 703, 770 and 803 cm^{-1} express a decrease of metaborate, borate and boroxols units, respectively. It should be noted that near the 770 cm^{-1} peak, the 780 cm^{-1} peak (vibrational mode of the "caged" silica tetrahedral) may also exist herein [9, 24, 27]. If it exists, then looking at the spectra it should be decreasing too. Irradiation in SBN 12 appears to reconnect the silica and borate networks, thus explaining the decrease of metaborate and boroxols rings.

SBN 14 glass exhibits a different behavior. The decrease of the danburite signal (peak at 603 cm^{-1}) between pristine and irradiated SBN 14 samples alludes to a decrease in the interconnection between the silicate and borate networks. This implies areas enriched in boron and areas enriched in silica are feasible. This is also coherent with the increase in the contribution of metaborate units (703 cm^{-1} band) and boroxols rings (770 cm^{-1} peak). The sizes of these domains have not been quantified. Variations in silicate/borate reorganization lead to a glass swelling. Finally, the degree of polymerization should not vary significantly before and after irradiation. Indeed the pristine glass is very reticulate (only 1% of NBO according to the Yun, Dell and Bray model [4,10,12,37]). The Raman structure after irradiation indicates that Na^+ ions dissociated with $^{[4]}B$ atoms under irradiation. It is feasible that the $^{[4]}B$ transform into $^{[3]}B$ as there is an increase in the Raman signal between 1200 to 1600 cm^{-1}. Moreover, the shift of the Si-O-Si bending vibration band shifts to smaller wave numbers could indicate one of the two followings: (1) larger Si-O-Si bond angles; and (2) a repolymerization of the glass. Na^+ ions segregation (i.e. not

linked to the borate or the silicate network) may be formed.

High sodium content: case of SBN 35 and SBN 55 glasses

High [Na_2O] glasses have a significantly different EPR spectra than low [Na_2O]. Low sodium content glasses exhibits a *five-plus-shoulder* spectra well-known as BOHC defects; yet, the EPR spectra of SBN 35 and SBN 55 exhibit a *four-plus-shoulder* spectra.

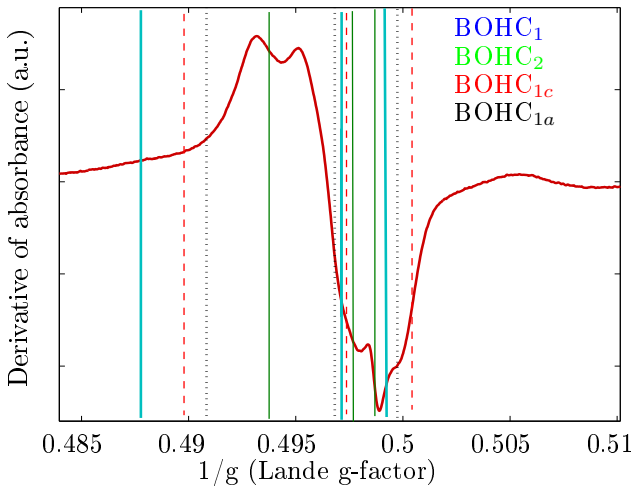

Figure 4.8: EPR spectra of SBN 55 glasses at P=1μW, f=9.82GHz. Each vertical line represent the expected 1/g values of BOHC: $BOHC_1$ (blue), $BOHC_2$ (green), $BOHC_{1c}$ (red) and $BOHC_{1a}$ (black) from [21, 22].

Kordas enumerated the $g-$values for several BOHC defects [21, 22]. Figure 4.8 presents the EPR spectra of the SBN 55 with the theoretical g-values proposed by Kordas for several BOHC defects (vertical lines). In high [Na_2O] glasses, no clear existence of BOHC defects exist. Moreover, the total amount of paramagnetic defects in SBN 35 and SBN 55 glasses is less than in SBN 12 and SBN 14 glasses.

Figure 4.9 depicts the evolution of defect concentration with NBO (left) and the percentage of [Na_2O] (right). Higher [Na_2O] decreases the concentration of defects. Sodium may change the trapping process as it is already known to occur with elements such as Fe^{3+} [11, 28]. This is also confirmed by a decrease in the E' center contribution for SBN 35 and SBN 55 glasses. Changing in processes leading to creation of defects could explain such discrepancies.

Thermal treatment of samples is known to eliminate defects. Annealing at controlled temperatures for both low and high sodium sample ideally eliminates the same type of defects and highlights differences between low and high sodium content. Figure 4.10 presents the difference between EPR spectra at

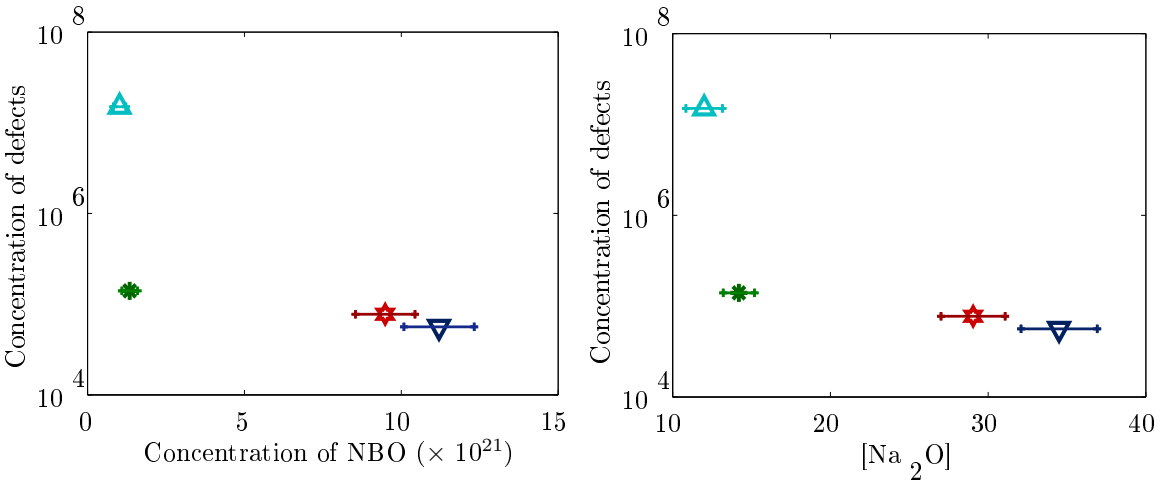

Figure 4.9: Correlation between the concentration of defects and (left) the concentration of NBO and (right) the percentage of Na_2O.

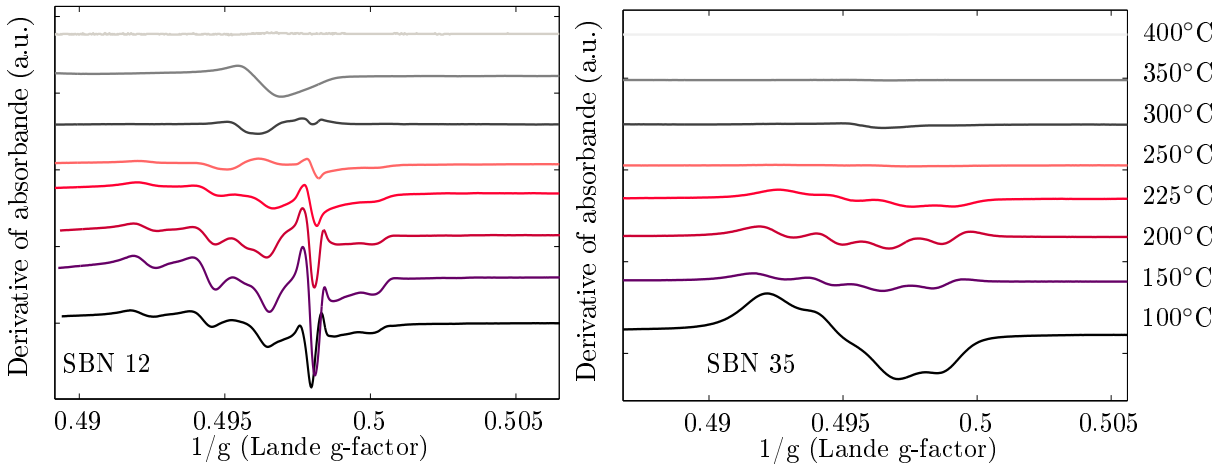

Figure 4.10: Difference between two EPR spectra after annealing at different temperatures: (left) SBN 12 and (Right) SBN 35. P=1 mW, f=9.82 GHz.

different annealing temperatures for the high and low $[Na_2O]$ content glasses[3]. In other words, the spectra presented give the defects annealed out between 100°C to 400°C. The left figure is for low $[Na_2O]$ content glasses, SBN 12. The spectra's shape remains similar from 100°C to 225°C, yet the amplitude varies. Annealing temperatures between 100-225°C probably eliminate $BOHC_1$ and E' centers. The SBN 12 spectra changes significantly from 225°C to 350°C. The spectra shape at 250°C is similar to the spectra observed by Boizot et al. who have annealed a 4-oxide glass at 290°C [6]. At this temperature, Oxy decreases. A null signal is reached at 400°C. Figure 4.10 right depicts variations in SBN 35 defects

[3]Annealing was has been done from 100°C to 450°C. Annealing and analyzing process was: (1) Samples were placed in an oven for 15 minutes; (2) the samples allowed to cool for 15 minutes; (3) EPR spectra collected; and (4) process repeats for a slightly higher annealing temperature (step of 25°C).

when the annealing is varied from 100°C to 400°C. A significant change in the shape occurs between 100°C and 150°C. The spectra are similar from 150°C to 225°C. Variation between spectra annealed between 150 and 225°C looks like $BOHC_1$ contribution. The location of the peaks are similar (albeit at lower amplitudes) to what was seen in SBN 12 with the exception of the E' center not being seen in the SBN 35 samples. Low and high sodium glasses contain both $BOHC_1$ but with different amount explaining the amplitude variations. At 250°C, no defects are annealed out. Yet, there is still an EPR response. With an annealing temperature of 300°C the EPR signal begins to vary again. Hence more defects are annealed out. At this temperature, Oxy contribution may decreases. A null signal is reached at 350°C.

Boizot et al. observed that the migration of $[Na_2O]$ can induce structural reorganization [8]. Migration and aggregation of sodium modify the glass structure by: (1) changing the polymerization degree in the silica network and (2) formation of oxygen bubbles. For high sodium content, sodium acts as a network modifier, rather than a charge compensator, making them more mobile. High sodium content glass appear to be less sensible to β_{e^-}-irradiation. Sodium clustering for SBN 35 and SBN 55 may exist further hindering the structural modifications and preventing for the creation of E' centers. The results on the 3-oxides glass differ from results observed after irradiation in 4- 5- and 6-oxides borosilicate glasses [6–8, 28–30, 36]. Boizot et al. observed an increase of the polymerization degree after irradiation like Yang et al. This results highlight the huge impact of the alkali content in the glass response to β_{e^-}-irradiation [29].

4.3 Mechanical properties

The glass structure notably impacts the mechanical response as presented in the part I.4. of this thesis. This section investigates the influence of β_{e^-} on SCC and hardness properties. AFM imaging permits to estimate the indentation shape (V_i^+, matter above the surface and V_i^-, matter below the surface.)

4.3.1 Hardness properties

Hardness variations correspond to a macroscopic consequence of microscopic structural variations in borosilicate glasses. This section details how the hardness varies with external β_{e^-}-irradiation. Since it was previously noted that β_{e^-}-irradiation has a more significant effect on low sodium concentration, this section is divided into low and high sodium concentration.

Low sodium content glasses: SBN 12 and SBN 14

SBN 12 Electron irradiation changes drastically the glass structure after irradiation. EPR measurement reveals a huge amount of point defects and Raman analysis unveils changes in connectivity between the borate and silicate networks. Figure 4.11 presents load-displacement curves from nano-indentation test on SBN 12 pristine and SBN 12 irradiated (electrons 2 GGy) samples at constant penetration depth. The load required to reach 300 nm of penetration depth decreases for the irradiated sample (red curve). This leads to a decrease in the hardness value as presented in table 4.5. At constant load by micro hardness tests, the indenter penetrates deeper in the irradiated samples without any significant pile-up processes.

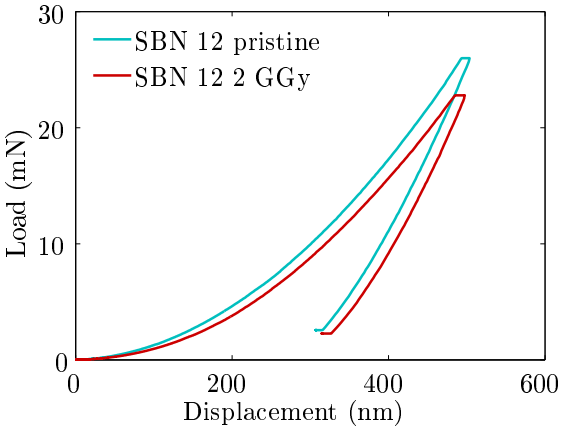

Figure 4.11: Evolution of load-displacement curves obtained by nanoindentation measurements at constant penetration depth for SBN 12 pristine (light blue line) and SBN 12 irradiated at 2 GGy (red line).

Both nano/micro indentations reveal a decrease in the hardness by about 20% (Table 4.5). Imaging

Properties	$SBN12_{pristine}$	$SBN12_{2GGy}$	Δ (%)
$H_V(MPa)$	$6900_{\pm 100}$	$5500_{\pm 70}$	-20
V^+/V^-	$7_{\pm 0.35}$	$3.4_{\pm 1.8}$	-50
c	$40.3_{\pm 2.5}$	$38.4_{\pm 1.5}$	//

Table 4.5: Evolution of hardness SBN 12 glass prior to and after electron irradiation, V^+/V^- determined from AFM imaging of indentation prints at 25 g and the average value of crack length (c) determined after Vickers indentation at 300 g for SBN 12 pristine and irradiated (2 GGy) samples.

(i.e. with an AFM) and analyzing the indentations topologies for irradiated samples follow the same methodology as for the pristine glasses (part I.2.3.4.). Hence, comparing and contrasting the two results is feasible. Table 4.5 provides V^+/V^- as determined from micro-indentation. These values underline the fact that indenter in the irradiated SBN 12 glasses penetrates deeper at low loads as compared to their pristine counterparts. V^+/V^- decreases by half after irradiation for 2 GGy samples. The glass structure after irradiation is less able to resist to indenter. Yet, SBN 12 does not have a significant change in ρ after irradiation.

In Part I chapter 4, I showed that by modulating the glass chemistry, we made P_C vary (crack appearance probability; defined in Part I.2.3.4). This modifies C_R (crack resistance). Figure 4.12 depicts P_C for increasing loads. Indentation loads for irradiated samples must exceed 50 g before cracks appear. Pristine samples require 25 g for crack appearance. As the indentation load increases, the pristine samples clearly have a higher tendency to form cracks as compared to their non-irradiated counterparts. Yet, observations in SBN 12 are load-dependent. For loads below 25 g (including nano- and micro-), the hardness decreases by 20 % between the pristine and irradiated samples. At higher loads ($>$ 25 g), the hardness value is similar prior to and after irradiation. A first guess of why the glass behaves differently

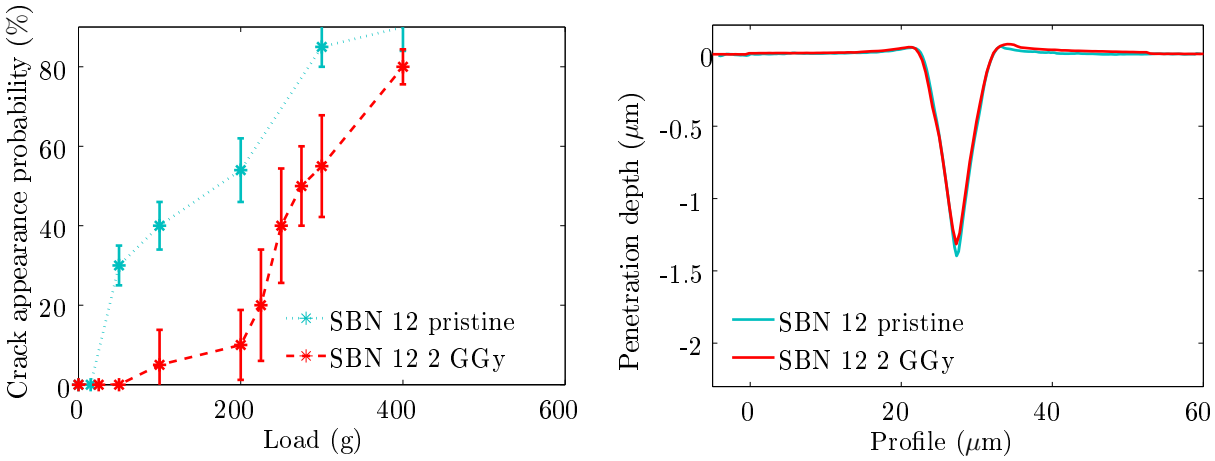

Figure 4.12: (Left) Crack appearance probability depending on applied load for SBN 12 pristine (blue line) and SBN 12 irradiated at 2 GGy (red line); (Right) Indentation profile for SBN 12 pristine (blue dotted line) and irradiated (red dotted line) at 2GGy at 100g

under low loads versus high loads, would be a variation in the glass's structure near the surface. Indeed, Abbas [2] found a sodium depletion close to the free surface, changing locally the glass structure. Figure 4.13 compares Raman signals recorded close to the surface and in the bulk. The spectra do not reveal any changes from the free surface towards the glass bulk. Thus, the reason why H decreases by ∼20% on surface remains unknown. Clarifications of the load dependency require more studies. The determination

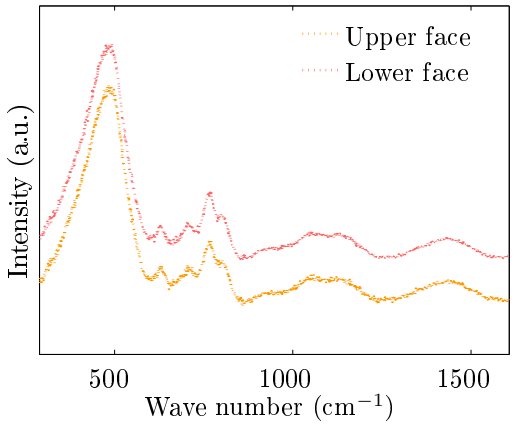

Figure 4.13: Raman spectra of SBN 12 irradiated at 1 GGy close to the surfaces (upper and lower faces)

of K_C by indentation is discussed in Part I.4. Half-penny median-radial cracks do not develop well in SBN 12 samples nor in their irradiated counterparts. As a consequence, K_C was not investigated by this method. Otherwise, the mean crack lengths, c, were similar prior to and after irradiation. Table 4.5 summarizes these results. **SBN 14** Figure 4.14 presents micro-indentation (left) and nano-indentation (right) test results for SBN 14. The micro-indentation test (Figure 4.14 left) compares pristine (green) and 2 GGy (β_{e^-}; red) irradiated samples for a load of 50 g. Clearly, the indenter penetrates deeper

after irradiation than before. The volume of indentation increases by $\sim$ 10% after irradiation. Nano-indentation tests (figure 4.14 right) compare pristine (green) and 2GGy (β_{e^-}; red) irradiated sample for a constant penetration depth. Clearly, irradiated samples require a lower load to reach the same penetration depth. Hence, H varies under irradiation for SBN 14. Table 4.6 presents SBN 14's H before and after β_{e^-}-irradiation. Irradiation induces a 17% decrease in the hardness.

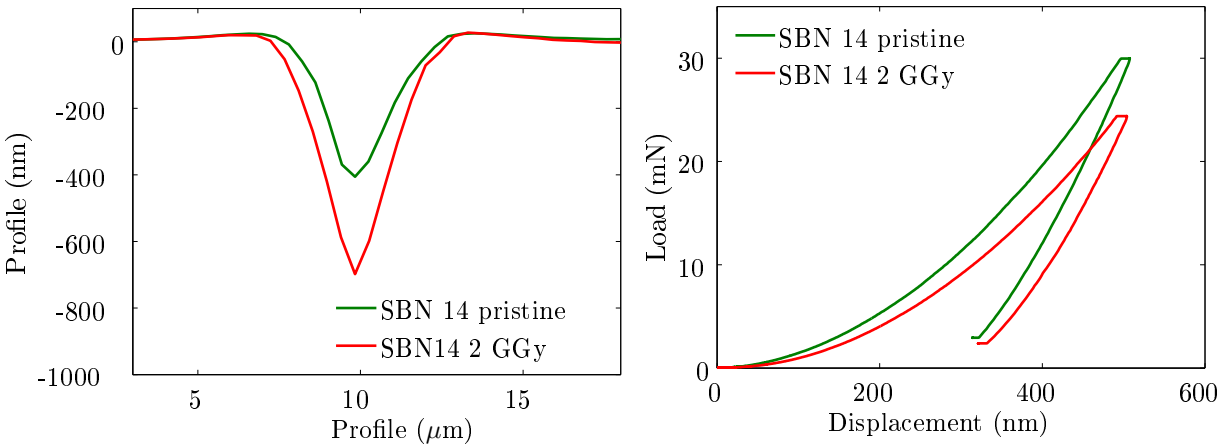

Figure 4.14: (Left) Profile evolution obtained by AFM imaging of residual indents from micro indentations for SBN 14 pristine and SBN 14 irradiated by electrons at 2 GGy. Experimental indentation took place in ambient conditions and the load was 50 g. (Right) Evolution of the load-displacement curves for constant depth nano-indentation tests.

Properties	SBN $14_{pristine}$	SBN 14_{2GGy}	Δ (%)
H_V(MPa)	$6520_{\pm 80}$	$5400_{\pm 120}$	-17
Evans & Charles model	SBN $14_{pristine}$	SBN $14_{1.5GGy}$	Δ (%)
K_C(MPa.$\sqrt{m}$)	$1.4_{\pm 0.2}$	$2_{\pm 0.3}$	+30

Table 4.6: Hardness measurements determined at 25 g for SBN 14 pristine and irradiated at 2 GGy by electrons and K_C variations obtained by indentation for SBN 14 samples at 300 g.

Due to the small amount of pile-up and increase in the penetration depth of irradiated samples, SBN 14 irradiated probably densifies more than its pristine counterpart. This can be correlated to a more open network. These variations lead to variations in P_C, crack appearance probability. The crack appearance probability decreases significantly between pristine and irradiated samples (4.15). Moreover comparing 1.5 GGy irradiated samples to 2 GGy, P_C decreases again. Estimating K_C requires a significantly high crack appearance probability. Hence, it is important to choose a load with enough cracks. Both 1.5 and 2.0 GGy samples require extremely high loads to initiate crack (Figure 4.15). Moreover, 2 GGy samples reach the limit of the load machine before having $P_C > 50\%$. Thus, K_C for 2 GGy samples is not accessible. For the 1.5 GGy sample a load of 300 g gives a significantly high P_C. A significant increase in K_C after irradiation occurs for SBN 14 irradiated at 1.5 GGy . This can be linked to the increase in densification processes which limits the propagation of median/radial cracks (as observed for

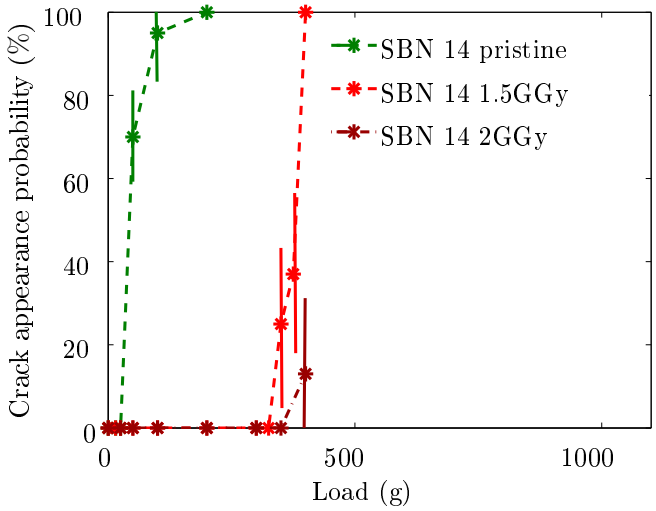

Figure 4.15: Crack appearance probability depending on load applied for SBN 14 pristine (green line) and SBN 14 irradiated at 1.5 GGy (red line) and 2 GGy (dark red line).

pristine glasses Part I.4.).

The mechanical indentation response of SBN 14 irradiated differs from its pristine counterpart. β_e--irradiation incudes glass swelling and structure reorganization making densification process easier. As a consequence, H_V is found to decrease whereas K_C increases.

High sodium content glasses: SBN 35 and SBN 55

Section 4.2.2 revealed that β_e--irradiation does not induce significant changes in the glass structure after irradiation. SBN 35 and SBN 55 pristine and irradiated samples undergo the same type of analysis as the low [Na_2O] glasses. The mechanical properties tests include micro- and nano-indentation. Electron irradiation levels of SBN 35 and SBN 55 samples studied herein is 1.5 GGy. The table 4.7 presents the evolution of H for SBN 35 and SBN 55. H_V decreases slightly in SBN 35 and SBN 55 irradiated samples.

	SBN $35_{pristine}$	SBN $35_{1.5GGy}$	Δ (%)
H_V(MPa)	$5050_{\pm 120}$	$4740_{\pm 80}$	6
	SBN $55_{pristine}$	SBN 55_{2GGy}	
H_V(MPa)	$5300_{\pm 110}$	$5160_{\pm 80}$	3

Table 4.7: Evolution of hardness for SBN 35 and SBN 55 glasses before and after electron irradiation.

However due to the error bar in pristine samples, the significance of the results is minimized. Figure 4.16 depicts the crack appearance probability with increasing load. For all indentation loads, SBN 35 and SBN 55 pristine and irradiated samples produce $P_C > 0\%$. As the indentation load increases, the SBN 35 pristine sample has a higher tendency to form cracks as compared to its -irradiated counterpart. Above 100 g both SBN 35 samples have $P_C = 100$ %. For SBN 55 pristine and irradiated samples have

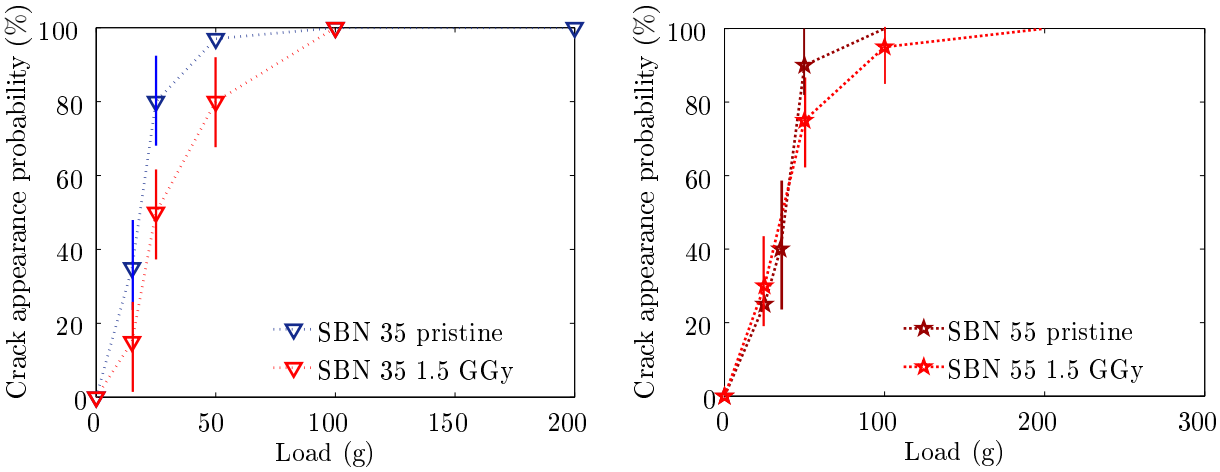

Figure 4.16: Crack appearance probability depending on load applied for: (left) SBN 35 pristine (dark red line) and SBN 35 irradiated at 1.5 GGy (red line); (right) SBN 55 pristine (dark blue line) and SBN 55 irradiated at 1.5 GGy (red line).

the same P_C (with in the error bars) for low loads. For loads greater than 50 g there appears to be a slight decrease in P_C for irradiated samples as compared to its pristine counterpart. Samples have a P_C =100% at 50 g (pristine) and 100 g (irradiated). For the two samples, irradiation only slightly impacts P_C. Table 4.8 shows that K_C increases with irradiation. In conclusion, the SBN 35 and SBN 55 response to nano/micro indentations appear to be weakly impacted by irradiation.

Evans & Charles model	SBN $35_{pristine}$	SBN $35_{1.5GGy}$	Δ (%)
K_C(MPa.$\sqrt{m}$)	$0.69_{\pm 0.05}$	$0.76_{\pm 0.06}$	+15
	SBN $55_{pristine}$	SBN $55_{1.5GGy}$	Δ (%)
K_C(MPa.$\sqrt{m}$)	$0.73_{\pm 0.09}$	$0.81_{\pm 0.06}$	+8

Table 4.8: K_C variations obtained by indentation for SBN 35 and SBN 55 glasses.

Discussion

SBN 12 and SBN 14 undergo structural modifications under electron irradiation. The mechanical behavior of SBN 12 under the indenter remains unclear. At low loads, H decreases, yet higher loads lead to a similar response in H prior to and after irradiation. Raman analysis close to the free surface does not reveal an explanation to this discrepancy.

SBN 14 swells after irradiation. This facilitates densification processes in irradiated samples and leads to a decrease in H. As mentioned in the first part of this thesis (Part I.4), variations in the densification/shear flow processes contribute to changes in the residual stresses during and after unloading. These variations reduce the tendency to form median/radial cracks in irradiated sample, thus K_C increases significantly after irradiation.

SBN 35 or SBN 55 differ from the SBN glasses with low [Na_2O] as they have a restrained indentation response to β_{e^-}- irradiation. Only small modifications in H (micro- and nano- indentation) occur due to irradiation. The RAMAN spectra do not evidence a significant difference between the irradiated and pristine samples. Thus, the lack of statistical variance in the mechanical behavior is linked to insignificant variations in the structure of the glasses.

Yang et al. investigated variations in the mechanical response of β_{e^-}-irradiated 7-oxides borosilicate glasses [36]. They found a 4 % decrease in H due to 1GGy β_{e^-}-irradiation. Results herein collaborate this result but they expose a higher response (but with a higher dose). The 4 SBN glasses herein also evidence the important role of the glasses chemical composition on variations of the glass's mechanical response due to irradiation.

4.3.2 Stress corrosion behavior

The first part of this thesis highlights the predominant role of the glass structure on the stress corrosion behavior. This section details how the SCC properties vary with external β_{e^-}-irradiation. Since it was previously noted that β_{e^-}-irradiation has a more significant effect on glasses with low sodium concentration, this section is divided into low and high sodium concentration. This section presents and compares the slope n estimated from the power law relationship between K_I and the velocity, v. K_I refers to the stress intensity factor determined from the external stress applied [19, 31], K_E refers to the fatigue limit below which the crack does not propagate.

Low sodium content: SBN 12 and SBN 14

SBN 12 Electron irradiation significantly affects the stress corrosion fracture regime in SBN 12, figure 4.17. Table 4.9 summarizes the evolution of n and K_E. The slope of the curve increases significantly between pristine and irradiated samples. Figure 4.18 depicts the evolution of fracture surfaces prior to and after irradiation. The color bar is the same for the two images. The velocity of the crack front used to create these two SCC surfaces was 10^{-8}-10^{-9} m.s^{-1}. The fracture surfaces highlight variations in the crack path via variation in the RMS value prior and after irradiation (4.9).

	SBN $12_{pristine}$	SBN 12_{2GGy}
n	20.1 ± 0.6	49 ± 1
K_E	$0.36_{\pm 0.02}$	$0.40_{\pm 0.03}$
RMS (nm)	0.81 ± 0.05	1.3 ± 0.1

Table 4.9: Variation of the slope n and K_E of the stress corrosion curves and RMS from fracture surfaces for SBN 12 pristine and irradiated at 2 GGy.

Electron irradiation changes significantly the slope n in the stress corrosion regime. The irradiated glass is less resistance to stress corrosion than its pristine counterpart.

SBN 14

Electron irradiation significantly alters the stress corrosion fracture regime in SBN 14 (figure 4.19). Table 4.10 summarizes the evolution of n and K_E. The stress corrosion curve shifts out to higher values

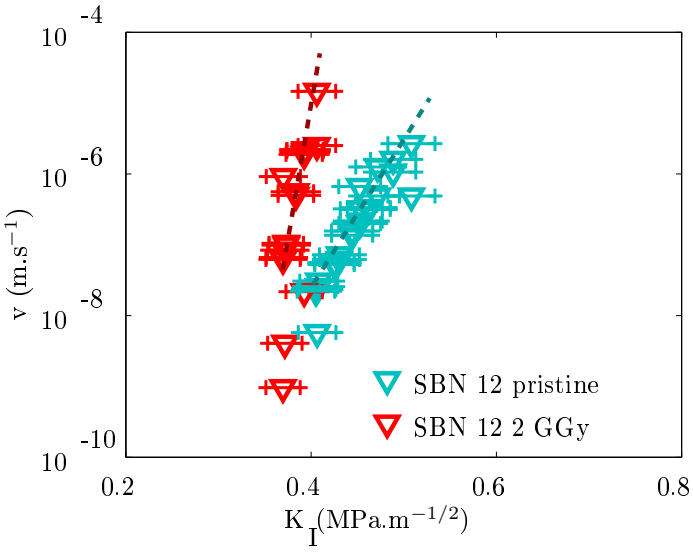

Figure 4.17: Evolution of failure behavior of SBN 12 pristine (light blue) and irradiated (red) in stress corrosion regime.

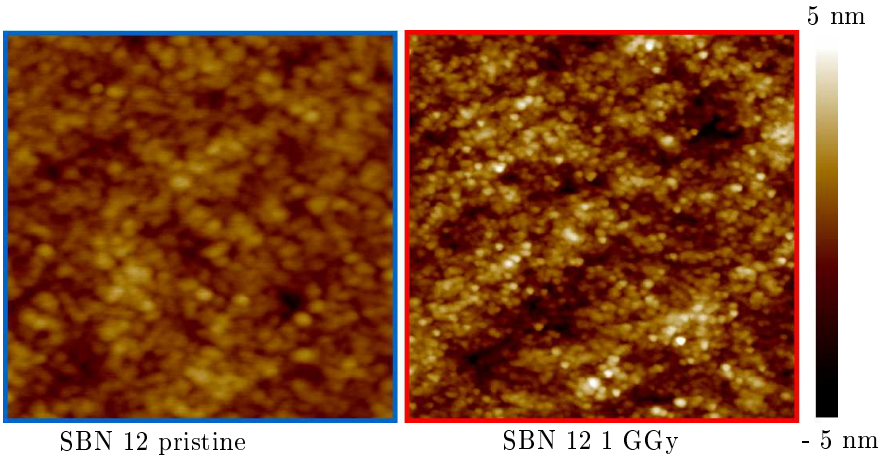

Figure 4.18: Fracture surfaces prior to and after irradiation. The velocity of the crack front used to create these two SCC surfaces was 10^{-8}-10^{-9} m.s^{-1}. The color bar remains the same for the two images.

of K_E. For the same crack front velocities, irradiated samples require higher applied forces. Moreover, the slope of the curve decreases by about 60% between pristine and irradiated samples.

The shift in K_E implies an increase of the glass's plasticity via an increase of the dissipation phenomena occurring during loading. The source of the plasticity variations lies within the changes in glass structure: (global swelling, decrease in danburite structures, increase in metaborate units and boroxols rings, etc.).

Cleary n decreases with irradiation in SBN 14. Wiederhorn et.al. (as discussed in Part I 4.2 of this thesis) theorized that the slope in region I should be proportional to activation volume (ΔV) for the chemical reaction at the crack tip. ΔV is the volume of a molecule between its unreacted state and that of the activated complex [13, 35]. Recalling, no data on how ΔV depends on tensile stresses exist.

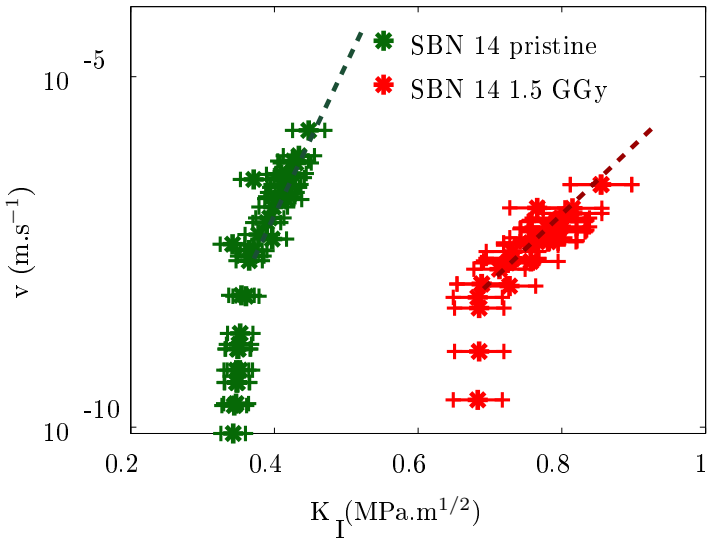

Figure 4.19: Evolution of failure behavior of SBN 14 pristine (green) and irradiated (red) in stress corrosion regime.

	SBN $14_{pristine}$	SBN $14_{1.5GGy}$
n	$20.2_{\pm 0.5}$	$8.3_{\pm 0.6}$
K_E	$0.35_{\pm 0.02}$	$0.68_{\pm 0.05}$
RMS (nm)	$0.65_{\pm 0.03}$	$0.95_{\pm 0.06}$

Table 4.10: Variations in the slope (n) and in K_E during SCC of SBN 14. RMS values result from analyzing pristine and irradiated (1.5 GGy) fracture surfaces which were created with crack tip velocities of 10^{-8}-10^{-9} m.s^{-1}.

Yet, decreasing n would imply a lower ΔV after irradiation. The Young modulus and the Poisson's ratio only may change slightly to expect such a huge n change. After irradiation, the glass structure changes significantly. This induces a huge decrease of the slope in the stress corrosion behavior. Radical changes in chemical reactions at the crack tip may occur explaining this variation. Moreover, the new glass structure should inhibit the penetration of water. Accordingly, irradiation in SBN 14 hinders SCC.

Variations in the crack path are confirmed by port-mortem analysis (figure 4.20). Table 4.10 summarizes the evolution of the RMS of the fracture surfaces. The RMS increases significantly between the irradiated and pristine samples. Its variations can be attributed to microscopic stresses associated with microstructural variations within the glass.

SBN 35 and SBN 55 Electron irradiation does not significantly alter the stress corrosion fracture regime for SBN 35 and SBN 55 samples. Figure 4.21 left and right presents the SCC curves of SBN 35 and SBN 55, respectively, pristine and irradiated samples. Visually, the stress corrosion curves (pristine and irradiated) overlap. Table 4.11 summarize K_E, n, and the RMS of the resulting fracture surfaces for pristine and irradiated SBN 35 and SBN 55 samples.

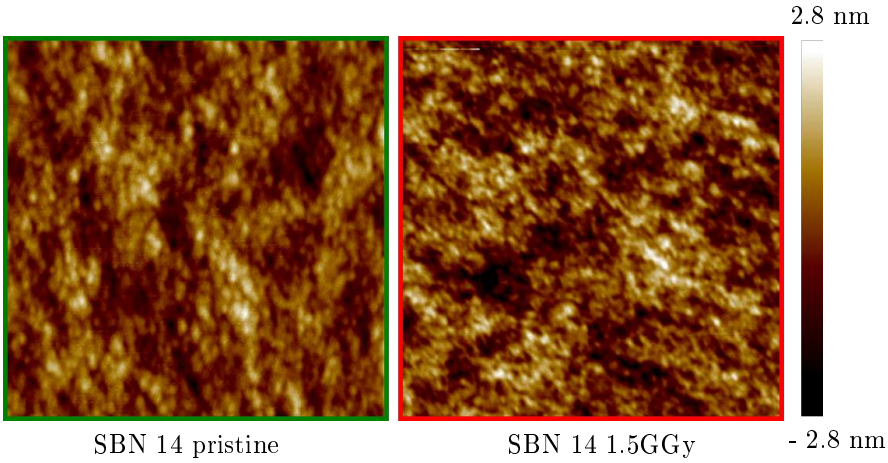

Figure 4.20: Images depict the evolution of fracture surfaces prior to and after irradiation. The velocity of the crack front used to create these two SCC surfaces was 10^{-8}-10^{-9} m.s^{-1} . The color bar is the same for the two images.

The vertical line of K_E for SBN 35 and SBN 55 was not acquired herein. Hence, no conclusion on a shift can be reached. Quantifying this result requires more data.

Table 4.11 presents the slope, n, in region I. SBN 35's slope decreases slightly, and SBN 55's slope increases slightly. However, due to the semi-log status of the equations, little significance can be extracted. Moreover it is hard to eliminate a null response in n due to irradiation, as the SCC overlap. In conclusion, election irradiation does not significantly impact high sodium glasses in the stress corrosion curves. Table

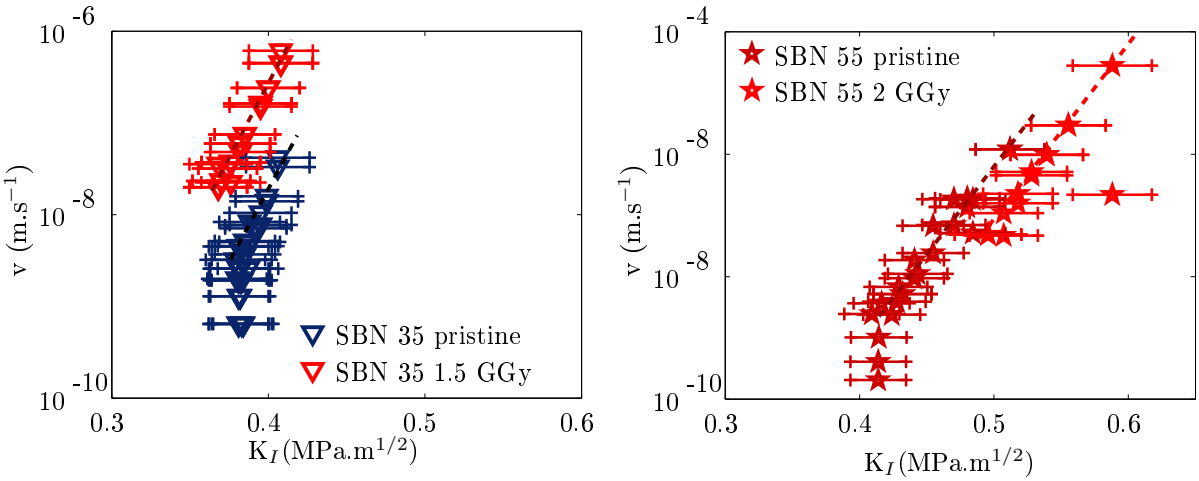

Figure 4.21: Evolution of failure behavior of: (left) SBN 35 pristine (dark blue) and irradiated (red) in stress corrosion regime; (right) SBN 55 pristine (dark red) and irradiated (red).

4.11 presents roughness variations for both SBN 35 and SBN 55. Variations of the roughness for post-mortem surfaces are not significant. Thus, β_{e^-}-irradiation does not significantly affect the crack path for SBN 35 and SBN 55.

	SBN $35_{pristine}$	SBN $35_{1.5GGy}$
n	$35.83_{\pm 0.4}$	$33.46_{\pm 0.2}$
K_E	$0.38_{\pm 0.03}$	//
RMS (nm)	$1.81_{\pm 0.08}$	$1.78_{\pm 0.09}$
	$SBN55_{pristine}$	$SBN55_{1.5GGy}$
n	$35.83_{\pm 0.4}$	$33.46_{\pm 0.2}$
K_E	$0.41_{\pm 0.01}$	//
RMS (nm)	$0.81_{\pm 0.08}$	$0.80_{\pm 0.09}$

Table 4.11: Variations in the slope (n) and in K_E during SCC of SBN 35 and SBN 55. RMS values result from analyzing pristine and irradiated (1.5GGy) fracture surfaces which were created with crack tip velocities of 10^{-8}-10^{-9} m.s^{-1}.

In conclusion, election irradiation does not significantly impact SBN 35 and SBN 55 glasses in the stress corrosion region.

Discussion

β_{e^-}-irradiation induces defects in the glass structure. Bonds break, and for low sodium glasses, the structure changes. Mechanical properties appear to be significantly impacted by the glass structure. Defects induced in SBN 35 and SBN 55 do not lead to significant changes in the stress corrosion curves. Low sodium glasses present significant changes after irradiation highlighting the huge impact of the glass structure on the stress corrosion behavior. Finally, residual stresses may be induced by irradiation. How this affects the mechanical response of stress corrosion cracking is unknown.

4.4 Conclusion

A glass's reaction to β_{e^-}-irradiation depends significantly on the glasses chemical composition:

1. **Sodium content diminishes the concentration of paramagnetic defects.** EPR investigation highlights variation in defects creation for low/high sodium content. The total amount of defects significantly increases as sodium content decreases.

2. **Structural modifications take place for low sodium glasses.** Migration of sodium during β_{e^-}-irradiation is known to induce structural modifications [6]. Sodium is generally a mobile element, and its mobility increases as sodium changes roles from charge compensator on ^{4}B units to network modifiers. Sodium clustering for SBN 35 and SBN 55 may exist further hindering structural modifications. Furthermore, as the quantity of sodium increases, as one Na^+ ion moves in the glass network another can easily takes its place.

3. **Hardness and stress corrosion behavior are strongly impacted by structural changes.** When β_{e^-}-irradiation alters the structural properties of the glass as seen by Raman, other properties vary in response: H, the glass' plasticity and its resistance to stress corrosion behavior.

A key question is how the residual stress impacts the mechanical response. This effect may be significant. Further investigations should be conducted to estimate this effect. *The β_{e^-}-irradiation can significantly*

change the mechanical behavior of SBN glasses. Two scenarios exist for low sodium and for high sodium content glasses. The low sodium content glasses present huge variation after irradiation (change in glass topology, change in the mechanical properties). The high sodium glasses structure do not evolve with irradiation. Thus, the sodium appears to inhibit structural variations. As a consequence, the mechanical properties do not evolve significantly. The next chapter investigates the same glass composition. They are submitted to ions irradiation to investigate the role of electronic and ballistic interaction through He^{2+}*- and* Au^{+}*- ions irradiation.*

Bibliography

[1] http://physics.nist.gov/physrefdata/star/text/estar.html.

[2] A. Abbas. *Contribution de l'etude de l'effets de l'irradiation alpha sur les verres nucleaires.* PhD thesis, Universite Paris VI, 2001.

[3] S. Baccaro, N. Catallo, A. Cemmi, and G. Sharma. Radiation damage of alkali borate glasses for application in safe nuclear waste disposal. *Nucl. Instrum. Methods Phys. Res. B, Beam Interact. Mater.*, 269:167–173, 2011.

[4] M. Barlet, A. Kerrache, J.-M. Delaye, and C.L. Rountree. Sio2-na2o-b2o3 density: A comparison of experiments, simulations, and theory. *J. Non-Cry. Solids*, 382:32 – 44, 2013.

[5] B. Boizot, S. Agnello, B. Reynard, R. Boscaino, and G. Petite. Raman spectroscopy study of beta-irradiated silica glass. *J. Non-Cryst. Solids*, 325:22–28, 2003.

[6] B. Boizot, G. Petite, D. Ghaleb, and G. Calas. Radiation induced paramagnetic centers in nuclear glasses: an epr spectroscopy study. *Vide Science, Technique et Applications*, 1998.

[7] B. Boizot, G. Petite, D. Ghaleb, and G. Calas. Dose, dose rate and irradiation temperature effects in beta-irradiated simplified nuclear waste glasses by epr spectroscopy. *J. Non-Cryst. Solids*, 283:179–185, 2001.

[8] B. Boizot, G. Petite, D. Ghaleb, B. Reynard, and G. Calas. Raman study of beta-irradiated glasses. *J. Non-Cryst. Solids*, 243:268–272, 1999.

[9] J Bonfils de, S. Peuget, G. Panczer, D Ligny de, S Henry, P. Y. Noel, A. Chenet, and B. Champagnon. Effect of chemical composition on borosilicate glass behavior under irradiation. *J. Non-Cryst. Solids*, 356:388–393, 2010.

[10] P.J. Bray, S.A. Feller, G.E. Jellison, and Y.H. Yun. B-10 nmr-studies of the structure of borate glasses. *J. Non-Cryst. Solids*, 38-9:93–98, 1980.

[11] R. Debnath. Thermally-reversible gamma-ray-induced redox reaction between substitutional iron and aluminium impurity centers in a silica glass. *J. Mat. Res.*, 16:127–131, 2001.

[12] W.J. Dell, P. J. Bray, and S. Z. Xiao. B-11 nmr-studies and structural modeling of Na_2O-B_2O_3-SiO_2 glasses of high soda content. *J. Non-Cryst. Solids*, 58(1):1–16, 1983.

[13] S. Freiman. The fracture of glass: Past, present and future. *Int. J. Appl. Glass Sci.*, 3:89–106, 2012.

[14] D. Griscom. Defect centers in a pure-silica-core borosilicate-clad optical fiber: Esr studies. *J. Appl. Phys.*, 47:960–967, 1976.

[15] D. Griscom. Self-trapped holes in amorphous silicon dioxide. *Phys. Rev. B*, 40:4224–4227, 1989.

[16] D. Griscom. Electron-spin-resonance characterization of self-trapped holes in amorphous-silicon dioxide. *J. Non-Cryst. Solids*, 149:137–160, 1992.

[17] D. Griscom, C. Merzbacher, R.A. Weeks, and R.A. Zuhr. Electron spin resonance studies of defect centers induced in a high-level nuclear waste glass simulant by gamma-irradiation and ion- implantation. *J. Non-Cryst. Solids*, 258:34–47, 1999.

[18] D.L. Griscom. Electron-spin-resonance studies of trapped hole-centers in irradiated alkali silicate-glasses - a critical comment on current model for hc1 and hc2. *J. Non-Cryst. Solids*, 64:229–247, 1984.

[19] M.Y. He, M.R. Turner, and Evans A. G. Analysis of the double cleavage drilled compression specimen for interface fracture energy measurements over a range of mode mixities. *Acta. Metall. Mater.*, 43:3453–3458, 1995.

[20] G. Kordas. Hyscore spectroscopy in the borate glasses. *J. Non-Cryst. Solids*, 331:122–127, 2003.

[21] G. Kordas. g-factor calculations for the species occurring in borate glasses. *J. Non-Cryst. Solids*, 343:159–162, 2004.

[22] G. Kordas. On the structure of the bohc in the borosilicate and borophosilicate glasses. *J. Non-Cryst. Solids*, 351:2358–2360, 2005.

[23] G. Kordas, B. Camara, and H.J. Oel. Electron spin resonance studies of radiation damage in silicate glasses. *J. Non-Cryst. Solids*, 50:79–95, 1982.

[24] H. Li, L.Y. Su, and D.M. Strachan. Raman spectroscopic study of gadolinium (iii) in sodium-aluminoborosilicate glasses. *J. Non-Cryst. Solids*, 292:167–176, 2001.

[25] D. Manara, A. Grandjean, and D.R. Neuville. Advances in understanding the structure of borosilicate glasses: A raman spectroscopy study. *Am. Mineral.*, 94:777–784, 2009.

[26] D.W. Matson, S.K. Sharma, and J.A. Philpotts. The structure of high-silica alkali-silicate glasses. a raman spectroscopic investigation. *J. Non-Cryst. Solids*, 58:323–352, 1983.

[27] D.A. McKeown, F. L. Galeener, and G.E. Brown Jr. Studies of al coordination in silica-rich sodium aluminosilicate glasses and some related minerals. *J. Non-Cryst. Solids*, 68:361–378, 1984.

[28] N. Ollier, B. Boizot, B. Reynard, D. Ghaleb, and G. Petite. Analysis of molecular oxygen formation in irradiated gkasses: a raman depth profile strudy. *J. Nucl. Mater.*, 340:209–213, 2005.

[29] N. Ollier, B. Boizot, B.and Reynard, D. Ghaleb, and G. Petite. Beta irradiation borosilicate glasses: the role of mixed alkali effect. *Nucl. Instrum. Methods Phys. Res. B, Beam Interact. Mater.*, 218:176–182, 2004.

[30] N. Ollier, B. Champagnon, B. Boizot, Y. Guyot, G. Panczer, and B. Padlyak. Influence of esternal β-irradiation in oxide glasses. *J. Non-Cryst. Solids*, 323:200–206, 2003.

[31] G. Pallares, L. Ponson, A. Grimaldi, M. George, G. Prevot, and M. Ciccotti. Crack opening profile in dcdc specimen. *Int. J. Fracture*, 156:11–20, 2009.

[32] I.A. Shkrob and V.F. Tarasov. On the structure of trapped holes in borosilicates. *J. Chem. Phys.*, 113(23):10723–10732, 2000.

[33] R. Stosser, G. Scholz, M. Nofz, T. Grande, and S. Assland. On the nature and role of fe^{3+} ions in oxide and fluoride glasses. *Ber. Bunsen-Ges. Phys. Chem.*, 100:1588–1592, 1996.

[34] W.L. Warren, M.R. Shaneyfelt, D.M. Fleetwood, P.S. Winokur, and S. Montagne. Electron and hole trapping in doped oxides. *IEEE Trans. Nucl. Sci.*, 42:1731–1739, 1995.

[35] S.M. Wiederhorn. Influence of water vapor on crack propagation in soda-lime glass. *Am. Ceram. Soc. Bull.*, 50:407–414, 1967.

[36] K.J. Yang, T.S. Wang, G.F. Zhang, H.B. Peng, L. Chen, L.M. Zhang, C.X. Li, F. Tian, and W. Yuan. Study of irradiation damage in borosilicate glass induced by he ions and electrons. *Nuclear Instruments and Methods in Physics Research B*, 307:541–544, 2013.

[37] Y.H. Yun, S.A. Feller, and P.J. Bray. Correction and addendum to nuclear magnetic-resonance studies of the glasses in the system Na_2O-B_2O_3-SiO_2. *J. Non-Cryst. Solids*, 33:273–277, 1979.

Chapter 5

SBN glass: Impact of light and heavy ions irradiations on glass structure and mechanical properties

Contents

The previous chapter presented the evolution of SBN glass properties after electron irradiation. Two different behaviors occur depending on the sodium content. Low sodium content glasses are significantly impacted by irradiation. Their structural changes and their mechanical properties are impacted. The high sodium content glasses are unaffected by the β_{e^-}-irradiation. The sodium content appears to inhibit the glass reorganization. This chapter presents the evolution of SBN glass structure after light (6 MeV He^{2+}) and heavy ions (multi energy Au^{+}) irradiation. The section tests the same four chemical compositions as presented in the section 2.1, and the section 2.2 details the conditions of irradiation. The first part of this chapter (section 5.1) details the structural damage induced in the thin layer where the ions penetrate. Raman investigates the structure variations from the surface of bombardment into the bulk material. Section 5.2 presents the impact of He^{2+} and Au^{+} on mechanical properties.

5.1 Damages induced by light and heavy ions

5.1.1 Damages induced by He^{2+} and Au^{+} irradiation

Part II chapter 2 presents the irradiation facility and conditions for He^{2+}- and Au^{+} irradiation. For SBN irradiated glasses with 6 MeV He^{2+} ions and multi-energy Au^{+}, SRIM calculations provides an estimation of the nuclear and electronic stopping power during the irradiation with the penetration depth. An exemple of damages induced by helium and gold irradiation is presented for the SBN 14 glass (Figure 5.2) . Similar damages occur for the 4 SBN compositions.

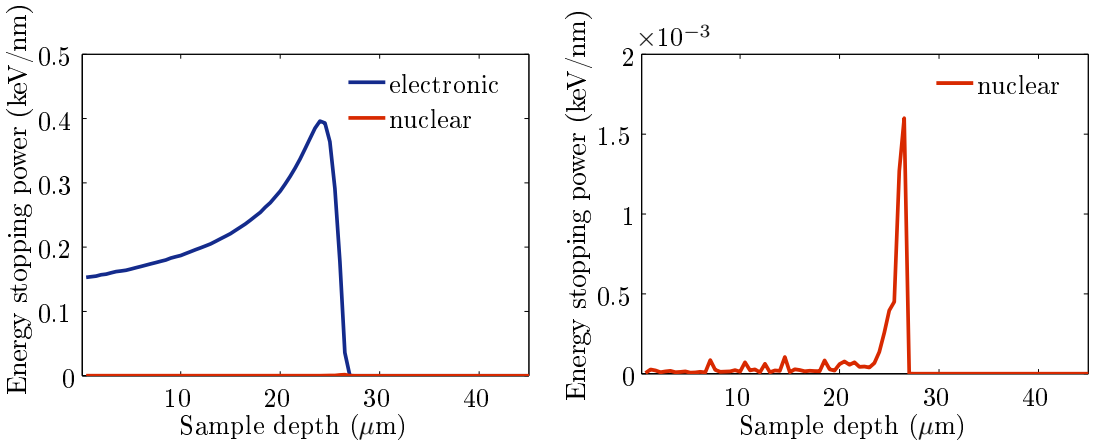

Figure 5.1: SRIM simulation for SBN 14 glass irradiated by 6 MeV helium ions at a dose of 3.8×10^{15} ions/cm^2 with the penetration depth: (Left) Electronic (blue line) and nuclear (red line) stopping power; (Right) nuclear stopping power. Electronic interactions dominate over the 30 μm into the glass sample. The nuclear interactions are maximum around 30 μm.

The energy deposited mainly takes place through electronic interactions ($\sim$ 99%), which increases from the free surface (0 μm) to (30 μm). The electronic deposited energy dose is maximum $\sim$30 μm . From the SRIM estimation, only the first 30 μm of the glass thickness will be damaged by the 6 MeV He^{2+} ions.

Nearly, when SBN glasses are irradiated by Au^{+} ions a homogenous nuclear energy stopping power

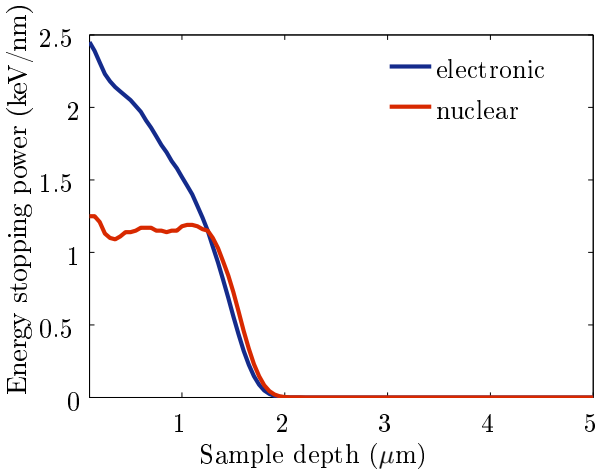

Figure 5.2: Electronic (blue line) and nuclear (red line) stopping power versus the irradiated depth for the SiO_2 glass irradiated by gold ions (Au^+) at different energy: 1, 3.5 and 7 MeV.

occurs over the first layer 3 μm in the glass sample (figure 5.2). 75 % of the energy loss is due to electronic interactions [3, 4]. Energy deposited through nuclear excitation is $5{\times}10^{20}$ keV/cm^3, i.e. above the dose required to damage the borosilicate glass sample [3, 4, 15].

5.1.2 Structural damages induced by He^{2+} irradiation

Recalling SRIM calculations in section 3.1.2, the He^{2+} bombarding ion loses energy electronic damage over the first 20 μm. In the next 10 μm, the He^{2+} bombarding ion loses energy due to both electronic and ballistic damages. The Raman studies provide a means to analyze structural variations with ion penetration depth.

SBN 12

Figure 5.3 depicts the variation of glass structure as a function of depth from free surface to bulk. As presented in section 5.1.2, the damage induced by helium irradiations are inhomogeneous in depth. The yellowish spectra probe areas close to the free surface (first 10 μm), where electronic interactions predominate. The brown/black spectra present the Raman spectra at $\sim$ 25-30 μm, where ballistic interactions are maximum. The two turquoise lines indicate Raman features of glasses in the bulk (40-50μm). Moreover, the features of these two lines compare favorably with its pristine counterpart (figure 3.5, chapter 3 of the part I).

Depending on the prevailing type of interactions (electronic and nuclear), the Raman spectra vary. Below highlights the varying features of SBN 12 with interactions:

1. Modifications in the zone where electronic interactions are predominant:

   - The Si-O-Si bending vibration band shifts to higher wavenumbers (β_e–-irradiated samples also had a shift to higher wavenumbers). One interpretation of the physical meaning of this shift

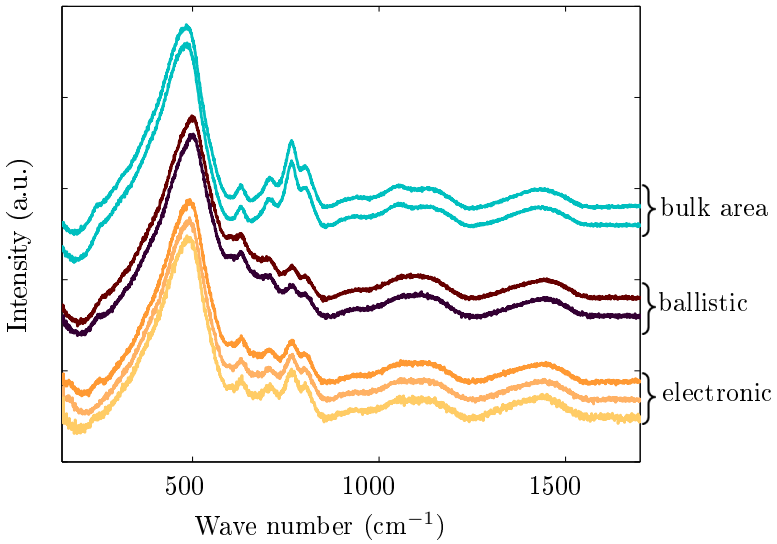

Figure 5.3: Raman spectra of SBN 12 glasses irradiated by He^{2+} ions from the free surface towards the bulk (bottom to top). The yellowish spectra probe regions predominantly impacted by electronic excitations (i.e. between 0 and 20 μm). The brown/black spectra concern areas where the maximum amount of ballistic damage occurs between 25 and 30 μm.

is a decrease of the mean Si-O-Si angle [13, 14]. Another interpretation is a variation in the number of NBO on the Si atoms [11].

- The metaborate, borate units and boroxol rings peaks decrease.
- A slight changes in Q_n band exists.

Variations resemble changes occurring after electron irradiation. Electronic processes in SBN 12 appear to give way to more connection between the boron/silica networks.

2. Modifications in the zone where electronic and nuclear interactions mix:

   - The Si-O-Si bending vibration band shifts to the right. The figure 5.4 zooms in the area between 400-900 cm^{-1}. The position of the D_2 band is marked by a dashed gray line. The contribution may appears around 600 cm^{-1}: the signature of the D_2 contribution and the shift in the Si-O-Si bending vibration express a reduction of bond angles. Irradiation may yield an increase of the number of smaller rings.
   - The peaks between 600-850 cm^{-1} decrease. According to literature [17], a decrease in the 770 cm^{-1} band may correspond to a reduction of the boron coordination number.

Electronic and ballistic interactions change the SBN 12 glass structure. A reduction of the Si-O-Si angle and changes in the borate- borosilicate rings appear to occur.

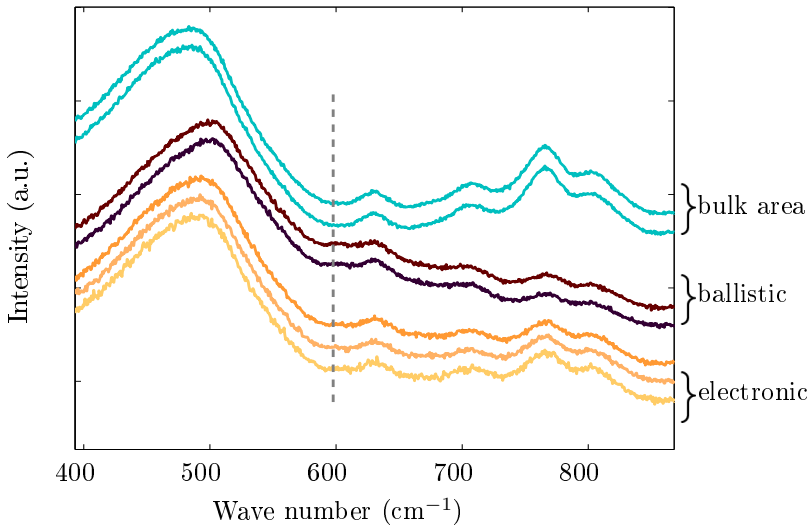

Figure 5.4: Zoom between 400-900 cm^{-1} of the figure 5.3. In the ballistic area, the D_2 peak contribution increases (gray dashed line).

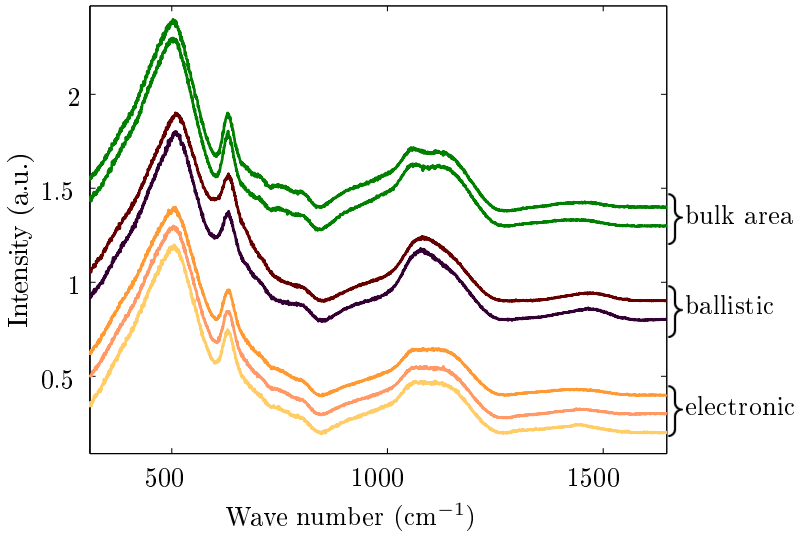

Figure 5.5: Raman spectra of SBN 14 glasses irradiated by He^{2+} ions from the free surface towards the bulk (bottom to top). Again, the yellowish spectra probe regions predominantly impacted by electronic excitations. The brown/black spectra concern areas where the maximum amount of ballistic damage occurs. The green spectra show the Raman features deep (i.e. deeper than the penetration depth of the ions) into the samples. Variation in the Raman spectra concerns the area, where ballistic interactions maximize.

SBN 14

Figure 5.5 depicts the evolution of the SBN 14 glass structure from the free surface to the bulk. The yellowish spectra probes areas close to the free surface (first 10 μm), where electronic interactions dom-

inate. The brown/black spectra present the Raman spectra at $\sim$ 25-30 μm, where ballistic interactions are maximum. The two green lines indicate Raman features of glasses in the bulk (40-50μm).

Again, Raman spectra are found to depend on the probed depth. Below highlights the varying features of SBN 14 with interactions:

1. Modifications in the zone where electronic interactions are predominant

   - A slight shift in the Si-O-Si bending vibration band occurs. Figure 5.6 compares the spectra of SBN 14 non-irradiated, β-irradiated and He^{2+}-irradiated acquired in the first 10 μm from the free surface (where electronic interactions predominate). From the pristine sample, the Si-O-Si band shifts towards high wavenumbers for He^{2+}-irradiated. Yet, for β-irradiated SBN 14 samples the spectra shifted to smaller wavenumbers.
   - The features between 600 and 850 cm^{-1} decrease slightly.

   Variations are not significant but are drastically different from what has been observed after β_{e^-}-irradiation (Figure 5.6).

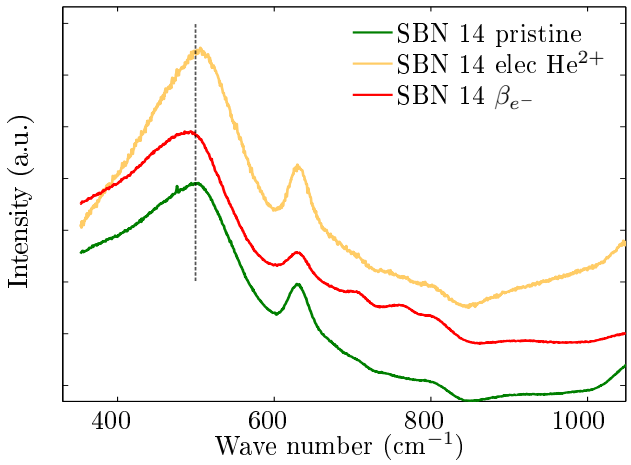

Figure 5.6: Raman spectra of SBN 14 pristine (green, bottom), irradiated by electron β_{e^-} (red, middle) and irradiated by He^{2+} where electronic interactions govern the structural variations (yellow, top). The variations induced by electronic interactions through He^{2+} are not equivalent to those induced by β_{e^-}-irradiation. The gray dashed line marks the peak position of the Si-O-Si bending vibration band of the pristine glass (green line).

2. Modifications in the zone where electronic and nuclear interactions mix (Figure 5.7 compares the spectra of the SBN 14 recorded in the bulk (green line) and recorded at 27 μm from the free surface.):

   - The Si-O-Si bending vibration shifts towards higher wavenumbers.
   - Slight variations around 600-800 cm^{-1} occur.
   - Changes in Q_n band and an increase in the $B-O^-$ contribution takes place.

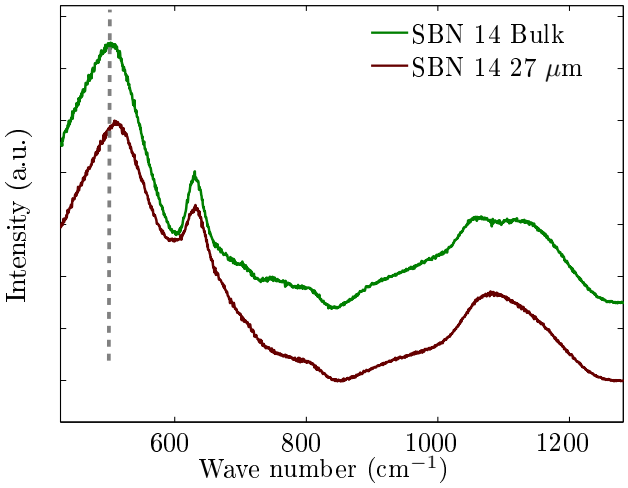

Figure 5.7: Raman spectra in SBN 14 He^{2+}-irradiated samples recorded at 27 μm from the free surface (dark red) and in the bulk (green). 27 μm from the free surface corresponds to where ballistic interactions maximize. The gray dashed line marks the position of the Si-O-Si bending vibration band in the bulk material (green line).

In the ballistic zone, the spectra imply a glass structure with a lower degree of polymerization (increase in the number of silica having NBO, an increase in the $B-O^-$ contribution, etc.).

Ballistic interaction changes the SBN 14 Raman spectra features. The shift in the Si-O-Si band may be correlated to a change in the degree of polymerization in the silica network. For this glass, the electronic excitations induced by β_{e^-} and He^{2+} ions are not equivalent.

SBN 35 and SBN 55

Figures 5.8 and 5.9 represent evolution of SBN 35 and SBN 55 (respectively) glass structure investigated by Raman analysis. The colors refer to the different zones as previously defined: the yellowish spectra probe areas close to the free surface (first 10 μm); the brown/black spectra present the Raman spectra at $\sim$ 25-30 μm, where ballistic interactions are maximum; and the two red (SBN 35) and two dark blue (SBN 55) lines indicate Raman features of glasses in the bulk (40-50μm). SBN 35 and SBN 55 do not exhibit significant structural variation in the irradiated zone. Electronic part for the two glasses matches the spectra within the bulk ($\sim$ 40μm). The figure 5.10 depicts the variation between the bulk and irradiated part where the maximum amount of nuclear interactions occurs for SBN 35 (left) and SBN 55 (right). Slight variations take place around the Q_n band. The crosses depict the peak for Q_3 (highest peak) and Q_2 (lower peak). Variations in intensity indicate a decrease in the polymerization degree of the glassy networks for the two glasses. Slight increase in the 1500 cm^{-1} occurs. **Variation due to helium irradiation is slight where the concentration of $[Na_2O]$ is high. Small variations occur in ballistic areas mainly affect the Q_n contribution. A slight decrease of the polymerization degree may take place.**

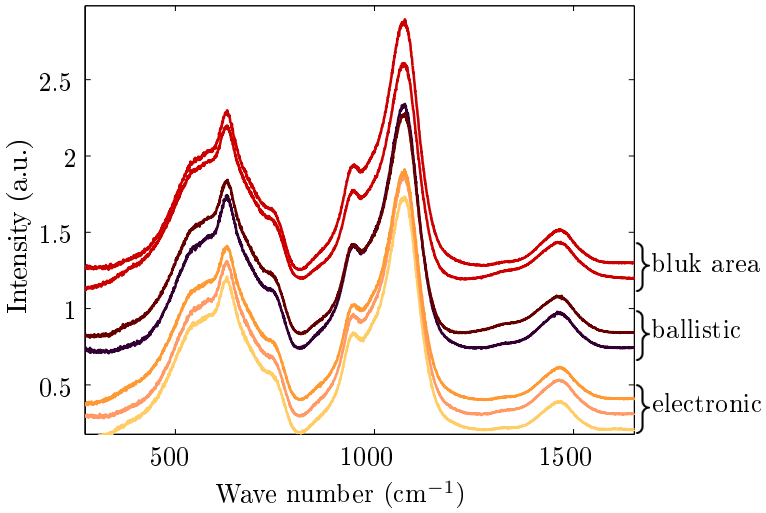

Figure 5.8: Raman spectra of SBN 35 glasses irradiated by He^{2+} ions from the free surface towards the bulk (bottom to top). From bottom to top: the yellowish spectra probe regions predominantly impacted by electronic excitations. The brown/black spectra concern areas where the maximum amount of ballistic damage occurs. The red spectra show the Raman features deep (i.e. deeper than the penetration depth of the ions) into the samples.

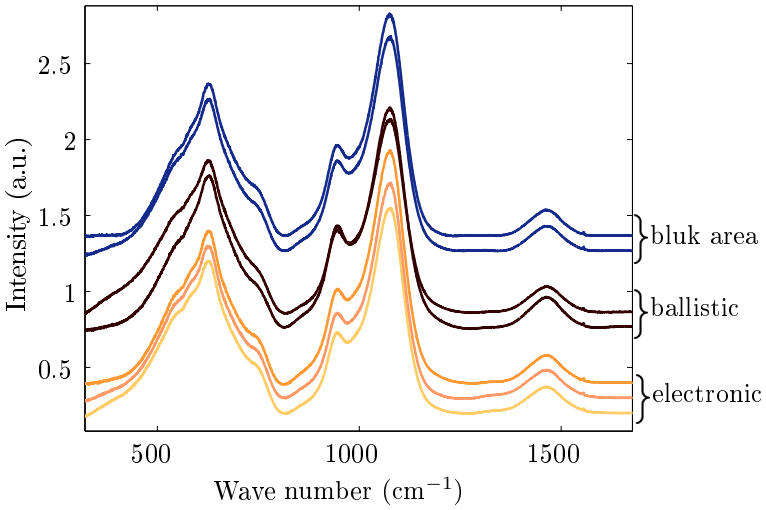

Figure 5.9: Raman spectra of SBN 55 glasses irradiated by He^{2+} ions from the free surface towards the bulk (bottom to top). The yellowish spectra probe regions predominantly impacted by electronic excitations. The brown/black spectra concern areas where the maximum amount of ballistic damage occurs. The dark blue spectra show the Raman features deep. Impact of helium irradiation is slight on this glass chemical composition.

Discussion

The He^{2+} irradiation at 6 MeV induces slight variations. The threshold of ion tracks formation remains unknown for SBN glasses [17]. The stopping power is low compared to other studies [15,17] on the same

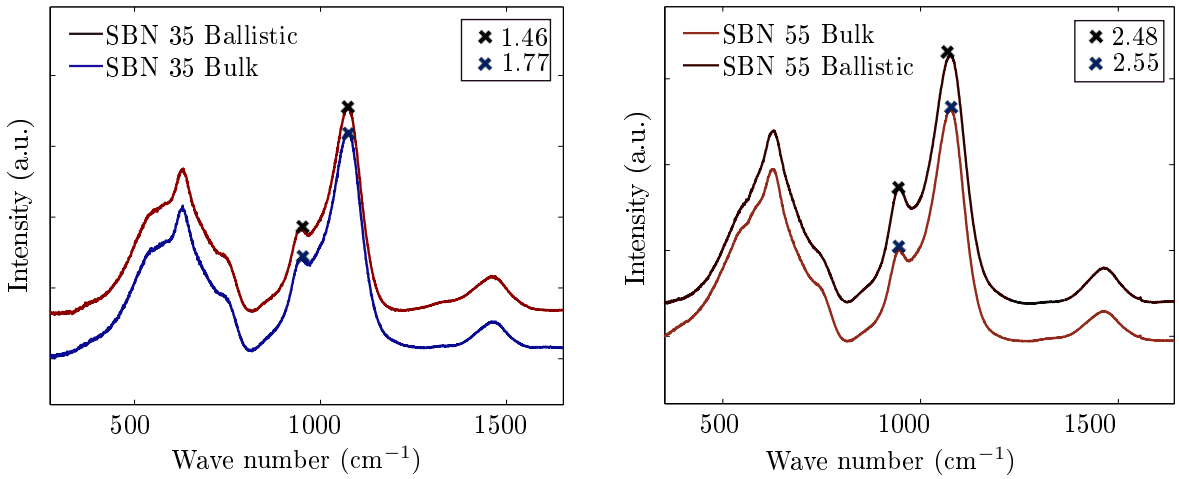

Figure 5.10: (Left) Raman spectra of SBN 35 glasses irradiated by He^{2+} ions. The dark blue spectrum probes the bulk and the brown spectrum concerns the area where ballistic damages are maximum; and (Right) Raman spectra of SBN 55 glasses irradiated by He^{2+} ions. The dark red spectrum probes the bulk and the brown spectrum part concerns area where the ballistic damages are maximum; the cross marks indicate the Q_2 (first) and Q_3 (second) peaks heights. The values are the ratio Q_2/Q_3.

type of glasses. As a consequence, irradiation slightly alters the glass. Neither SBN 35 nor SBN 55 spectra present significant structural variations; SBN 14 glass' spectrum does exhibit a pronounced variation located in the ballistic part but not significant variations in the electronic region. Finally, the SBN 12 spectra presents variation in the electronic and the ballistic part. Structural changes take place in the entire region impacted by 6 MeV He^{2+} irradiation, i.e. from the free surface to ~ 30 μm. For all the glass compositions herein, ballistic interactions produce more noteworthy changes in the Raman features.

Finally, the structural variations induced by electron and helium irradiation are not equivalent. SBN 14 after β_e^--irradiation appears to have areas enriched in silica and others enriched in boron. This trend does not take place after He^{2+} irradiation. Abbas et al. already observed this discrepancy [1]. He specifically observed variations in Na^+ migration: the He^{2+} irradiation increases the sodium concentration close to the free surface, whereas a depletion take place after β_e^--irradiation. Finally the dose integrated is equivalent for β_{e^-}- and He^{2+} ions irradiation and equal 1 GGy. The discrepancies observed in structural changes are maybe due to penetration depth of the incidented particle. The β_{e^-} particles penetrate the 0.8 mm of the sample thickness, whereas the He^{2+} ions go through the first ~ 30 μm of the glass sample and hence concentrate the damage in a thin layer.

5.1.3 Structural damages induced by Au^+ irradiation

The first 2 μm energy loss is due to electronic and ballistic damage. Again, the qualitative variation in the structure is given by the Raman analysis.

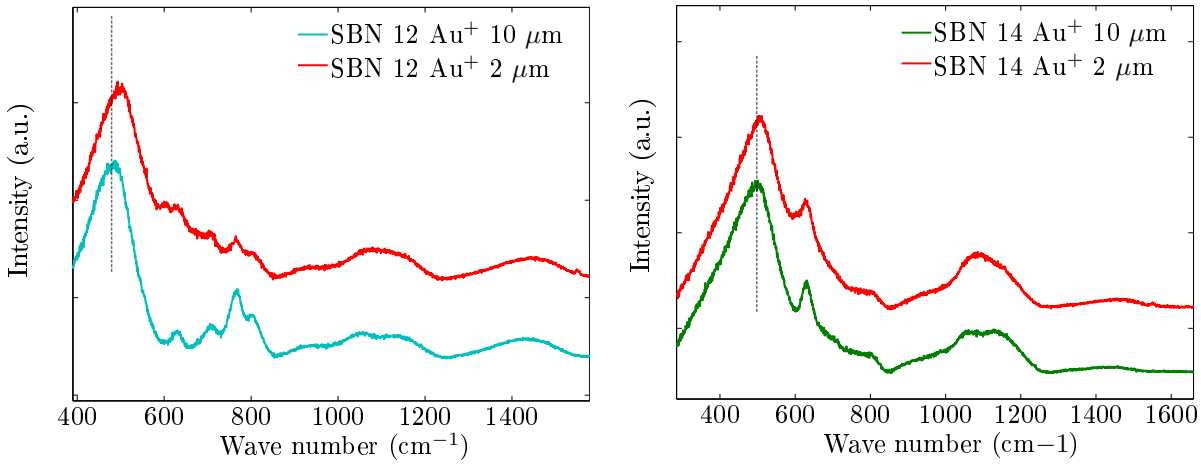

Figure 5.11: Raman spectra of SBN 12 (left) and SBN 14 (right) irradiated by Au^+ ions from the irradiated zone (top red curve; 2-3μm from the free surface) towards the bulk (bottom curve; 10μm).

SBN 12

Figure 5.11 left depicts the evolution of Raman features of SBN 12 in the irradiated zone (red curve, 2-3μm from the free surface) and in the bulk (turquoise curve; 10μm from the free surface). Several significant modifications take place:

- The Si-O-Si bending vibration band shifts towards high wave number values
- The D_2 peak increases.
- The contribution between 650 and 800 cm^{-1} vary.
- The Q_n band changes.
- The O_2 molecular peak around 1550 cm^{-1}.

Again, the shift in the Si-O-Si bending vibration band may be associated with a decrease in the mean value of Si-O-Si angle. Matson [14] link the Si-O-Si shift depolymerization of the silicate network. This can be correlated to an increase of NBO in the silicate network. Finally, the decrease in borate- and borosilicate-rings may be linked to a higher connectivity between the borate and the silicate networks. The increase in the O_2 contribution is usually associated to sodium migration and is explained by a polymerization of the silica network following: $2\ Si-O^- \rightarrow Si-O-Si + \frac{1}{2}O_2$ [16].

The figure 5.12 left compares the Raman spectra of pristine, He^{2+}-irradiated (ballistic area) and Au^+ ion irradiated SBN 12 samples. Variations of the Raman feature induced by 6 MeV helium and multi energy gold ions resemble each other, but the latter induce more pronounced variation: the increase of D_2 band is clearly seen after Au^+ irradiation. The Au^+-irradiation may increase the connectivity between the silica and boron networks.

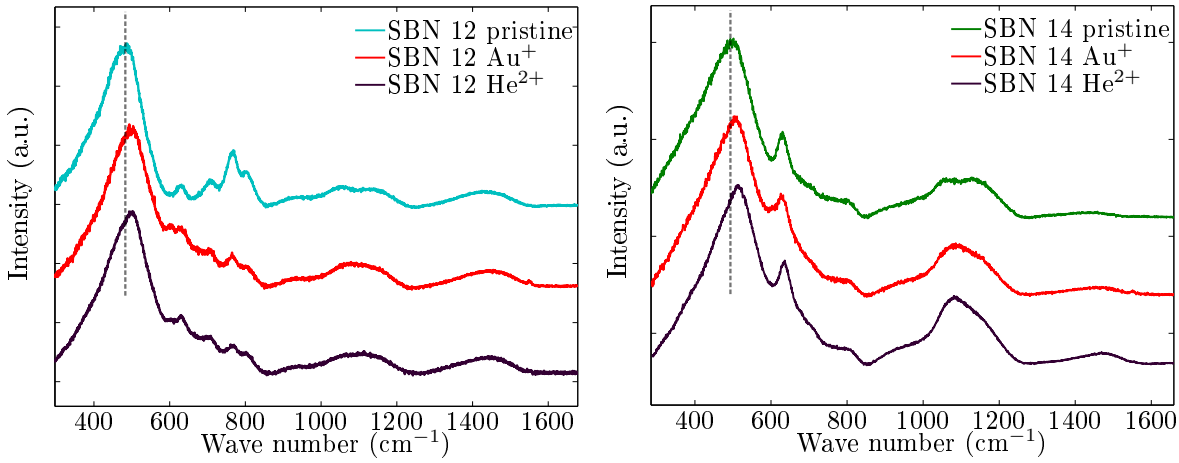

Figure 5.12: Raman spectra of pristine (top), Au^+-irradiated (ballistic area and red curve) and He^{2+}-irradiated (brown curve) SBN 12 (left) and SBN 14 (right) irradiated samples. The two plots present a dashed gray line which marks the position of the Si-O-Si bending vibration band for the two pristine glasses. A shift is observed towards high wavenumber values.

SBN 14

The figure 5.11 right depicts the evolution of Raman features of SBN 14 in the irradiated zone (red curve, 2-3μm from the free surface) and in the bulk (green curve; 10μm from the free surface). Variations can be seen with different strengths between the Raman spectra:

- The Si-O-Si peak shifts to higher wavenumbers.
- The Q_n band changes.
- The $B-O^-$ band contribution increases slightly.

SBN 35 and SBN 55

Figures 5.13 present the Raman spectra of SBN 35 (left) and SBN 55 (right) after multi-energy Au^+-irradiation. SBN 35 (figure 5.13 left) spectra reveal the modifications primarily around the Q_n bands and the $B-O^-$ contribution. Changes occur in the Q_2/Q_3 ratio, and a slight increase in $B-O^-$ band takes place. The SBN 55 sample presents more pronounced variations after Au^+ ions irradiation. First, slight changes appear in the shoulder around 730 cm^{-1}. As presented in Part I chapter 3, literature attributes this peak to chain of metaborate units, but the signification is rather unclear [12]. A second modification takes place around the Q_n band. The 950 cm^{-1} increases at the expense of the 1080 cm^{-1} peak. Finally, the $B-O^-$ band increases significantly. The molecular O_2 contribution also appears. Au^+-irradiation induces minor changes in the SBN 35 Raman features. The modifications of the spectra imply depolymerization and a slight change in the coordination number of boron. The SBN 55 presents more pronounced variations (significant increase in the $B-O^-$ contribution). NMR measurement should permit to estimate the amplitude of variations.

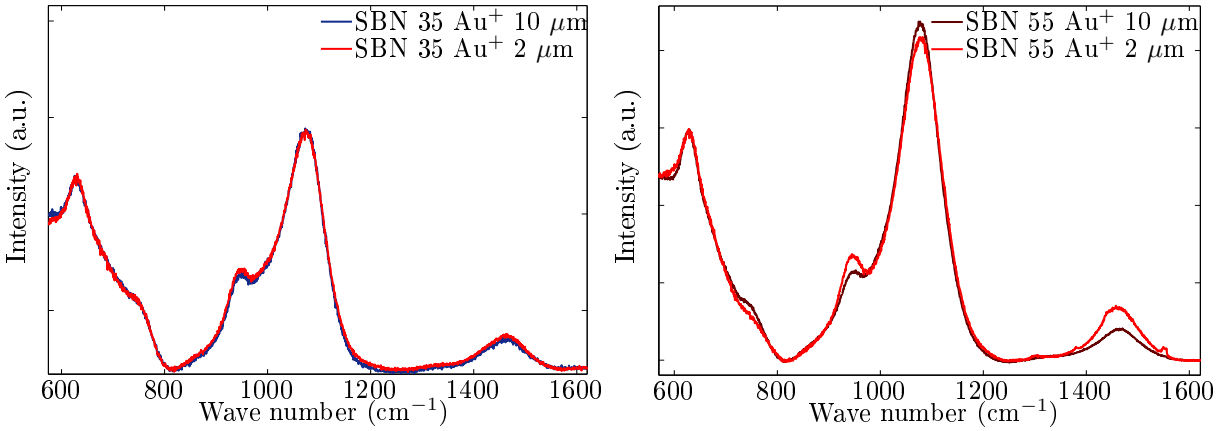

Figure 5.13: (Left) Raman spectra of SBN 35 before and after irradiation. The blue spectrum concerns the non-irradiated glass and the red spectrum the gold irradiated at 2μm from the free surface; (Right) Raman spectra of SBN 55 before (red) and after (dark red) irradiation.

5.1.4 Discussion

The nuclear energy deposited by Au^+-ions is below 10^{20}keV/cm^3 which is the threshold set by Mendoza et al. above which one can expect significant damage in borosilicate glass [15]. Herein, the irradiation conditions are similar to those of J. de Bonfils [3,4] on the SBN 14 glass. He observed significant changes after irradiation: (1) glass swelling; (2) the conversion of $^{[4]}$B into $^{[3]}$B; (3) the depolymerization of the silicate network with a decrease in the mean Si-O-Si angle. Overall modifications observed after gold irradiation on the SBN series are coherent with J. de Bonfils' results. The amplitude of variation depends on the chemical compositions. For low sodium content, a decrease of the Si-O-Si angle occurs (and a clear increase in the D_2 band for the glass SBN 12). For high sodium content, the Raman analysis mainly shows variations in the Q_n band and the $B-O^-$ band. The Raman analysis qualitatively describes variations induced by irradiation. Mendoza et al. [15] performed NMR analysis on similar glasses irradiated by 74 MeV Kr ions. After irradiation, the quantity of $^{[4]}$B decreases with respect to $^{[3]}$B and also a huge dependence in the chemical composition is also observed. The SBN series probably follows the same trend after gold irradiation; but NMR measurements need to be performed to quantify these variations. The next section examines the impact of structural variations on the mechanical properties.

5.2 Mechanical properties

Light and heavy ion irradiations alter the structure of the glasses. This section details how these variations impact hardness values (section 5.2.1). Despite the fact that I did not have access to the SCC curves, I will also present the resulting fracture surfaces observed at different depths, from the free surface toward the bulk of the material. This will highlight variations in the crack paths between irradiated zones and bulk material (5.2.2) via the fluctuations in the RMS of the fracture surfaces.

5.2.1 Hardness

Chapters 3 and 4 of this part evidence changes in the glass structures can drastically change the behavior of the glass under an indenter. Yet, the damage region remains very close to the surface. Probing this thin layer requires nano-indenters where the control parameter is the depth of penetration. Both He^{2+} and Au^{+} irradiations use nano-indenters. The absolute values of the hardness cannot be compared directly with micro-indentation tests, but the differences can provide information (table 3.11). The hardness value is estimated using a Berkovich tip and is referred as H_B.

He^{2+} irradiation

The understanding on how hardness varies with the depth of penetration provides insight on the consequences of irradiation damages. As presented in the chapter 2, I performed nano-indentation measurement on the fracture surfaces. It gives the evolution of the hardness with the ion penetration depth. Figure 5.14 left depicts series of indentations from the free surface into the bulk of the material. The black band on the left part of the figure corresponds to the free surface. From SRIM calculations, the first 4 indents correspond predominantly to electronic interactions (0-20 μm). The next 3 indents probe the region with ballistic interactions ($\sim$20-35 μm). Subsequent, indents predominantly probe the bulk material. Figure 5.14 right depicts the evolution of hardness versus the distance from the free surface. The different glasses reveal slightly different behaviors:

- SBN 12 (cyan line): The hardness value decreases in the irradiated area. The first 20 μm concerns the zone where electronic damages are predominant. Then, around 20-30 μm, the hardness values continue to decreases until 30 μm. The variation is of $\sim$30% decrease in H_B value. At $\sim$ 35 μm, the indent probes areas not impacted by irradiation, the variation in H_B value is null.
- SBN 14 (green line): For the first 5μm H_B value is very close to the bulk value. Then, it decreases about 10% for the next 2 indents. Afterwards H_B continues to decrease as it moves more into the ballistic damage region. The minimum is obtained at 25-30 μm from the free surface. After, the non-irradiated zone is probed and the hardness value does not evolve. It should be noted that, even if a slight decrease in the first 15 μm is observed, this is not conclusive regarding the error bars.
- SBN 35 (dark blue line): Variations in the hardness value of SBN 35 follow SBN 14's trends. The exception to this is in the first 5 μm where hardness decreases slightly. The minimum occurs at 25 μm. Then, the hardness variation decreases to $\sim$ 0 % because the probed region is not impacted by irradiation.
- SBN 55 (dark red line): The hardness variations decreases continuously until they reach an extremum around 25μm. A zero variation occurs at $\sim$ 35 μm from the free surface corresponding to the bulk material.

All H_B values reach a minimum around 25 μm with the exception of SBN 14 which the minimum ranges between 25 and 30 μm. Subsequently for all samples, H_B values increase and reach its bulk value (within the error bar) by $\sim$30 μm. We can note trends in SBN 14, SBN 35, and SBN 55 for regions impacted by electronic irradiation (0-20 μm) due to error bars. On the other hand, SBN 12 has a noteworthy decrease of H_B in the electronic regions. The changes in the glass structure change drastically alter the mechanical

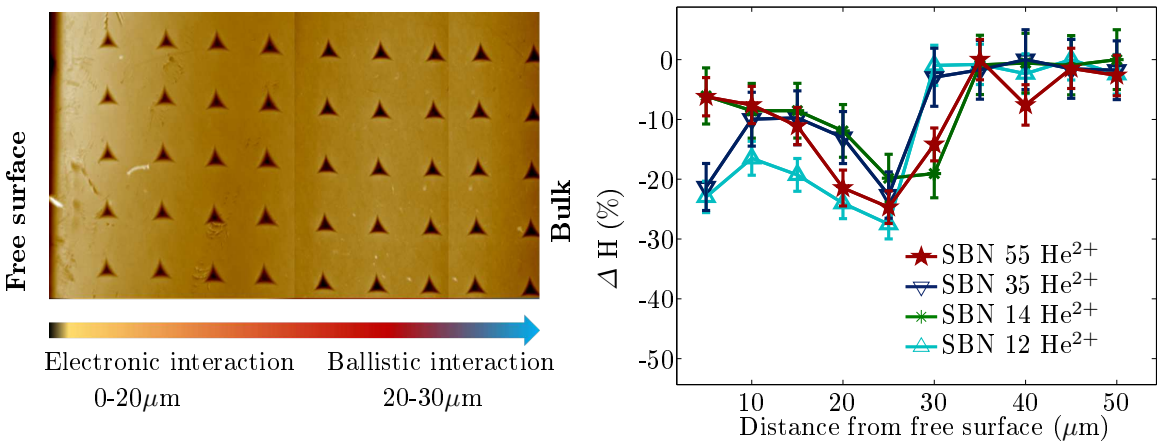

Figure 5.14: (Left) AFM images of nano-indentations performed on the SBN 12 from the free surface (left side of image) towards the bulk; (Right) Evolution of the hardness from the free surface towards the bulk for SBN 12, SBN 14, SBN 35 and SBN 55 glasses.

response of the SBN glasses. Major modifications occur after He^{2+} ions: (1) depolymerization of the silica network; (2) conversion of $^{[4]}B$ into $^{[3]}B$. The increase of weak spots including NBO can explain variations in hardness observed [2]. SBN 12 presents the most significant decrease in H_B value in the electronic part. Raman analysis points out structural variations similar to those observed in the ballistic part but less pronounced. This can explained the slight decrease of hardness. Finally, the maximum decrease for H_B ranges from $\sim$ 20 % for SBN 14 to $H_B \sim$ 28 % for SBN 12. Yet, the difference is questionable. Some of the uncertainties in these measurements arise from the matrix around the indenter. For example, the indenter's response between15-30 μm is a mixture of electronic and ballistic damage. In the case of SBN 12 which is significantly impacted by electronic damage (i.e. 20% decrease in H_B), H_B at 25 μm represents a mixed response. Despite this, it is clear that ballistic interactions play a major role in decreasing H_B [4, 18].

Au^+ irradiation

The previous section revealed how 6 MeV He^{2+}-irradiation varies the hardness with penetration depth as measured on SCC fracture surfaces. The Au^+-irradiation produces an even thinner layer ($\sim$3μm). Thus indentations on the fracture surfaces are not reasonable. Au^+-irradiation undergoes both nuclear and ballistic interactions from the free surface inwards. Hence, indentations occur on the irradiated surface. The penetration depth is kept constant at 500 nm. Figure 5.15 depicts H_B value for the pristine glasses and H_B for its Au^+ counterpart. The left figure present the real value; and the right figure the variation calculated between the pristine and the irradiated glasses. The multi-energy Au^+-irradiations induce a decrease in H_B. H_B variations are similar to those observed after He^{2+}-irradiation.

Mendoza et al. correlates this decrease with an increase in the number of weak spots [15]. J. de Bonfils found similar results on SBN14 [3, 4]. He associated a global decrease in the hardness with a conversion of $^{[4]}B$ into $^{[3]}B$ and a glass swelling. The sodium released enables the depolymerization of the silica network, which should also impact the behavior under the indenter. Kilymis et al. [10] investigated

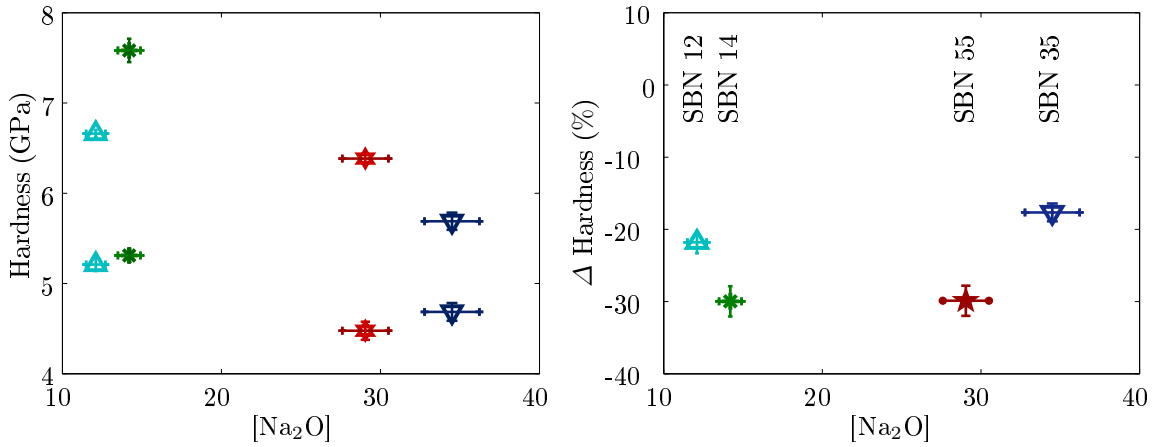

Figure 5.15: Evolution of the hardness for SBN 12 (light blue), SBN 14 (green), SBN 35 (dark blue) and SBN 55 (dark red) glasses versus [Na_2O]. The same vertical line contains H_B for the pristine and Au^+-irradiated. The left figure presents the true values and the right one the variations between the pristine and its irradiated counterpart. Gold irradiation induces a decrease in hardness and the amplitude of variation depends on the chemical composition.

hardness evolution after irradiation via MD simulations. Our trend is coherent with this study: he observed a decrease in hardness values associated to the conversion of $^{[4]}$B into $^{[3]}$B and the creation of NBOs.

The second observation is the amplitude of variation which depends on the initial glass composition. For the SBN 14 and SBN 55 glasses, H_B value decreases by $\sim$ 30 %, whereas H_B value of SBN 12 and SBN 35 decreases by $\sim$ 20 %. G. Bureau [5] pointed out the role of the initial glass composition on changes observed after irradiation. She concluded that glasses with a high degree of polymerization are more sensitive to irradiation than depolymerized glasses [5]. This is not observed here. Both SBN 35 and SBN 55 contain a significant number of NBO and $^{[3]}$B. Conversely, SBN 14 contains a few NBO, and its decrease is similar to that of SBN 55. The results herein fall more in line with K_{SBN} series trends. Raman analysis aids in describing qualitatively the structural variation induced by irradiation. Yet, NMR analysis could quantify variations: (1) evolution of the NBO in the silica network, (2) evolution of the coordination number of boron atoms. Mendoza et al. quantified on similar glasses variation induced by 74 MeV Kr ions. They showed a chemical composition dependency on the structural changes [15]. Finally, this study underlines the dominant role of ballistic interactions on the changes in H_B.

5.2.2 SCC behavior

Light and heavy ions irradiations only impact a thin layer of the glass samples. Thus, samples broken in the DCDC format depend on the bulk behavior rather than the surface properties. SCC curves in the future will arise from the new experimental setup presented in section 2.4.2. Until that time, direct measurements of SCC curves remain out of reach. Yet, indirect information arises from SCC fracture surfaces in these regions which reveal how the crack tip broke the samples.

He^{2+} ion irradiation

For each glass, an AFM images the fracture surfaces from the free surface inwards in pristine and He^{2+}-irradiated samples. Figure 5.16 depicts the fracture surfaces of the He^{2+}-irradiated SBN 14. The images correspond to the electronic region (yellowish frames), ballistic/electronic region (marron frames), and bulk (green frames). No significant variations occur in the electronic (yellowish) zone. The pattern and the RMS values ($RMS_{electronic\ zone} \sim 0.6$ nm) do not evolve. A change in the roughness occurs around 28 μm. The RMS values increase by 50% ($RMS_{ballistic\ zone}$ ~0.91 nm). Then, the RMS decreases back to about 0 around 34 μm. The $RMS_{bulk\ zone}$ and $RMS_{electronic\ zone}$ are nearly equivalent for SBN 14 glass. The figure 5.17 presents RMS variations in the fracture surface from the free surface to the bulk for all SBN samples. The reference value is taken at 50 μm from the free surface. The measurements are done on the SBN glasses irradiated and on their non-irradiated counterpart. For clarity, figure 5.17 only shows SBN 14 non-irradiated (black line) of the non-irradiated samples. The area very close to the free surface (few μm) often contains damaged. Both irradiated and non-irradiated sample have damage near the free surface. For all the SBN glasses, irradiation impacts the path followed by the crack and highlight the glass disorder. Overall, the highest RMS variation takes place around 25-30 μm from the free surface. SBN 12 displays also a variation in the RMS for the region which undergoes electronic interactions. The other glasses do not display a significant difference and damage localizes around 25-30μm. This results match with the Raman analysis. Variations observed for the SBN 14, SBN 35 and SBN 55 localize in the region of maximum ballistic interactions. The increase in the glass disorder is coherent with results in literature [9,10,15,17].

Au^{+} ion irradiation

AFM images gather topographical measurements from the free surface inwards on Au^{+} ion irradiated samples. Figure 5.18 presents evolutions of SBN 14's fracture surface from the free surface towards the bulk after Au^{+}-irradiation. The left AFM image presents the zone close to the free surface and impacted by irradiation. The middle image presents the fracture surface around 3-4 μm. the last image displays the fracture surfaces around 5 μm where the ions are not supposed to penetrate. The color bar is the same for all three images. A clear decrease in the RMS occurs from the free surface (left image) to the bulk (right image). Finally, a clear transition line is observed between the irradiated zone and the non-irradiated part. This indicates the limit of Au^{+} ions penetration. Figure 5.19 presents the variation in the fracture surface's RMS (with respect to the bulk) from the free surface into the bulk. The damaged zone localizes in the few first μm from the free surface, as predicted by the SRIM simulations. A significant increase in the RMS value occurs for the first 3 μm. The variations become irrelevant after 4μm. The RMS variations (50 %) for SBN 12 and SBN 35 are less than the variations for the SBN 14 (78 %) and SBN 55 (slight increasing trend from 63 % to 75 %). As in He^{2+}-irradiation, K_{SBN} groupings could be relevant; yet more glasses in these series should be studied before reaching a conclusion.

5.2.3 Discussion

Both light and heavy ion irradiations change the crack path. The RMS depends on heterogeneities in the glass structure [7, 19]. Increasing the glass disorder leads to an increase in RMS value which is

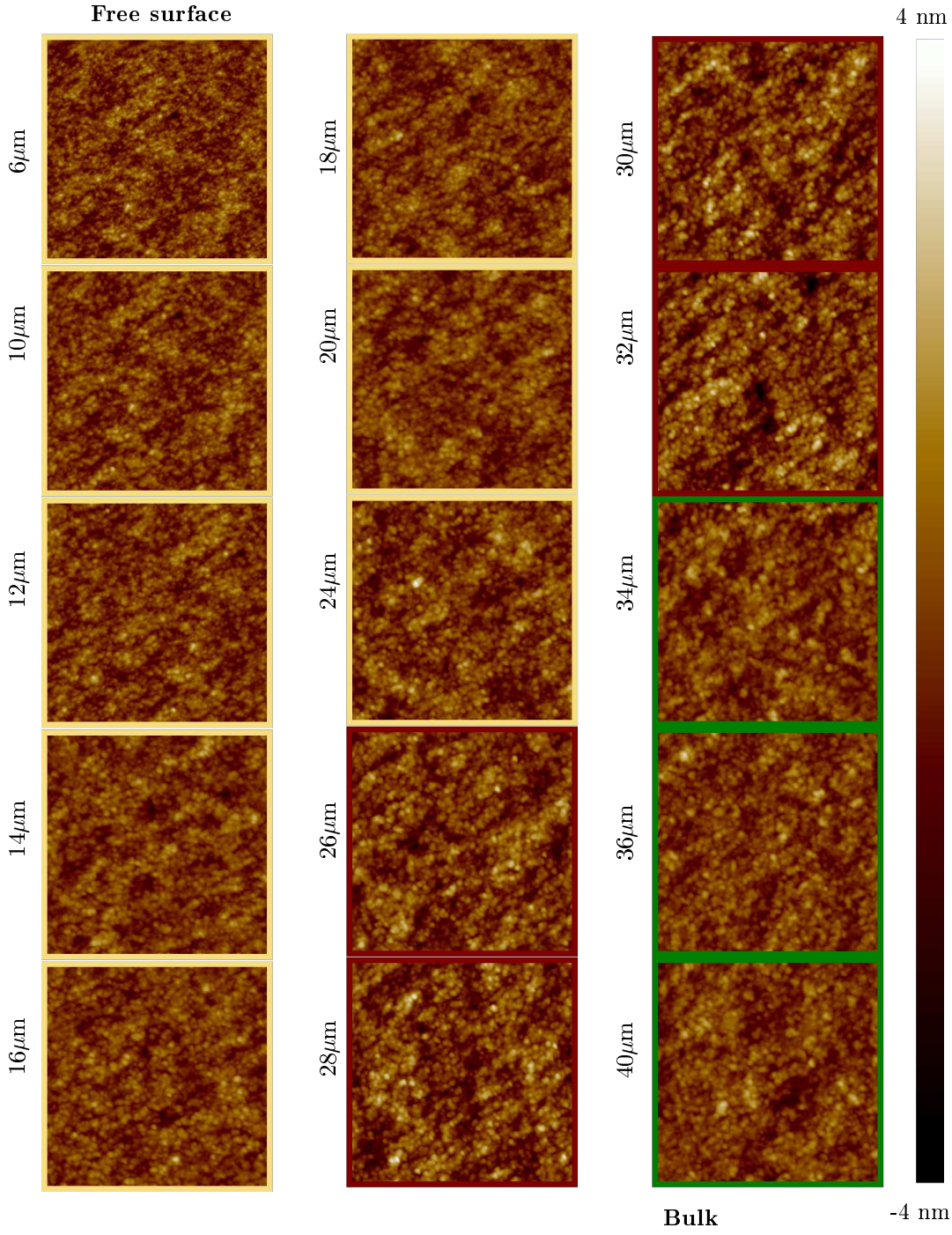

Figure 5.16: The series of images depicts the fracture surfaces from the free surface to the bulk for the SBN 14 irradiated by helium ions. The frame color corresponds to the zone previously defined: the yellow zone marks the area where interaction are dominated by electronic interaction, the brown zone, the area where ballistic interactions are maximum and the green area correspond to the bulk of the sample. The color bar is kept constant for all the AFM images.

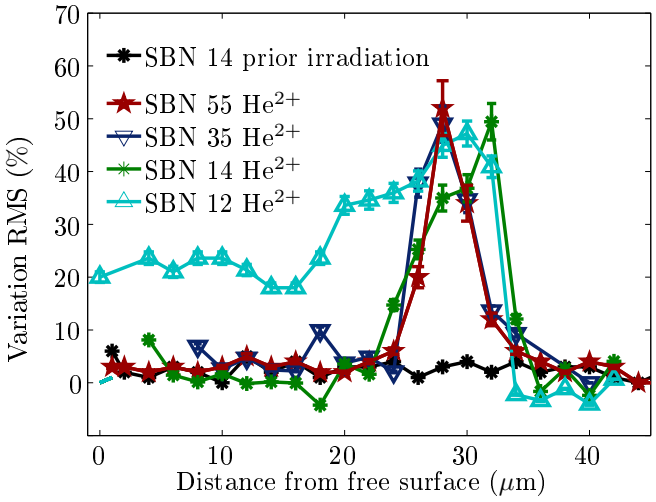

Figure 5.17: Evolution of the RMS value of the SBN glasses after helium irradiation. The SBN 12 (light blue), SBN 14 (green), SBN 35 (dark blue) and SBN 55 (dark red) are investigated from the free surface (0 μm) towards the bulk (45μm). For each SBN glasses, both irradiated and pristine samples are also investigated. For clarity, only the SBN 14 (black) is plotted.

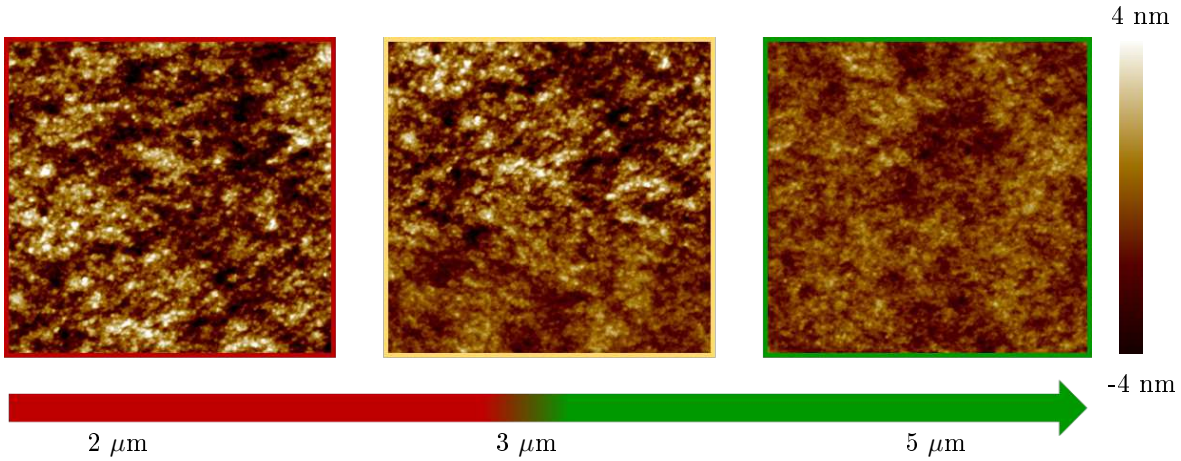

Figure 5.18: Evolution of the fracture surfaces roughness from AFM images at 2 μm, 3 μm and 5 μm from the free surface.

coherent with literature [4, 6, 8–10]. L.-H. Kieu investigated the evolution of fracture surfaces roughness via simulations. He simulated irradiated glasses by quenching at high rate and studied the behavior in dynamics fracture. He concluded that increase in the glass disorder lead to an increase in the post-mortem fracture surfaces [8]. Analysis of the fracture surfaces' roughness also highlights the increase in the RMS with the glass disorder. Depolymerization of the silicate network, changes in the coordination number of the borate atom, and/or densification of the silica ring structure leads to variations in the number of weakest points and the glass' response to stress. The increase in the glass disorder should lead to variation in the SCC behavior. The next step in this study is the finalization of the 4-point bending experimental set-up, and its implementation. This apparatus will permit the investigation of the SCC

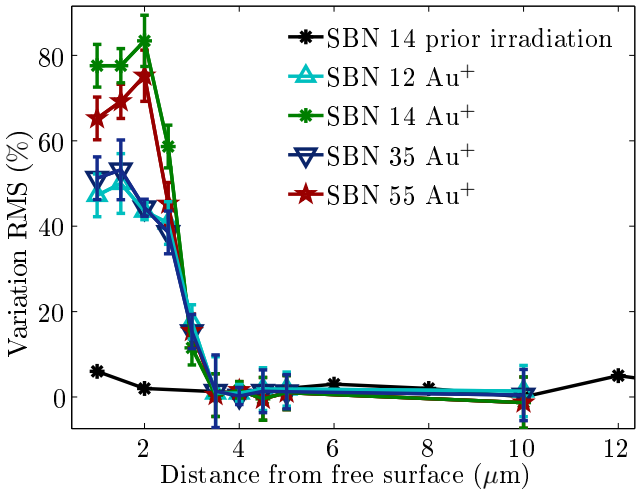

Figure 5.19: Evolution of the RMS value of the SBN glasses after gold irradiation. The SBN 12 (light blue), SBN 14 (green), SBN 35 (dark blue) and SBN 55 (dark red) are investigated from the free surface (0 μm) towards the bulk (10μm). For each SBN glasses, their non-irradiated counterparts are also investigated. For clarity, the figure contains only pristine SBN 14 (black).

properties in He^{2+} and Au^{2+} irradiated zones.

The hardness behavior is also significantly impacted. Experimental investigations on irradiated glasses and MD simulation performed on fast quenched glass confirm this trend [4,10,15]. Recently, Kilymis et al. simulated irradiated SBN 12, SBN 14 and SBN 55 and estimated the evolution of hardness. First, these simulations revealed an increasing disorder which lead to an increase in $^{[3]}$B and the depolymerization of the silicate network. The amplitude of hardness variation depends on the initial chemical glass composition as observed here experimentally. These authors conclude that the amplitude variation depends on the amount of structural variation: the conversion of $^{[3]}$B and the number of NBO. To understand the variation in amplitude, this study requires NMR measurements to quantify each variation for each chemical composition. Finally, the study herein also highlights the important role of ballistic interaction in changing the mechanical response of glasses. Variations in the mechanical response dominate where ballistic interactions maximize.

5.3 Conclusion

The ions irradiation induces different damages depending on the nature, the energy and the fluence of the ions. The helium irradiation mainly induce electronic damages (99 %). Gold irradiation induce both electronic and nuclear damages (75 % and 25 %, respectively).

- **Glass disorder increases** The RMS estimated from fracture surface increase significantly in the irradiated zone. This is associated to structural variation: change in the borate- borosilicate rings (conversion of $^{[4]}$B into $^{[3]}$B, decrease in the mean Si-O-Si angle) and an increase in NBO concentration.

- **Hardness decreases** An increase of the glass plasticity leads to a decrease of the hardness. Depending on the glass chemical composition, the amplitude of variation ranges from 20-30 μm. Variation in the coordination number of boron atom and increase in NBO appear to be the relevant parameter to govern the hardness behavior.
- **Evolution of the crack path** The increase in the glass disorder and the change in the glass topology impact the path followed by the crack. As a consequence, changes in the SCC behavior are expected. Further studies are required to investigate how the SCC is impacted.

Bibliography

[1] A. Abbas. Contribution à l'étude des effets de l'irradiation α sur les verres nucleaires. Technical report, CEA Direction de l'énergie nucléaire, 2002.

[2] N. Bibent, A. Faivre, G. Ferru, J.L. Bantignies, and S. Peuget. Silica structural changes induced by thermal treatment or ionic implantation as probed by ir reflectance spectroscopy. *J. Appl. Phys.*, 106:063512, 2009.

[3] J Bonfils de. *Effets d'irradiations sur la structure de verres borosilicates-Comportement a long terme des matrices vitreuses de stockage des dechets nucleaires.* PhD thesis, Université Claude Bernard - Lyon I, 2007.

[4] J Bonfils de, S. Peuget, G. Panczer, D Ligny de, S Henry, P. Y. Noel, A. Chenet, and B. Champagnon. Effect of chemical composition on borosilicate glass behavior under irradiation. *J. Non-Cryst. Solids*, 356:388–393, 2010.

[5] G. Bureau. *Comprehension structurale des effets d'auto-irradiation alpha dans les verres: couplage entre etudes spectroscopiques et modelisation atomistique.* PhD thesis, Universite Pierre et Marie Curie (Paris VI), 2008.

[6] N. Deladerriere, J.M. Delaye, F. Augereau, G. Despaux, and S. Peuget. Molecular dynamics study of acoustic velocity in silicate glass under irradiation. *J. Nucl. Mater.*, 375:120–134, 2008.

[7] R.V. Goldstein and R.L. Salganik. Brittle fracture of solids with arbritary cracks. *Int. J. Fracture*, 10:507–523, 1974.

[8] L.-H. Kieu. *Compréhension de l'origine de l'évolution sous irradiation de la ténacite des verres nucléaires.* PhD thesis, Ecole Doctorale Polytechnique, 2011.

[9] D. A. Kilymis and J. . M. Delaye. Nanoindentation of pristine and disordered silica: Molecular dynamics simulations. *J. Non-Cryst. Solids*, 382:87–94, 2013.

[10] D. A. Kilymis and J-.M. Delaye. Nanoindentation studies of simplified nuclear glasse using molecular dynamics. *J. Non-Cryst. Solids In press*, 2014.

[11] W.L. Konijnendijk and J.M. Stevels. The structure of borate glasses studied by raman scattering. *J. Non-Cryst. Solids*, 18:307–331, 1975.

[12] H. Li, L.Y. Su, and D.M. Strachan. Raman spectroscopic study of gadolinium (iii) in sodium-aluminoborosilicate glasses. *J. Non-Cryst. Solids*, 292:167–176, 2001.

[13] D. Manara, A. Grandjean, and D.R. Neuville. Advances in understanding the structure of borosilicate glasses: A raman spectroscopy study. *Am. Mineral.*, 94:777–784, 2009.

[14] D.W. Matson, S.K. Sharma, and J.A. Philpotts. The structure of high-silica alkali-silicate glasses. a raman spectroscopic investigation. *J. Non-Cryst. Solids*, 58:323–352, 1983.

[15] C. Mendoza, S. Peuget, T. Charpentier, M. Moskura, R. Caraballo, O. Bouty, A.H. Mir, I. Monnet, C. Grygiel, and C. Jegou. Oxide glass structure evolution under shift heavy ion irradiation. *Nucl. Instr. Meth. Phys. Res. B*, 325:54–65, 2014.

[16] D.R. Neuville, K. Cormier, B. Boizot, and A.M. Flanck. Structure of beta-irradiated glasses studied by x-ray absorption and raman spectroscopies. *J. Non-Cryst. Solids*, 323:207–213, 2003.

[17] S. Peuget, J. M. Delaye, and C. Jegou. Specific outcomes of the research on the radiation stability of the french nuclear glass towards alpha decay accumulation. *J. Nucl. Mater.*, 444:76–91, 2014.

[18] S. Peuget, P.Y. Noel, J.L. Loubet, S. Pavan, P. Nivet, and A. Chenet. Effects of deposited nuclear and electronic energy on the hardness of r7t7-type containment glass. *Nucl. Instrum. Methods Phys. Res. B, Beam Interact. Mater.*, 246:379–386, 2006.

[19] S. M. Wiederhorn, J.M. Lopez-Cepero, J. Wallace, J. P. Guin, and T. Fett. Roughness of glass surfaces formed by sub-critical crack growth. *J. Non-Cryst. Solids*, 71:1582–1591, 2007.

Conclusion Part II

Part II investigates how tweaking the structure of silica and SBN glasses via external irradiation alters the mechanical properties.

From the eight borosilicate glasses studied in the part I, four SBN glass compositions plus pure silica are selected. Samples undergo three types of external irradiation: electron, helium ions and gold ions. Electrons bombard the samples with an energy of 2.5 MeV which permit a penetration through the sample thickness of 0.8 mm. β_{e^-}-irradiations induce homogeneous damages, whereas the helium and the gold ion irradiations only impact a thin layer of the glass samples, 30 μm and 3 μm, respectively. Irradiation with helium and gold ions investigates the role of each interaction on the structural and mechanical properties. Helium irradiation induces damages mainly through electronic excitations ($\sim$ 99 %). Gold irradiation induces damages through both electronic and damages excitations, $\sim$ 75 % and $\sim$ 25 %, respectively. The energy of He^{2+} is 6 MeV with a dose of 3.8×10^{15}ions/cm^2. Gold ions irradiations were done with multi-energy ions to get an almost constant nuclear interaction deposited over the 3 μm impacted. Density measurements, Raman and EPR analysis give access to the physical and the structural properties of glasses after irradiation. The estimations of the mechanical properties take place through the hardness tests, K_C and SCC tests. Non-homogeneous deposition of energy for ion-irradiations gave way to a new experimental 4-bending test which is currently going through the testing phase.

The pure silica glass properties remain unchanged after β_{e^-}-irradiation. The variations in the stress corrosion behavior and the hardness are not significant. Compaction of the silica ring structure occurs after ion irradiations. He^{2+} ions irradiations lead to a decrease in the hardness values ($\sim$ 10 %). Micro crack marks are also observed on post-mortem fracture surfaces. Irradiation induces a densification in the silica network and the creation of microcracks which can join the main crack front during experiments and explaining the pattern observed. Such features were not observed after Au^+-irradiation. Similarly to helium ions irradiation, the damaged zone is denser and presents a lower hardness values ($\sim$ 10 %). Due to the thin layer impacted by ions irradiation, SCC information is not available. Finally, these experiments highlight the predominant role of the ballistic interactions in variations of mechanical properties.

This part also investigates the impact of irradiation on the SBN glass properties. The impact of β_{e^-}-irradiation on the SBN series depends on [Na_2O]. Low sodium content glasses are significantly

impacted: high concentration of paramagnetic defects, significant structural variations, and changes in the mechanical properties. For high sodium content, [Na_2O] inhibits the structural modifications. As a consequence, the hardness and the behavior in SCC regime are not impacted. Finally, how the residual stress impacts the mechanical response is not known. Further investigations should be conducted to estimate this effect because it may be significant. Ion irradiations induce variation in all the SBN glasses investigated. He^{2+} and Au^{+} ions increase the glass disorder. Helium irradiation increases the RMS value in an area localized around 20-30 μm from the free surface, where the ballistic interactions are maximum. Gold irradiations induce damages in the area localized in the first 3 μm from the free surface and the RMS increases significantly. After irradiation, the hardness value decreases due to an increase in the glass plasticity. The relevant parameters are the NBOs and the coordination number of the boron atom. The increase in $^{[3]}$B and NBO makes the penetration of the indenter easier. Again the modification of the hardness behavior after 6 MeV helium irradiation is localized around 20-30 μm from the free surface, where the ballistic interactions maximize. This highlights the predominant role of the ballistic interactions on the evolution of the glass properties.

Future works concerns the estimation on how the residual stress impacts the mechanical response. This effect may be significant, and thus, the interpretation on how irradiation impacts the mechanical response is tricky. Finally, variations induced by β_{e^-}-irradiation and variations induced by the electronic interactions due to He^{2+}-irradiation are not equivalent. This effect may be explained by the fact that β_{e^-}-irradiation penetrates though the entire sample thickness (0.8 mm) whereas He^{2+} only impacts a thin layer. Further studies should investigate this discrepancy.

Discussion and General Conclusion

This thesis investigates the impact of borosilicate structure on its mechanical properties. Working in the SiO_2-B_2O_3-Na_2O glass system permits to modulate the chemical glass composition and to understand the role of each oxide.

Generalizing complex glasses by their three main components (SiO_2-B_2O_3-Na_2O) is tricky. The oxide ratios in glasses significantly alter the glasses mechanical behavior and its response under external irradiation. Glasses containing high amounts of oxides relax and to adjust their stresses readily.

The mechanical response of SBN glasses greatly depends on their structure (tweaked via chemical composition and irradiation). H_V depends on the glass network reticulation: increasing the NBO concentration decreases H_V. Irradiation causes H_V to decrease. Several modifications occur depending on the type of irradiation: (1) a glass swelling; (2) variation in $^{[3]}B/^{[4]}B$ ratio and (3) increase of NBO concentration. All of these variations lead to an increase in the glass plasticity and a decrease of resistance to a sharp indenter.

This work also investigates how the matter flows under an indenter. Two processes may occur: densification and shear flow. Depending on the glass topology, the contribution of the two processes differs. The glasses with a poor concentration of NBO and higher packing fraction densify preferentially. On the other hand, glasses with a high amount of NBO deform via shear flow mechanism. How the matter flows under an indenter depends on the glass structure and more specifically the Poisson's ratio. Low Poisson's ratio implies a glass with a high degree of reticulation and low packing fraction. The converse is true for a high Poisson ratio. These factors impact residual stresses. As a consequence, the crack morphology changes with the contribution of densification/shear flow processes. Shear flow processes favor the propagation of median/radial cracks, whereas densification induces preferentially cone cracks. This directly impacts the K_C measured by indentation. (K_C estimations arise from measurements of median/radial crack length). Glasses with high Poisson's ratio, i.e. with lower degree of polymerization and high packing fraction, favor shear flow and the propagation of median/radial cracks present a lower K_C.

The consequences of irradiation on K_C values required more investigations. Irradiation changes the glass plasticity. Glass swelling should permit a better densification under indenter of the glassy network and an increase in K_C. A contradictory scenario is also feasible increasing the number of NBO should favor shear flow and the propagation of median/radial cracks and K_C decrease as is the case of pristine

SBN samples. NMR experiments should be performed to quantify these topological variations to estimate how they can impact the K_C.

Studies herein re-highlight a lack of general understanding of the mechanisms occurring at the crack tip. Despite this, SCC curves herein provide pertinent information. The shifts in the SCC curves indicate changes in the glass's plasticity. Increasing the [Na_2O] increases K_E. This is understood by a shielding effect which screens the external stress applied due to structural accommodations. Thus, higher loads initiate the crack. The irradiations also change the glass plasticity and depend on the glasses structure. A shift in K_E occurs. Part of this shift could be due to residual stresses, yet annealing them out could reverse the structural trends frozen in by irradiation. Furthermore, polarizers can reveal residual stresses, yet irradiation caused the glasses to become opaque making this not a suitable technique. In the future it would be interesting to conduct residual stress tests on irradiated samples. Finally, increasing [Na_2O] changes significantly the SCC slope. This is understood as an increase in the glass's reactivity with the water. [Na_2O] induces preferential path to water. After irradiation only glasses with significant structural modifications changes their behavior under irradiation. It is seen that paramagnetic defects (estimated by EPR measurements) have limited effect on the hardness and the SCC behavior.

Tweaking the glass structure via changes in the chemical composition and irradiations are not equivalent. (The latter one has the potential to induce residual stresses which were not taken into consideration here.) This investigation underlines a specific response of SBN glasses to external irradiation. Glasses with higher sodium content are more stable under β_{e^-}-irradiation. For these glasses, irradiation does not alter their hardness nor SCC behavior, whereas low [Na_2O] glasses present huge variations. The role of the initial glass composition before irradiation is also seen in the amplitude of the evolution in the mechanical properties after ion irradiation. Ballistic interactions predominantly change the mechanical response. This is clearly seen after 6 MeV helium ions irradiation. The variations in the hardness and in the crack path (as observed from stress corrosion experiment) localize in the thin layer where the ballistic interactions maximize. Finally, the electronic interactions simulated by electron and helium ions are not equivalent. Further investigations should be conducted, a reason maybe be the volume of deposited energy. Electron irradiation penetrates through the 0.8 mm whereas, helium ions penetrate only a thin layer of the sample ($\sim$ 30 μm). In summary this work underlines some still open questions. Concerning the pristine glass studies, a better understanding in the glass behavior in stress corrosion is needed. Specially, how the crack propagates is unclear. Simulations using ReaxFF could help in a better understanding these processes. This investigation is crucial to predict the glass behavior in stress corrosion; and hence, the life time of these materials. Other experiments with larger chemical compositions range can also be conducted. It is important to extract the relevant parameter which describes the behavior in the stress corrosion region. Finally, the investigations on hardness behavior underline the huge role of the residual stress in the cracking behavior. Understanding these stresses is a major challenge for the future. Finally, the discrepancy in the electronic interactions between electron and helium ions irradiation should be understood.

Appendices

Appendix A

AFM image analysis: extraction of information

Pure silica samples present protuberances after irradiation on their post-mortem fracture surfaces. Treatment of AFM images enables tracking the evolution of the number and size of spots. Tracking features on topographical images proved to be difficult at first because they are small. On the other hand, adhesion image (acquired at every pixel) provide the need contrast. In a first turn, these high contrast images form a mask to via their visible features. Overlaying this mask onto height images reveals: the size, the height and the area of the spots. Figure A.1 displays a raw AFM adhesion image acquired via the PeakForce Tapping mode on a Bruker Icon AFM. This image corresponds to a fracture surface in the ballistic damage region of a He^{2+}-irradiated silica sample. The spots correspond due to microdamage created during helium irradiation.

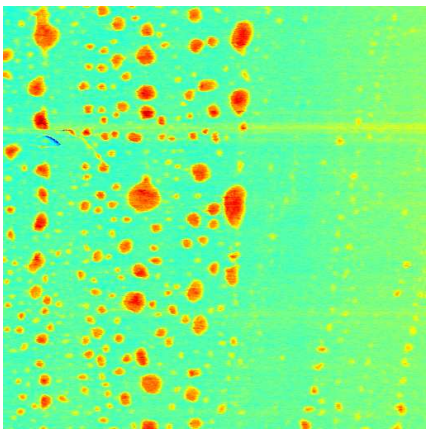

Figure A.1: Adhesion AFM image of pure silica glasses He^{2+}-irradiated. This area corresponds to a zone around $\sim$ 20 % from the free surface. Only a mean plane is subtracted.

Figure A.2 left presents the protuberances due to irradiation. A rough mask is created from this image. In first step, a judicious threshold value enables the detection of the most visible defects on the surface. Figure A.2 right depicts the resulting mask from the threshold test to detect the major defects.

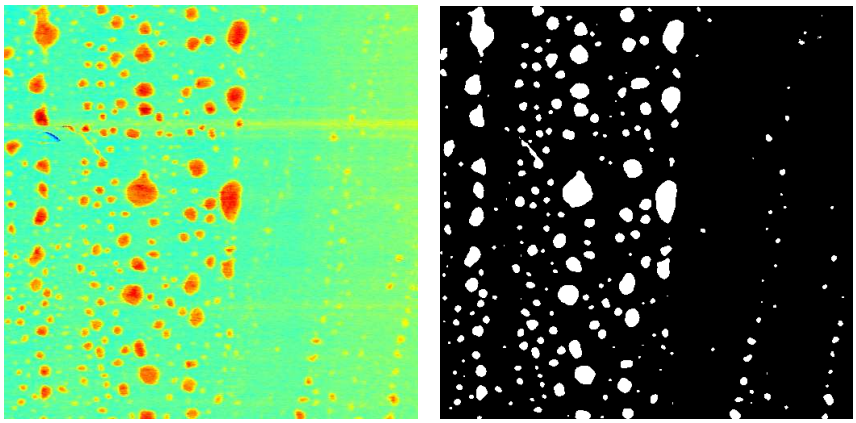

Figure A.2: (Left) Adhesion AFM image of pure silica glasses He^{2+}-irradiated. This image is the same than presented in A.1. (Right) The image depicts resulting "mask" ("rough" binary image due to the threshold test to detect the major defects).

This "mask" does not depict smaller defects. Subtracting mask (figure A.2 right) from the original AFM image (figure A.1) reveals finer details of the ordinal mask. . Figure A.3 left depicts the resulting image. Figure A.3 results from a second threshold pass with a new value. This becomes the new mask take and takes into account thinner features. This procedure is repeated as many times as necessary. Adding the

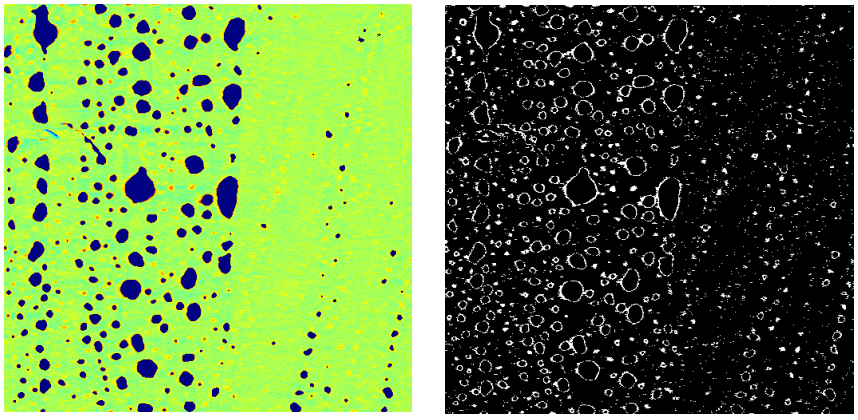

Figure A.3: (Left) Adhesion AFM image of pure silica glasses He^{2+}-irradiated. This image is the same as presented in A.1 with the image A.2 right removed. (Right) The image depicts the second "mask" finer details are revealed.

two mask (figure A.2 right and figure A.3 right) gives the final mask. The final mask is noisy. Image treatment cleans the mask giving mostly correct associations however some wrong ones are feasible. Figure A.5 left reveals incorrect associations due to image treatments. These deformations occur during the treatment and must be corrected. Figure A.4 right shows the final mask. Now treating the images

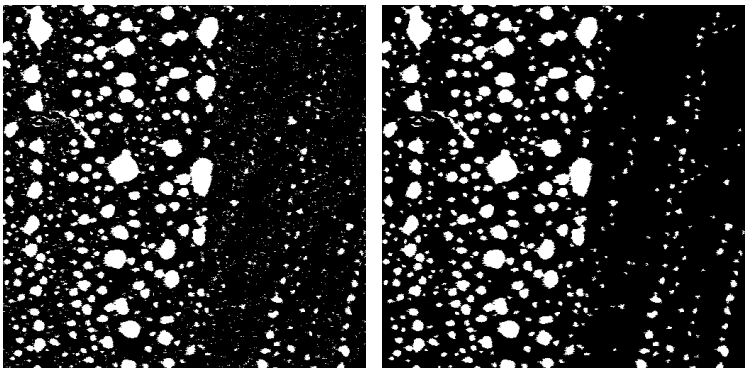

Figure A.4: Mask obtained after two iterations: (Left) raw; (Right) after image treatment.

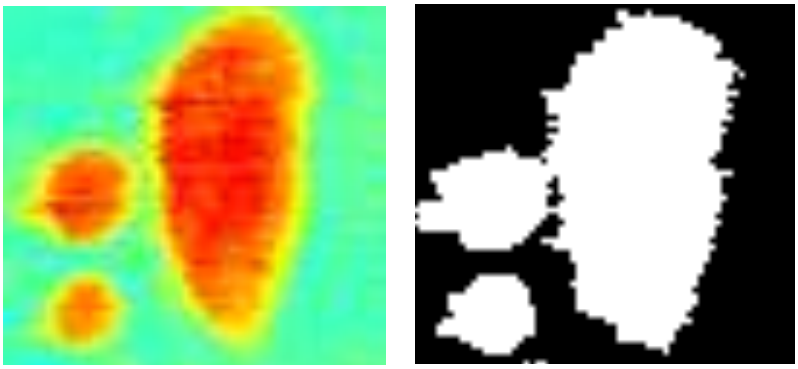

Figure A.5: Example of distortion before and after images treatment.

reveals the number, the size, etc. of protuberances.